# Investigations of electron dynamics in ion-dimer collisions that facilitate interatomic Coulombic decay

Darij Starko

A Dissertation submitted to the Faculty of Graduate Studies in Partial Fulfillment of the Requirements for the Degree of Doctor of Philosophy

Graduate Program in Physics and Astronomy

York University

Toronto, Ontario

May 2026

## ABSTRACT

In the field of atomic physics, there have been developments and investigations into emergent processes in clusters. One specific process that has gained interest in recent times is called interatomic (or intermolecular) Coulombic decay (ICD). This is a decay mechanism in which electron removal from one atom (molecule), which leaves the ion in an excited state, results in low-energy electron emission from a neighbouring atom (molecule) and cluster fragmentation. This process is extremely quick and has attracted considerable attention due to its ubiquity across various research fields coupled with the applied relevance of low-energy electrons owing to their effectiveness in breaking molecular bonds and inflicting damage to biological matter, such as in radiotherapy treatment of cancer patients. To study this process, I developed models to describe the interactions that occur and facilitate ICD through ion-cluster collisions.

These collisions present challenges in the form of quantum-mechanical many-body problems that cannot be solved analytically, requiring approximation methods such as the independent atom model and independent electron model. In this case, each atom's electrons' quantum-mechanical $N$-body Hamiltonian is treated as $N$ single-electron problems.

With regards to facilitating ICD, the electron dynamics of the system that precede cluster fragmentation are important in understanding the structure of the fragmented parts and their relative yields. With research groups conducting ion-cluster collision experiments, there is ample opportunity to test the predictions of my work by experimental measurements.

The system is arranged with fixed targets and a projectile travelling in parallel to the dimer target axis, in order to simplify the study and understand the electron dynamics in the collision. The theoretical underpinning of the research is based on employing a simplified time-dependent Hartree-Fock approximation alongside the two-center basis generator method that constructs the basis states for calculating transition amplitudes. These amplitudes and subsequently calculated probabilities are employed in statistical analyses to study the electron dynamics of the collisions and how they can facilitate ICD.

The analyses used include a combinatoric multinomial probability method and a determinantal method employing inclusive probabilities. Submodels for each analysis change the character of the interactions as a function of the charge number of the projectile during the

collision.

The results from these investigations show agreement between the analyses across sub-models. For a neon dimer target with a $He^+$ projectile there is a strong indication that interatomic Coulombic decay is highly efficient for single $2s$ electron removal. Interatomic Coulombic decay is also highly efficient for the argon dimer target with a $He^+$ projectile through single $3p$ electron removal with simultaneous $3p$ electron excitation to a higher orbital.

*To my parents, my wife, and my brother, whose steadfast encouragement, love, and belief in my potential have sustained me throughout the course of my long journey.*

*Моїм батькам, дружині та братові, чия стійка підтримка, любов і віра в мій потенціал супроводжували мене протягом моєї довгої подорожі.*

**ACKNOWLEDGEMENTS**

I want to thank my supervisor Dr.Tom Kirchner for his wisdom, guidance, and patience throughout my research. None of this work would have been possible without his support and mentorship. I also want to thank Dr. Marko Horbatsch and Dr. René Fournier for their thoughtful evaluations and constructive feedback that supported the progress of my research.

**CONTENTS**

**LIST OF FIGURES**

## LIST OF TABLES

## Glossary

| | |
|---|---|
| **BGM** | Basis Generator Method |
| **CE** | Coulomb Explosion |
| **CMI** | Capture Model I |
| **CMII** | Capture Model II |
| **COLTRIMS** | Cold Target Recoil Ion Momentum Spectroscopy |
| **DA** | Determinantal Analysis |
| **DFT** | Density Functional Theory |
| **FCM** | Fixed-Charge Model |
| **FEL** | Free-Electron Laser |
| **IAM** | Independent Atom Model |
| **ICD** | Interatomic Coulombic Decay |
| **IEM** | Independent Electron Model |
| **KS** | Kohn-Sham |
| **LEE** | Low-Energy Electrons |
| **MA** | Multinomial Analysis |
| **MCMI** | Modified Capture Model I |
| **MCMII** | Modified Capture Model II |
| **OPM** | Optimized Potential Method |
| **RCT** | Radiative Charge Transfer |
| **TC-BGM** | Two-Center Basis Generator Method |
| **TDHF** | Time-Dependent Hartree-Fock |
| **TDSE** | Time-Dependent Schrödinger Equation |

# INTRODUCTION

The focus of the present dissertation is the theoretical analysis of ion-cluster collisions from low to intermediate projectile impact energies that facilitate interatomic Coulombic decay (ICD). ICD is an ultrafast decay process in which an outer valence electron in an ionized atom de-excites to fill a vacancy, and the energy released from this transition is transferred to a neighbouring atom, inducing ionization [1]. This mechanism was first theorized by Cederbaum and others in 1997, where it was predicted that a set of singly and doubly ionized states emerge below the double- and triple-ionization thresholds of $(HF)_3$ and $(H_2O)_3$ clusters respectively [2]. The first experimental evidence for this decay mechanism was observed by Marburger et al. [3] in neon clusters. Shortly thereafter, Jahnke et al. reported an unambiguous ICD signal in the neon dimer system [4], a rare-gas compound formed by two atoms bound via weak van der Waals interactions [5]. In this minimal two-center system, the ICD process leads to the emission of a low-energy electron and the formation of a $Ne^+$–$Ne^+$ ion pair, which fragments via Coulomb explosion driven by the mutual repulsion of the two positive charges [4].

Short ICD decay times imply a dominant relaxation mechanism that out-competes other potential channels resulting in a high efficiency. The predicted high efficiency of ICD was confirmed by Öhrwall and coworkers by measuring the $2s$ vacancy lifetime in neon clusters [6]. The $2s$ vacancy in neon atoms is important as subsequent valence electron relaxation to the ionic ground state has enough energy to transfer to a neighbouring neon atom to initiate ICD, being the most dominant pathway in neon dimers [6]. The short vacancy lifetime is attributed to the coordination dependent ICD which is very sensitive to internuclear distances [6]. The equilibrium bond length of neon dimers is 5.86 a.u., which allows for ICD to occur and is the internuclear distance of the target system under consideration. For the argon dimer target, this distance is 7.15 a.u. [7].

Since its discovery, investigations into ICD have been extensively done for a variety of target systems, such as van der Waals clusters [3, 4, 8–15], molecular anions [16], hydrogen-bonded clusters [17–20], nanodroplets [21–23], solids [24], solvated ions [25], and unbounded molecules [26]. Over the last 20 years, multiple methods for facilitating ICD have been employed to detect this decay mechanism. A popular method for instigating ICD has been

from photoionization through synchrotron radiation [3, 4, 21, 23] or free-electron laser (FEL) radiation [12, 27–29]. Other methods include using electron beams [20, 30–34] and ion projectiles [11, 13, 24, 35, 36].

Synchrotron radiation is a popular method for facilitating ICD because it provides tunable electromagnetic radiation over a broad photon-energy range, enabling selective ionization of inner- and outer-valence shells [1]. This tunability allows precise preparation of initial electronic states and well-controlled excitation pathways. Modern synchrotron facilities also deliver pulsed radiation with sufficiently high pulse rates to support multi-particle coincidence and time-of-flight (TOF) measurements, which are central to kinematically complete ICD experiments. A limitation of synchrotron-based approaches in linewidth and lineshape studies is that the instrumental bandwidth and pulse structure must be well characterized, and reliable extraction of natural linewidths requires accurate knowledge of the underlying spectral profile [1].

Time-resolved investigations of ICD dynamics frequently employ pump–probe techniques, in which an initial short light pulse prepares an excited or ionized state and a second, time-delayed pulse probes the subsequent relaxation dynamics [1]. Such measurements benefit from very high peak intensities and ultrashort pulse durations. FELs are particularly well suited for this purpose, as they deliver femtosecond or even sub-femtosecond pulses with very high peak brilliance in the XUV and x-ray regimes. Compared with synchrotron sources, FEL radiation provides substantially higher peak intensities, thereby enabling nonlinear excitation pathways and multiphoton processes in addition to single-photon ionization [1]. These characteristics make FEL facilities especially powerful for time-resolved ICD studies and for exploring excitation regimes that are inaccessible with conventional synchrotron radiation. However, FELs typically provide less overall flux than synchrotron radiation and the experimental setup is complex and expensive.

Complementary to photon-based methods, ICD can also be initiated by charged-particle impact using electron or ion beams. In these collision-driven experiments, inner-valence vacancies are produced through direct impact ionization, after which ICD proceeds as an interatomic relaxation channel. A principal advantage of particle-impact methods is that they closely resemble collision environments encountered in plasmas and radiation damage scenarios, and they can provide access to excitation pathways that differ from photoionization [37]. In addition, reaction microscopes and multi-coincidence detection techniques can

be combined with ion and electron beams to obtain kinematically complete measurements of fragments and emitted electrons [1]. A popular technique for coincidence measurements of fragmented ions and ejected electrons is Cold Target Recoil Ion Momentum Spectroscopy (COLTRIMS). A projectile ion beam and target gas jet intersect perpendicularly in the plane in a small region the size of $1mm^3$ [1, 11]. A homogenous magnetic field and a parallel weak electric field guide the fragmented ions and electrons to time and position sensitive plate detectors. The electric fields are typically generated by ring-shaped electrodes and the magnetic field by a pair of Helmholtz coils.

Another advantage of this experimental method for ICD generation is the availability of electron beam sources and control of electron energy for ionization of dimers and clusters. A benefit in using ion beams is that they can participate in the relaxation process involving charge and energy transfers. However, in contrast to photoionization, where the deposited energy is sharply defined by the photon frequency, the energy transfer in charged-particle collisions is distributed over a broad range and depends on impact parameter and scattering dynamics. There is also a more limited spatial resolution in experiments, complicating studies of small or geometrical complex systems. This leads to less selective initial-state preparation and more complex interpretation of the excitation mechanism relative to photon-driven ICD [1].

The ICD process was only discovered over 20 years go, especially considering that this process occurs in gas clusters and diverse groupings of molecular systems with the modified name of intermolecular Coulombic decay. A reason as to why this process may not have been previously observed in experiments could be due to the low kinetic energy of ICD electrons [1]. Experiments on clusters, especially those in the gas phase, observe a low-energy electron background due to inelastic scattering, masking ICD electrons [38]. When a large quantity of ICD processes occur in a system, when large showers of these low kinetic energy electrons are emitted, these are called low-energy electrons (LEE). LEE are an identifiable feature of ICD, especially in systems involving ion collisions with matter. LEE can appear as a shower of electrons from radiotherapy for cancer treatments, where it has been suggested that ICD contributes significantly to generating them [39]. The showers come from the colliding ions striking molecules and triggering a cascade of electron emissions that cause damage to DNA [40, 41] and the radical species leftover can react with biomolecules in living tissue [42, 43].

Given the importance of understanding secondary effects of radiotherapy treatments, investigating ion-cluster collision systems and the electron shower profile are of interest. This study explores a theoretical analysis of ion-dimer collisions as a method of facilitating ICD.

The collision systems are chosen to have projectile ions $He^{2+}$ and $He^{+}$ with neon and argon dimers as targets. The $He^{2+}$ and $He^{+}$ projectiles are chosen given their ability to facilitate multi-electron processes without over-complicating the necessary electron dynamics of the system. The target systems were chosen given the efficient and well known ICD channels in Ne($2s$) and in excited argon states, and experimental investigations into them [11, 35]. The clusters impacted by these ions undergo various electron processes that result in several forms of cluster fragmentation, with one of the outcomes being ICD. For the argon dimer target, a single electron vacancy in $3s$ is insufficient to facilitate ICD, and instead two $3p$ vacancies alongside an $nl$ excited electron state are energetically viable for ICD. Measurements of ICD to direct ionization electron ratios were conducted by Kim et al [11] for medium projectile impact energies over 100 keV/amu, and that energy regime is used to test the statistical analysis techniques developed in the following chapters given the dominance of capture and ionization processes in the energy regimes considered.

Given the two systems of neon and argon dimer targets, different statistical analyses were done to compare results, with submodels that change the impact of electron capture and ionization processes on projectile charge. Different models were used to test various ways electrons may or may not be captured by the projectile and its effect on electron dynamics while exploiting collision geometry.

With the breadth of theoretical and experimental work conducted on ICD in gas dimers, especially such as $Ne_2$ and $Ar_2$ [11, 35, 44, 45], the models we have developed offer an expanded theoretical treatment of ion-dimer collisions over the few that have been proposed. In Iskandar et al. [46], a Monte Carlo Coulomb Over-the-Barrier Model was employed. The Coulomb Over-the-Barrier Model treats the collision before and after projectile approach with each atom, all while considering an effective projectile and target charge. Monte Carlo simulations are used to obtain capture multiplicity probabilities based on the combinatorial ways electrons can be captured into quantum states either on the projectile or target. The projectile travels in a straight line while each atom in the dimer is treated independently and remains fixed during the collision. Finally, the authors included an analysis of the transverse

momentum exchange between the projectile and target by partitioning the collision as a series of charge exchange.

Another theoretical treatment of ion-dimer collisions comes from Kirchner [45, 47], on which this research builds on. The collision system is modeled in the framework of a semi-classical approximation, where the projectile travels in a straight line and the dimer remains fixed in space during the collision. An independent atom model is used to treat each atom in the dimer target separately, allowing for the removal probabilities to be statistically combined for each atom. An independent electron model (IEM) was used for ion-atom collision calculations, where the two-center basis generator method (TC-BGM) built the basis states to solve the single-particle Schrödinger equations for each of the electron states. Static and dynamic response potentials were also used to model the electron removal processes. The transition amplitudes obtained from these calculations are used to find capture and removal probabilities, and used in a combinatoric final state multinomial analysis to obtain collision cross-sections.

We expand on this work to include further statistical analysis techniques and excitation channels. This includes developing projectile impact energy dependent models that account for change in projectile charge during collision, and multiple variants of these models based on statistical techniques. A dynamical response model is implemented, in combination with various projectile charge models and statistical techniques for ion-dimer collisions. Theoretical treatments are also implemented for different initially charged projectiles and the change in availability of reaction channels within these new models. The investigations result in calculated cross-sections and in understanding of the ICD yield based on electron vacancy production channels that facilitate it and their dependence on model and projectile charge.

The results of this work suggest new avenues of experimental investigations to validate this research.

## 1. INDEPENDENT ATOM AND ELECTRON MODELS IN ION-DIMER COLLISIONS

---

In the collision systems presented, a semi-classical approximation is taken to treat the motion of the nuclei in linear trajectories. At low to intermediate energies (10 - 150 keV/amu), the projectile travels fast enough relative to the dimer such that the linear trajectory is a valid approximation. The projectiles travel at constant speed $|\mathbf{v}|$ in a straight line parallel to the target dimer axis, where the impact parameter is the same with respect to both atomic centers. The dimers in this system are set at a fixed bond length throughout the collision, given that the dimer vibrational period is an order of $10^4$ greater than the collision time.

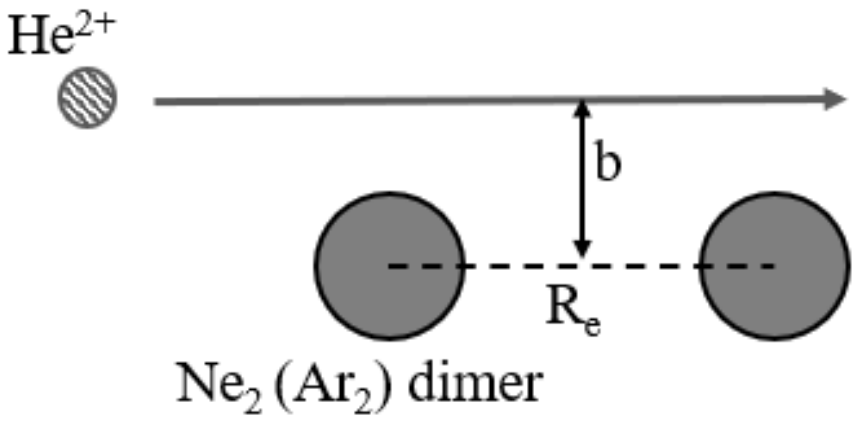


Figure 1: $He^{2+}$-$Ne_2(Ar_2)$ ion-dimer collision system in parallel orientation.

The collision system in Figure 1 presents a $He^{2+}$ projectile with a neon or argon dimer target, at impact parameter $b$ and highlights the sequential nature of the collisions. The parallel orientation is specifically chosen so as to exploit a sequential collision sequence of the projectile with the target atoms in the dimer. The change in the projectile's charge by electron capture will affect its interaction with the second atom in the sequential collision with the dimer, offering an interesting test bed for models with changing projectile charge throughout the course of a collision. The impact of this will be discussed in the models presented in section 3.

In Figure 2 the distances with respect to the center of mass of the projectile and a target atom are presented, where distances $\mathbf{R}_T(t)$ and $\mathbf{R}_P(t)$ are the distances from center of mass

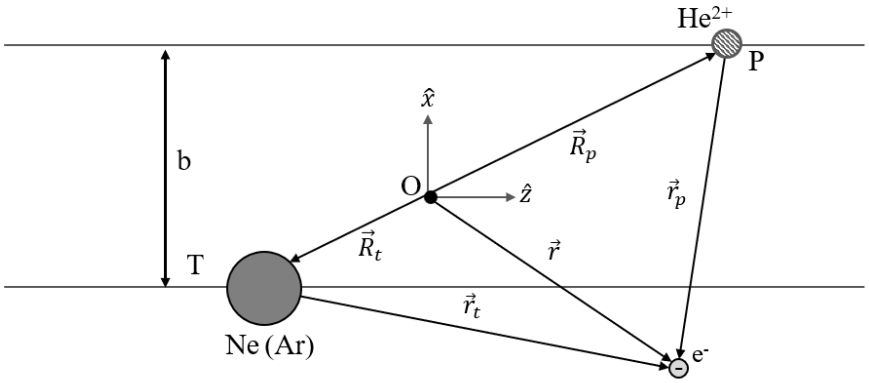


Figure 2: $He^{2+}$-Ne(Ar) center of mass frame

to the target and projectile respectively.

The orientation of the collision system is the same for all combinations of projectile and dimer studied here, though only projectiles with energy of 10 keV/amu are considered for the neon dimer target, while a set of impact energies in the 10-150 keV/amu range are studied in the case of $Ar_2$.

### 1.1. Independent Atom Model

Given the orientation of the system as described, frameworks are chosen to simplify the collision system modeling. The atoms in these dimers and their interactions with the projectile are treated independently of each other with their own time-dependent Hamiltonians, which is called the independent atom model (IAM). Using the assumption that the dimer can be treated as a composite of atomic systems, the collision net cross-sections can be calculated as a sum of atomic cross-sections using Bragg's additivity rule (AR) [48]. A variant of the AR assumes that a large molecule can be decomposed into smaller ones and the cross-sections of the latter added up [49]. The AR yields reasonable results for collision energies where the cross-sections of the constituents are relatively small, and when not, they tend to overestimate experimental results [49, 50].

## 1.2. Independent Electron Model

### *1.2.1. Multi-Electron Problem*

Within a semi-classical approximation and non-relativistic framework, the ion-atom collision system is reduced to a many-electron problem described by a time-dependent Schrödinger equation (TDSE) in atomic units ($\hbar = m_e = e = 4\pi\varepsilon_0 = 1$)

$$\left(\hat{H}(t) - i\partial_t\right)\Psi(t) = 0, \tag{1}$$

with the initial condition $\Psi(t_0) = \Psi_0$. The Hamiltonian $\hat{H} = \hat{T} + \hat{v}_{ee} + \hat{v}_{ext}(t)$ comprises the kinetic energy of the electrons, electron-electron interactions, and the external Coulomb potential energy of the collision centers. This is an $N$-electron system, where $N = N_T + N_P$ ($N_T$ and $N_P$ are the total number of target and projectile electrons respectively) [51]. The Hamiltonian for this system is expressed as

$$\hat{H} = \sum_{i=1}^{N}\left(-\frac{1}{2}\Delta_i\right) + \sum_{i<j}^{N}\frac{1}{|\mathbf{r}_i - \mathbf{r}_j|} + \sum_{i=1}^{N}\left(-\frac{Q_T}{|\mathbf{r}_i - \mathbf{R}_T(t)|} - \frac{Q_P}{|\mathbf{r}_i - \mathbf{R}_P(t)|}\right) \tag{2}$$

where the first, second and third terms correspond to $\hat{T}$, $\hat{v}_{ee}$ and $\hat{v}_{ext}(t)$ respectively [51]. $Q_T$ and $Q_P$ correspond to the target and projectile charges respectively. The distances between the $i$-th electron and each of the other electrons is given by $|\mathbf{r}_i - \mathbf{r}_j|$, while its distances to the target and projectile centers are $|\mathbf{r}_i - \mathbf{R}_T(t)|$ and $|\mathbf{r}_i - \mathbf{R}_P(t)|$ respectively [51].

Given the difficulty of addressing such a many body problem, a simplification is employed to treat the electrons by what is referred to as the independent electron model (IEM). In this model the many body $N$-electron problem is reduced to $N$ single-electron problems. Given that the projectiles either have none or one bound electron, in the systems studied here the problem is addressed as having $N_P = 0$ or $N_P = 1$ electrons. The model is based on the time-dependent Hartree-Fock approximation (TDHF), which starts with the assumption that the wavefunction of the electronic system can be described by a single Slater determinant for all times $|\Psi\rangle = \left|\psi_{1\sigma_1}\ldots\psi_{N_T\sigma_{N_T}}\phi_\sigma\right\rangle$ in which the spin orbitals $|\psi_{i\sigma_i}\rangle$ and $|\phi_\sigma\rangle$ denote the occupied target and projectile electron states respectively, with spin indices $\sigma_i = \uparrow, \downarrow$ [51].

The TDHF equations are obtained from the variation of the action based on the Hamil-

tonian (1)

$$S[\Psi] = \int_{t_i}^{t_f} dt \langle \Psi(t) | i\partial_t - \hat{H}(t) | \Psi(t) \rangle. \tag{3}$$

Imposing the condition that the variation of the action vanishes, $\delta S = 0$, results in the following TDHF equations

$$\begin{aligned} i\partial_t \psi_{i\sigma_i}(\mathbf{r},t) = & \left( -\frac{1}{2}\Delta - \frac{Q_T}{r_T} - \frac{Q_P}{r_P} + \sum_{k=1}^{N_T} \int d^3r' \frac{|\psi_{k\sigma_k}(\mathbf{r}',t)|^2}{|\mathbf{r}-\mathbf{r}'|} \right) \psi_{i\sigma_i}(\mathbf{r},t) \\ & - \sum_{k=1}^{N_T} \delta_{\sigma_i\sigma_k} \psi_{k\sigma_k}(\mathbf{r},t) \int d^3r' \frac{\psi^*_{k\sigma_k}(\mathbf{r}',t)\,\psi_{i\sigma_i}(\mathbf{r}',t)}{|\mathbf{r}-\mathbf{r}'|} \\ & + \int d^3r' \frac{|\phi_\sigma(\mathbf{r}',t)|^2}{|\mathbf{r}-\mathbf{r}'|} \psi_{i\sigma_i}(\mathbf{r},t) - \delta_{\sigma_i\sigma} \int d^3r' \frac{\phi^*_\sigma(\mathbf{r}',t)\,\psi_{i\sigma_i}(\mathbf{r}',t)}{|\mathbf{r}-\mathbf{r}'|} \phi_\sigma(\mathbf{r},t), \end{aligned} \tag{4}$$

for initial target electron states $i = 1, ..., N_T$, and

$$\begin{aligned} i\partial_t \phi_\sigma(\mathbf{r},t) = & \left( -\frac{1}{2}\Delta - \frac{Q_T}{r_T} - \frac{Q_P}{r_P} + \sum_{k=1}^{N_T} \int d^3r' \frac{|\psi_{k\sigma_k}(\mathbf{r}',t)|^2}{|\mathbf{r}-\mathbf{r}'|} \right) \phi_\sigma(\mathbf{r},t) \\ & - \sum_{k=1}^{N_T} \delta_{\sigma\sigma_k} \int d^3r' \frac{\psi^*_{k\sigma_k}(\mathbf{r}',t)\,\phi_\sigma(\mathbf{r}',t)}{|\mathbf{r}-\mathbf{r}'|} \psi_{k\sigma_k}(\mathbf{r},t) \end{aligned} \tag{5}$$

where $r_T = |\mathbf{r} - \mathbf{R}_T|$ and $r_P = |\mathbf{r} - \mathbf{R}_P|$. Equation (4) corresponds to the time-evolution of initially occupied target orbitals with the kinetic energy, combined potentials of the nuclei and effective electron interactions. The first term with the sum of integrals in the first line and the first term in the third line of (4) are the Hartree potentials due to the target and projectile electrons:

$$v_H^\psi(\mathbf{r},t) = \sum_{k=1}^{N_T} \int d^3r' \frac{|\psi_{k\sigma_k}(\mathbf{r}',t)|^2}{|\mathbf{r}-\mathbf{r}'|} \tag{6}$$

$$v_H^\phi(\mathbf{r},t) = \int d^3r' \frac{|\phi_\sigma(\mathbf{r}',t)|^2}{|\mathbf{r}-\mathbf{r}'|}. \tag{7}$$

The other terms in equation (4) correspond to electron exchange terms. This same potential structure is reflected in equation (5), though it is simplified given a single bound electron on the projectile [51]. The implementation of the TDHF approach provides an approximation of electron-electron interactions, with correlation effects ignored. A possible definition of correlation for a stationary problem as proposed by Löwdin [52], is the difference between a Hartree-Fock calculation and the exact solution of the Schrödinger equation [53]. However, in the time-dependent case, the definition of correlation is less straightforward [54, 55]. One proposal, by Stolterfoht, defines it as the difference between the exact transition amplitudes

and those predicted by the TDHF approximation [55]. This definition has the issue that TDHF calculations can oscillate in time [56, 57].

Over the course of the collision, the wave function evolves in time and consequentially the Hartree potential is changing, which physically describes the changing charge cloud screening the nuclei. Together with the time-dependent exchange terms this results in non-linearity of the TDHF equations, and as a consequence the transition amplitudes obtained by projecting propagated wave functions onto final states oscillate in time, even at asymptotically large distances [51].

The single-particle equations (4) and (5) are approximated in a simplified format as follows [51]:

$$i\partial_t \psi_i(\mathbf{r},t) = \hat{H}_\psi \psi_i(\mathbf{r},t) \quad i = 1, ..., N_T, \tag{8}$$

$$i\partial_t \phi(\mathbf{r},t) = \hat{H}_\phi \phi(\mathbf{r},t), \tag{9}$$

with Hamiltonians

$$\hat{H}_\psi = -\frac{1}{2}\Delta - \frac{Q_T}{r_T} - \frac{Q_P}{r_P} + v_{ee}^{\psi}(\mathbf{r},t) + v_H^{\phi}(\mathbf{r},t), \tag{10}$$

$$\hat{H}_\phi = -\frac{1}{2}\Delta - \frac{Q_T}{r_T} - \frac{Q_P}{r_P} + v_H^{\psi}(\mathbf{r},t), \tag{11}$$

where the potentials $v_H$ are the Hartree potentials (6,7) and $v_{ee}^{\psi}(\mathbf{r},t) = v_{ex}^{\psi}(\mathbf{r},t) + v_H^{\psi}(\mathbf{r},t)$, where $v_{ex}^{\psi}$ is a local exchange potential that cancels the self-interaction contribution contained in the Hartree potential $v_H^{\psi}$ [51].

As the orbitals from equations (8) and (9) evolve in time, they lose their orthogonality [51]. These equations will be combined as addressed in section 1.3, with the various approaches discussed.

Focusing on the target Hamiltonian (10), the single-electron target potential is summarized as an effective potential

$$v_{eff}^{\psi}(\mathbf{r},t) = -\frac{Q_T}{r_T} + v_{ex}^{\psi}(\mathbf{r},t) + v_H^{\psi}(\mathbf{r},t), \tag{12}$$

and the projectile potential as

$$v_{eff}^{\phi}(\mathbf{r},t) = -\frac{Q_P}{r_P} + v_H^{\phi}(\mathbf{r},t). \tag{13}$$

The target potential is separated into a static and dynamic part

$$v_{eff}^{\psi}(\mathbf{r},t) = v_{eff}^{0}(\mathbf{r}) + \delta v_{eff}(\mathbf{r},t), \tag{14}$$

where the static potential $v_{eff}^{0}(\mathbf{r})$ is the ground-state potential, while the time-dependent potential is $\delta v_{eff}(\mathbf{r},t)$, which satisfies $\delta v_{eff}(\mathbf{r},t_0) = 0$ at initial time. First, the ground-state potential is addressed, followed by a description of the time-dependent potential.

### *1.2.2. Ground State Potential*

The application of an effective potential description is useful in providing a simplification that separates potentials into components that are more manageable and offer insights into the system under consideration. The static effective potential $v_{eff}^{0}(\mathbf{r})$ is treated as the ground state potential for an unperturbed collision partner. When specifically looking at the effective target potential $v_{eff}^{0}(\mathbf{r})$, it is an effective potential that includes the nuclear Coulomb potential as well as Hartree and exchange terms. It is calculated by an (exchange-only) optimized potential method (OPM) [58]. This is an iterative method developed by Talman and Shadwick to find a well-suited local potential to replace the non-local HF scheme [59]. The single-electron orbitals $\psi_i$ are obtained from the Schrödinger equation

$$\left(-\frac{1}{2}\Delta + v_{eff}^{0}(\mathbf{r})\right)\psi_i = \varepsilon_i \psi_i. \tag{15}$$

The energy expectation value of the Hamiltonian $\left\langle \hat{H} \right\rangle$ with respect to the Slater determinant of the electron orbitals $\psi_i$ is obtained by minimizing the variation of the orbitals that determine the effective potential [59]. This leads to linear integral equations which are the OPM equations

$$\int d^3\boldsymbol{r}' K(\boldsymbol{r},\boldsymbol{r}')\, v_{ex}(\boldsymbol{r}') = Q(\boldsymbol{r}) \tag{16}$$

where $K$ is the kernel and $Q$ is an inhomogeneity, and both are functionals of the orbitals and their energy eigenvalues [59]. In the case of closed shell atoms, the angular dependence can be eliminated, resulting in spherically symmetric radial OPM equations for the exchange potential $v_{ex}$

$$v_{ex}(r_T) = v_{eff}^{0}(r_T) - v_H(r_T) + \frac{Q_T}{r_T}. \tag{17}$$

Using an iterative numerical process, the OPM equations and the Schrödinger equation are solved for the self-consistent orbitals $\psi_i$ and effective potential $v_{eff}^{0}$. This approach has

been shown to be the exchange-only limit of the Kohn-Sham (KS) scheme [60] of density functional theory (DFT) [61]. When the exact HF energy expression is used, then the DFT approach to OPM is identical to the HF potential by Talman and Shadwick, where there is the addditional constraint that the effective potential remain local. A notable and relevant feature of OPM potentials is the cancellation of self-interaction contributions contained in the Hartree potential, such that the correct asymptotic behaviour

$$v_{ee}^{OPM}(r_T) \xrightarrow{r_T \to \infty} \frac{N_T - 1}{r_T} \tag{18}$$

is observed [62]. A further overview of the OPM within the DFT framework can be found in the following resources [58, 61, 63, 64].

The projectile potential (13) is a Coulomb potential for $He^{2+}$ impact and a sum of the Coulomb potential and the screening potential of (7) in the case of $He^{+}$. In the latter case, the term $\phi_\sigma$ in (7) is selected as the (numerical) ground-state HF orbital $\phi_{1s}$ of neutral helium [65]. This particular choice of $1s$ orbital ensures that an electron captured into the ground state of the projectile has the HF binding energy of neutral helium ($\epsilon_{1s} = -0.918$ au) [65]. Another choice would be of a hydrogen-like $1s$ orbital of $He^{+}$ [51], resulting in a less-realistic binding energy ($\epsilon_{1s} = -0.821$ au) of a captured electron [65].

Regardless of the choice of orbital, at close distance the projectile potential goes as $-2r^{-1}$ and decays as $-r^{-1}$ asymptotically.

### *1.2.3. Response Model*

In the previous section, the static potential was considered in what is referred to as the no-response model. This model is valid with the assumption that the projectile impact velocity is greater than an average orbital velocity. This quantity is called $\bar{v}$, which is the average orbital velocity of an outer target electron, where $\bar{v}$ corresponds to an impact energy of 43 keV/amu for Ne [66], and 30 keV/amu for Ar [67]. At these higher velocities, the electron density of the target potential does not substantially change over the course of the brief collisions. However, at low to intermediate projectile impact energies, time-dependent screening effects play an important role. This results in a nonzero time-depedent potential $\delta v_{eff}(\mathbf{r}, t)$ in (14) in what is called the response model.

The present work uses the approach presented in [68], which was designed to account in

a global fashion for how the target potential changes during ionization and capture throughout the collision. It is assumed that the dynamic target potential is described by a linear combination of ionic ground-state potentials $v_q(r_T)$, weighted by time-dependent probabilities $P_q^{loss}(t)$ to produce a target charge state $q$ during the collision [68]. This corresponds to the following ansatz for the time-dependent effective potential:

$$v_{eff}^{\psi}(\mathbf{r},t) = \sum_{q=0}^{N_T} P_q^{loss}(t) v_q(r_T). \tag{19}$$

It is further assumed that $v_q(r_T)$ can be expressed through the self-consistent scaled potential of the neutral target atom for all charge states $q$ [68]. The atomic potential of the neutral atom is written as

$$v_0\left(r_T\right) = -\frac{Q_T}{r_T} + v_{ee}^0(r_T). \tag{20}$$

where

$$v_q\left(r_T\right) = \begin{cases} v_0\left(r_T\right) & \text{for } q = 0 \\ v_0(r_T) - \dfrac{q-1}{N_T-1} v_{ee}^0(r_T) & \text{for } q \geq 1. \end{cases} \tag{21}$$

Some conditions that are needed to satisfy the physical asymptotic behaviour of the potentials are the following: 1) $v_0 = v_{eff}^0(r_T)$, given that the undisturbed atom has $\delta v_{eff} = 0$; 2) for $q = N_T$, $v_q(r)$ reduces to the bare Coulomb target potential (i.e. $-Q_T/r_T$); 3) for $q = 1$, $v_q(r_T)$ equals the neutral atom case so that $v_1(r_T) = v_0\left(r_T\right)$; 4) for $N_T \geq q \geq 1$, $v_q(r_T)$ exhibits an asymptotic behaviour of $-q/r_T$ [68].

Condition 1) can be explained in terms of the physical picture, in which the removal of a single electron results in it being subject to the nuclear Coulomb potential and the remaining $N_T - 1$ bound electrons. This potential goes as $-1/r_T$ at large $r_T$, because it does not reduce the screening from other electrons. Condition 2) ensures that the removal of all target electrons reduces to the Coulomb potential of a bare nucleus. Condition 3) is explained as a method to correct the problem within the TDHF mean field where dynamical screening sets in immediately for some fractional charge removal, and is undesirable for zerofold and onefold electron removal [68].

Applying the first condition into (19) results in

$$v_{eff}^{\psi}(r_T,t) = v_0\left(r_T\right) + \delta v_{ee}(r_T,t) \tag{22}$$

Substituting (21) into (19) one obtains

$$v_{eff}^{\psi}(r_T,t) = v_0(r_T) - v_{ee}^0(r_T)\sum_{q=1}^{N_T} P_q^{loss}(t)\frac{q-1}{N_T-1}, \tag{23}$$

i.e., a separation between the static and dynamic parts, as in (14). The probabilities $P_q$ are calculated using a statistical model, where the target occupation probability is found from

$$P_{net}^{loss} = \sum_{q=1}^{N_T} qP_q^{loss}(t). \tag{24}$$

With the normalization

$$P_0^{loss} = 1 - \sum_{q=1}^{N_T} P_q^{loss}(t), \tag{25}$$

and the net electron removal term from (24), the response potential can be described as

$$\delta v_{ee}(r_T,t) = -\frac{Q_s\,(t)}{N_T-1} v_{ee}^0(r_T) \tag{26}$$

where the screening function $Q_s\,(t)$ is [68]

$$Q_s\,(t) = P_{net}^{loss}(t) + P_0^{loss}(t) - 1. \tag{27}$$

Using this ansatz, and the interpretation of $P_{net}^{loss}/N_T$ as the average single-electron removal probability from the target, $P_0^{loss}$ is obtained using the binomial formula [68]

$$P_0^{loss}(t) = \left(1 - \frac{P_{net}^{loss}(t)}{N_T}\right)^{N_T}. \tag{28}$$

Combining (28), (27), (26) and (22), and calling the net target occupation as the simplified variable $P_{net}^T(t) = N_T - P_{net}^{loss}(t)$, this results in a time-dependent effective potential of

$$v_{eff}^{\psi}(r_T,t) = -\frac{Q_T}{r_T} + a(t)v_{ee}^0(r_T) \tag{29}$$

where $a(t)$ is a scaling factor [69] defined as

$$a(t) = \frac{P_{net}^T - \left(P_{net}^T/N_T\right)^{N_T}}{N_T-1}. \tag{30}$$

The second term in the numerator of (30) can be interpreted as the probability for no electrons to be removed, with the condition that $P_{net}^T$ must never be greater than $N_T$.

### 1.3. Combined Target and Projectile

With the response potential defined, the single-particle target Hamiltonian (10) is fleshed out to be

$$\hat{H}_{\psi} = -\frac{1}{2}\Delta - \frac{Q_T}{r_T} - \frac{Q_P}{r_P} + a(t)v_{ee}^{0}\left(r_T\right) + v_H^{\phi}\left(r_T\right). \tag{31}$$

The target and projectile single-electron Hamiltonians can be combined to include active electrons from both centers in two ways. The first is the *coupled-mean-field approach* of [51] in which the target and projectile electrons are propagated by independently solving the single-electron equations of (8) and (9). This results in the response potential coupling to the projectile through the target Hartree potential in the projectile Hamiltonian. An advantage of this approach is that the electrons of both centers experience potentials that exhibit the correct asymptotic behaviour prior to collision. In particular, a projectile electron has the Coulomb potential of the target nucleus completely screened at asymptotic distances. However, the coupled-mean-field method is disadvantaged by the loss of orthogonality between the propagated target and projectile wave functions. This results in a noticeable error in the final-state analysis [70]. This error was addressed through renormalization of the many-electron wave function [70].

Another approach is the *common-mean-field approach* in which the target and projectile electrons are propagated by the same Hamiltonian. The target and projectile electron wave functions are no longer explicitly distinguished as was done at the beginning of the chapter, with $|\Psi\rangle = |\psi_0 ... \psi_N\rangle$. The single-electron Hamiltonians of (8) and (9) are combined into

$$i\partial_t \psi_i\left(\mathbf{r}, t\right) = \hat{H}\psi_i\left(\mathbf{r}, t\right) \quad i = 1, ..., N, \tag{32}$$

where the common single-electron Hamiltonian is $\hat{H}_{\psi}$ from (31). An advantage of this approach is that the orthogonality between projectile and target wave functions is preserved. However, the behaviour of the target potential at asymptotic distances for a projectile electron is incorrect, going as $-1/r$. Another issue is that the projectile ion is less attractive to its electron given the lack of the projectile exchange potential $v_{ex}^{\phi}$. Given that $N_t > N_P = 1$, and that target electron processes are of interest and less so projectile electron behaviour, this approach is good enough for the needs of this work.

### 1.4. Amplitudes and Probabilities

Transition amplitudes are obtained as inner products of initial to final electron states defined as

$$c_j^i = \langle \phi_j | \psi_i \rangle \,. \tag{33}$$

With these transition amplitudes, $p_j^i = |c_j^i|^2$ is the probability for an electron in an initial state $|\psi_i\rangle$, to be found in a final bound state $|\phi_j\rangle$ of the target $\{\phi_j | 1 \leq j \leq J_T\}$, or projectile $\{\phi_j | J_T < j \leq J\}$ after a collision. The number of target and projectile electrons states respectively being $J_T$ and $J_P = J - J_T$.

Given $p_j^i$, the probability for an electron to be bound to the target, projectile or released to the continuum are given by the following

$$p_i^T = \sum_{j=1}^{J_T} |c_j^i|^2, \qquad p_i^P = \sum_{j=J_T+1}^{J} |c_j^i|^2, \qquad p_i = 1 - \sum_{j=1}^{J} |c_j^i|^2. \tag{34}$$

A feature of single-electron probabilities is that they can be summed to obtain a net probability. This net probability for electrons to occupy the target and projectile respectively is given by

$$P_{net}^T = \sum_{i=1}^{N} \sum_{j=1}^{J_T} |c_j^i|^2, \qquad P_{net}^P = \sum_{i=1}^{N} \sum_{j=J_T+1}^{J} |c_j^i|^2 \tag{35}$$

These net probabilities can then be used in statistical models to understand the electron dynamics that occur during a process, which will be explored in chapter 3.

These probabilities need to be reexamined in the context of the time-dependent potentials. In the case of the *no-response model*, with $\delta v_{eff} = 0$, the bound target and projectile eigenstates at the final time $|\phi_j\rangle$ in (33) are equal to the initial eigenstates $\left|\phi_j^0\right\rangle$ defined by

$$\left(-\frac{1}{2}\Delta + v_{eff}^{0\psi}(r_T)\right) \phi_j^0(r_T) = \epsilon_j^0 \phi_j^0(r_T) \qquad \text{for } j = 1, ..., J_T \tag{36}$$

$$\left(-\frac{1}{2}\Delta + v_{eff}^{0\phi}(r_P)\right) \phi^0(r_P) = \epsilon^0 \phi^0(r_P). \tag{37}$$

However, in the case of the *response model* the eigenstates are different over time throughout the course of the collision [68]. The eigenstates $\left|\phi_j^0\right\rangle$ of the neutral target atom are not the eigenstates of the ionized atom. This results in a need to calculate the probabilities over the course of the collision, and not just in its final state. The dynamically changing target

potential causes projections of the propagated single-particle states onto the unperturbed eigenstates to result in fluctuating transition amplitudes, which were also previously identified in [56, 71]. In the case of this work, to alleviate this problem these probabilities are calculated for 11 different times by sampling at various distances and averaged (from $z = 30$ a.u. to 50 a.u. in the present work) [72].

## 2. BASIS GENERATION

### 2.1. Finite Basis Model Space

Using the *common-mean-field approach* discussed in section 1.3, the Hamiltonian (31) defining the single-electron equation (32) can be decomposed in terms of a stationary $\hat{H}_0$ and time-dependent external potential $\hat{v}(t)$

$$\hat{H}(t) = \hat{H}_0 + \hat{v}(t), \tag{38}$$

which vanishes for asymptotic times.

The single-electron Schrödinger equations are then written as $\hat{O}\,|\psi_i\rangle = 0$ with

$$\hat{O} = \hat{H} - i\partial_t. \tag{39}$$

A simplification is applied given that the propagated wave functions are the same for either spin, reducing the required solutions for the single equations to odd values of $i$ only.

To solve the single-electron Schrödinger equations, a basis expansion approach is taken. This method generates basis sets based on the two centers of the collision, namely the projectile and target atoms. The method was developed in [73], and is an extension of the basis generator method (BGM) described in [74]. The BGM is in essence a coupled-channel method in which the single-electron equations are projected onto a finite set of basis states. The promise of this method is that the model space $\mathcal{A}$ spanned by the basis functions is dynamically adapted to the time-dependent problem, thereby minimizing the couplings to the Hilbert space not covered by the basis states [74]. This has the benefit of reducing the size of the basis system. It was argued in [74], that the model space $\mathcal{A}$ constructed by repeated application of a regularized projectile potential onto atomic eigenfunctions achieves the dynamical representation of $\psi_i(t)$.

The coupled-channel equations that represent this system, can be found by first considering the model space $\mathcal{A}$ and its complement $\mathcal{B}$, and their idempotent and hermitian projection operators $\hat{A}$ and $\hat{B} = 1 - \hat{A}$ onto their respective spaces [74]. It follows from this operator relation that $\hat{A}\hat{B} = \hat{B}\hat{A} = 0$. Using these operators, the propagated state can be separated

into components of each model subspace (subscript $i$ is assumed for $\psi$) [74]

$$|\psi\rangle = \hat{A}\,|\psi\rangle + \hat{B}\,|\psi\rangle = \left|\psi^A\right\rangle + \left|\psi^B\right\rangle. \tag{40}$$

Substituting (40) into $\hat{O}\,|\psi_i\rangle = 0$, the TDSE can be written as

$$\hat{A}\hat{O}\hat{A}\left|\psi^A(t)\right\rangle = -\hat{A}\hat{O}\hat{B}\left|\psi^B(t)\right\rangle \tag{41}$$

$$\hat{B}\hat{O}\hat{B}\left|\psi^B(t)\right\rangle = -\hat{B}\hat{O}\hat{A}\left|\psi^A(t)\right\rangle \tag{42}$$

where the terms on the right hand side correspond to the coupling of the sub spaces to their complementary spaces [75]. A formal solution to the $\mathcal{B}$-space part of the TDSE is given as

$$\left|\psi^B(t)\right\rangle = -i\int_{t_0}^{t}\hat{B}(t,t')\hat{O}(t')\left|\psi^A(t')\right\rangle dt', \tag{43}$$

where $\hat{B}(t,t')$ is the propagator in the $\mathcal{B}$ space that satisfies $\hat{B}\hat{O}\hat{B}(t,t') = 0$ [75]. Inserting (43) into (41) yields

$$\hat{A}\hat{O}\hat{A}\left|\psi^A(t)\right\rangle = \hat{V}_{opt}(t)\left|\psi^B(t)\right\rangle \tag{44}$$

$$\hat{V}_{\rm opt}(t)\left|\psi^A(t)\right\rangle = i\hat{A}\hat{O}(t)\int_{t_0}^{t}\hat{B}(t,t')\hat{O}(t')\left|\psi^A(t')\right\rangle dt', \tag{45}$$

where $\hat{V}_{\rm opt}(t)$ is an optical potential that globally accounts for the coupling between $\mathcal{A}$- and $\mathcal{B}$-spaces [75]. These equations are non-local in time and depend on the history of the dynamics of the system. If $\mathcal{A}$ is spanned by a finite orthonormal set of basis functions $\{|X_j\rangle\,, j = 1, ..., N\}$, this results in coupled-channel equations

$$\mathrm{i}\dot{c}_k = \sum_{j=1}^{N} c_j(t)\left\langle X_k|\hat{O}(t)|X_j\right\rangle - \mathrm{i}\sum_{j=1}^{N}\int_{t_0}^{t} c_j(t')\left\langle X_k|\hat{O}(t)\hat{B}(t,t')\hat{O}(t')|X_j\right\rangle \tag{46}$$

with the coefficients defined as $c_k(t) = \left\langle X_k|\psi^A(t)\right\rangle$ [75]. As introduced in [75], a time evolution of the system can be constructed from a finite set of basis functions designed in a hierarchical structure of finite subspaces, that minimizes the coupling between $\mathcal{A}$- and $\mathcal{B}$- spaces. These basis functions are generated from $K$ eigenstates of the unperturbed Hamiltonian $\hat{H}_0$ from (38)

$$\hat{H}_0\left|\phi_j^0\right\rangle = \epsilon_j^0\left|\phi_j^0\right\rangle, \qquad\qquad j = 1, ..., K. \tag{47}$$

The rest of the basis states are generated from applying the Schrödinger operator with the following recursion relation

$$\left|\phi_j^M\right\rangle = \hat{O}\left|\phi_j^{M-1}\right\rangle = \hat{O}^M\left|\phi_j^0\right\rangle. \qquad\qquad j = 1, ..., K \tag{48}$$

Even though the resulting basis functions lack orthonormality, they are all linearly independent [75]. This implies that the mapping $\left|\phi_j^{M+1}\right\rangle = \hat{O}\left|\phi_j^{M}\right\rangle$ creates states that lie partially outside the defined $M$-fold hierarchy of $\mathcal{R}^{\mathcal{M}}$ space, which is $(1-\hat{R}^M)\left|\phi_j^{M+1}\right\rangle \neq 0$, where the projection operator $\hat{R}^M$ is expressed in terms of the nonorthogonal basis [75]

$$\hat{R}^M = \sum_{\lambda,\mu=0}^{M}\sum_{l,j=0}^{N}\left|\phi_l^{\lambda}\right\rangle\left\langle\phi_l^{\lambda}|\phi_j^{\mu}\right\rangle^{-1}\left\langle\phi_j^{\mu}\right|. \tag{49}$$

$\left\langle\phi_l^{\lambda}|\phi_j^{\mu}\right\rangle^{-1}$ is understood to be a matrix element of the inverse overlap matrix [75]. The $\mathcal{R}^{\mathcal{M}}$-space is identified with the finite model space $\mathcal{A}$, and $\mathcal{Q}^{\mathcal{M}}$ as the infinite complement space. Using the resulting basis functions, the coupled-channel equations (46) can be rewritten as

$$\mathrm{i}\sum_{u=0}^{M}\sum_{j=1}^{K}\dot{c}_j^u\left\langle\phi_k^{u'}|\phi_j^u\right\rangle = \sum_{u=0}^{M}\sum_{j=1}^{K}c_j^u\left\langle\phi_k^{u'}|\hat{O}|\phi_j^u\right\rangle - \mathrm{i}\sum_{u=0}^{M}\sum_{j=1}^{K}\int_{t_0}^{t}c_j^u(t')\left\langle\phi_k^{u'+1}(t)|\hat{B}(t,t')|\phi_j^{u+1}(t')\right\rangle \tag{50}$$

where $0 < u' < M$ [75]. It can be observed that

$$\hat{Q}^M\left|\phi_j^{u+1}\right\rangle = \left(1-\hat{R}^M\right)\left|\phi_j^{u+1}\right\rangle = \left|\phi_j^{u+1}\right\rangle - \sum_{\lambda,\mu=0}^{M}\sum_{l,j=0}^{N}\left|\phi_l^{\lambda}\right\rangle\left\langle\phi_l^{\lambda}|\phi_j^{\mu}\right\rangle^{-1}\left\langle\phi_j^{\mu}|\phi_j^{u+1}\right\rangle \tag{51}$$

$$= \begin{cases} 0 & u \leq M-1 \\ \left|\phi_j^{u+1}\right\rangle & u \geq M \end{cases} \tag{52}$$

i.e., for all basis states less than the maximum index $M$, projection onto the complementary space results in a vanishing coupling as seen with $\hat{B}\left|\phi_j^{u+1}\right\rangle = 0$ [75]. Projection onto the highest hierarchy level results in $\hat{B}\left|\phi_j^{M+1}\right\rangle = \left|\phi_j^{M+1}\right\rangle$, meaning that only states belonging to the $M$-th subset couple to the complementary space through the optical potential [75]. This reduces the coupled equations in (50) to only the first term on the right hand side for $u < M$, and both terms on that side for $u = M$.

A reasonable assumption is that the populations of states (48) decrease for higher order $M$, as the number of interactions required to reach the highest subset increases. The complexity of the basis states rapidly grows for larger $u$, making the recursion relation untenable for large $M$.

### 2.2. Basis Generator Method

To handle the issue of complex basis sets, an alternate approach is taken as introduced in [74] whereby a larger space $\mathcal{A}'$ containing the optimized model space $\mathcal{A}$, $\mathcal{A} \subseteq \mathcal{A}'$, is

constructed from a more easily generated set of basis states $\{\left|\chi_j^u(t)\right\rangle | j = 1, ..., K, u = 1, ..., M\}$. There are two conditions that these basis states need to satisfy: $\mathcal{A}'$ must contain the generating basis (47) of the hierarchy space, and $\hat{O}\left|\chi_j^u(t)\right\rangle$ maps to a linear combination of states $\left|\chi_{j'}^{u'}(t)\right\rangle$ [74]. In [74], the following ansatz is made to generate the basis set $\{\chi_j^u\}$:

$$\chi_j^u(\mathbf{r}) = \hat{W}_p \chi_j^{u-1}(\mathbf{r}) \tag{53}$$

where $\hat{W}_p$ is a regularized projectile potential. As demonstrated in [74], the repeated application of this regularized potential on $\chi_j^0$ (which are spherical Slater-type orbitals) satisfies the conditions for generating a basis in (53). In practice, these orbitals are approximated by the eigenfunctions of the system in the ground state (36) [74]. The BGM introduced in [74] has been used in multiple studies, for example [51, 68, 70, 76–80].

### 2.3. Two-Center Basis Generator Method

Given the interest in investigations of electron capture processes, an extension of the BGM is required to incorporate the projectile center as well, called the two-center basis generator method (TC-BGM). The eigenstates are separated into a number of target and projectile states $J_T$ and $J_P = J - J_T$ respectively [73]. Thus, the generating basis is split in terms of target and projectile eigenfunctions

$$\chi_j^0(\mathbf{r}) = \begin{cases} \phi_j^0(\mathbf{r}_t)\, e^{i\mathbf{v}_t \cdot \mathbf{r}_t}, & \text{if } j \leq J_T. \\ \phi_j^0(\mathbf{r}_p)\, e^{i\mathbf{v}_p \cdot \mathbf{r}_p}, & \text{otherwise} \end{cases} \tag{54}$$

where $(\mathbf{r}_t, \mathbf{v}_t)$ and $(\mathbf{r}_p, \mathbf{v}_p)$ are the positions and velocities with respect to the center of mass of the system for the target and projectile respectively as seen in Figure 2 [73]. The translation factors $e^{i\mathbf{v}_t \cdot \mathbf{r}_t}$ and $e^{i\mathbf{v}_p \cdot \mathbf{r}_p}$ are needed to take into account for the zeroth order of the basis given that the eigenfunctions are in the frame of their respective collision centers [73]. This allows the potential in (53) to be defined as

$$\hat{W}_p(t) = \frac{1}{r_P}\{1 - \exp[-r_P]\}. \tag{55}$$

The basis size and structure are determined by the number of generating basis states $J$ and the size of the hierarchy levels for each state $M_1, ..., M_J$ [73]. For the current systems, no BGM states are generated from the projectile basis states, namely for $j > J_T$ we have

$M_j = 0$. The basis generated from the approximation of $\chi_j^0$ is evaluated on the convergence of the numerical results with respect to the basis size and structure [73]. In the present work, the generating basis is composed from the undisturbed states $\chi_j^0(\mathbf{r})$ of the target (LMN shells) and projectile (KLMN shells), and the set $\{\chi_j^u(\mathbf{r},t), u \geq 1, j \leq J_T\}$ up to order $u = 5$ and $u = 9$ for neon and argon dimer targets respectively [65, 67]. The K-shell of the target is ignored as the necessary energy required to remove these electrons greatly exceeds that of the L and higher shell electrons.

The electron wavefunction for the $i^{th}$ electron can be rewritten using (54) and (53) to result in

$$\psi_i(\mathbf{r},t) = \sum_{u=0}^{M(u)} \sum_{j=1}^{J} c_{uj}^i(t)\, \chi_j^u(\mathbf{r},t) \qquad\qquad M(u) = \begin{cases} M, & \text{if } j \leq J_T. \\ 0, & \text{otherwise,} \end{cases} \tag{56}$$

where the resulting differential equations for the coefficients $c_{uj}^i$ are solved by standard means [73]

$$i \sum_{j=1}^{K} \sum_{u=0}^{M_j} \dot{c}_{uj}^i \left\langle \chi_{j'}^{u'} | \chi_j^u \right\rangle = \sum_{j=1}^{K} \sum_{u=0}^{M_j} c_{uj}^i \left\langle \chi_{j'}^{u'} \left| \hat{O} \right| \chi_j^u \right\rangle . \tag{57}$$

The resulting basis constructed from (53) and the potential (55) is not orthogonal [69]. If the states $\left|\chi_j^u\right\rangle, u > 0$ are not orthogonal, then the transition amplitudes (33) extracted for the final analyses will not be meaningful [75]. This is why the basis states are orthogonalized before amplitudes are extracted.

The transition amplitudes (33) can be expressed in the BGM basis as

$$c_i^j = \sum_{j'}^{J} \sum_{u'_j}^{M_j} c_{u'j'}^i \left\langle \phi_j | \chi_{j'}^{u'} \right\rangle . \tag{58}$$

The transition amplitudes become equal to the coefficients in the coupled-channel equations (57) for the no-response approximation and the response model when projecting on initial eigenstates $\left|\phi_j^0\right\rangle$ (36,37), if the higher-order states are orthogonalized.

## 3. FINAL STATE ANALYSES

Statistical analyses are developed in this section in order to calculate many-electron observables based on (33) and electron occupancy probabilities (34). As observables are necessary to test models against experiments, the final calculated results are total cross-sections defined by

$$\sigma = 2\pi \int_0^\infty P(b) b db, \tag{59}$$

where $b$ and $P(b)$ are the impact parameter and the probability at $b$ respectively. The probabilities are obtained from either multinomial single-electron probability combinations or from inner products of Slater determinants for transitions from initial to final electron state configurations, where the name of these two analyses are given as the multinomial (MA) and determinantal (DA) analysis respectively. Each analysis is further subdivided by models that describe the change in projectile charge over the course of the collision. A simplified model in which the projectile's charge remains unchanged after electron capture is called the *fixed-charge model*, while a changed projectile charge due to electron capture is called the *capture model*. In the determinantal analysis the capture model is separated into two submodels, where electron transfer from the projectile to the target is and is not considered. One assumption that is included in the analyses and models is that neutral He cannot capture any more electrons to form negative helium ions, as that is considered a highly unlikely scenario in the context of these collisions.

These analyses have been shown for helium ion-neon dimer collisions in [47] and [65] for projectile impact energies of 10 keV/amu. The calculations done in [47] confirmed experimental results in [11] regarding the relative strength of ICD in comparison to direct electron emission by a projectile impact energy of 150 keV/amu. The present work also explores an argon dimer target in the DA for a range of projectile energies from 10-150 keV/amu [67]. Excitation processes are explored in the context of the DA for the argon dimer target.

The following sections are based on the work published in [65] and [67].

### 3.1. Multinomial Analysis

In the multinomial analysis, a straightforward approach is employed in which products of single-particle probabilities in ion–atom collisions are combined to obtain a particular final state (channel) [47]. To illustrate this approach, the simplest case of removing a single $2s$ electron from one neon atom in the dimer is examined [47], with electron capture by the projectile assumed not to alter its charge:

$$P^{\rm rem}_{2s^{-1}}(b) = 4p^{\rm rem}_{2s}(b)[1-p^{\rm rem}_{2s}(b)]^3[1-p^{\rm rem}_{2p_0}(b)]^4[1-p^{\rm rem}_{2p_{1g}}(b)]^4[1-p^{\rm rem}_{2p_{1u}}(b)]^4. \qquad (60)$$

The quantity $p^{\rm rem}_{2s}(b)$ denotes the removal probability of a $2s$ electron, where $2s$, $2p_0$, and $2p_{1g/u}$ indicate the electronic states considered, and $g/u$ refers to gerade/ungerade[1] symmetry [65]. At low projectile impact energy (less than $\bar{v}$), direct ionization is assumed to be sufficiently weak as to be neglected, allowing removal to be identified with capture. The $K$-shell electrons are taken to be passive. The factor of four in equation (60) reflects the four possible $2s$ electrons in the dimer that can be captured. $(1-p^{\rm rem}_{2s}(b))$ describes the probability that an electron remains bound to the target. Since target excitation for neon is a weak process, this probability is identified with the elastic probability. The overall product of probabilities can then be interpreted in terms of the projectile's interactions with each atom along its trajectory through the dimer. Equation (60) represents the projectile not changing charge due to electron capture, which is an example of the *fixed-charge model*. In the case of the argon dimer target, the formulation of (60) is identical except that the principal quantum number is $n = 3$.

To build a comprehensive calculation, the rest of the electron dynamics that can occur is examined as well. Given the filled $2p$ electron shell in the neon atom, the removal probability is also calculated using the same procedure as in the case of $2s$. The removal probability for $2p$ is calculated as

[1] Transform the spherical harmonics into real functions to separate the basis into independent even and odd subspaces [81], exploiting the symmetry with respect to the collision plane: $\{Y_{lm}(\theta,\phi), -l \le m \le l\} \rightarrowtail \{P^m_l \cos\theta\cos m\phi, P^m_l \cos\theta \sin m\phi, 0 \le m \le l\}$, where $\theta, \phi$ are the polar and azimuthal angles respectively and $l, m$ are the angular momentum quantum numbers.

$$P_{2p^{-1}} =4[1-p_{2s}]^4\Big(p_{2p_0}[1-p_{2p_0}][1-p_{2p_{1g}}]^2[1-p_{2p_{1u}}]^2+p_{2p_{1g}}[1-p_{2p_{1g}}][1-p_{2p_0}]^2[1-p_{2p_{1u}}]^2 + p_{2p_{1u}}[1-p_{2p_{1u}}][1-p_{2p_0}]^2[1-p_{2p_{1g}}]^2\Big)[1-p_{2p_0}]^2[1-p_{2p_{1g}}]^2[1-p_{2p_{1u}}]^2. \tag{61}$$

For convenience, the superscript rem and the argument $(b)$ are suppressed. Since all one- and two- electron removal processes are investigated, two-electron removal probabilities from a single atom are included. The possible combinations are those with two $2s$ removal, two $2p$ removal and one $2s$ and one $2p$ removal. The following probabilities are obtained using the same techniques as in (60) and (61) that account for all combinations of electrons being removed. The probability for the $2s^{-2}$ channel is

$$P_{2s^{-2}} = 2p_{2s}^2[1-p_{2s}]^2[1-p_{2p_0}]^4[1-p_{2p_{1g}}]^4[1-p_{2p_{1u}}]^4 \tag{62}$$

for the $2p^{-2}$ removal channel it is

$$\begin{aligned} P_{2p^{-2}} =&2[1-p_{2s}]^4\Big(p_{2p_0}^2[1-p_{2p_{1g}}]^2[1-p_{2p_{1u}}]^2+p_{2p_{1g}}^2[1-p_{2p_0}]^2[1-p_{2p_{1u}}]^2 \\ &+p_{2p_{1u}}^2[1-p_{2p_0}]^2[1-p_{2p_{1g}}]^2+4p_{2p_0}p_{2p_{1g}}[1-p_{2p_0}][1-p_{2p_{1g}}][1-p_{2p_{1u}}]^2 \\ &+4p_{2p_0}p_{2p_{1u}}[1-p_{2p_0}][1-p_{2p_{1u}}][1-p_{2p_{1g}}]^2 \\ &+4p_{2p_{1g}}p_{2p_{1u}}[1-p_{2p_{1g}}][1-p_{2p_{1u}}][1-p_{2p_0}]^2\Big)[1-p_{2p_0}]^2[1-p_{2p_{1g}}]^2[1-p_{2p_{1u}}]^2. \end{aligned} \tag{63}$$

and for the $2s^{-1}2p^{-1}$ channel the probability is

$$P_{2s^{-1}2p^{-1}} =8p_{2s}[1-p_{2s}]^3\Big(p_{2p_0}[1-p_{2p_0}][1-p_{2p_{1g}}]^2[1-p_{2p_{1u}}]^2+p_{2p_{1g}}[1-p_{2p_{1g}}][1-p_{2p_0}]^2[1-p_{2p_{1u}}]^2 + p_{2p_{1u}}[1-p_{2p_{1u}}][1-p_{2p_0}]^2[1-p_{2p_{1g}}]^2\Big)[1-p_{2p_0}]^2[1-p_{2p_{1g}}]^2[1-p_{2p_{1u}}]^2. \tag{64}$$

For the two-site two electron removal channels, the probabilities are combined from atomic components of $P_{2s^{-1}}$ and $P_{2p^{-1}}$ removal. The probability combinations for two-site two electron removal are $2s^{-1}, 2s^{-1}$; $2p^{-1}, 2p^{-1}$ and $2s^{-1}, 2p^{-1}$.

For $2s^{-1}, 2s^{-1}$ the probability is

$$P_{2s^{-1},2s^{-1}} = 4p_{2s}^2[1-p_{2s}]^2[1-p_{2p_0}]^4[1-p_{2p_{1g}}]^4[1-p_{2p_{1u}}]^4, \tag{65}$$

the $2p^{-1}, 2p^{-1}$ channel is

$$P_{2p^{-1},2p^{-1}} = 4[1-p_{2s}]^4\Big(p_{2p_0}[1-p_{2p_0}][1-p_{2p_{1g}}]^2[1-p_{2p_{1u}}]^2 + p_{2p_{1g}}[1-p_{2p_{1g}}][1-p_{2p_0}]^2[1-p_{2p_{1u}}]^2 + p_{2p_{1u}}[1-p_{2p_{1u}}][1-p_{2p_0}]^2[1-p_{2p_{1g}}]^2\Big)^2, \tag{66}$$

and the $2s^{-1}, 2p^{-1}$ channel probability equals equation (64).

$$P_{2s^{-1},2p^{-1}} = P_{2s^{-1}2p^{-1}}. \tag{67}$$

The multinomial analysis is then modified to incorporate the projectile's change in charge state due to electron capture, forming what is called the capture model. In this model, the probability terms are recalculated to reflect the presence of a $He^+$ projectile. The same multinomial construction is used, but with probability terms appropriate for the projectile after capturing an electron. For notational convenience, a superscript $*$ denotes interaction probabilities for $He^+$ (e.g., $p^*_{2p_0}$, $1-p^*_{2p_0}$). The resulting $2s$ electron removal probability in the capture model is

$$P_{2s^{-1}} = 2p_{2s}[1-p_{2s}][1-p_{2p_0}]^2[1-p_{2p_{1g}}]^2[1-p_{2p_{1u}}]^2[1-p^*_{2s}]^2[1-p^*_{2p_0}]^2[1-p^*_{2p_{1g}}]^2[1-p^*_{2p_{1u}}]^2 + 2p_{2s}[1-p_{2s}]^3[1-p_{2p_0}]^4[1-p_{2p_{1g}}]^4[1-p_{2p_{1u}}]^4. \tag{68}$$

The first term on the right-hand side of equation (68) corresponds to removal of a single electron from the first atom, while the second term corresponds to removal from the second atom. In the first term, removal of an electron from the first atom alters the projectile's charge state and thus modifies the elastic interaction probabilities for the second atom. In the limit $p_{2s} = p^*_{2s}$, equation (60) for the fixed-charge model is recovered.

For the $2p^{-1}$ electron removal channel the probability is

$$P_{2p^{-1}} = 2[1-p_{2s}]^2\Big(p_{2p_0}[1-p_{2p_0}][1-p_{2p_{1g}}]^2[1-p_{2p_{1u}}]^2 + p_{2p_{1g}}[1-p_{2p_{1g}}][1-p_{2p_0}]^2[1-p_{2p_{1u}}]^2 + p_{2p_{1u}}[1-p_{2p_{1u}}][1-p_{2p_0}]^2[1-p_{2p_{1g}}]^2\Big)\Big([1-p^*_{2s}]^2[1-p^*_{2p_0}]^2[1-p^*_{2p_{1g}}]^2[1-p^*_{2p_{1u}}]^2 + [1-p_{2s}]^2[1-p_{2p_0}]^2[1-p_{2p_{1g}}]^2[1-p_{2p_{1u}}]^2\Big) \tag{69}$$

where in the limit of $p^*_x = p_x$ equation (61) is recovered. If the projectile captures two electrons from the first atom encountered, it becomes neutral, and its interaction with the

second atom is assumed to be negligible; the corresponding elastic probabilities therefore become unity. The impact of this model on the rest of the electron channel probabilities from (62)-(67) can be seen in the implementation of the capture model for them. For one-site two electron removal in the capture model, interaction of the neutral He after capture with Ne (or Ar) is assumed to be negligible. The probability for the $2s^{-2}$ removal channel is

$$P_{2s^{-2}} = p_{2s}^2[1-p_{2p_0}]^2[1-p_{2p_{1g}}]^2[1-p_{2p_{1u}}]^2\Big(1+[1-p_{2s}]^2[1-p_{2p_0}]^2[1-p_{2p_{1g}}]^2[1-p_{2p_{1u}}]^2\Big). \tag{70}$$

For the $2p^{-2}$ removal channel:

$$\begin{aligned} P_{2p^{-2}} =&[1-p_{2s}]^2\Big(p_{2p_0}^2[1-p_{2p_{1g}}]^2[1-p_{2p_{1u}}]^2 + p_{2p_{1g}}^2[1-p_{2p_0}]^2[1-p_{2p_{1u}}]^2 \\ &+ p_{2p_{1u}}^2[1-p_{2p_0}]^2[1-p_{2p_{1g}}]^2 + 4p_{2p_0}p_{2p_{1g}}[1-p_{2p_0}][1-p_{2p_{1g}}][1-p_{2p_{1u}}]^2 \\ &+ 4p_{2p_0}p_{2p_{1u}}[1-p_{2p_0}][1-p_{2p_{1u}}][1-p_{2p_{1g}}]^2 \\ &+ 4p_{2p_{1g}}p_{2p_{1u}}[1-p_{2p_{1g}}][1-p_{2p_{1u}}][1-p_{2p_0}]^2\Big)\Big(1+[1-p_{2s}]^2[1-p_{2p_0}]^2[1-p_{2p_{1g}}]^2[1-p_{2p_{1u}}]^2\Big) \end{aligned} \tag{71}$$

for $2s^{-1}2p^{-1}$:

$$\begin{aligned} P_{2s^{-1}2p^{-1}} =&4p_{2s}[1-p_{2s}]\Big(p_{2p_0}[1-p_{2p_0}][1-p_{2p_{1g}}]^2[1-p_{2p_{1u}}]^2 + p_{2p_{1g}}[1-p_{2p_{1g}}][1-p_{2p_0}]^2[1-p_{2p_{1u}}]^2 \\ &+ p_{2p_{1u}}[1-p_{2p_{1u}}][1-p_{2p_0}]^2[1-p_{2p_{1g}}]^2\Big)\Big(1+[1-p_{2s}]^2[1-p_{2p_0}]^2[1-p_{2p_{1g}}]^2[1-p_{2p_{1u}}]^2\Big). \end{aligned} \tag{72}$$

For the two-site two electron removal channels, the channels are also calculated. For $2s^{-1}, 2s^{-1}$ the probability is

$$P_{2s^{-1},2s^{-1}} = 4p_{2s}[1-p_{2s}][1-p_{2p_0}]^2[1-p_{2p_{1g}}]^2[1-p_{2p_{1u}}]^2 p_{2s}^*[1-p_{2s}^*][1-p_{2p_0}^*]^2[1-p_{2p_{1g}}^*]^2[1-p_{2p_{1u}}^*]^2 \tag{73}$$

and the $2p^{-1}, 2p^{-1}$ channel is

$$
\begin{aligned}
P_{2p^{-1},2p^{-1}} =& 4[1-p_{2s}]^2\Big(p_{2p_0}[1-p_{2p_0}][1-p_{2p_{1g}}]^2[1-p_{2p_{1u}}]^2 + p_{2p_{1g}}[1-p_{2p_{1g}}][1-p_{2p_0}]^2[1-p_{2p_{1u}}]^2 \\
&+ p_{2p_{1u}}[1-p_{2p_{1u}}][1-p_{2p_0}]^2[1-p_{2p_{1g}}]^2\Big)[1-p^*_{2s}]^2\Big(p_{2p^*_0}[1-p^*_{2p_0}][1-p^*_{2p_{1g}}]^2[1-p^*_{2p_{1u}}]^2 \\
&+ p_{2p^*_{1g}}[1-p^*_{2p_{1g}}][1-p^*_{2p_0}]^2[1-p^*_{2p_{1u}}]^2 + p^*_{2p_{1u}}[1-p^*_{2p_{1u}}][1-p^*_{2p_0}]^2[1-p^*_{2p_{1g}}]^2\Big)
\end{aligned} \tag{74}
$$

and the $2s^{-1}, 2p^{-1}$ channel is

$$
\begin{aligned}
P_{2s^{-1},2p^{-1}} =& 4p_{2s}[1-p_{2s}][1-p_{2p_0}]^2[1-p_{2p_{1g}}]^2[1-p_{2p_{1u}}]^2[1-p^*_{2s}]^2\Big(p^*_{2p_0}[1-p^*_{2p_0}][1-p^*_{2p_{1g}}]^2[1-p^*_{2p_{1u}}]^2 \\
&+ p^*_{2p_{1g}}[1-p^*_{2p_{1g}}][1-p^*_{2p_0}]^2[1-p^*_{2p_{1u}}]^2 + p^*_{2p_{1u}}[1-p^*_{2p_{1u}}][1-p^*_{2p_0}]^2[1-p^*_{2p_{1g}}]^2\Big) \\
&+ 4[1-p_{2s}]^2\Big(p_{2p_0}[1-p_{2p_0}][1-p_{2p_{1g}}]^2[1-p_{2p_{1u}}]^2 + 2p_{2p_{1g}}[1-p_{2p_{1g}}][1-p_{2p_0}]^2[1-p_{2p_{1u}}]^2 \\
&+ p_{2p_{1u}}[1-p_{2p_{1u}}][1-p_{2p_0}]^2[1-p_{2p_{1g}}]^2\Big)p^*_{2s}[1-p^*_{2s}][1-p^*_{2p_0}]^2[1-p^*_{2p_{1g}}]^2[1-p^*_{2p_{1u}}]^2.
\end{aligned} \tag{75}
$$

For the $He^+$ projectile, the fixed-charge model probabilities have identical equations as (60) to (67), using the $He^+$ projectiles. However, in the capture model an initial $He^+$ projectile can capture only a single electron. This element of the capture model aligns with the assumption that direct ionization remains negligibly small for all projectile charge states and with the additional neglect of (metastable) negative helium ion formation [82]. Under these considerations, the $2s$ electron removal probability for $He^+$ becomes

$$
\begin{aligned}
P_{2s^{-1}} =& \Big(1+[1-p^*_{2s}]^2[1-p^*_{2p_0}]^2[1-p^*_{2p_{1g}}]^2[1-p^*_{2p_{1u}}]^2\Big) \\
&\times 2p^*_{2s}[1-p^*_{2s}][1-p^*_{2p_0}]^2[1-p^*_{2p_{1g}}]^2[1-p^*_{2p_{1u}}]^2.
\end{aligned} \tag{76}
$$

Equation (76) shows that the electron removal probability associated with a neutral He projectile is set to zero. Since no two-electron removal channels are available in the capture model, the remaining channel for capture is $2p^1$ with probability

$$
\begin{aligned}
P_{2p^{-1}} =& 2[1-p^*_{2s}]^2\Big(p^*_{2p_0}[1-p^*_{2p_0}][1-p^*_{2p_{1g}}]^2[1-p^*_{2p_{1u}}]^2 + p^*_{2p_{1g}}[1-p^*_{2p_{1g}}][1-p^*_{2p_0}]^2[1-p^*_{2p_{1u}}]^2 \\
&+ p^*_{2p_{1u}}[1-p^*_{2p_{1u}}][1-p^*_{2p_0}]^2[1-p^*_{2p_{1g}}]^2\Big)\Big([1-p^*_{2s}]^2[1-p_{2p^*_0}]^2[1-p^*_{2p_{1g}}]^2[1-p^*_{2p_{1u}}]^2+1\Big).
\end{aligned} \tag{77}
$$

### 3.2. Determinantal Analysis

In this analysis the transition amplitudes are assumed to be given by inner products of Slater determinants, which inherently account for the Pauli exclusion principle. The transition from initial- to final-state electron configurations yields a probability equal to the determinant of a single-particle density matrix [65]:

$$
\begin{aligned}
P_{f_1 \dots f_{N_T}} &= |\langle \phi_1 \dots \phi_{N_T} | \psi_1 \dots \psi_{N_T}, t_f \rangle|^2. \\
&= \begin{vmatrix} \langle \phi_1 | \psi_1 \rangle & \cdots & \langle \phi_1 | \psi_{N_T} \rangle \\ \vdots & \ddots & \vdots \\ \langle \phi_{N_T} | \psi_1 \rangle & \cdots & \langle \phi_{N_T} | \psi_{N_T} \rangle \end{vmatrix} \times \begin{vmatrix} \langle \psi_1 | \phi_1 \rangle & \cdots & \langle \psi_1 | \phi_{N_T} \rangle \\ \vdots & \ddots & \vdots \\ \langle \psi_{N_T} | \phi_1 \rangle & \cdots & \langle \psi_{N_T} | \phi_{N_T} \rangle \end{vmatrix} \\
&= \begin{vmatrix} \gamma_{11} & \cdots & \gamma_{1N_T} \\ \vdots & \ddots & \vdots \\ \gamma_{N_T 1} & \cdots & \gamma_{N_T N_T} \end{vmatrix} \equiv \det(\gamma).
\end{aligned}
\tag{78}
$$

Here $|\psi_j, t_f\rangle$ denotes the time-propagated orbital corresponding to the initial state $|\psi_j\rangle$, $|\phi_j\rangle$ is a final state, $\gamma_{jk}$ are the density matrix elements computed from Slater determinants, and $N_T$ is the number of electrons ($N_T = 8$ for the neon dimer, $N_T = 8$ for the argon dimer) [65]. The density matrix elements can be written as sums of products of single-particle transition amplitudes between initial and final states [65]:

$$
\gamma_{jk}(t_f) = \langle \phi_j | \gamma(t_f) | \phi_k \rangle = \sum_{i=1}^{N_T} \langle \phi_j | \psi_i, t_f \rangle \langle \psi_i, t_f | \phi_k \rangle = \sum_{i=1}^{N_T} c_k^{i^*}(t_f) c_j^i(t_f). \tag{79}
$$

When all final states of all electrons are explicitly specified, as in equation (78), the resulting probability is referred to as an exclusive probability, corresponding to a complete measurement [65]. In realistic scenarios such full information is generally unavailable. The probability for specified transitions of only a subset of electrons, without fixing the final states of the remaining electrons, is known as an inclusive probability [83]. It is given by the sum over the relevant set of exclusive probabilities:

$$
P_{\phi_1 \dots \phi_q} = \sum_{\phi_{q+1} < \dots < \phi_{N_T}} P_{\phi_1 \dots \phi_{N_T}}. \tag{80}
$$

Here $q$ electrons out of $N_T$ occupy the final state $|\phi_1 \dots \phi_q\rangle$, while the remaining $N_T - q$ electrons are unspecified [65]. Consistent with (78), $P_{\phi_1 \dots \phi_q}$ is the determinant of a $q \times q$ matrix corresponding to the sub-configuration $|\phi_1 \dots \phi_q\rangle$. Because electron removal necessarily

creates unoccupied states (holes), it is also useful to quantify the probabilities associated with these hole states. Using the structure of (80), an inclusive particle–hole probability may be calculated as

$$\begin{aligned} P^{\bar{\phi}_1 \ldots \bar{\phi}_k}_{\phi_1 \ldots \phi_q} &\equiv \textstyle\sum^{\bar{\phi}_1 \ldots \bar{\phi}_k}_{\phi_{q+1} < \ldots < \phi_{N_T}} P_{\phi_1 \ldots \phi_{N_T}} \\ &= P_{\phi_1 \ldots \phi_q} - \sum_{l=1}^{k} P_{\phi_1 \ldots \phi_q \bar{\phi}_l} + \sum_{l_1 < l_2}^{k} P_{\phi_1 \ldots \phi_q \bar{\phi}_{l_1} \bar{\phi}_{l_2}} - \cdots , \end{aligned} \tag{81}$$

where $\bar{\phi}_i$ denote the hole states. The resulting particle–hole probability is a sum of alternating addition and subtraction of contributions [83, 84]. This formalism is applied below to determine the electron-removal channel probabilities relevant to this work.

### *3.2.1. Removal without Electron Excitation*

The inclusive model can also incorporate the projectile ion. For $He^{2+}$ collisions, two variants accounting for electron capture to form $He^{+}$, and the resulting change in the interaction with the second atom of the dimer, are considered—model I and model II [65].

Model I uses the inclusive probability formulation with transition amplitudes computed for both $He^{2+}$–Ne and $He^{+}$–Ne interactions [65]. Channel probabilities are then modified analogously to the multinomial capture model, but within the determinantal fixed-charge framework [65].

Model II has the same structural form as model I in the computation of final channel probabilities, but the density matrix elements additionally include the possibility of an electron occupying a projectile orbital [65]. Only the $1s$ state is included, as it is the dominant bound state following capture. The modified density matrix therefore reads

$$\gamma_{kj} = \sum_{i=1}^{N_T+1} \langle \phi_k | \psi_i, t_f \rangle \langle \psi_i, t_f | \phi_j \rangle, \tag{82}$$

where the term $+1$ accounts for the projectile $1s$ state [65].

The application of these models is illustrated by examining the $2s$ electron-removal probability.

The fixed-charge model is considered first. As in the multinomial analysis, changes in the projectile charge after capture are ignored. The $2s$ removal process is recognized as a sum of particle–hole probabilities, beginning with the removal of a single $2s$ electron from

one neon atom:

$$P^{Ne}_{2s^{-1}} = P^{2\bar{s}\uparrow}_{2s\downarrow,2p_0^2,2p_{1g}^2,2p_{1u}^2} + P^{2\bar{s}\downarrow}_{2s\uparrow,2p_0^2,2p_{1g}^2,2p_{1u}^2}. \tag{83}$$

The arrows represent electron and hole spin orientations. Two terms appear because either a spin-up or spin-down electron may be removed. Applying (81) to the first term yields

$$P^{2\bar{s}\uparrow}_{2s\downarrow,2p_0^2,2p_{1g}^2,2p_{1u}^2} = P_{2s\downarrow,2p_0^2,2p_{1g}^2,2p_{1u}^2} - P_{2s^2,2p_0^2,2p_{1g}^2,2p_{1u}^2}. \tag{84}$$

The first term corresponds to a configuration with a spin-down $2s$ electron and a filled $2p$ subshell, with one final electron state left unspecified [65]. The second term is the elastic probability, representing the probability that all electrons remain in place. In the present regime of 10 keV/amu impact energy and neon dimer, target excitation and direct ionization are negligible, so the difference of the two contributions describes the probability of finding a hole in the $2s\uparrow$ state with the missing electron captured by the projectile [65].

Inserting (84) into (83) gives

$$P^{Ne}_{2s^{-1}} = P_{2s\downarrow,2p_0^2,2p_{1g}^2,2p_{1u}^2} - P_{2s^2,2p_0^2,2p_{1g}^2,2p_{1u}^2} + P_{2s\uparrow,2p_0^2,2p_{1g}^2,2p_{1u}^2} - P_{2s^2,2p_0^2,2p_{1g}^2,2p_{1u}^2}. \tag{85}$$

Since the Hamiltonian is spin independent, the inclusive probabilities for spin-up and spin-down electrons are equal. This leads to

$$P^{Ne}_{2s^{-1}} = 2\left(P_{2s,2p_0^2,2p_{1g}^2,2p_{1u}^2} - P_{\text{elastic}}\right), \tag{86}$$

with

$$P_{\text{elastic}} = P_{2s^2,2p_0^2,2p_{1g}^2,2p_{1u}^2}. \tag{87}$$

The spin index on $2s$ has been omitted due to this symmetry.

Within the independent-atom model, the one- and two-site electron-removal probabilities for the dimer follow directly from the inclusive probabilities in the *fixed-charge* model:

$$\begin{gathered}
P^{\text{dimer}}_{s^{-1}} = 2P_{s^{-1}}P_{\text{elastic}}, \qquad P^{\text{dimer}}_{p^{-1}} = 2P_{p^{-1}}P_{\text{elastic}}, \\
P^{\text{dimer}}_{s^{-1},s^{-1}} = P_{s^{-1}}P_{s^{-1}}, \qquad P^{\text{dimer}}_{p^{-1},p^{-1}} = P_{p^{-1}}P_{p^{-1}}, \\
P^{\text{dimer}}_{s^{-1},p^{-1}} = 2P_{s^{-1}}P_{p^{-1}}, \\
P^{\text{dimer}}_{s^{-2}} = 2P_{s^{-2}}P_{\text{elastic}}, \qquad P^{\text{dimer}}_{p^{-2}} = 2P_{p^{-2}}P_{\text{elastic}}, \\
P^{\text{dimer}}_{s^{-1}p^{-1}} = 2P_{s^{-1}p^{-1}}P_{\text{elastic}}.
\end{gathered} \tag{88}$$

Here the subscript "2" has been omitted for simplicity, and the superscript Ne is dropped on the right-hand side. Terms such as $s^{-1},s^{-1}$ and $s^{-2}$ correspond to two-site and one-site $2s$ electron removal, respectively, with commas indicating two-site processes.

The extension to *capture model I* follows the multinomial capture modifications, yielding

$$\begin{aligned}
P^{\rm dimer}_{s^{-1}} &= P_{s^{-1}}P^*_{\rm elastic} + P_{\rm elastic}P_{s^{-1}},\\
P^{\rm dimer}_{p^{-1}} &= P_{p^{-1}}P^*_{\rm elastic} + P_{\rm elastic}P_{p^{-1}},\\
P^{\rm dimer}_{s^{-1},s^{-1}} &= P_{s^{-1}}P^*_{s^{-1}}, \qquad P^{\rm dimer}_{p^{-1},p^{-1}} = P_{p^{-1}}P^*_{p^{-1}},\\
P^{\rm dimer}_{s^{-1},p^{-1}} &= P_{s^{-1}}P^*_{p^{-1}} + P_{p^{-1}}P^*_{s^{-1}},\\
P^{\rm dimer}_{s^{-2}} &= P_{s^{-2}} + P_{\rm elastic}P_{s^{-2}},\\
P^{\rm dimer}_{p^{-2}} &= P_{p^{-2}} + P_{\rm elastic}P_{p^{-2}},\\
P^{\rm dimer}_{s^{-1}p^{-1}} &= P_{s^{-1}p^{-1}} + P_{\rm elastic}P_{s^{-1}p^{-1}}.
\end{aligned} \tag{89}$$

The final three expressions assume negligible interaction between a neutral He atom and neon.

Model II differs from model I through the inclusion of the projectile $1s$ state in the density matrix. For example,

$$\gamma_{2s\uparrow 2p_0\uparrow} = c^{1s(P)}_{2s}c^{1s(P)*}_{2p_0} + c^{2s(T)}_{2s}c^{2s(T)*}_{2p_0} + c^{2p_0(T)}_{2s}c^{2p_0(T)*}_{2p_0} + c^{2p_{1g}(T)}_{2s}c^{2p_{1g}(T)*}_{2p_0}, \tag{90}$$

where $(P)$ and $(T)$ denote projectile and target initial states. This expression assumes a spin-up projectile electron; while for the corresponding spin-down electron the first term on the right vanishes, so that $\gamma_{2s\uparrow 2p_0\uparrow} \neq \gamma_{2s\downarrow 2p_0\downarrow}$.

The effects of including the projectile state become apparent in a simplified example where all $2p$ states are neglected and the removal of a single $2s$ electron is examined. If the $He^+$ electron is spin-up, the removal probability from one atom is

$$P_{2s^{-1}} = (P_{2s\uparrow} - P_{2s^2}) + (P_{2s\downarrow} - P_{2s^2}), \tag{91}$$

where $P_{2s\uparrow}$ and $P_{2s\downarrow}$ are the inclusive probabilities for removing a spin-down or spin-up electron from the target respectively, and $P_{2s^2}$ is the elastic probability. Since the projectile electron is fixed in the spin-up state, transitions to target spin-down states are excluded, producing a spin asymmetry:

$$P_{2s\uparrow} = c^{1s\uparrow(P)}_{2s\uparrow}c^{1s\uparrow(P)*}_{2s\uparrow} + c^{2s\uparrow(T)}_{2s\uparrow}c^{2s\uparrow(T)*}_{2s\uparrow} + c^{2s\downarrow(T)}_{2s\uparrow}c^{2s\downarrow(T)*}_{2s\uparrow}, \tag{92}$$

where the final term vanishes since no spin flips are allowed. Similarly,

$$P_{2s\downarrow} = c_{2s\downarrow}^{2s\downarrow(T)} c_{2s\downarrow}^{2s\downarrow(T)*}. \tag{93}$$

For

$$P_{2s^2} = \begin{vmatrix} P_{2s\uparrow} & 0 \\ 0 & P_{2s\downarrow} \end{vmatrix}, \tag{94}$$

substitution of (92)–(93) yields

$$P_{2s^2} = (c_{2s\uparrow}^{1s\uparrow(P)} c_{2s\uparrow}^{1s\uparrow(P)*} + c_{2s\uparrow}^{2s\uparrow(T)} c_{2s\uparrow}^{2s\uparrow(T)*}) \, (c_{2s\downarrow}^{2s\downarrow(T)} c_{2s\downarrow}^{2s\downarrow(T)*}). \tag{95}$$

Inserting these expressions into (91) gives

$$\begin{aligned} P_{2s^{-1}} = \; & \left(c_{2s\uparrow}^{1s\uparrow(P)} c_{2s\uparrow}^{1s\uparrow(P)*} + c_{2s\uparrow}^{2s\uparrow(T)} c_{2s\uparrow}^{2s\uparrow(T)*}\right)\left[1 - c_{2s\downarrow}^{2s\downarrow(T)} c_{2s\downarrow}^{2s\downarrow(T)*}\right] \\ & + \left(c_{2s\downarrow}^{2s\downarrow(T)} c_{2s\downarrow}^{2s\downarrow(T)*}\right)\left[1 - c_{2s\uparrow}^{2s\uparrow(T)} c_{2s\uparrow}^{2s\uparrow(T)*} - c_{2s\uparrow}^{1s\uparrow(P)} c_{2s\uparrow}^{1s\uparrow(P)*}\right], \end{aligned} \tag{96}$$

showing explicitly the asymmetry introduced through the projectile-electron contribution. When the projectile electron is assumed spin-down, the final expression is unchanged. Neglecting capture from the projectile ($c_{2s\uparrow}^{1s\uparrow(P)} = 0$) recovers model I. These generalized expressions (including $2p$ states) are inserted into the channel probabilities of (89).

For a $He^+$ projectile, only single-electron removal processes contribute in the capture model for the reasons outlined in the Multinomial Analysis section. The corresponding probabilities are

$$\begin{aligned} P_{s^{-1}}^{\text{dimer}} &= P_{s^{-1}} + P_{\text{elastic}} P_{s^{-1}}, \\ P_{p^{-1}}^{\text{dimer}} &= P_{p^{-1}} + P_{\text{elastic}} P_{p^{-1}}, \end{aligned} \tag{97}$$

where the first terms describe capture from the first atom, neutralizing the projectile, and the second terms correspond to capture from the second atom.

### *3.2.2. Electron Excitation*

In the argon dimer target, electron excitation plays a significantly more prominent role for facilitating ICD in the energy regime considered here than in the case of the neon dimer target [11]. These electron excitations occur through single–electron removal accompanied by the promotion of another electron to a higher orbital, leading to valence–shell configurations of the form $3p^{-2}nl$. The probability of populating a specific excited state $nl$ is evaluated using

the inclusive formalism introduced in the previous section, equation (81) in particular [67]. As an illustrative example, the probability for one electron to be removed from the $3p_0$ subshell while another electron is excited to an $nl$ orbital is given by

$$P^{3\bar{p}_0{}^2}_{3s^2,3p_{1g}^2,3p_{1u}^2,nl\uparrow} = P_{3s^2,3p_{1g}^2,3p_{1u}^2,nl\uparrow} - P_{3s^2,3p_0\downarrow,3p_{1g}^2,3p_{1u}^2,nl\uparrow}, \tag{98}$$

where $nl\uparrow$ denotes the excited state with spin up (chosen without loss of generality). The first term on the right-hand side in (98) represents configurations containing two $3p$ vacancies together with one electron in the excited orbital. The second term accounts for configurations with a single spin–up vacancy and an electron promoted to $nl$. All such combinations contributing to a given excited state $nl$ are evaluated explicitly.

The combination of states associated with a particular excited configuration is determined from its term symbol $^{2S+1}L$, where $L$ and $S$ are the orbital and spin angular momentum quantum numbers respectively, and $(2S+1)$ is the spin multiplicity [67]. The number of states for a particular term symbol is $(2S+1)(2L+1)$, with $\{L|S=0,P=1,D=2,F=3,\ldots\}$ and $\{S=0,1/2,1,3/2,..\}$ [85].

Not all LS coupled states for a particular configuration exceed the energetic threshold to initiate ICD, and this needs to be be accounted for. A procedure for scaling the probability given an energy threshold cutoff is developed.

The procedure is implemented by first summing all configurations that contain two $3p$ vacancies and one excited electron, without imposing the impossibility of spin flips [67]. The calculation is then repeated for configurations with only a single $3p$ vacancy and the excited electron. This ensures that all relevant electron configurations are included. After these contributions are obtained, each total is scaled by the fraction of states whose excitation energies exceed the minimum threshold required for ICD. For instance, for the $3d$ excited state the corresponding scaling factor is 42/90. To calculate the scaling factor it is necessary to first determine the total number of states of $Ar^+(3p^{-2}3d)$ type, which is 150. However, 60 of these correspond to spin quartet states which are not accessible without spin flips and have to be removed from the list of allowed states, leaving a total of 90. Out of these 90 states, only 42 exceed the necessary energy threshold [85] for facilitating ICD.

In the case of the $n=4$ excited states, the scaling factors are 1/9 for $4s$ and 1 for the remaining excitation channels, i.e. all LS coupled states lie above the ICD threshold for the latter.

Once this scaling is obtained, the probability for electron removal with simultaneous electron excitation $P_{p^{-2}nl}$ is used to supplement (88), (89) and (97) with the following dimer probabilities for the fixed-charge model:

$$P^{\text{dimer}}_{p^{-2}nl} = 2P_{p^{-2}nl}P_{\text{elastic}}, \tag{99}$$

for the capture models with the $He^{2+}$ projectile:

$$P^{\text{dimer}}_{p^{-2}nl} = P_{p^{-2}nl}P^{*}_{\text{elastic}} + P_{\text{elastic}}P_{p^{-2}nl} \tag{100}$$

and for the capture models with the $He^{+}$ projectile

$$P^{\text{dimer}}_{p^{-2}nl} = P_{p^{-2}nl} + P_{\text{elastic}}P_{p^{-2}nl}. \tag{101}$$

### *3.2.3. Energy Scaling*

The calculated probabilities obtained from the capture models for both $He^{2+}$ and $He^{+}$ projectiles have thus far relied on the assumption that for projectile impact energies less than $\bar{v}$, electron capture strongly dominates over ionization. As the projectile impact energy increases into the regime greater than $\bar{v}$, this assumption ceases to hold, and ionization must be explicitly incorporated.

A simple method of factoring in the balance between electron ionization and capture processes is to incorporate their relative contributions to the total electron removal in the model [67]. With equation (35), these ratios are obtained from

$$P^{rem}_{net} = N_T - \sum_{i=1}^{N_T}\sum_{j=1}^{J_T}|c^i_j|^2, \qquad P^{cap}_{net} = \sum_{i=1}^{N_T}\sum_{j=J_T+1}^{J}|c^i_j|^2, \qquad P^{ion}_{net} = p^{rem}_{net} - p^{cap}_{net}, \tag{102}$$

where $J_T$ and $J_P$ are the number of target and projectile basis states respectively, and $P^{rem}_{net}$, $P^{cap}_{net}$, and $P^{ion}_{net}$ are the net electron removal, capture and ionization probabilities respectively. Given (102), a balance between ionization and capture probabilities is found utilizing the fixed-charge and capture model probabilities from (88), (89) and (97). The fixed-charge model assumes no change in projectile charge, effectively representing a pure ionization model, while capture models I and II describe a capture process. Scaling the probabilities

between these two types of models is done through the use of the ratio of probabilities in (102) to give a final electron probability $P$ for a particular projectile impact energy as

$$P = \alpha P_{FCM} + \beta P_{CM} \tag{103}$$

where $P_{FCM}$, $P_{CM}$ are fixed-charge and capture model probabilities respectively, while $\alpha$ and $\beta$ are the ratio of ionization and capture with respect to removal, defined as

$$\alpha = \frac{P_{net}^{ion}}{P_{net}^{rem}}, \qquad \beta = \frac{P_{net}^{cap}}{P_{net}^{rem}}. \tag{104}$$

At low projectile impact energies, capture dominates the removal channel, and the contribution from $P_{CM}$ is large, while $P_{FCM}$ provides only a minor correction [67]. As the impact energy increases, the situation reverses: ionization becomes the dominant mechanism, and the relative weight shifts toward the fixed-charge model. Going forward, the capture models will be reclassified as the modified capture models I (MCMI) and II (MCMII) to account for this weighting scheme that balances ionization and capture dominance.

# 4. HELIUM ION - NEON DIMER COLLISION SYSTEM

---

This chapter is based on results that were first presented in [65].

In the following we consider $He^{2+}$ projectiles first, followed by $He^{+}$ projectiles, with emphasis on the $2s^{-1}$ channel associated with ICD. The projectile has an impact energy of 10 keV/amu for collisions with the neon dimer target, and so electron removal is deemed equivalent to capture. Throughout this section, references to electron channels in figures omit the principal quantum number $n = 2$ (e.g., $2s$ is denoted as $s$). The abbreviation *res* denotes calculations including dynamical response, while *hep* indicates results obtained using a $He^{+}$ projectile.

For clarity, the multinomial and determinantal analyses are denoted by MA and DA, respectively. Models are identified using acronyms, such as FCM for the fixed-charge model and CMI/CMII for capture models I and II. A specific combination of analysis and model is labeled using the notation XX.YYY, where XX refers to the analysis and YYY to the model (e.g., MA.FCM).

## 4.1. $He^{2+}$ Projectiles

Building on previous work [47], the comparison begins with MA.FCM and DA.FCM for single $2s$ electron removal from the dimer with the orientation shown in 1. As shown in Fig. 3, the two analyses yield nearly indistinguishable results, indicating that Pauli exclusion effects are negligible for this single-vacancy production channel.

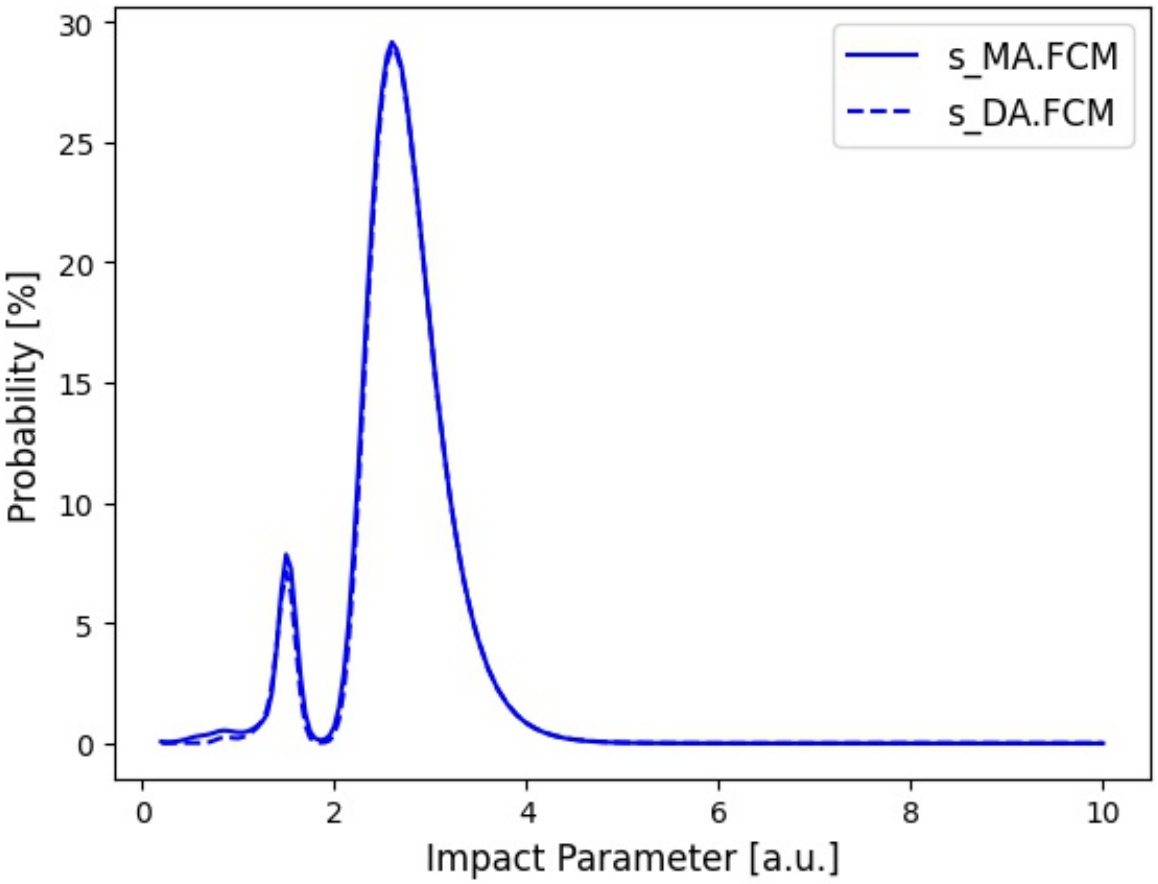


Figure 3: $He^{2+}$–$Ne_2$ ion–dimer collisions in parallel orientation at 10 keV/amu. Single $2s$ electron removal probability comparing MA.FCM (solid line) and DA.FCM (dashed line) [65].

Figure 3 also provides validation for the determinantal analysis, as its FCM is nearly identical with the multinomial analysis's for the $2s$ electron removal channel given in equation (60). This gives confidence that the determinantal analysis is a valid method to use, especially given that it is a more fundamental approach for investigating electron removal channels than the multinomial analysis.

This comparison between analyses for the FCM is further explored for other electron removal channels, namely one- and two-electron vacancy production channels.

Figure 4 compares single $2s$ removal with single $2p$ removal across analyses for the FCM.

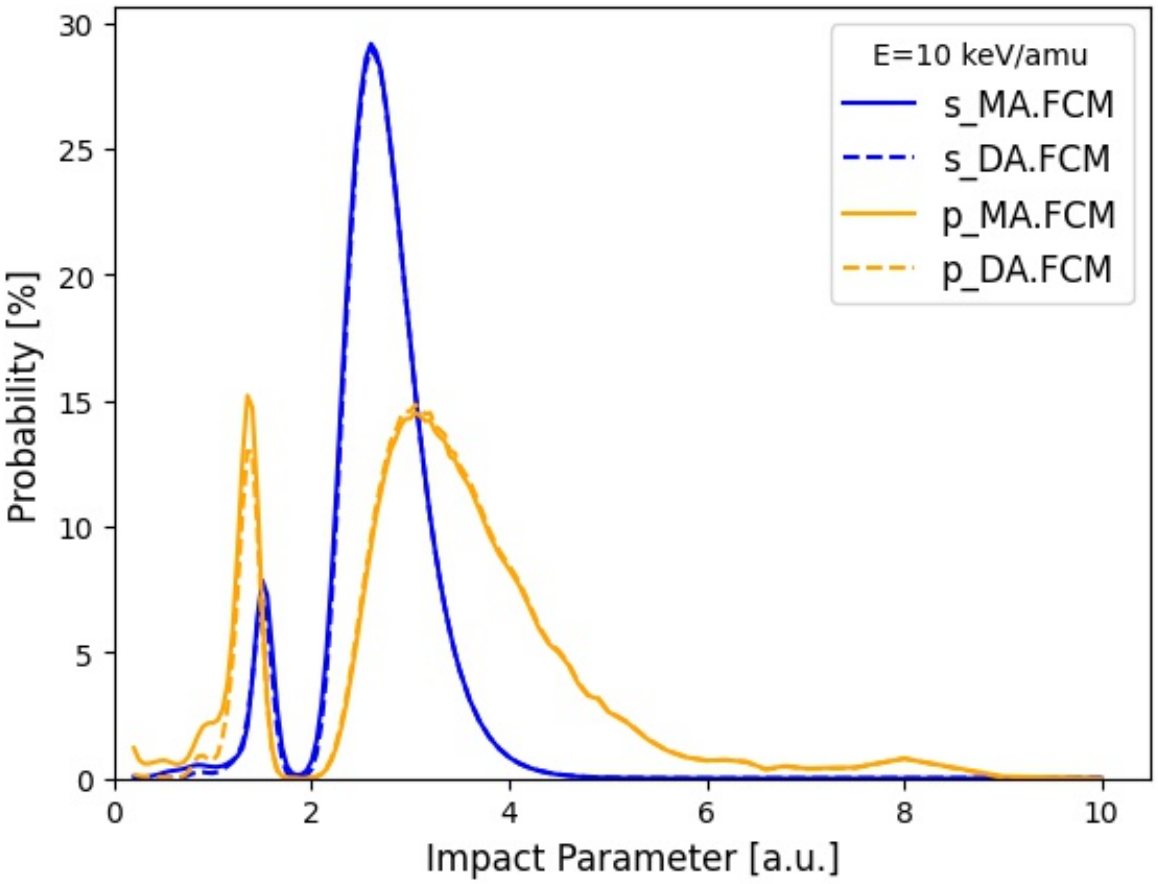


Figure 4: $He^{2+}$–$Ne_2$ ion–dimer collisions in parallel orientation at 10 keV/amu. One-electron removal channel probabilities comparing MA.FCM (solid lines) and DA.FCM (dashed lines).

As can be seen, not only are the analyses within the FCM consistent with each other for $2p$ electron removal, that probability is also smaller in comparison to the $2s$ channel, despite the lower binding energy of $2p$ electrons. This is due to the closeness in single-particle energy eigenvalues of the initial ($\varepsilon^{OPM}_{Ne(2s)} = -1.718$ a.u.) and final ($\varepsilon_{He^+(1s)} = -2$ a.u.) states [47]. The initial Ne($2p$) electrons are energetically further away ($\varepsilon^{OPM}_{Ne(2p)} = -0.851$ a.u.) and thus less likely to be captured.

The probabilities for two-site two electron removal channels in the fixed-charge model are also explored as a means of producing $Ne^+$-$Ne^+$ dimer fragments through CE.

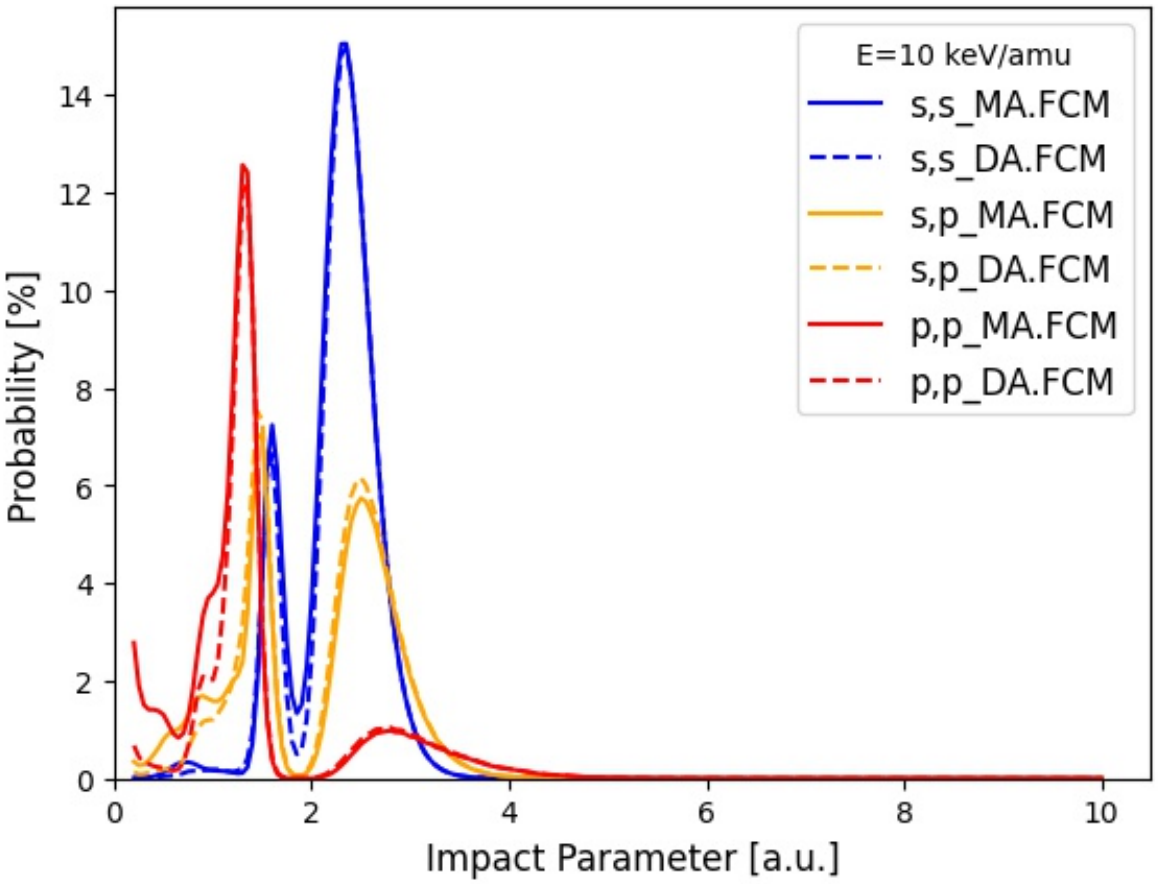


Figure 5: $He^{2+}$–$Ne_2$ ion–dimer collisions in parallel orientation at 10 keV/amu. Two-site two-electron removal probabilities comparing MA.FCM (solid line) and DA.FCM (dashed line).

Figure 5 confirms that for the FCM there is no meaningful difference between the multinomial and determinantal analyses for two-site two-electron removal. It is also noteworthy that two-site two $2s$ electron removal has the largest peak probability around 2.3 a.u., and the smallest for two-site two $2p$ removal. Given that the $2s^{-1}, 2p^{-1}$ peak is in between the other two channels, it indicates $2p$ removal ($2p^{-1}$ vacancy production) is more suppressed in comparison to $2s^{-1}$ vacancy production.

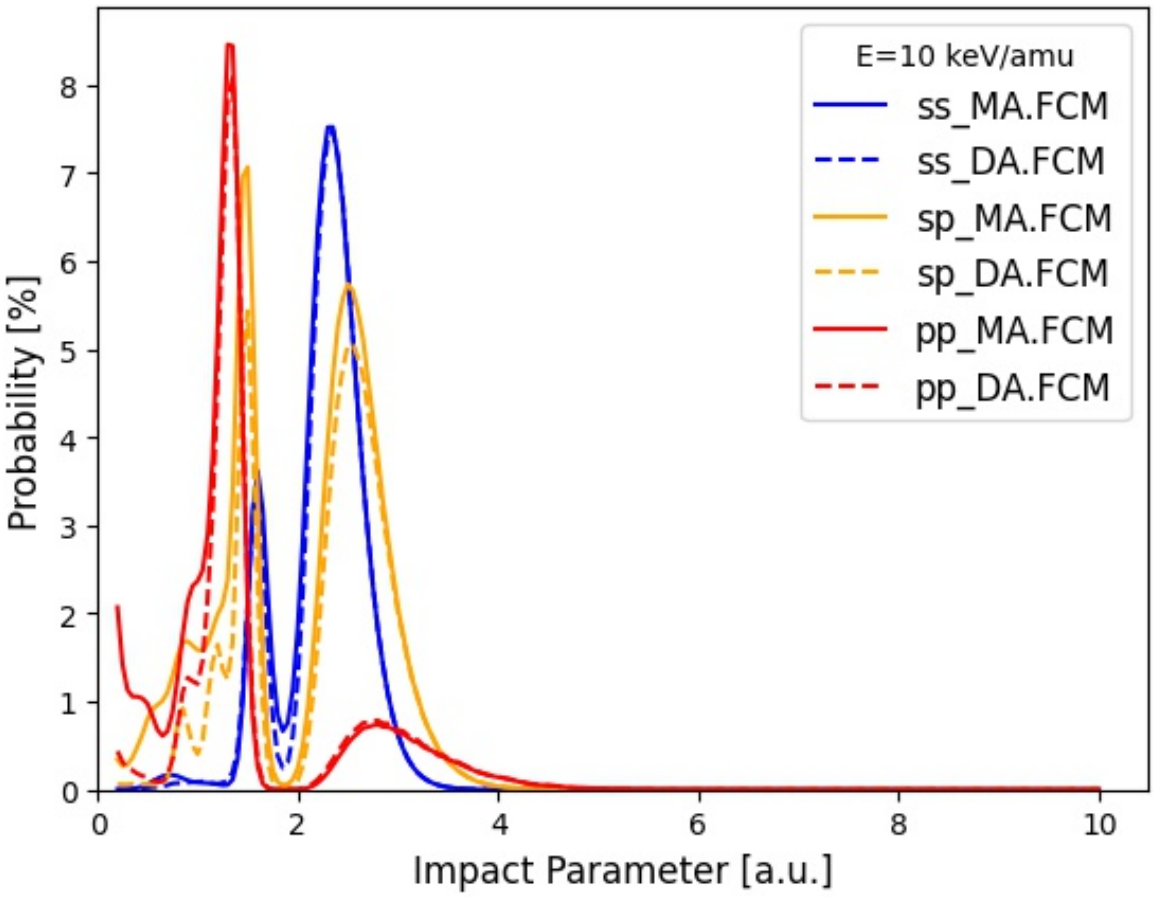


Figure 6: $He^{2+}$–$Ne_2$ ion-dimer collisions in parallel orientation at 10 keV/amu. One-site two-electron removal probabilities comparing MA.FCM (solid lines) and DA.FCM (dashed lines).

In Figure 6, the FCM for both multinomial and determinantal analyses are compared for the one-site two-electron removal channels. As can be seen, there are only minor differences between the two analyses, further indicating that the analyses are consistent. A difference between Figures 5 and 6 is how double $2s$ electron removal has half the height in comparison to two-site removal, which is in line with equation (62) being a factor of 2 smaller than equation (65). It is also noteworthy that the peak for $2p^{-2}$ in Figure 6 is not exactly half that of $2p^{-1}, 2p^{-1}$ in Figure 5 due to the difference in the cross-terms from equation (66) in comparison to (63).

Given that the DA is a more fundamental approach, it is more insightful to compare the differences between its FCM and the two capture models. Comparisons of the multinomial analyses and its models can be found in the Appendix from A.33 to A.36.

Figure 7 presents this comparison for the $2s$ and $2p$ removal channels. Both capture models are similar to the fixed-charge model, indicating that changes in projectile charge due to collision order have only a minor effect for single electron removal. Inspection of the first term on the right-hand side of (89) shows that the elastic probability $P^{*}_{\text{elastic}}$ constitutes the only modified contribution in the capture models. In capture model II, additional projectile-to-target electronic transitions are included, leading to a modest increase in the total probability for $2s^{-1}$ vacancy production.

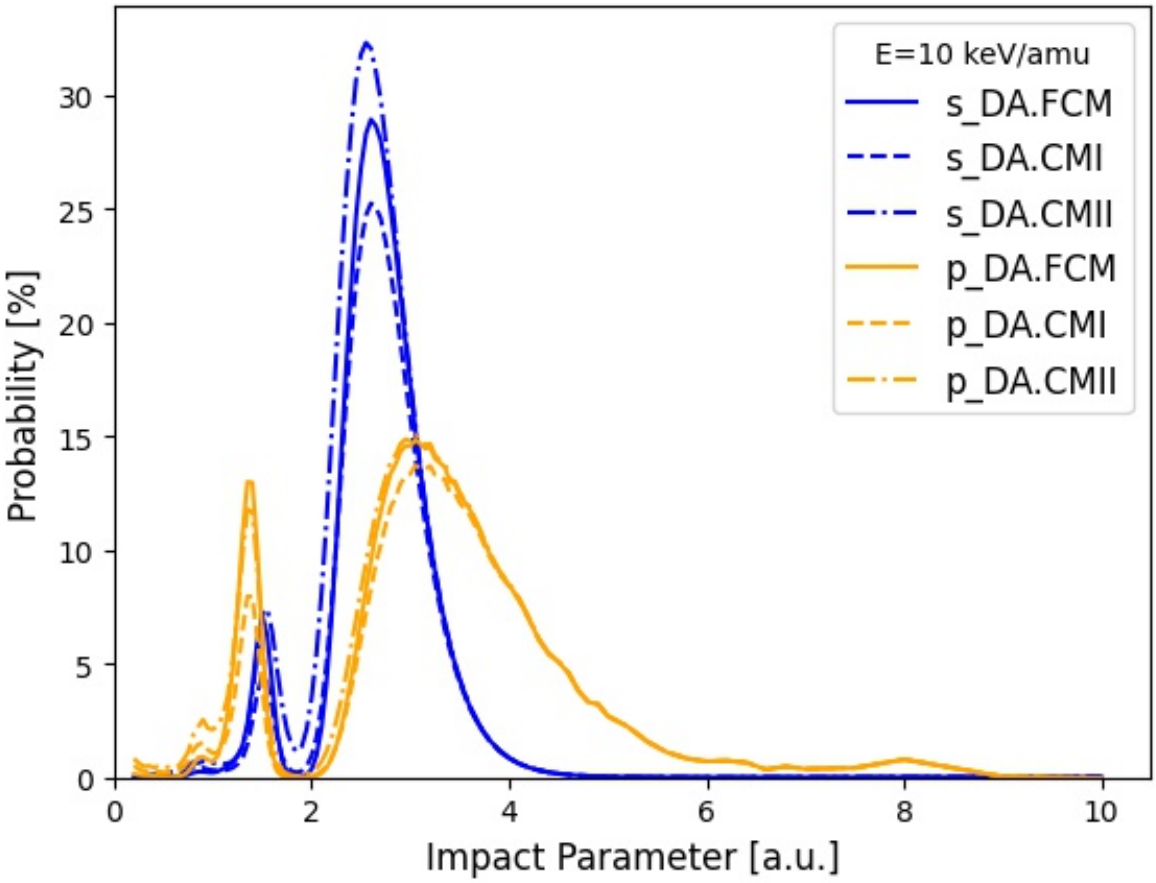


Figure 7: $He^{2+}$–$Ne_2$ ion–dimer collisions in parallel orientation at 10 keV/amu. Single-electron removal probabilities comparing DA.FCM (solid lines), DA.CMI (dashed lines), and DA.CMII (dash-dotted lines) [65].

More pronounced differences between the determinantal analysis' models emerge when additional electron removal channels are considered, particularly two-site processes involving one electron removal from each atom in the dimer. As illustrated in Fig. 8, the $2s^{-1}, 2s^{-1}$ channel exhibits a substantial reduction in probability for the capture model relative to

the fixed-charge model. This behavior reflects electron capture by the projectile during the first encounter, which suppresses subsequent capture events. In contrast, the $2s^{-1}, 2p^{-1}$ and $2p^{-1}, 2p^{-1}$ channels show considerably smaller differences, owing to the comparatively easier removal of $2p$ electrons by a $He^{+}$ projectile.

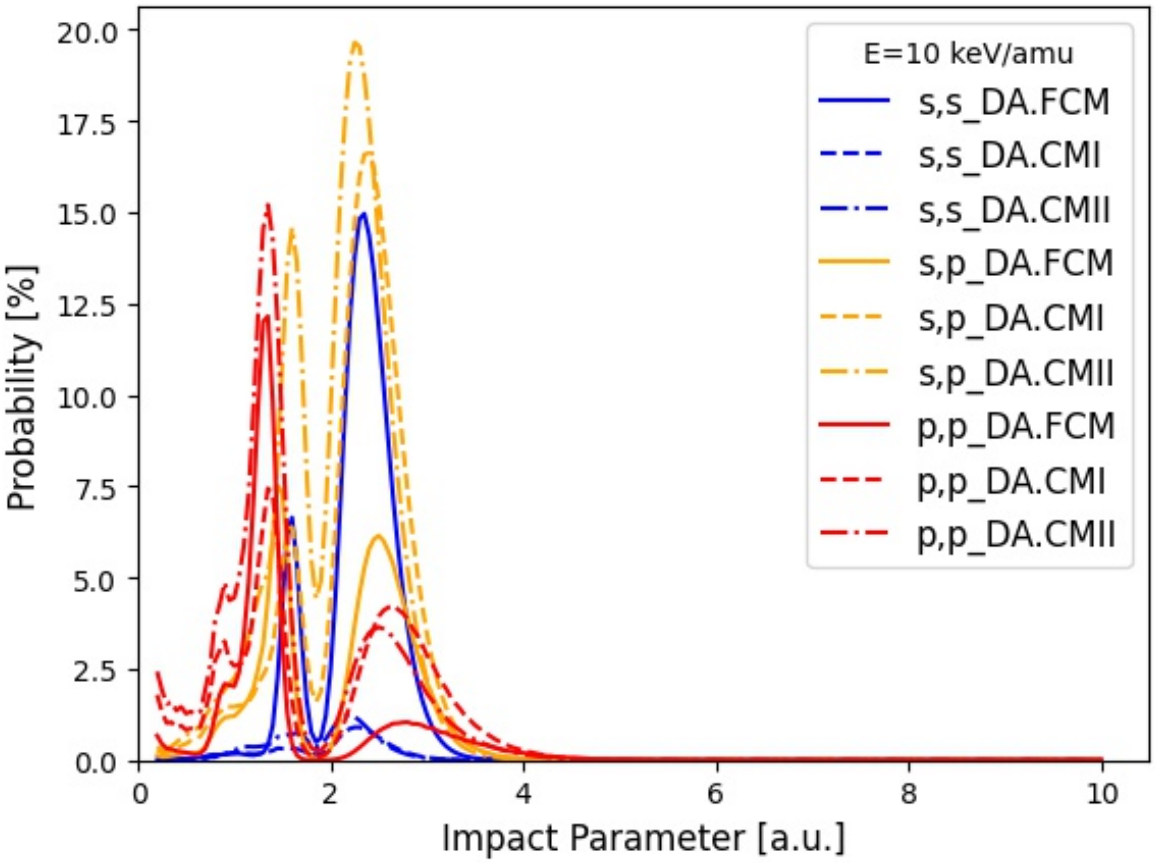


Figure 8: $He^{2+}$–$Ne_2$ ion–dimer collisions in parallel orientation at 10 keV/amu. Two-site two-electron removal probabilities comparing DA.FCM (solid lines), DA.CMI (dashed lines) and DA.CMII (dashed-dotted lines).

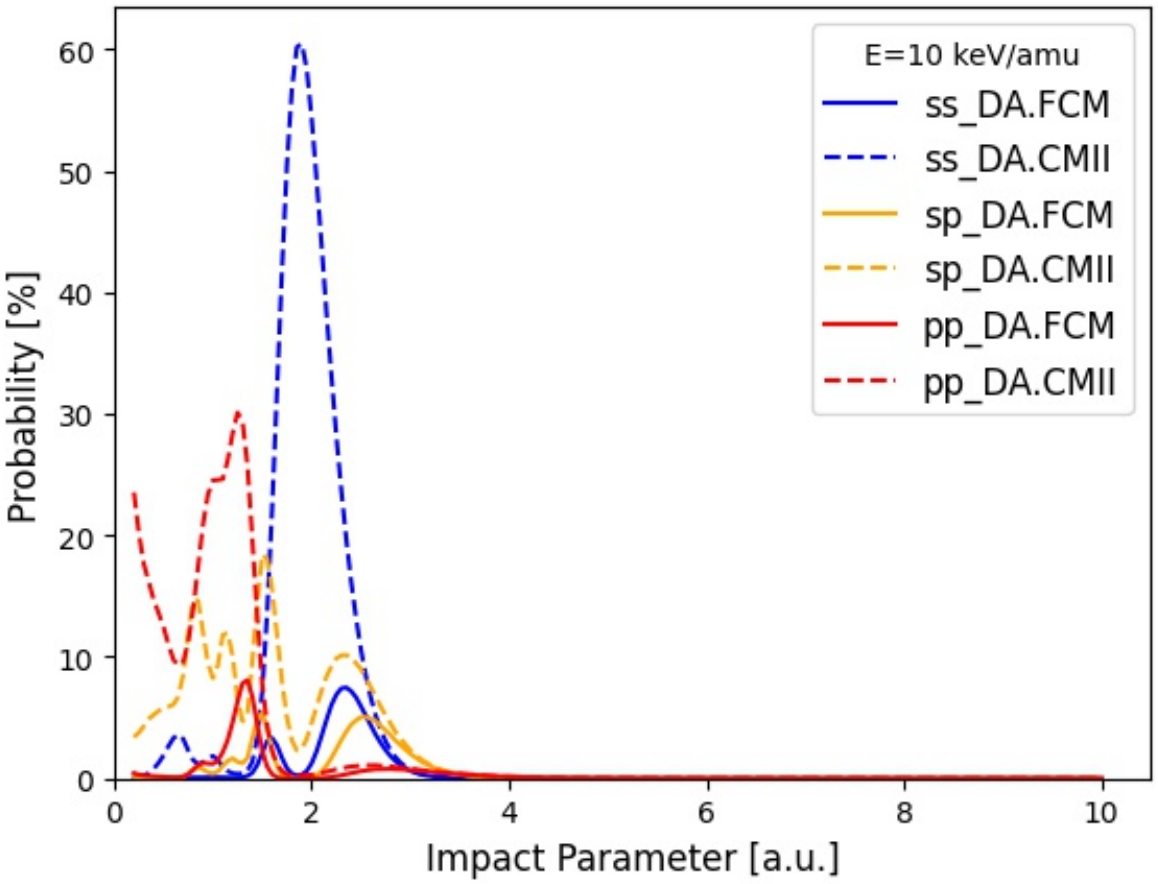


Figure 9: $He^{2+}$–$Ne_2$ ion–dimer collisions in parallel orientation at 10 keV/amu. One-site two-electron removal probabilities comparing DA.FCM (solid lines) and DA.CMII (dashed lines).

Figure 9 further demonstrates the divergence between the capture models and the fixed-charge model for the one-site two-electron removal channels, with the $2s^{-2}$ channel showing the largest difference. DA.CMI is not shown as it has identical probabilities as DA.CMII. This is due to the $He^{2+}$ projectile becoming neutral helium after double capture, and its resulting interaction with the second atom in the dimer being negligible. Both capture models have the resulting probability calculated as described in (89), where there are no interactions with a $He^{+}$ projectile, so that there are no differences in both capture models of the determinantal analysis.

The results so far have examined the no-response model, but it is instructive to explore the dynamic response model for these electron removal channels as well. The response model is first compared in the determinantal analysis with the capture model II.

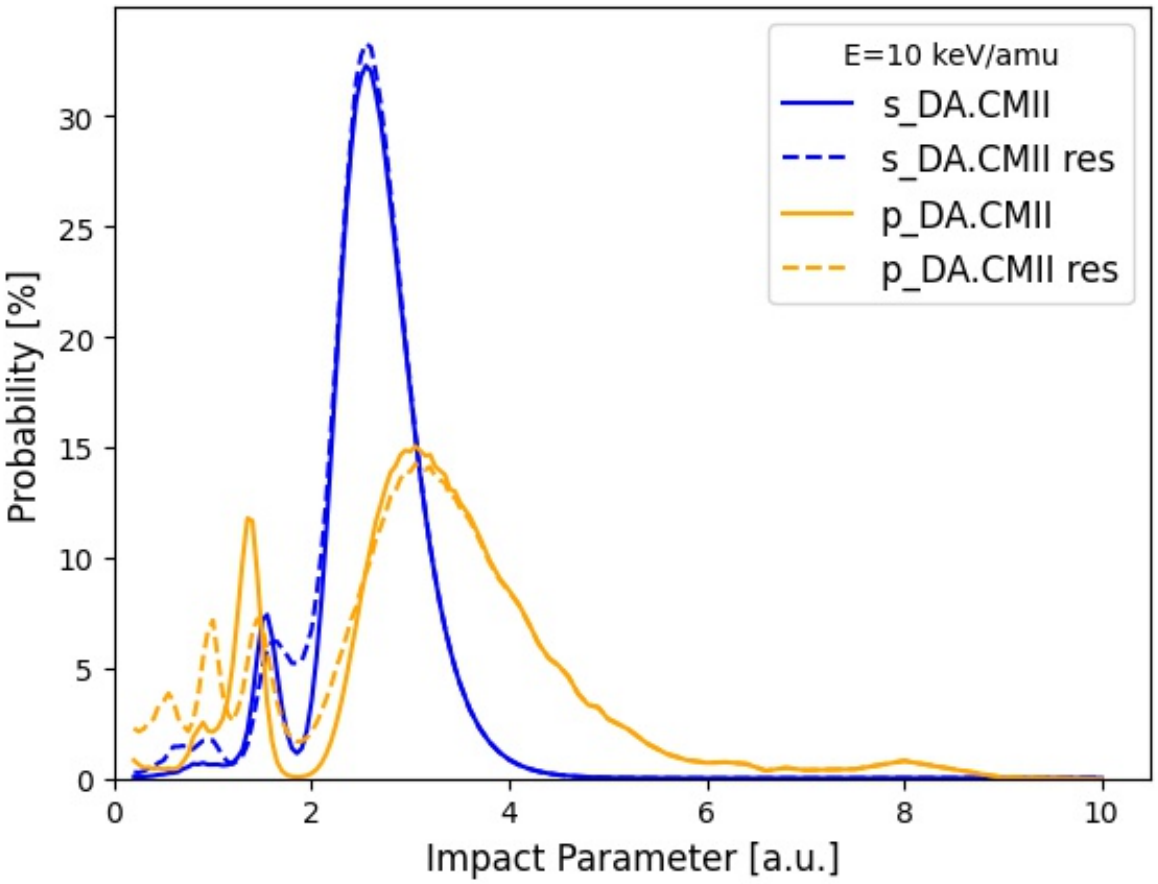


Figure 10: $He^{2+}$–$Ne_2$ ion–dimer collisions in parallel orientation at 10 keV/amu. Single-electron removal probabilities comparing DA.CMII without response (solid line) and with response (dashed line) [65].

The influence of dynamical response is illustrated in Fig. 10, which compares DA.CMII results obtained with and without response for $2s^{-1}$ and $2p^{-1}$ vacancy production. Only minor differences are observed, consistent with the design of the response model, which primarily affects higher charge states [68]. Larger response effects appear in certain two-electron removal channels as seen in Figures 11 and 12 with the cross-sections listed in Table I, and the importance of dynamical response is expected to increase for higher projectile charge multiplicities ($q > 2$).

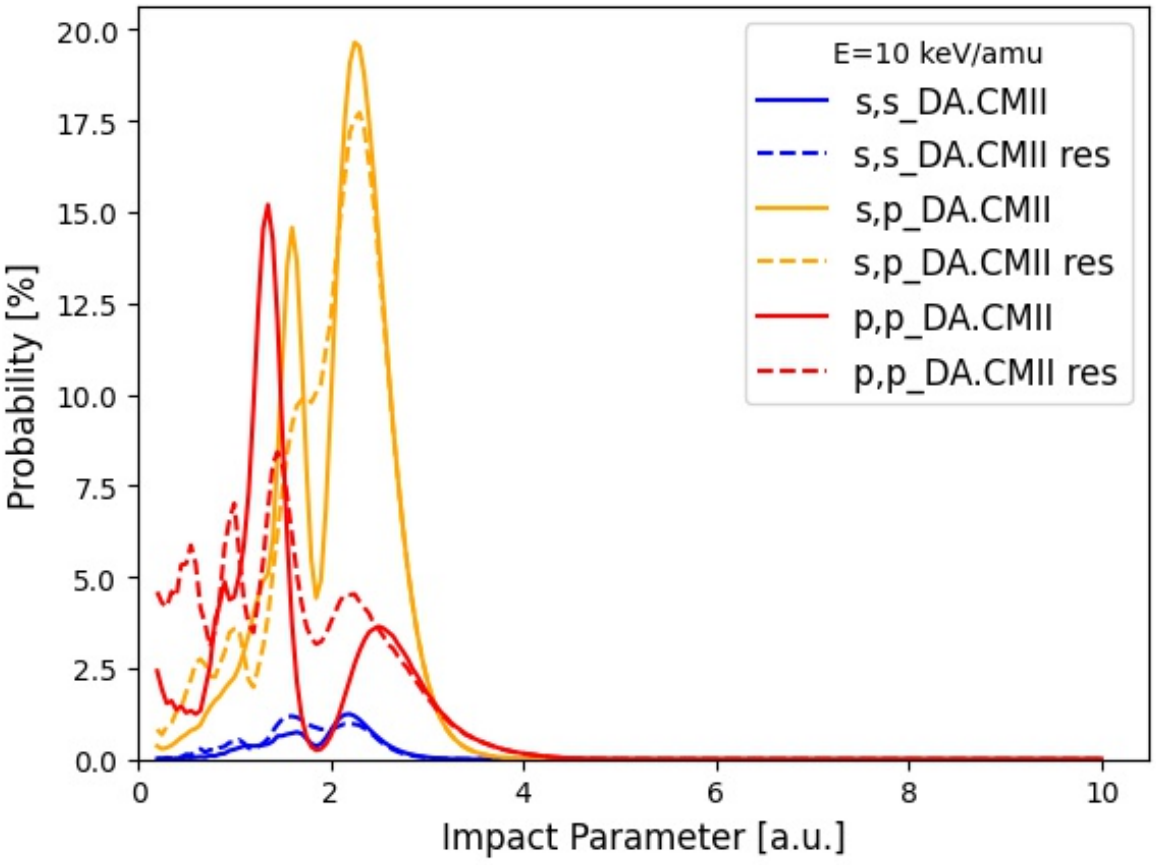


Figure 11: $He^{2+}$–$Ne_2$ ion–dimer collisions in parallel orientation at 10 keV/amu. Two-site two-electron removal probabilities comparing DA.CMII without response (solid lines) and with response (dashed lines).

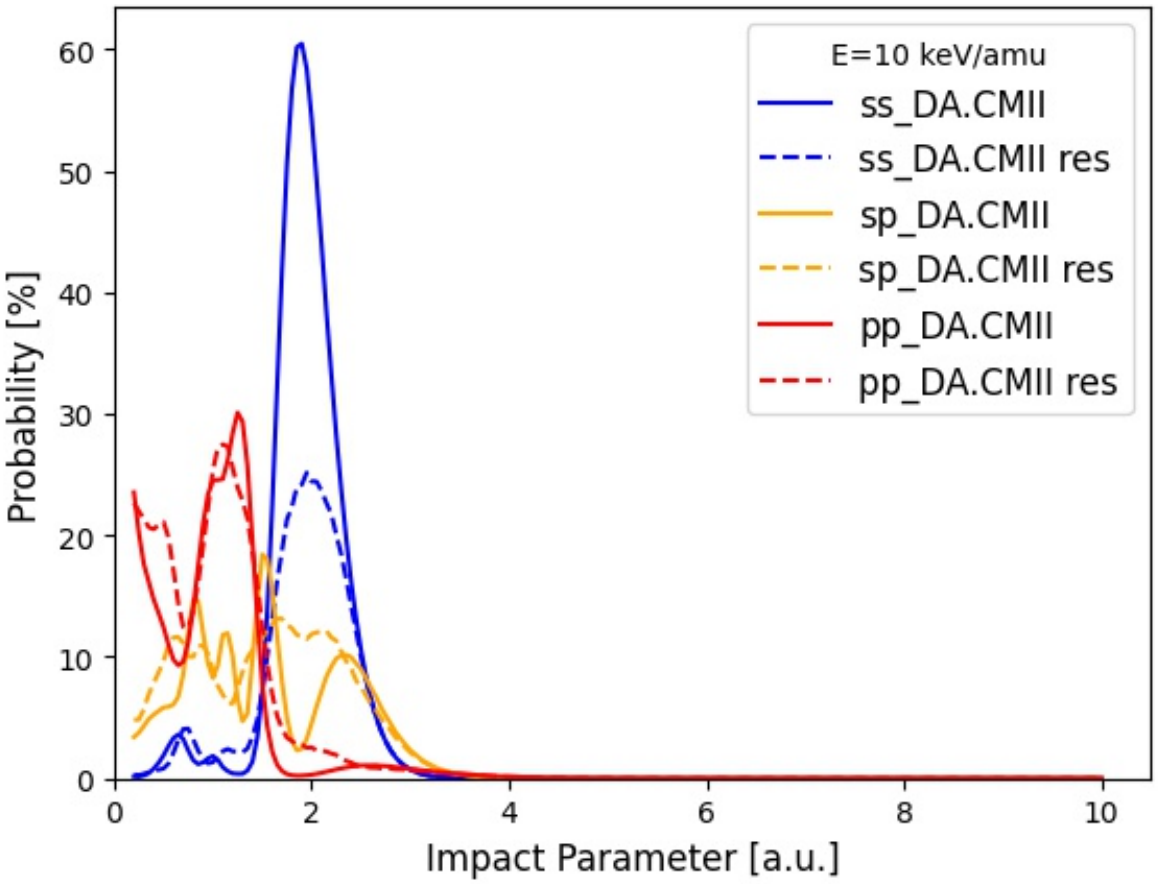


Figure 12: $He^{2+}$–$Ne_2$ ion–dimer collisions in parallel orientation at 10 keV/amu. One-site two-electron removal probabilities comparing DA.CMII without response (solid lines) and with response (dashed lines).

The differences in probabilities for two-site two-electron removal between no-response and response models is more pronounced than for single-electron removal, but not large except for impact parameter less than 2 a.u.. However, the differences are more significant for one-site two-electron removal, which is a function of multiple electron capture from a single target atom. The difference is largest for $2s^{-2}$ vacancy production, with half the peak height around $b = 2$ a.u. for the response model.

The total cross-sections, obtained by integrating the probabilities over the impact parameter, are summarized in Table I (results slightly differ from those in [67] due to a previous minor error in the calculation).

The ICD yield represents the fraction of $Ne^+$+$Ne^+$ fragmentation events associated with $2s^{-1}$ production. The predicted yield remains substantial across all models, although it is

| Models | $2s^{-1}$ | $2s^{-1}, 2s^{-1}$ | $2s^{-1}, 2p^{-1}$ | $2p^{-1}, 2p^{-1}$ | $2p^{-2}$ | ICD yield |
|---|---|---|---|---|---|---|
| MA.FCM | 1.28 | 0.44 | 0.26 | 0.17 | 0.12 | 0.56 |
| DA.FCM | 1.24 | 0.39 | 0.29 | 0.16 | 0.08 | 0.57 |
| DA.CMII | 1.39 | 0.05 | 0.77 | 0.36 | 0.47 | 0.46 |
| DA.CMII res | 1.47 | 0.05 | 0.73 | 0.37 | 0.61 | 0.46 |

Table I: Total cross-sections (in Å$^2$) for various models and electron removal processes in the $He^{2+}$–$Ne_2$ ion–dimer system. The ICD yield is defined as the ratio of the $2s^{-1}$ cross-section to the sum of all channels leading to $Ne^+$+$Ne^+$ fragmentation [65].

somewhat reduced in the capture models. All two-site two-electron removal processes lead to Coulomb explosion and are therefore included. The $2p^{-2}$ channel is included because $Ne^{2+}(2p^{-2})$+Ne may decay into $Ne^+$+$Ne^+$ via radiative charge transfer (RCT). For simplicity, it is assumed that RCT occurs with unit probability in this channel, although this assumption remains debatable (see, e.g., Ref. [47]). The $2s^{-2}$ and $2s^{-1}2p^{-1}$ channels are excluded, as these primarily lead to $Ne^{2+}$+$Ne^+$ fragmentation via ICD [11]. These omitted channels are notable in that they constitute the only allowed three-electron processes in the capture model, implying a purely ICD-driven $Ne^{2+}$+$Ne^+$ fragmentation pathway.

### 4.2. $He^+$ Projectiles

Changing the initial charge of the projectile has an impact on the collision dynamics and is reflected in the removal probabilities for models. Examining single-electron removal between analyses in the fixed-charge model for a $He^+$ projectile is a good way to observe the change in the collision system.

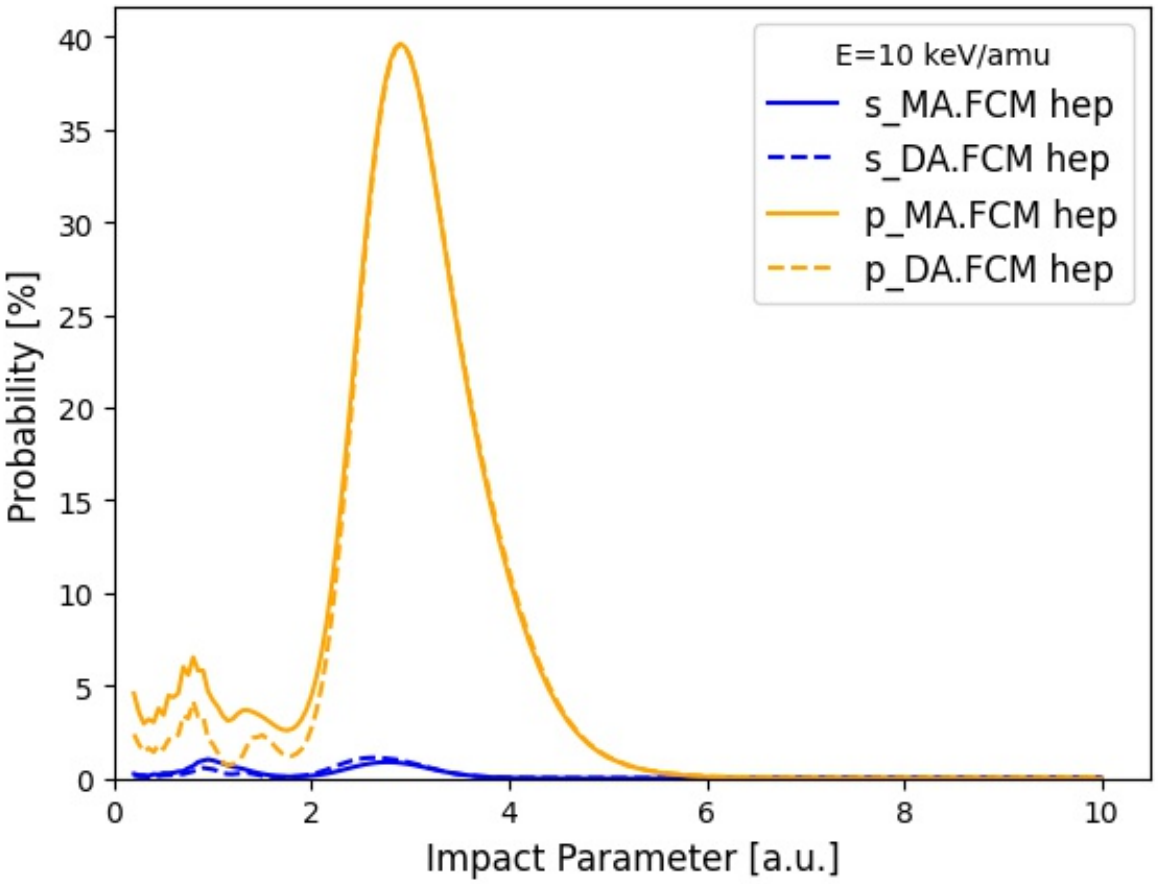


Figure 13: $He^+$–$Ne_2$ ion–dimer collisions in parallel orientation at 10 keV/amu. Single-electron removal probability comparison for MA.FCM (solid lines) and DA.FCM (dashed lines).

The differences between the two analyses for the fixed-charged model in Figure 13 are negligible. However, it is important to note how much smaller the probabilities for $2s$ electron removal is in comparison to a $He^{2+}$ projectile as seen in Figure 4. This implies a substantially weaker removal probability with a $He^+$ projectile. It is also noteworthy that the peak $2p$ electron removal probability has greatly increased.

A distinguishing feature of $He^+$ projectiles within the capture model is the restriction to single-electron removal from the dimer. After capture of one electron, the projectile becomes neutral and can no longer induce additional capture.

Figure 14 compares the $2s$ and $2p$ electron removal probabilities for $He^+$ projectiles between the FCM and capture models of the determinantal analysis. It is important to note the reduction in probability in comparison to the collision with $He^{2+}$ ions shown in Figure

7. As in the $He^{2+}$ case, DA.CMII produces the largest probabilities among the considered models.

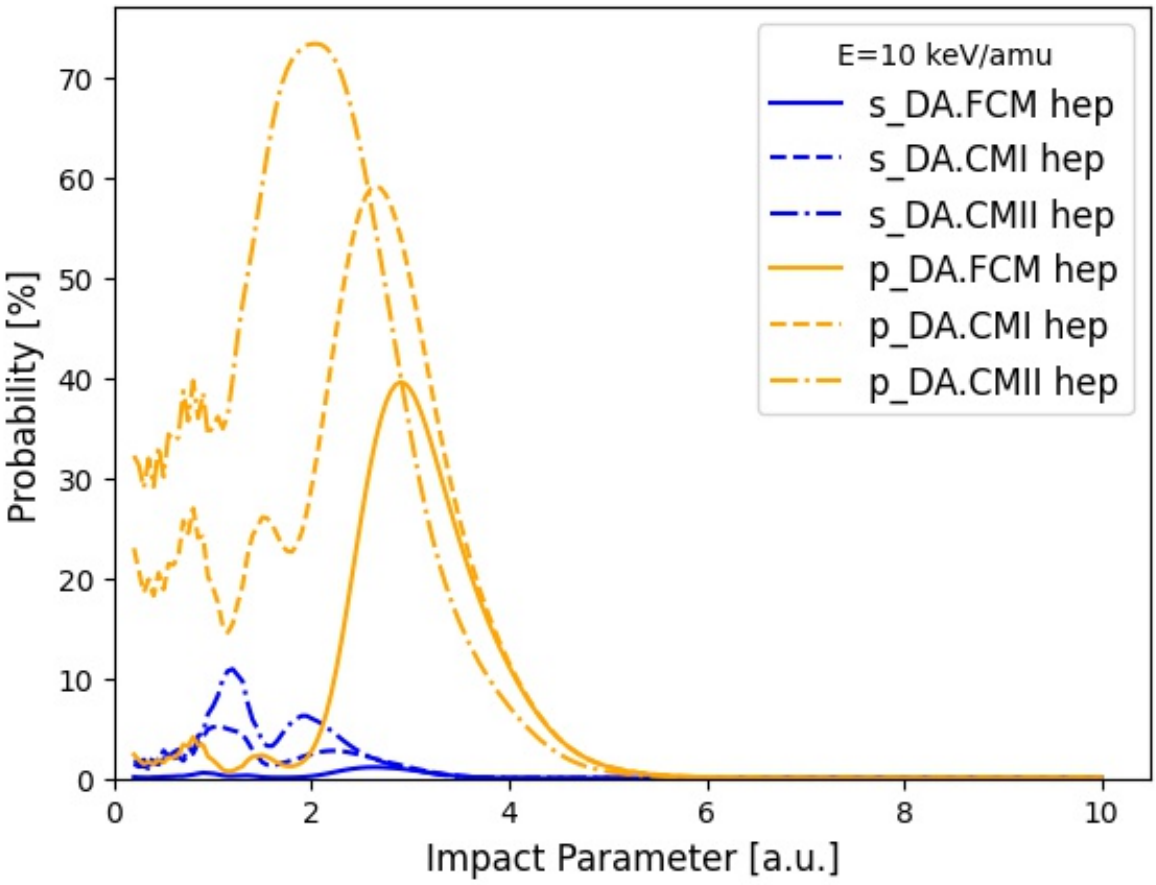


Figure 14: $He^+$–$Ne_2$ ion–dimer collisions in parallel orientation at 10 keV/amu. Single-electron removal probability comparison for DA.FCM (solid lines), DA.CMI (dashed lines) and DA.CMII (dashed-dotted lines).

An interesting feature is that the variance is greatest among the capture models, with large discrepancies that are not seen in the case of a $He^{2+}$ projectile. The reduced projectile charge makes $2s$ capture less likely, while $2p$ is easier to capture, resulting in a higher probability and overall cross-section. This is due to the single-electron binding energies of an initial Ne($2p$) and final He($1s$) being closer than for an initial Ne($2s$). Another insight is that the peak probability of single-electron channels, most notably for $2p$ removal, shifts towards smaller impact parameters from FCM to CMI and then finally to CMII.

The effects of dynamic response are examined for $He^+$ impact in the DA.CMII in Figure 15, where the differences between no-response and response models is not significant, except

for impact parameters less than 2 a.u..

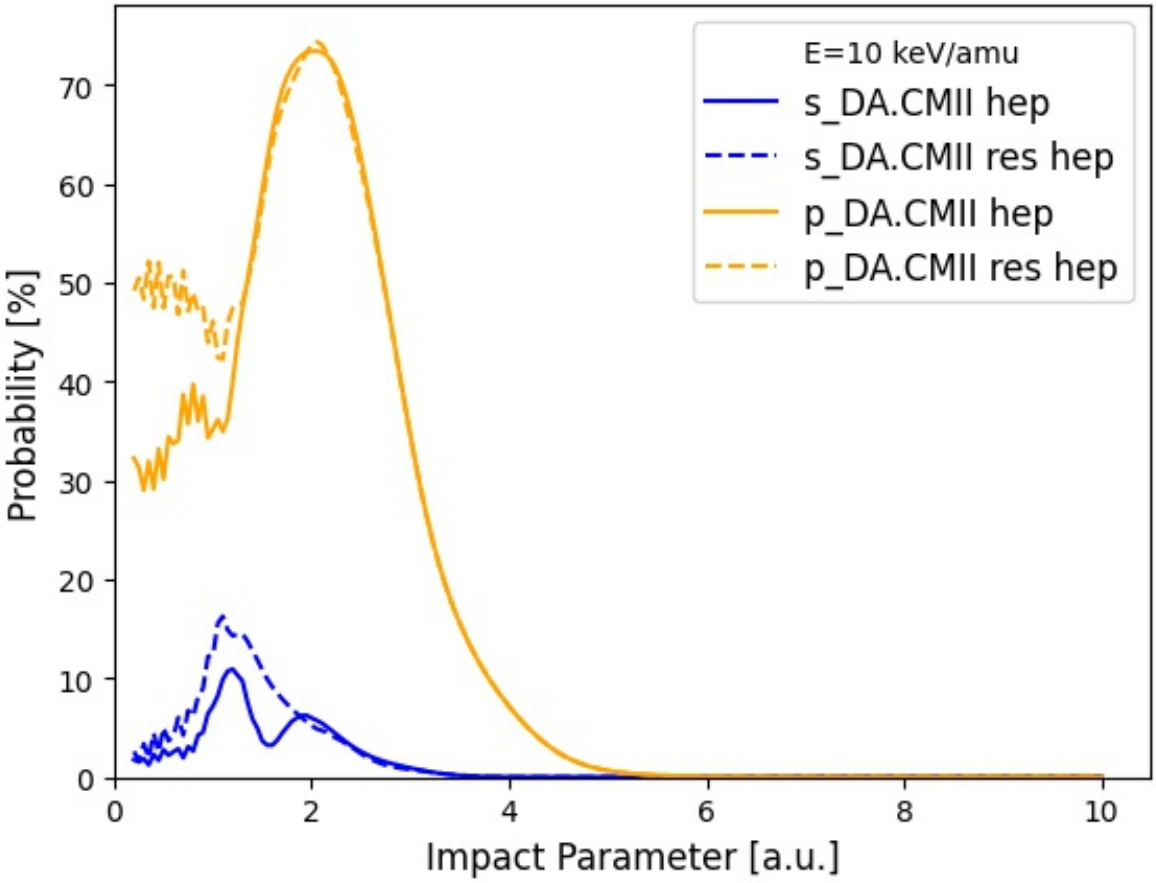


Figure 15: $He^+$–$Ne_2$ ion–dimer collisions in parallel orientation at 10 keV/amu. Single-electron removal probability comparison for DA.CMII without response (solid line) and with response (dashed line).

The dynamic response difference is also minor for the determinantal analysis across both fixed-charge and capture models for all electron removal channels as can be seen in the Appendix from Figures A.58 to A.63.

Overall, there are no significant probability differences between no-response and response models, except for the $2p^{-1}$ channel for impact parameter less than 2 a.u..

For a $He^+$ projectile the total DA.CMII cross-section for $2s$ electron removal is substantially smaller than for $He^{2+}$ impact (0.47 Å$^2$ compared to 1.39 Å$^2$). However, this channel corresponds to a perfect ICD yield, in the sense that $Ne^+$+$Ne^+$ fragmentation events are exclusively associated with ICD in the capture model. Although the absolute probability is low, this feature renders $He^+$ projectiles particularly attractive for generating clean ICD

signatures in ion-dimer collisions [65]. Experimental results reported by Kim *et al.* [11] for $He^+$ impact on neon dimers at 125 and 162.5 keV/amu show evidence of strong ICD yields; however, direct ionization channels are open at those energies and contribute to $Ne^+$+$Ne^+$ fragmentation. Experimental investigations at lower energies, where capture dominates, would therefore provide a stringent test of the predictions presented here.

# 5. HELIUM ION - ARGON DIMER COLLISION SYSTEM

---

A subset of the results discussed in this chapter were first presented in [67].

Unlike the neon dimer, the argon dimer target system does not offer the same simple pathway for ICD through single inner valence electron removal. This means that the channels previously explored in Chapter 4 do not facilitate ICD. However, they are investigated to understand the change in behaviour of the electron dynamics in this new collision system and the resulting dimer fragmentation.

The labeling rules from the neon dimer target collision system are carried over, with the $M$ shell being the analogue of the $L$ shell electrons of neon. Ionization and excitation of electrons from the $K$ and $L$ shells are treated as negligible given the projectile impact energy regime from 10 keV/amu to 150 keV/amu under consideration in these investigations. Electrons from the $3p$ orbital are able to undergo excitation to higher electron shells such as $3d$, $4s$, $4p$, $4d$ and $4f$. These excitations if accompanied by electron removal can give rise to ICD that results in $Ar^+$-$Ar^+$ fragmentation.

As described in section 3 2.3, the capture models for the helium ion-argon dimer target system are modified to balance capture and ionization processes as a function of projectile impact energy. These models are called the *modified capture models*, and the models are labelled in the figures MCMI and MCMII for modified capture model I and II respectively.

## 5.1. $He^{2+}$ Projectiles

As with the neon dimer target, the discussion will be limited to electron removal and capture of up to two electrons for the $He^{2+}$ projectile in the argon dimer target collision system. It is instructive to look at the single $3s$ electron removal channel in the no-response model with impact energy 10 keV/amu for the models under consideration.

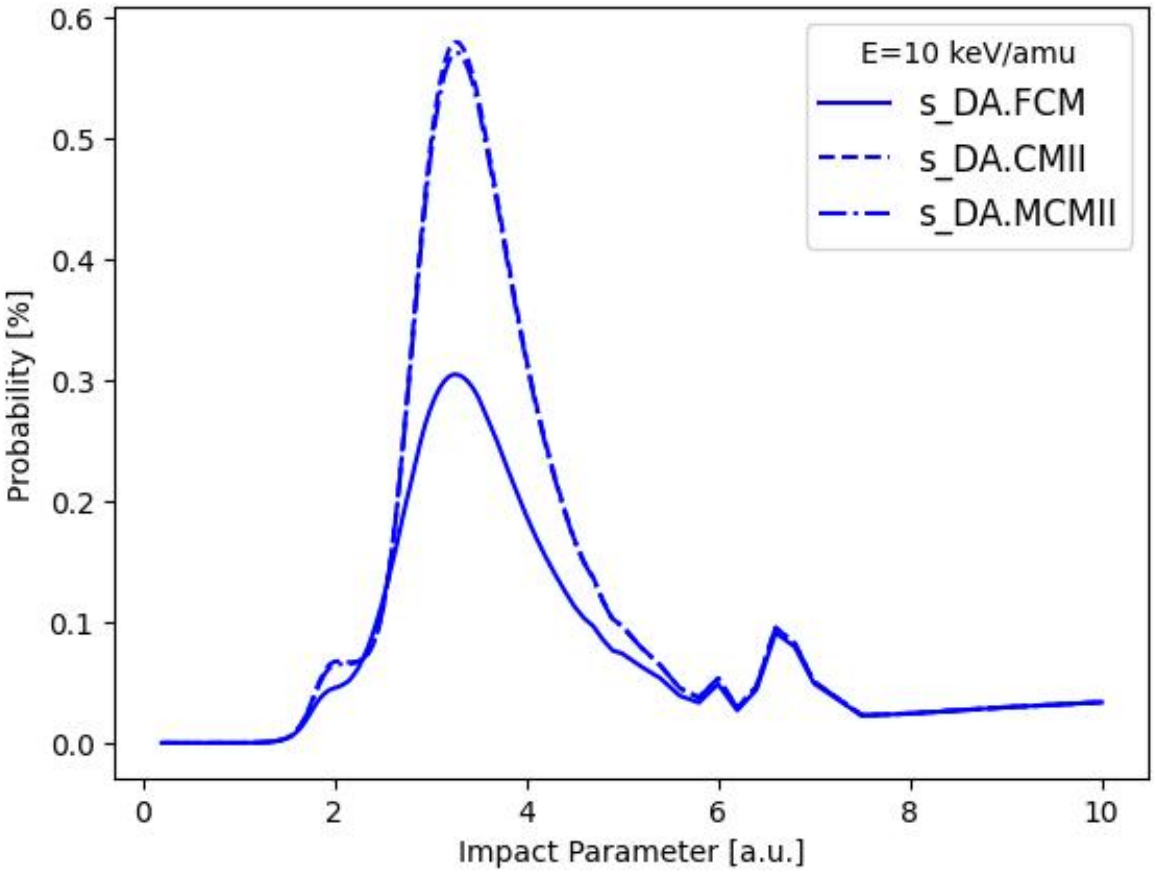


Figure 16: $He^{2+}$–$Ar_2$ ion–dimer collisions in parallel orientation at 10 keV/amu. Single $3s$ electron removal probability comparing DA.FCM (solid line) and DA.MCMI (dashed line) and DA.MCMII (dashed-dotted line).

The minuscule probabilities for single electron removal from the $l = 0$ orbital in Ar($3s$) vs Ne($2s$) can be seen in the difference between Figure 16 and 7 for the neon dimer. The differences in models are more pronounced, though this is less surprising given the small probability for this particular channel.

As modified capture models are used for these collision systems, it is instructive to compare them with the unmodified models to see change in capture dominance as a function of impact energy.

This is done in Figure 17. The two models are practically identical at the projectile impact energy 10 keV/amu (Figure 16), which supports the initial assumption about the capture model that at projectile velocity less than $\bar{v}$ electron removal is equivalent to capture by the projectile. However, as the impact energy increases the differences with the modified

model become more pronounced.

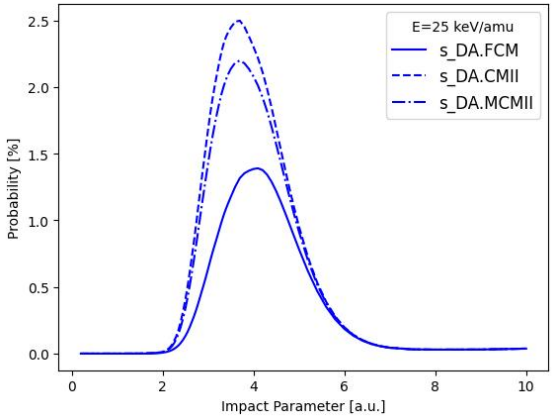


(a) 25 keV/amu

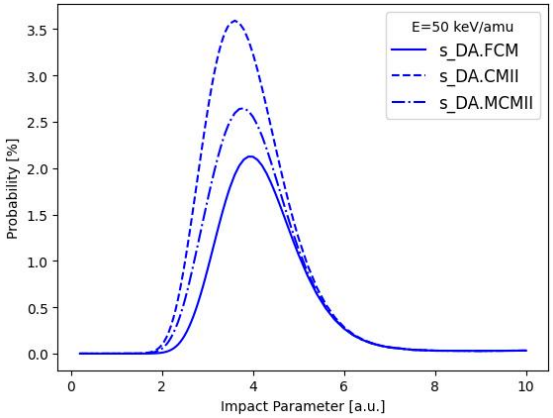


(b) 50 keV/amu

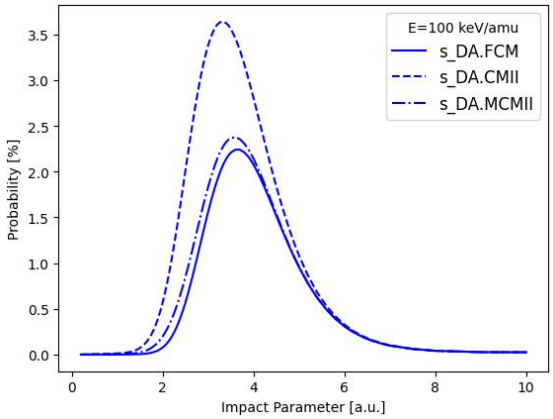


(c) 100 keV/amu

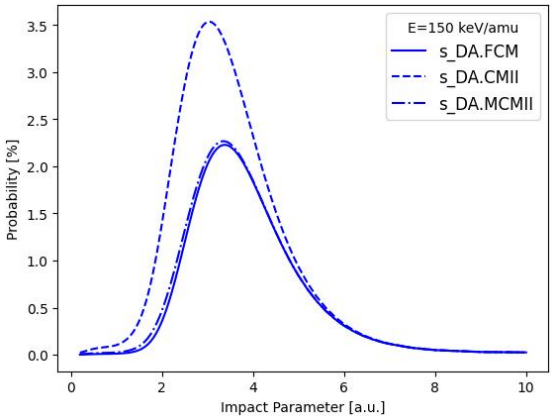


(d) 150 keV/amu

Figure 17: $He^{2+}$–$Ar_2$ ion–dimer collisions in parallel orientation. Single $3s$ electron removal probability comparing DA.FCM (solid line), DA.CMII (dashed line), and DA.MCMII (dashed-dotted line) for different projectile impact energies.

This is due to ionization processes dominating over capture processes at higher impact energies, reaffirming the fact that the unmodified capture models are only valid at low impact energy. At 150 keV/amu, the modified capture model is nearly equivalent to the FCM, as expected with the energy scaling.

Two-electron removal probabilities are presented in Figures 18 and 19 across models and energy regimes, as two-site removal processes contribute to the overall $Ar^+$-$Ar^+$ dimer fragmentation.

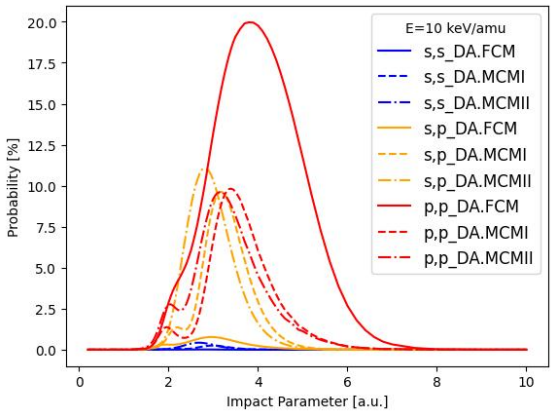


(a) 10 keV/amu

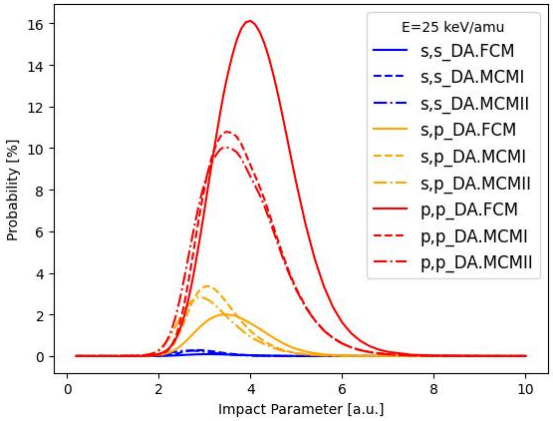


(b) 25 keV/amu

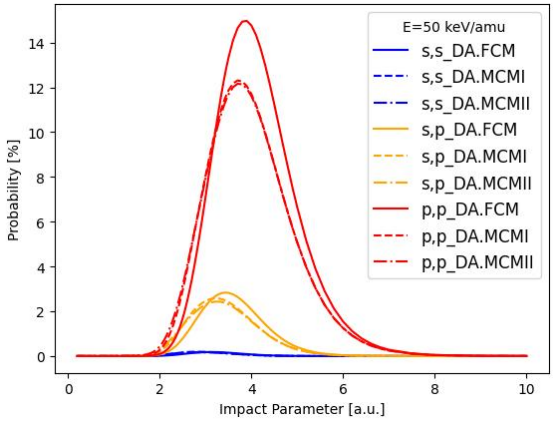


(c) 50 keV/amu

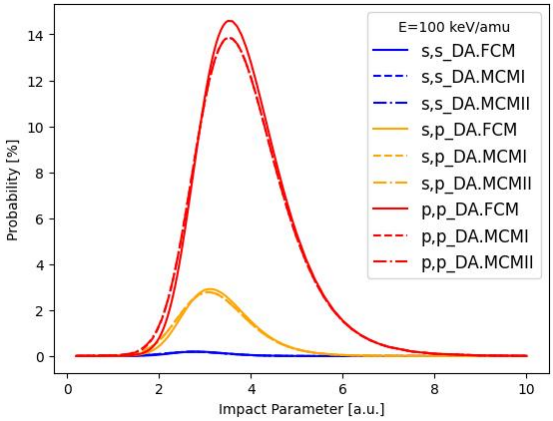


(d) 100 keV/amu

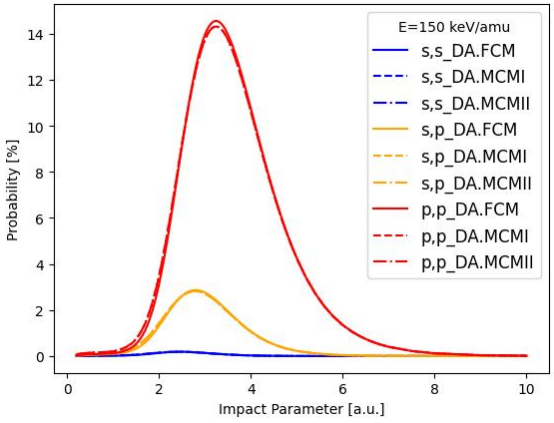


(e) 150 keV/amu

Figure 18: Two-site two-electron removal probabilities for $He^{2+}$–$Ar_2$ collisions in parallel orientation. Comparison of DA.FCM (solid lines), DA.MCMI (dashed lines), and DA.MCMII (dashed-dotted lines) across different projectile impact energies.

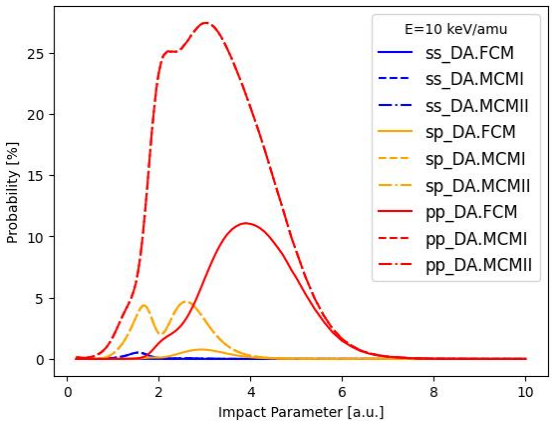


(a) 10 keV/amu

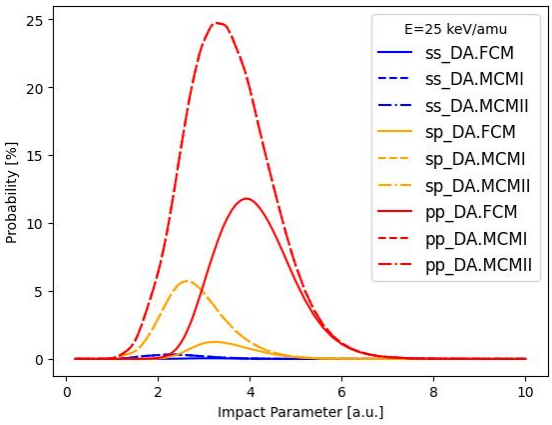


(b) 25 keV/amu

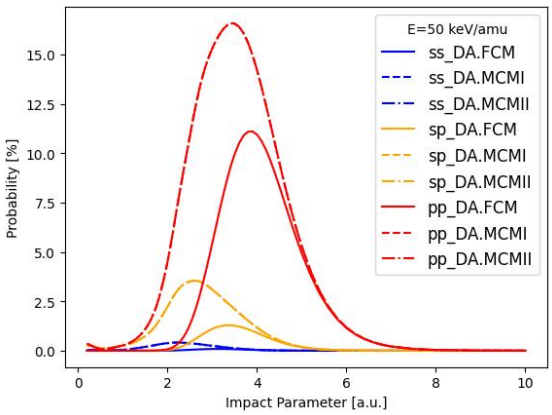


(c) 50 keV/amu

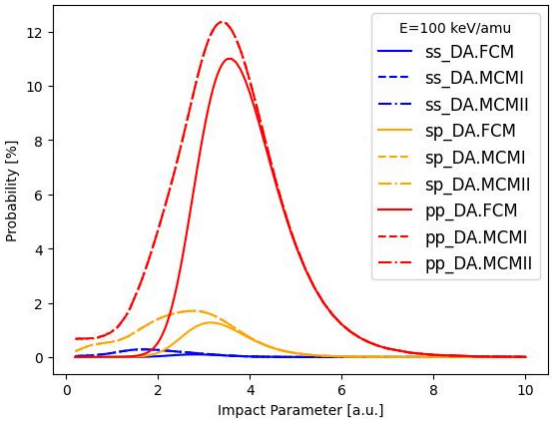


(d) 100 keV/amu

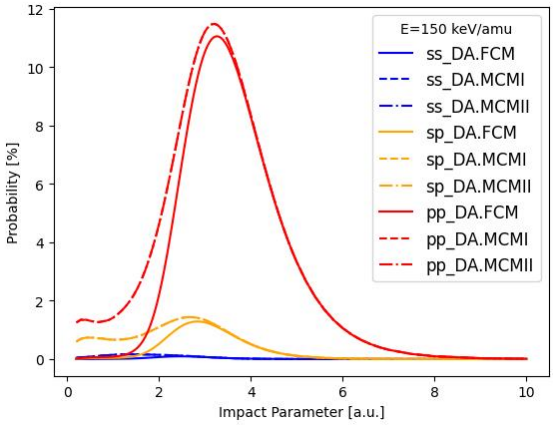


(e) 150 keV/amu

Figure 19: One-site two-electron removal probabilities for $He^{2+}$–$Ar_2$ collisions in parallel orientation. Comparison of DA.FCM (solid lines), DA.MCMI (dashed lines), and DA.MCMII (dashed-dotted lines) across different projectile impact energies.

There are some notable differences between the two-site and one-site two-electron removal processes in Figures 18 and 19 respectively across projectile impact energy. The peak height of the $3p^{-1}, 3p^{-1}$ channel in the FCM shrinks as the impact energy increases from 18a to 18e. Simultaneously, the peak heights for the $3p^{-1}, 3p^{-1}$ production in the MCMI and MCMII increase and converge with the FCM peak as the impact energy approaches 150 keV/amu. For the $3s, 3p$ removal channel the behaviour is the opposite regarding the models, with the FCM peak being smaller at 10 keV/amu and increasing to 150 keV/amu and modified capture model peak probabilities shrinking for increasing energy. For the $3p^{-2}$ vacancy production in Figure 19, the modified capture models have the largest probability peak in Figure 19a and are shrinking for increasing projectile impact energy towards 150 keV/amu in Figure 19e. This behaviour is similar for $3s^{-1}3p^{-1}$ production, though the channel has a much smaller probability peak. In Figure 19 MCMI and MCMII are equal due to neutral He having a negligible interaction. The modified capture models converge with the fixed-charge model at higher impact energies, regardless of removal channel, for both two-site and one-site removal channels as expected.

As all the collision systems investigated so far have been in the no-response model, it is also instructive to look at a comparison of the no-response and response models. Single $3s$ electron removal as a baseline metric is examined for the MCMII at an impact energy of 10 keV/amu in Figure 20.

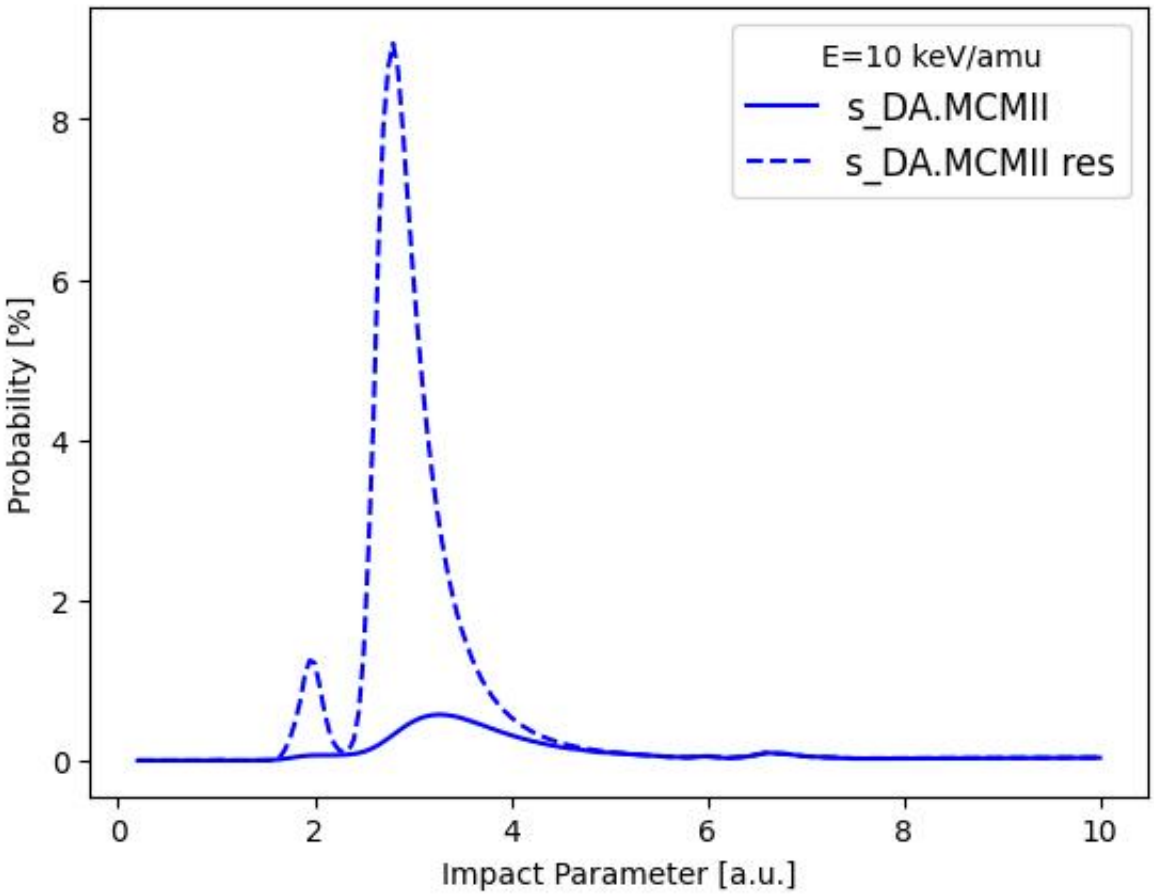


Figure 20: $He^{2+}$–$Ar_2$ ion–dimer collisions in parallel orientation at 10 keV/amu. Single $3s$ electron removal probability comparing DA.MCMII (solid line) and DA.MCMII res (dashed line).

In Figure 20 with the MCMII a large discrepancy is observed between the no-response and response models for $3s$ electron removal, with a large probability peak between $b = 2.5$ a.u. to $b = 3$ a.u.. To understand this effect, it is instructive to examine the differences in orbital energy levels under consideration, which are $\mathrm{Ar}(3s) = -1.099$ a.u. and $\mathrm{He}(1s) = -0.918$ a.u. according to the OPM calculations described in [58]. Although the energy levels are not close enough for a resonance transition, the dynamic response of the potential may result in a bending of the energy curves and an enhancement of the radial coupling as was observed in certain ion-atom collision systems in [86]. However, this difference is not present when observing the $3p$ removal channel (see Figure B.75), indicating that the initial and final single-particle energy levels are not close in the response model.

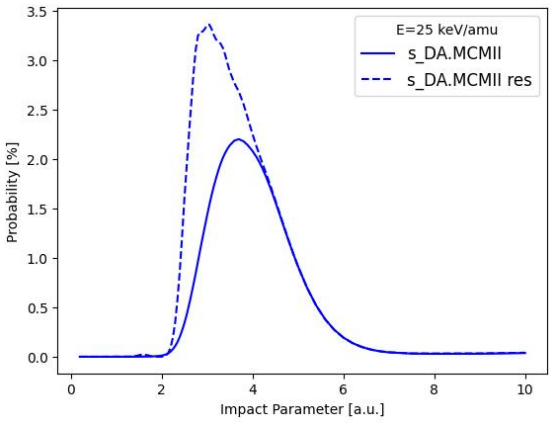


(a) 25 keV/amu

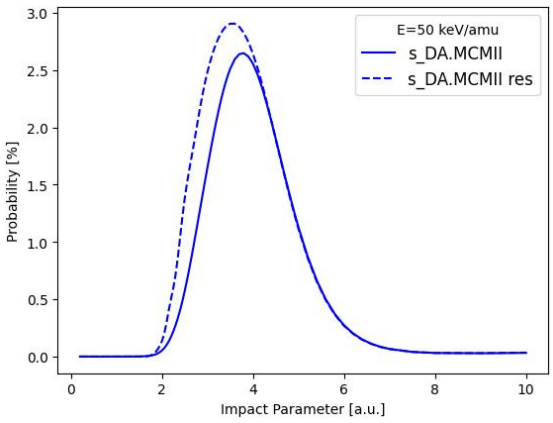


(b) 50 keV/amu

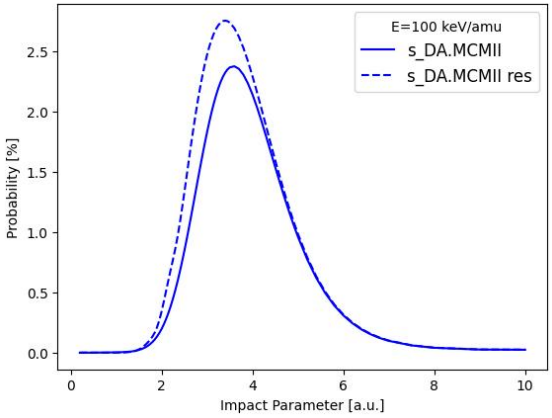


(c) 100 keV/amu

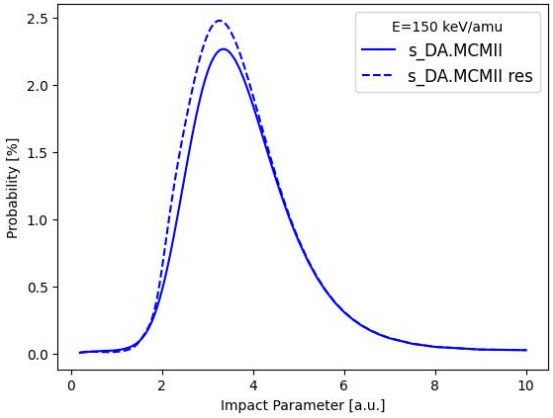


(d) 150 keV/amu

Figure 21: $He^{2+}$–$Ar_2$ ion–dimer collisions in parallel orientation. Single $3s$ electron removal probability comparing DA.MCMII (solid line) and DA.MCMII res (dashed line) for different projectile impact energies.

Figure 21 shows the difference between response and no-response models for $3s$ removal in the MCMII as a function of projectile impact energy. It is clear that as the impact energy increases towards 150 keV/amu, the probability differences between the models decreases. This is in line with the fact that at higher projectile energies dynamic response converges to the static potential.

To further check if the discrepancy between the response and no-response models is solely due to $3s$ electron removal, two-electron removal channels are investigated.

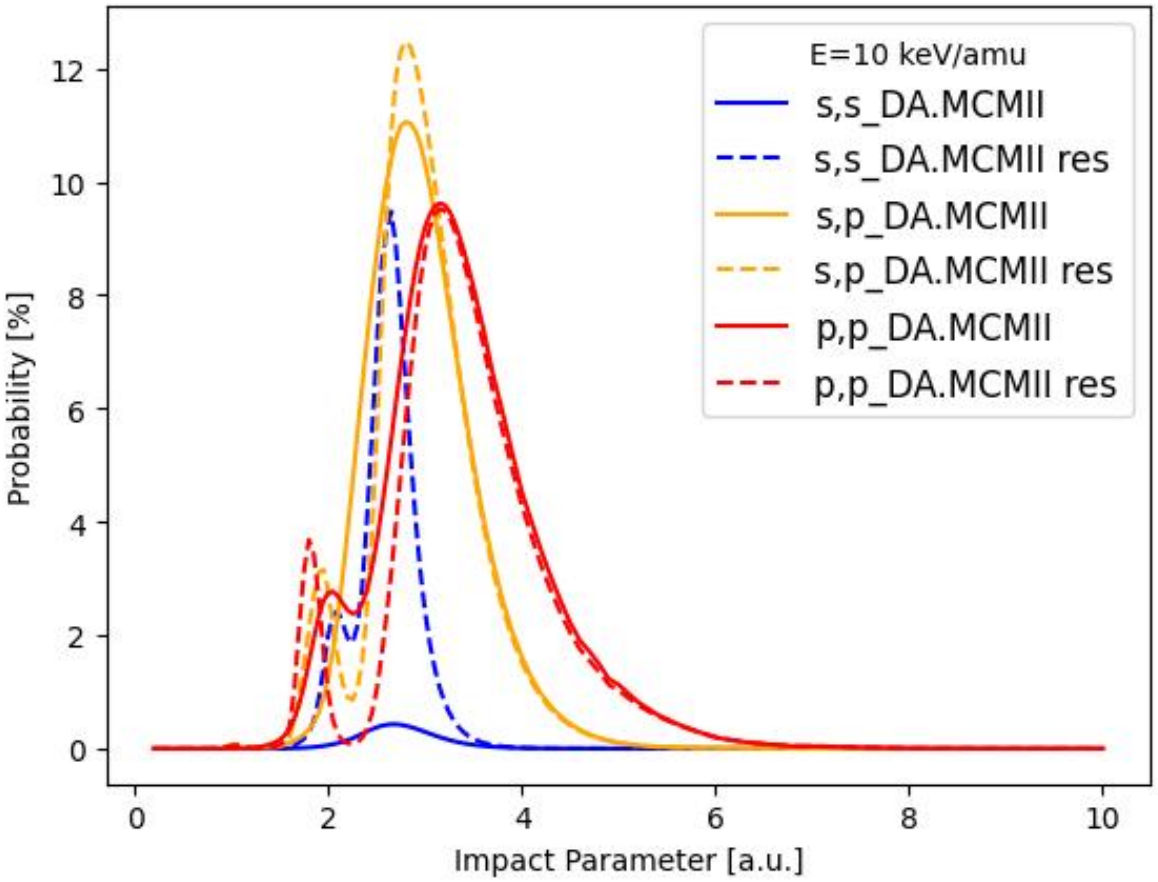


Figure 22: $He^{2+}$–$Ar_2$ ion–dimer collisions in parallel orientation at 10 keV/amu. Two-site two-electron removal probability comparing DA.MCMII (solid lines) and DA.MCMII res (dashed lines).

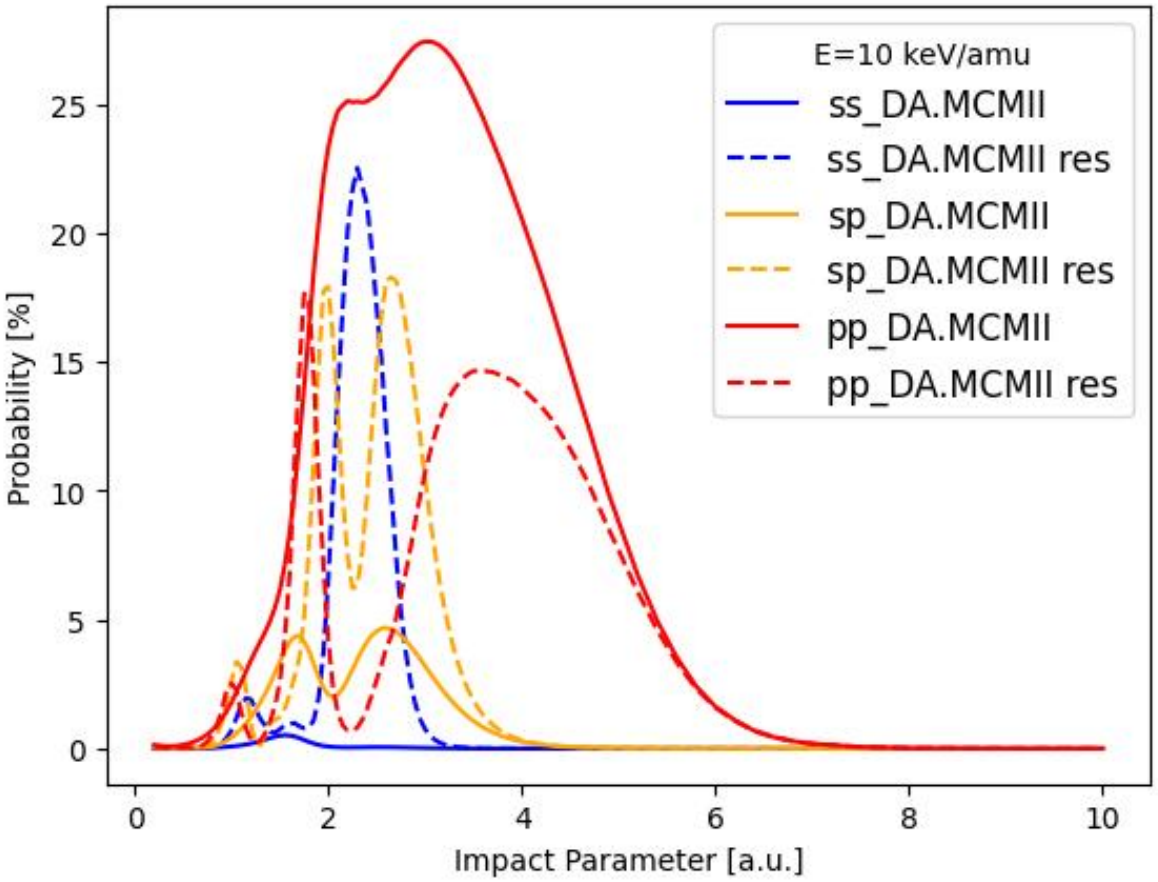


Figure 23: $He^{2+}$–$Ar_2$ ion–dimer collisions in parallel orientation at 10 keV/amu. One-site two-electron removal probability comparing DA.MCMII (solid lines) and DA.MCMII res (dashed lines).

It is evident in Figures 22 and 23 for two-site and one-site two-electron removal, respectively that as fewer $3s$ vacancies are produced per atom, the difference between the no-response and response models decreases.

Given the relevance of electron excitation channels for facilitating ICD in the argon dimer, it is important to understand how they are described by the models presented. The first excitation channel that is of interest is single $3p$ electron removal with simultaneous $3p$ excitation to the $3d$ state. For shorthand, this is labeled as $pp3d$, with other electron excitation channels similarly referred to as $ppnl$. A comparison between the FCM, MCMI and MCMII models is shown for the $pp3d$ channel at a projectile impact energy of 10 keV/amu in Figure 24.

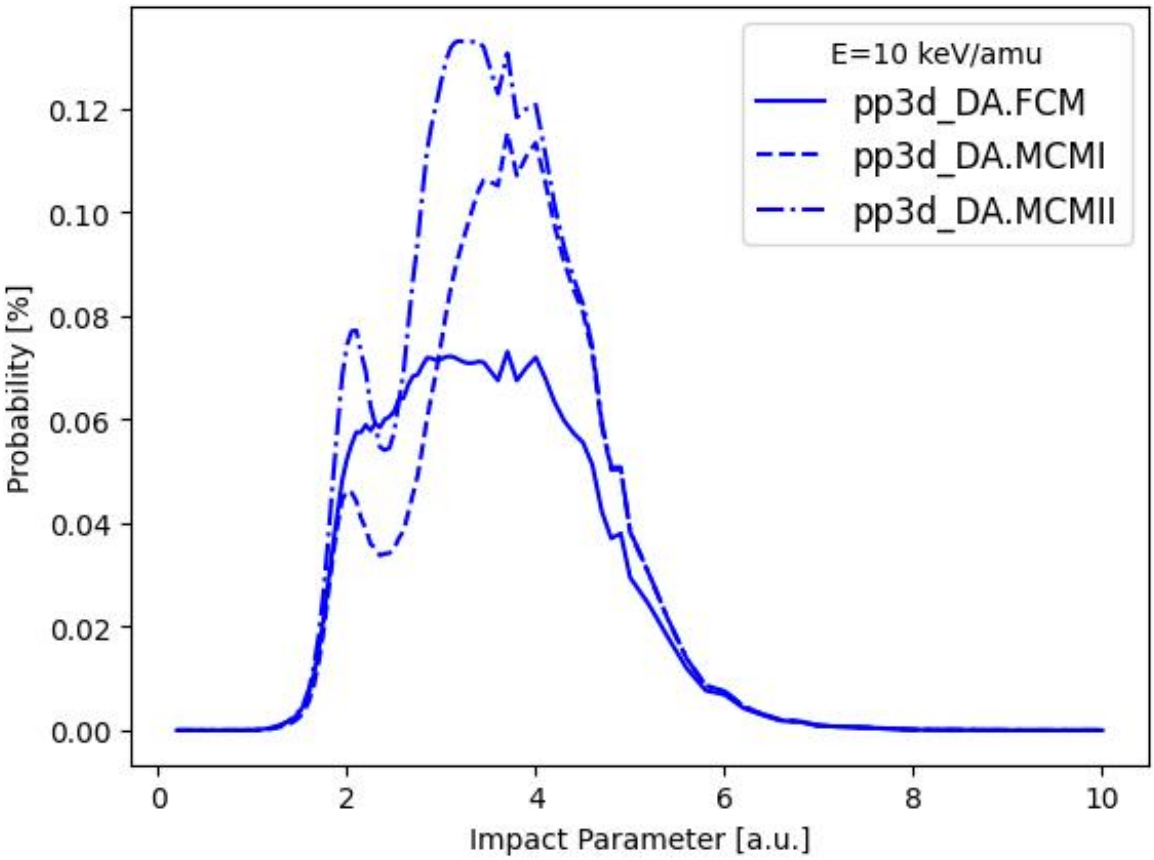


Figure 24: $He^{2+}$–$Ar_2$ ion–dimer collisions in parallel orientation at 10 keV/amu. Single $3p$ electron removal with simultaneous $3p$ excitation to the $3d$ state probability comparing DA.FCM (solid line) and DA.MCMI (dashed line) and DA.MCMII (dashed-dotted line).

It is evident that the models are overall similar, though the probabilities are small which results in a jagged probability structure.

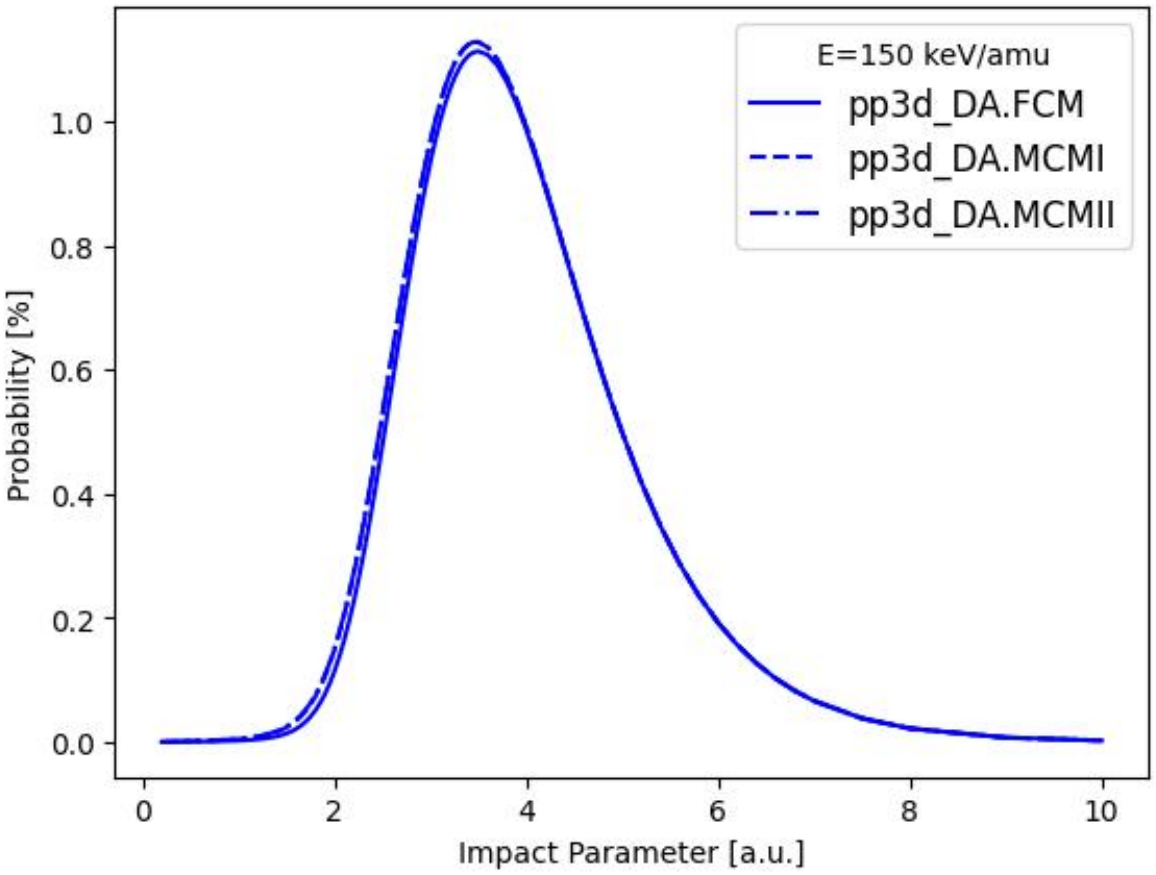


Figure 25: $He^{2+}$–$Ar_2$ ion–dimer collisions in parallel orientation at 150 keV/amu. Single $3p$ electron removal with simultaneous $3p$ excitation to the $3d$ state probability comparing DA.FCM (solid line) and DA.MCMI (dashed line) and DA.MCMII (dashed-dotted line).

The probability for the $pp3d$ channel increases with projectile impact energy, such that is over an order of magnitude larger at 150 keV/amu (Figure 25) than at 10 keV/amu. This indicates that the excitation channel is more relevant at higher impact energies.

Other excitation channels that are able to facilitate ICD are examined, from low to higher impact energies, such as $pp4s$, $pp4p$, $pp4d$ and $pp4f$ in Figure 26 and Figures B.67 to B.74. These channels require scaling to account for the states corresponding to each configuration whose excitation energies do not exceed the minimum threshold required for ICD, as described in section 3.2. Together, they correspond to all the channels that facilitate ICD resulting in $Ar^+$-$Ar^+$ dimer fragmentation.

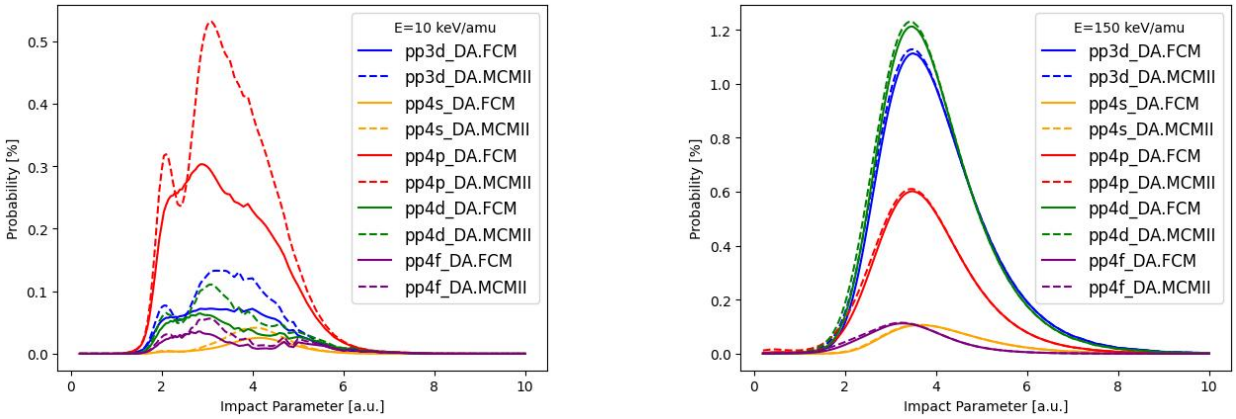


(a) 10 keV/amu

(b) 150 keV/amu

Figure 26: $He^{2+}$–$Ar_2$ ion–dimer collisions in parallel orientation impact energies a) 10 keV/amu and b) 150 keV/amu. Single $3p$ electron removal with simultaneous $3p$ excitation to the $3d$, $4s$, $4p$, $4d$, $4f$ state probabilities comparing DA.FCM (solid line) and DA.MCMII (dashed lines).

As seen in Figure 26, the overall probabilities at 10 keV/amu are small and with less smooth curves, while at 150 keV/amu the probabilities are smooth and larger. Another difference that is observed is that at 10 keV/amu the FCM and MCMII have different probabilities, but converge as expected at 150 keV/amu. The lack of smoothness at low impact energies is explained as a function of low probabilities values, where minor differences are exaggerated, while the model convergence at high impact energies ionization processes are dominant with MCMII becoming more similar to FCM.

The impact of dynamic response on excitation channels is also explored, first for the $pp3d$ channel at both 10 keV/amu to 150 keV/amu in Figure 27.

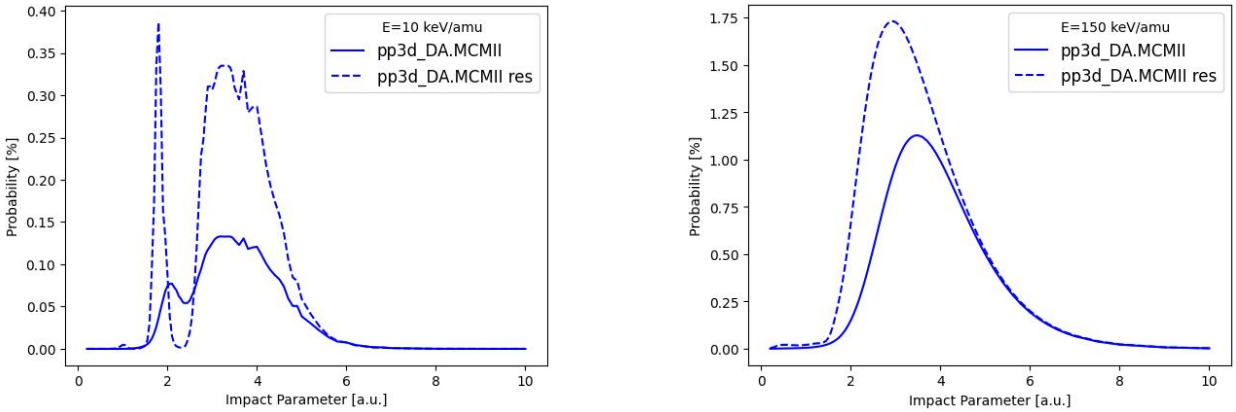


(a) 10 keV/amu

(b) 150 keV/amu

Figure 27: $He^{2+}$–$Ar_2$ ion–dimer collisions in parallel orientation. Single $3p$ electron removal with simultaneous $3p$ excitation to the $3d$ state probability comparing DA.MCMII (solid line) and DA.MCMII res (dashed line).

Differences between the no-response and response model for the $pp3d$ excitation channel are observed at both 10 and 150 keV/amu. Although there are differences between no-response and response models across the impact energy range, it is notable that the models are more similar at 150 keV/amu [67]. This is an expected behaviour as the dynamic potential evolves more when the target has a longer exposure to the projectile, and as impact energy increases the projectile passes by the target much quicker with greater impact to an increased probability but less time. If we were to explore this system at impact energies larger than 150 keV/amu, we would expect convergence between response and no-response.

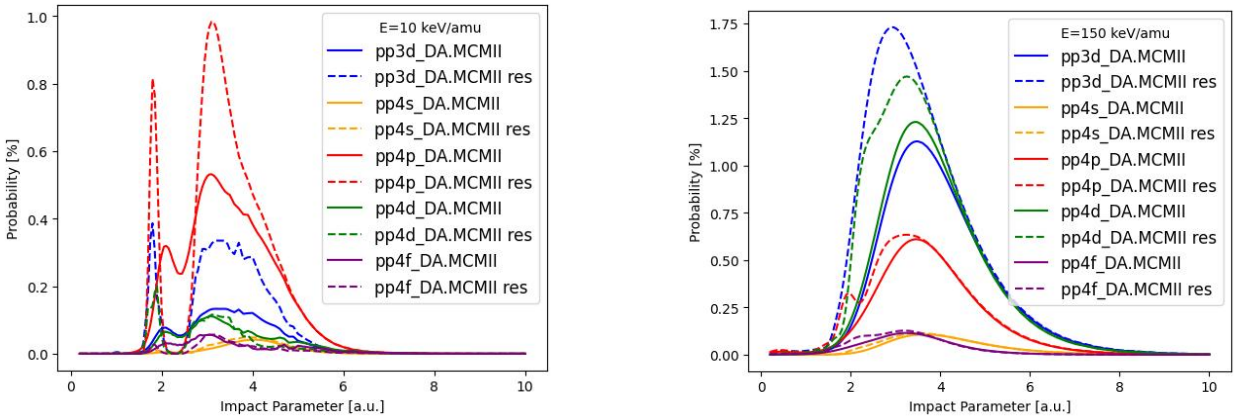


(a) 10 keV/amu

(b) 150 keV/amu

Figure 28: $He^{2+}$–$Ar_2$ ion–dimer collisions in parallel orientation. Single $3p$ electron removal and $3p$ electron excitation to $3d, 4s, 4p, 4d$, and $4f$ state probability comparisons of DA.MCMII between no-response (solid line) and response (res) (dashed line) models [67]. Reprinted from D. Starko and T. Kirchner, *Eur. Phys. J. Spec. Top.* (2026), pp. 1–11.© The Author(s) 2026, under exclusive licence to EDP Sciences, Springer-Verlag GmbH Germany, part of Springer Nature. Reproduced with permission.

Figure 28 shows that the response and no-response models start converging at higher impact energies (though not fully as for non-excitation channels) for the other channels [67]. It can be seen that various channels dominate at different energies. At 10 keV/amu impact energy, the $4p$ excitation channel is dominant in both no-response and response models while $3d$ is the second largest. However, at 150 keV/amu impact energy the $3d$ and $4d$ excitation channels dominate, with $3d$ being the most dominant in the response model. It is noted that there is a clear difference in structure between both sets of plots 28a and 28b in Figure 28, where the excitation channels all exhibit similar structures and main peaks near the same impact parameter $b$ in the range of $3 - 3.5$ a.u. for both response and no-response models. There are also more fractured probability curves at 10 keV/amu where each channel differentiates itself from the others.

Comparisons between response models across impact energy for the rest of the excitation channels for DA.MCMII can be found in the Appendix from Figures B.75 to B.85.

With all these calculated probabilities for the various channels and energy regimes, it is useful to take a look at the cross-sections for the electron excitation channels as a function

of $He^{2+}$ impact energy.

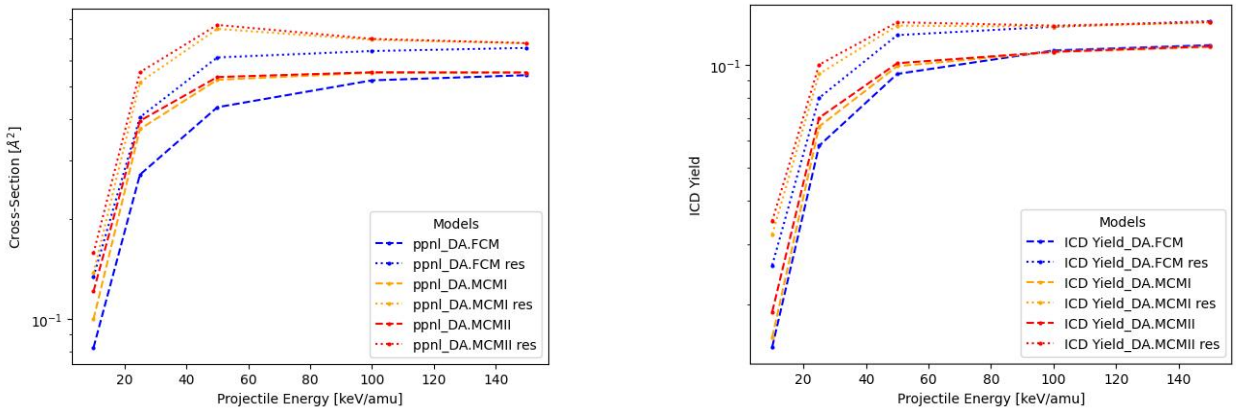


(a) Sum of $3d$ to $4f$ $3p^{-2}nl$ cross-sections

(b) ICD Yield

Figure 29: $He^{2+}$-$Ar_2$ ion-dimer collisions in parallel orientation from 10 keV/amu to 150 keV/amu; a) $3p$ electron removal and $3p$ electron excitation to $nl$ state cross-sections comparison of DA.FCM, DA.MCMI and DA.MCMII between no-response (dashed lines) and response (res) (dotted lines) models b) ICD yield in $Ar^+$-$Ar^+$ dimer fragmentation comparison of DA.FCM, DA.MCMI and DA.MCMII models between no-response (dashed lines) and response (res) (dotted lines) models [67]. Reprinted from D. Starko and T. Kirchner, *Eur. Phys. J. Spec. Top.* (2026), pp. 1–11.© The Author(s) 2026, under exclusive licence to EDP Sciences, Springer-Verlag GmbH Germany, part of Springer Nature. Reproduced with permission.

Plots 29a and 29b from Figure 29 show the sum electron excitation cross-sections and ICD yield respectively over the range from 10 keV/amu to 150 keV/amu. The ICD yield is defined as the fraction of resulting $Ar^+$-$Ar^+$ fragmentation processes that originate from ICD facilitating channels, compared to all channel cross-sections that result in this fragmentation, including all two-site two-electron removals that result in CE and RCT from $3p^{-2}$ removal. As can be seen, the ICD yield shows a similar pattern as the total cross-section across the projectile impact energy range, plateauing towards 150 keV/amu with capture and fixed-charge models converging as expected. There is also a noticeable gap in cross-sections and ICD yield between the response and no-response models, from low to high impact energies. This gap appears to slowly narrow as impact energy increases, and is expected to eventually vanish, as faster projectile speeds reduce the impact of dynamical response.

Experimental results from [11] at 150 keV/amu for $He^{2+}$ projectiles indirectly indicate a high ICD yield due to a large ICD to continuum electron ratio. It does appear that the present results are lower than theirs, though this may be due to these results being inclusive in the final projectile charge state, while the data of [11] were recorded in coincidence with $He^{+}$ production. In addition, the focus of the present study on parallel ion-dimer collisions inhibits a quantitative comparison.

### 5.2. $He^{+}$ Projectiles

The same electron dynamics are examined with a $He^{+}$ projectile, with the limitation of the capture model applied to single-electron removal channels, including the electron excitation channels, only.

The single-electron removal channel probabilities are investigated for FCM, MCMI and MCII for impact energies ranging from 10 keV/amu to 150 keV/amu in Figure 30.

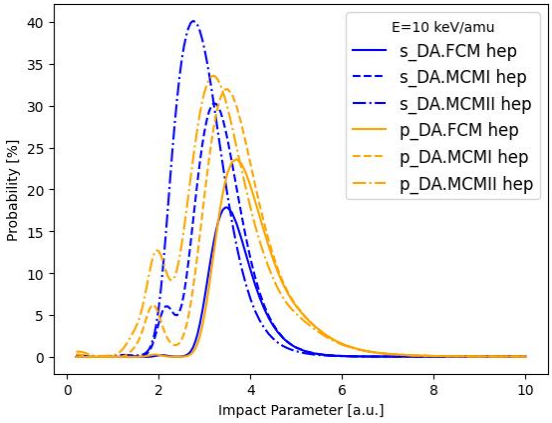


(a) 10 keV/amu

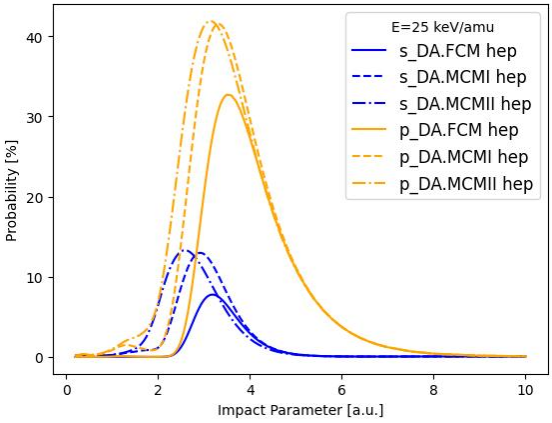


(b) 25 keV/amu

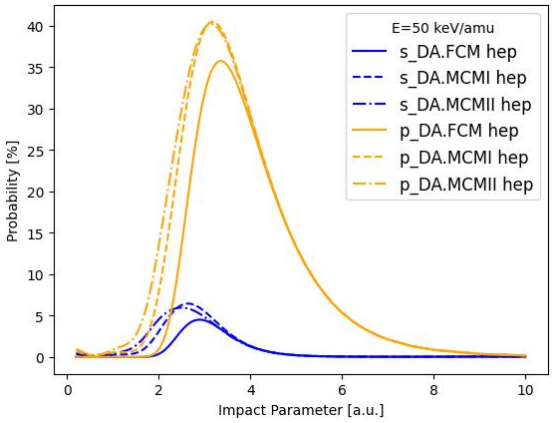


(c) 50 keV/amu

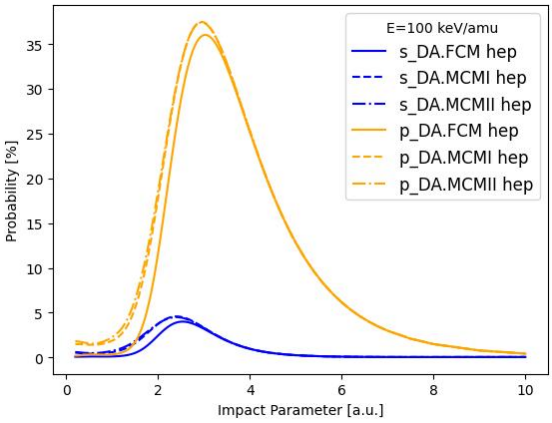


(d) 100 keV/amu

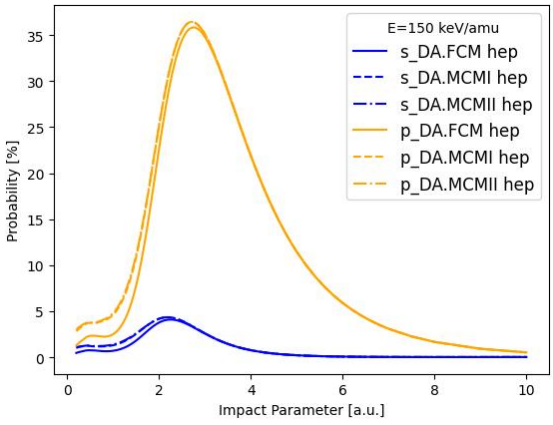


(e) 150 keV/amu

Figure 30: $He^+$–$Ar_2$ ion–dimer collisions in parallel orientation. Single-electron removal probabilities comparing DA.FCM (solid line), DA.MCMI (dashed line), and DA.MCMII (dashed-dotted line) across different projectile impact energies.

For the impact energy of 10 keV/amu in Figure 30a, the $3s$ removal probabilities are of comparable height with the $3p$ removal channel. This is a consequence of the $3s$ removal channel having a larger cross-section at lower impact energies due to the dominance of the capture process. However, as impact energy increases to 150 keV/amu in Figure 30e, the $3s$ removal probabilities shrink by an order of magnitude, while $3p$ removal has not greatly changed, except fort the modified capture model probabilities converging with those of the FCM. It is noteworthy in Figure 30a that all the models have different probabilities for single-electron removal at 10 keV/amu, even amongst the modified capture models. As impact energy increases, at 50 keV/amu in Figure 30c MCMI and MCMII probabilities converge, and at around 150 keV/amu the modified capture models and FCM converge, as is expected with ionization dominance.

Since two-electron removal channels are forbidden in the capture model for a $He^+$ projectile, these channels are not discussed.

Instead, as the electron excitation channels are the ones that are able to facilitate ICD and are allowed in the capture model for a $He^+$ projectile, their probabilities are examined in Figures 31a and 31b at 10 and 150 keV/amu.

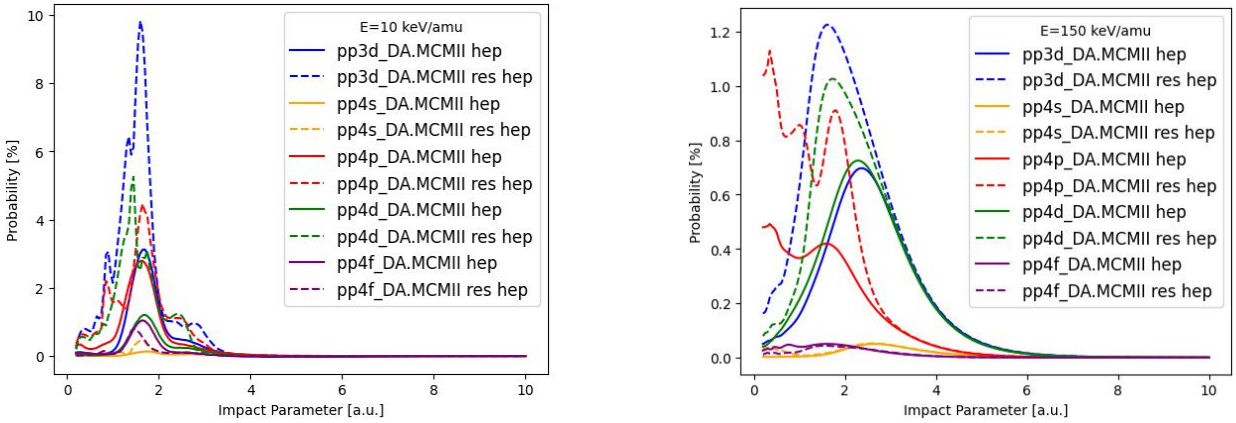


(a) 10 keV/amu

(b) 150 keV/amu

Figure 31: $He^{2+}$–$Ar_2$ ion–dimer collisions in parallel orientation. Single $3p$ electron removal and $3p$ electron excitation to $3d, 4s, 4p, 4d$, and $4f$ state probability comparisons of DA.MCMII between no-response (solid lines) and response (res) (dashed lines) models [67]. Reprinted from D. Starko and T. Kirchner, *Eur. Phys. J. Spec. Top.* (2026), pp. 1–11.© The Author(s) 2026, under exclusive licence to EDP Sciences, Springer-Verlag GmbH Germany, part of Springer Nature. Reproduced with permission.

It is noteworthy that the $3p^{-2}3d$ channel is the most dominant channel in comparison to the rest of the excitation pathways in each category of no-response or response models. The dominance of $3p^{-2}3d$ is also consistent at higher projectile impact energies. This is in line with the results observed for these excitation channels with a $He^{2+}$ projectile.

The cross-sections and ICD yield for electron excitation ranging from 10 keV/amu to 150 keV/amu are displayed in Figures 32a and 32b.

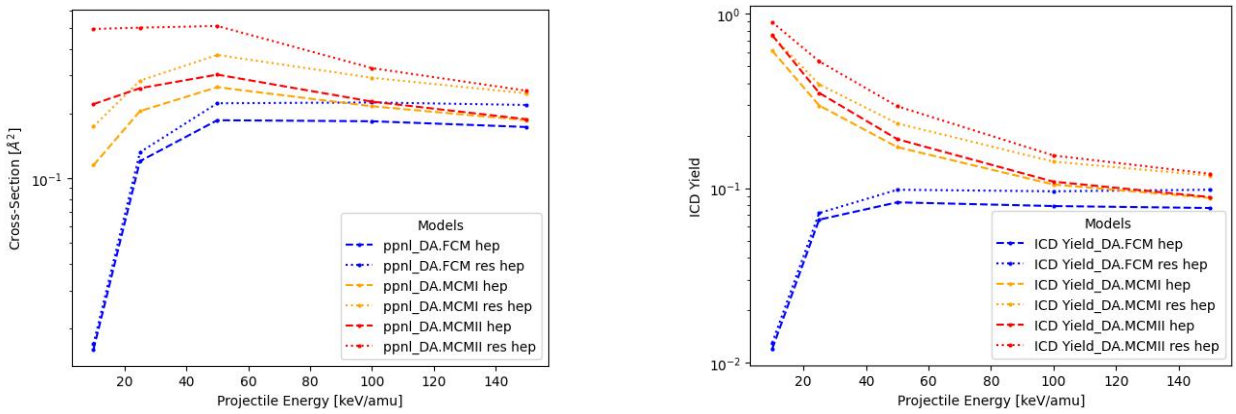


(a) Sum of $3d$ to $4f$ $3p^{-2}nl$ cross-sections

(b) ICD Yield

Figure 32: $He^+$-$Ar_2$ ion-dimer collisions in parallel orientation from 10 keV/amu to 150 keV/amu; a) $3p$ electron removal and $3p$ electron excitation to $nl$ state cross-sections comparison of DA.FCM, DA.MCMI and DA.MCMII between no-response (dashed lines) and response (res) (dotted lines) models b) ICD yield in $Ar^+$-$Ar^+$ dimer fragmentation comparison of DA.FCM, DA.MCMI and DA.MCMII models between no-response (dashed lines) and response (res) (dotted lines) models [67]. Reprinted from D. Starko and T. Kirchner, *Eur. Phys. J. Spec. Top.* (2026), pp. 1–11.© The Author(s) 2026, under exclusive licence to EDP Sciences, Springer-Verlag GmbH Germany, part of Springer Nature. Reproduced with permission.

There is substantially different behaviour of cross-sections vs yield as seen in Figure 32. The cross-sections for the capture models exhibit similar structures across models with response results being larger than their no-response counterparts across the entire projectile impact energy range [67]. More notably, the ICD yield for the capture models approaches unity at 10 keV/amu projectile energy, and decays toward high energy. This is very different from the results shown in Figure 32b for $He^{2+}$ projectiles. The reason is that $He^+$ is limited to single electron capture in CMI and CMII (i.e.,$Ar^+$-$Ar^+$ fragmentation via CE or RCT is impossible).

The prediction of a pure ICD yield for a $He^+$ projectile at low impact energy within the capture model of the determinantal analysis warrants experimental investigations.

# 6. CONCLUSIONS

In this dissertation, the results of theoretical calculations for $He^{2+}$ and $He^{+}$ ion impact on neon and argon dimers are presented. The collision systems are arranged such that the projectile travels in a straight line trajectory parallel to the dimer axis, where the projectile speed exceeds the characteristic vibrational motion of the target. This allows for the assumption that the dimer is fixed throughout the course of the collision. The electron dynamics that precede dimer fragmentation are investigated, particularly processes that facilitate ICD. Independent atom and electron models are employed as overarching frameworks for the structure of the collision systems under investigation. A TDHF ansatz is used to express the many-electron system as a single Slater determinant comprised of single-electron wavefunctions. The non-perturbative TC-BGM is used to construct basis states for the calculation of single-electron transition amplitudes from the solution of single-electron TDSEs. Time dependence of the electron screening of the target nucleus in a global response model is tested in combination with the various approaches presented.

Two statistical methodologies are employed to calculate multi-electron probabilities and cross sections: the multinomial and determinantal analyses. The former is a combinatoric approach of single-electron probabilities that are used to calculate electron removal processes of the ion-dimer collision system. This approach does not consider the antisymmetry of the many-electron state and does not respect Pauli blocking. The latter method involves calculating many-electron processes from inner products of Slater determinants that represent propagated states at final time and the configurations of interest, while adhering to the Pauli exclusion principle. A central contribution of this work has been the development and systematic comparison of two broad classes of models: the fixed-charge model, which neglects changes in projectile charge state during the collision, and the capture models, which explicitly account for electron capture by the projectile and its influence on subsequent target interactions. Within the determinantal framework, capture models are subdivided into Models I and II, depending on whether the projectile $1s$ orbital is occupied. The determinantal analysis for the argon dimer collision system includes balancing capture and ionization removal as a function of projectile impact energy. Electron excitation channels are also specifically calculated and scaled based on spin-multiplicity for the determinantal analysis

in the argon dimer target.

*Helium Ions and Neon Dimer Target*

Statistical analyses are used to calculate electron removal channels for $He^{2+}$ and $He^{+}$ projectiles and the neon dimer target at an impact energy of 10 keV/amu. Single $2s$ electron removal probabilities obtained in the multinomial analysis fixed-charge model are consistent with the corresponding determinantal analysis, confirming that exchange effects are minimal for single-electron channels. Multi-electron removal channels show greater sensitivity across modeling approaches, while the fixed-charge model produces consistent results across both statistical analyses.

The analysis is further expanded to incorporate comparisons between the fixed-charge and capture models of each analysis, where the differences are minor for single-electron removal channels and larger for double-electron channels. The MA.CM and DA.CMI show closer agreement in comparison to DA.CMII, where the differences are slightly larger. DA.CMII represents the most fundamental approach, as it incorporates the projectile $1s$ occupancy and provides the most comprehensive representation of the projectile's evolving charge state during collisions.

Inclusion of dynamic response — wherein the target potential adjusts to fractional ionization during the collision — was found to have a modest effect on single-electron channels but more substantial influence on multi–electron removal channels, consistent with the time-dependent mean-field character of the response model. The dynamical response tends to enhance cross sections for higher multiplicity channels, indicating that relaxation effects in the residual target can play a significant role once multiple electrons are removed. These results are consistent across analyses and models.

Using the $He^{+}$ projectile restricts the capture model to single-electron capture, as the probability for further capture of electrons by neutral helium is negligible. Minor differences in electron removal probabilities across analyses and target response models are found.

For $He^{2+}$ impact, the predicted ICD yield, defined as the ratio of the $2s^{-1}$ cross section to all channels leading to $Ne^{+}$+$Ne^{+}$ fragmentation, remains substantial in all models but is systematically lower in capture models than in fixed-charge models. This reduction arises from the capture of electrons by the projectile, which effectively removes pathways that

would otherwise lead to ICD in the fixed-charge description. For $He^+$ impact, the capture model inherently restricts electron removal to single–electron processes due to projectile neutralization after capture, resulting in a lower absolute cross-section but a near-perfect ICD yield: once $Ne^+$+$Ne^+$ fragmentation occurs, it is exclusively associated with ICD channels. This highlights the unique suitability of $He^+$ as a probe of pure ICD mechanisms at low collision energies where direct ionization is suppressed.

*Helium Ions and Argon Dimer Target*

The determinantal analysis is exclusively used with the argon dimer target system for calculating electron removal probabilities in the fixed-charge and capture models, as well as with and without dynamic response. The collision studies include $He^{2+}$ and $He^+$ projectile impact energies ranging from 10 keV/amu - 150 keV/amu, and incorporating capture model readjustment to balance capture and ionization dominance as a function of energy. It is found that as the projectile impact energy increases, ionization processes dominate, while electron capture dominates at lower impact energies.

Unlike the neon dimer, single $3s$ electron removal is not energetically sufficient to facilitate ICD in argon dimers. However, relaxation from a channel with $3p$ electron removal occuring simultaneously with electron excitation provides sufficient energy to ionize a neighbouring atom's valence electron, resulting in CE.

Investigations of single-electron removal channels across models indicate similar results, while for two-electron removal channels the differences grow between fixed-charge and modified capture models, especially for one-site processes. It is found that the fixed-charge and modified capture models converge at projectile impact energies of 150 keV/amu. This is expected given that the fixed-charge model is a simplified ionization model, while the modified capture model is dominated by ionization processes at higher impact energies.

The dynamic response model probabilities are found to strongly deviate from the no-response model at impact energies less than 50 keV/amu for $3s$ electron removal. However, for $3p$ electron removal there is little difference between response and no-response model results. This may be explained by Ar($3s$) and He($1s$) having close but not resonant orbital energy levels. As the projectile collides with the target, the dynamic response of the potential may bend the energy curves and enhance the radial coupling. As the projectile impact energy

increases, the differences in the no-response and response models decrease and are minor at 150 keV/amu, as expected of dynamic response.

The $3p^{-2}3d$ channel is found to be the most dominant channel with the largest cross-section of all the considered excitation channels i.e. $3p^{-2}3d$, $3p^{-2}4s$, $3p^{-2}4p$, $3p^{-2}4d$, $3p^{-2}4f$. Experimental results reported in [11] hint at the $3p^{-2}3d$ channel having a stronger yield for generating ICD electrons.

For $He^{2+}$ impact, the predicted ICD yield, defined as the ratio of a $3p^{-2}nl$ cross section to all channels leading to $Ar^{+}$+$Ar^{+}$ fragmentation, is small at low impact energies, while gradually rising and plateauing at 150 keV/amu. The capture models exploit $He^{+}$ impact due to its restriction to single-electron capture, resulting in a near-perfect ICD yield at low impact energy. An interesting aspect of this system is that for the capture models, the cross-sections are relatively unchanged over the range of impact energies, with only a slight decrease. This is a function of the MCMI/MCMII models where excitation cross-sections are larger at higher projectile energy. This highlights the unique suitability of $He^{+}$ as a probe of pure ICD mechanisms at low collision energies for the argon dimer target system.

*Discussion and Outlook*

In their current state, the multinomial and determinantal analyses are excellent statistical techniques to explore the electron dynamics of ion-dimer systems. Overall, this work illustrates that the interplay between projectile charge evolution, many-electron effects, and dynamical potential response critically shapes electron removal probabilities and ICD yields in ion–dimer collisions. The comparative analysis between multinomial and determinantal frameworks underscores the importance of including antisymmetry and channel coupling in modeling, particularly for channels involving multiple electrons. The capture models developed here provide a physically motivated extension of the fixed-charge picture by accommodating the sequential capture of electrons and its consequences for ICD fragmentation. The response model offers an expanded perspective on the underlying assumptions of the local potentials used, highlighting the dynamic nature of the collisions.

Ultimately, the most fundamental, comprehensive and physically consistent approach out of all those presented in this work is the determinantal analysis capture model II response model. This approach respects the Pauli exclusion principle, factors in electron capture

changing the projectile charge with its inclusion of the $1s$ orbital of the helium ion, and accounts for time evolution of the target potential.

Future research should aim to extend these models to a broader range of rare-gas systems and collision geometries, and to benchmark predictions against experimental measurements. One way this work can be expanded is to investigate projectile trajectories that are not parallel to the target dimers, and understand angular dependence of the models. Given the scope of this work was limited to a parallel projectile trajectory with the dimer axis, orientation averaged cross-sections can be calculated in such an expanded approach. Some of these orientations can include those trajectories that are at various angles to the dimer axis in the xz- and yz-planes. This would incorporate into the cross-section and ICD yield calculations given that in an experiment the gas dimers will not be all in the same parallel orientation with the projectile trajectories, but will be randomly oriented.

Studying a water dimer target would also be an interesting next step in the development of the analyses and models introduced in this work. The water dimer would be a more complex target given that each water molecule has more internal structure, with a lack of spherical symmetry. A simple IAM would be insufficient, where either the molecule needs to be approximated as a single atomic structure to then apply the IEM and TC-BGM. Another approach is to treat the water molecule as it is and update the approximations employed in the IEM, including the collision geometry with a non-spherically symmetric effective mean-field potential.

Such advances will enhance the predictive power of theoretical models for ICD and related interatomic decay phenomena in weakly bound systems.

## Appendix A: Helium Ion - Neon Dimer Target

### 1. $He^{2+}$ Projectile

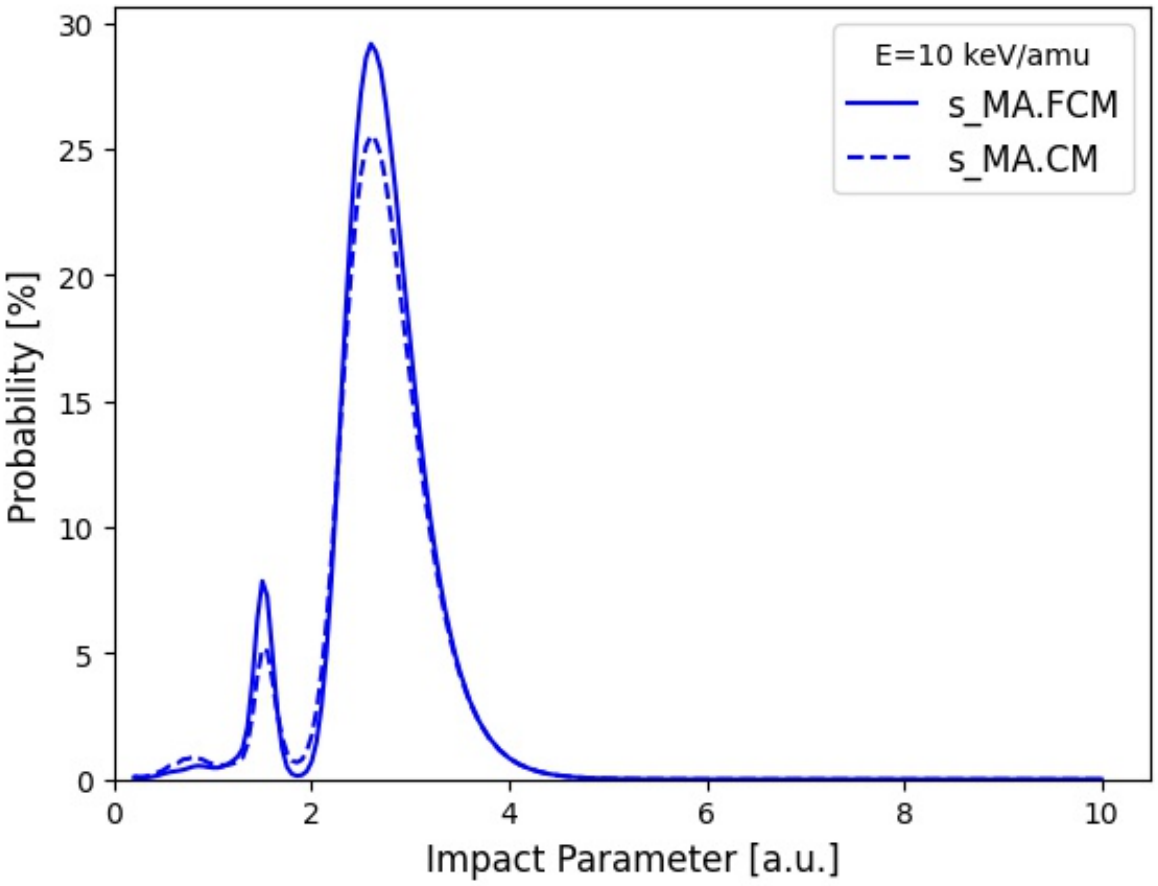


Figure A.33: $He^{2+}$-$Ne_2$ ion-dimer collisions in parallel orientation at 10 keV/amu. Single $2s$ electron removal probability comparing MA.FCM (solid line) and MA.CM (dashed line) [65].

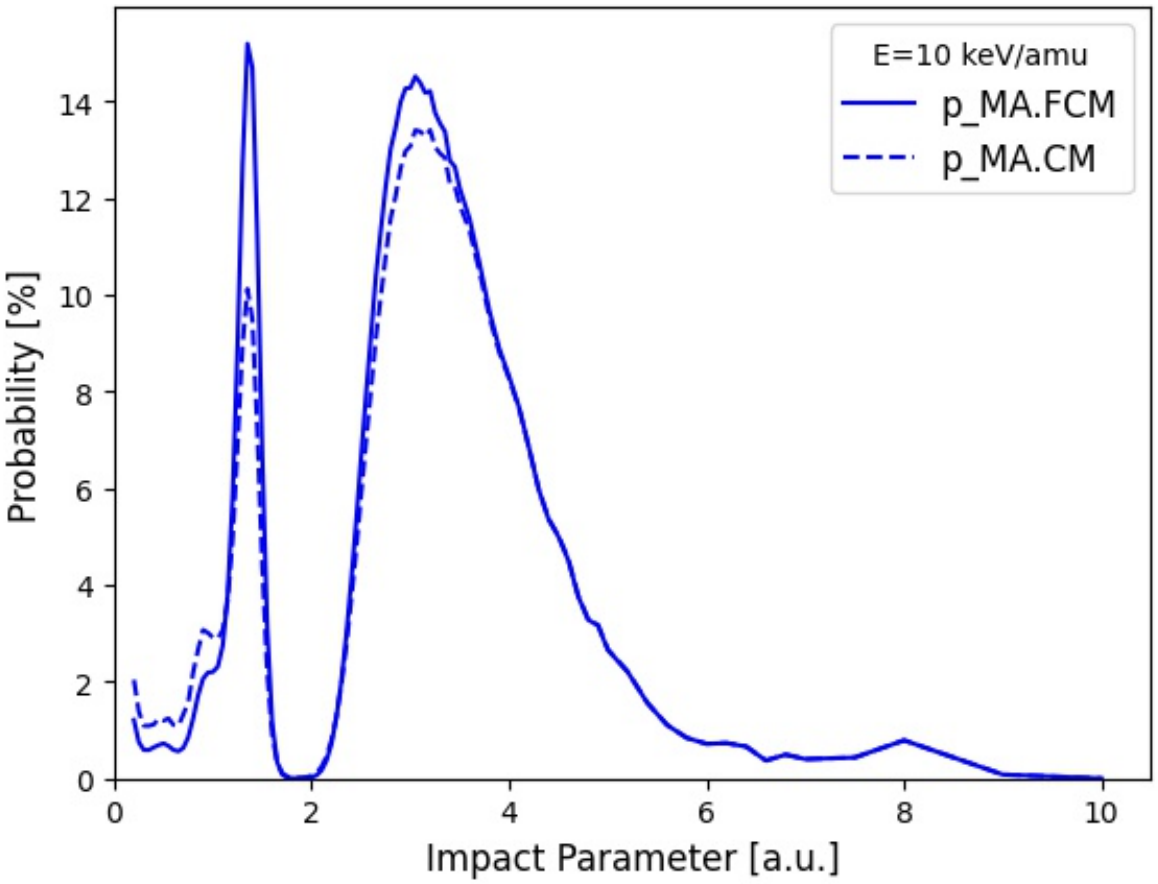


Figure A.34: $He^{2+}$–$Ne_2$ ion–dimer collisions in parallel orientation at 10 keV/amu. Single $2p$ electron removal probability comparing MA.FCM (solid line) and MA.CM (dashed line).

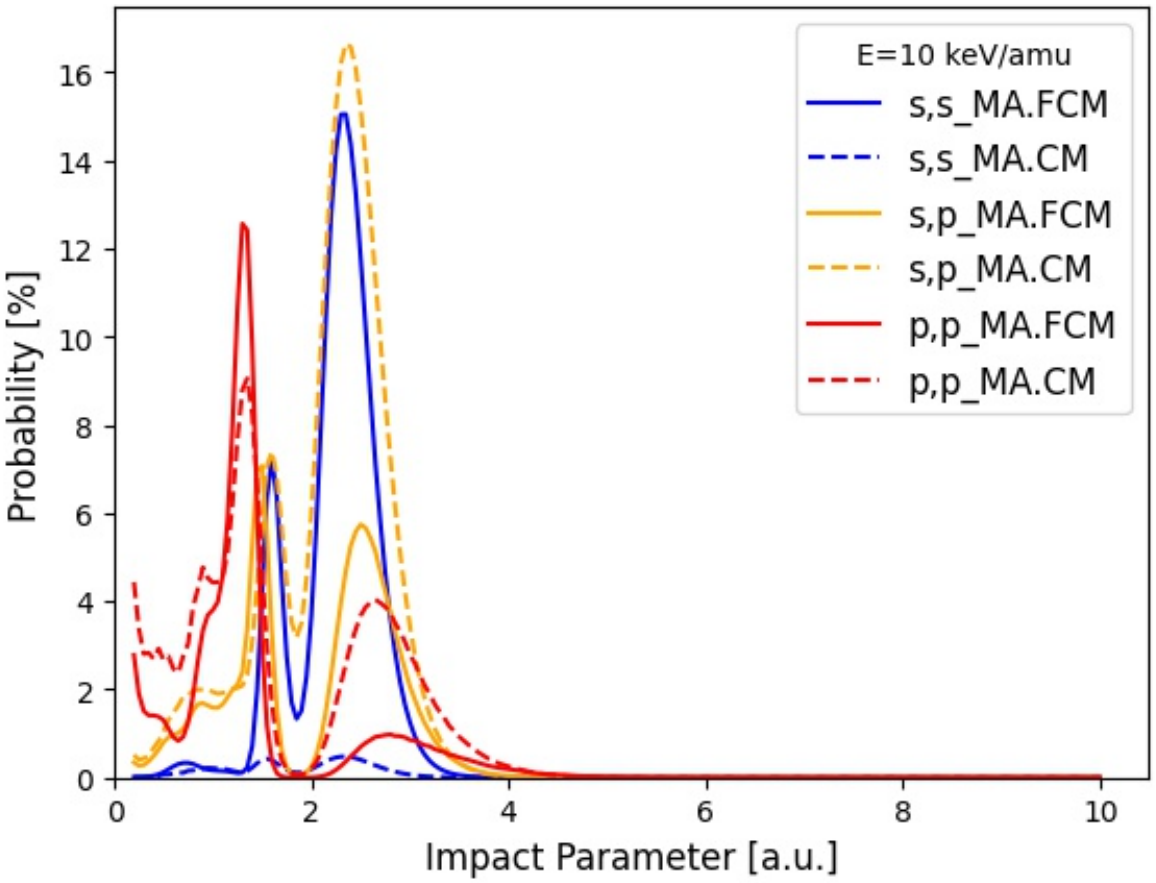


Figure A.35: $He^{2+}$–$Ne_2$ ion–dimer collisions in parallel orientation at 10 keV/amu. Two-site two-electron removal probability comparing MA.FCM (solid line) and MA.CM (dashed line).

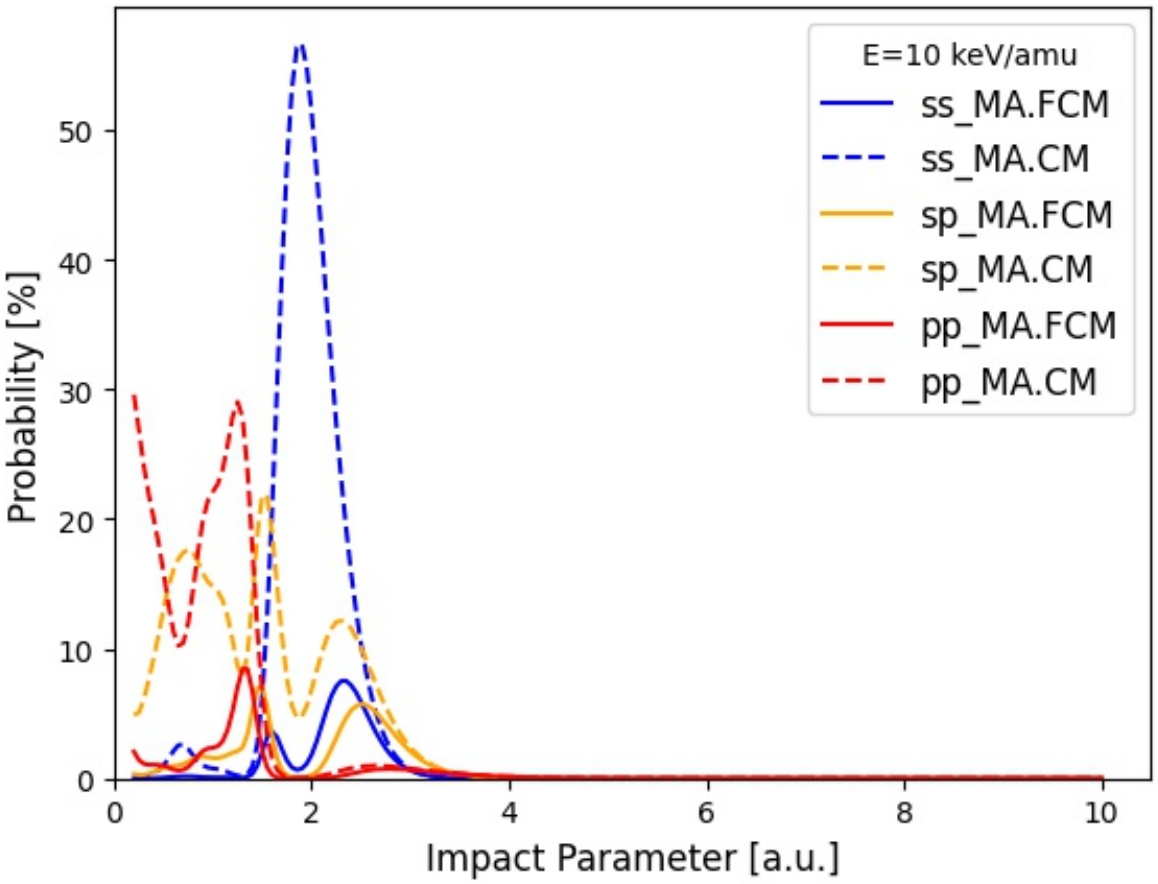


Figure A.36: $He^{2+}$–$Ne_2$ ion–dimer collisions in parallel orientation at 10 keV/amu. Two-site two-electron removal probability comparing MA.FCM (solid line) and MA.CM (dashed line).

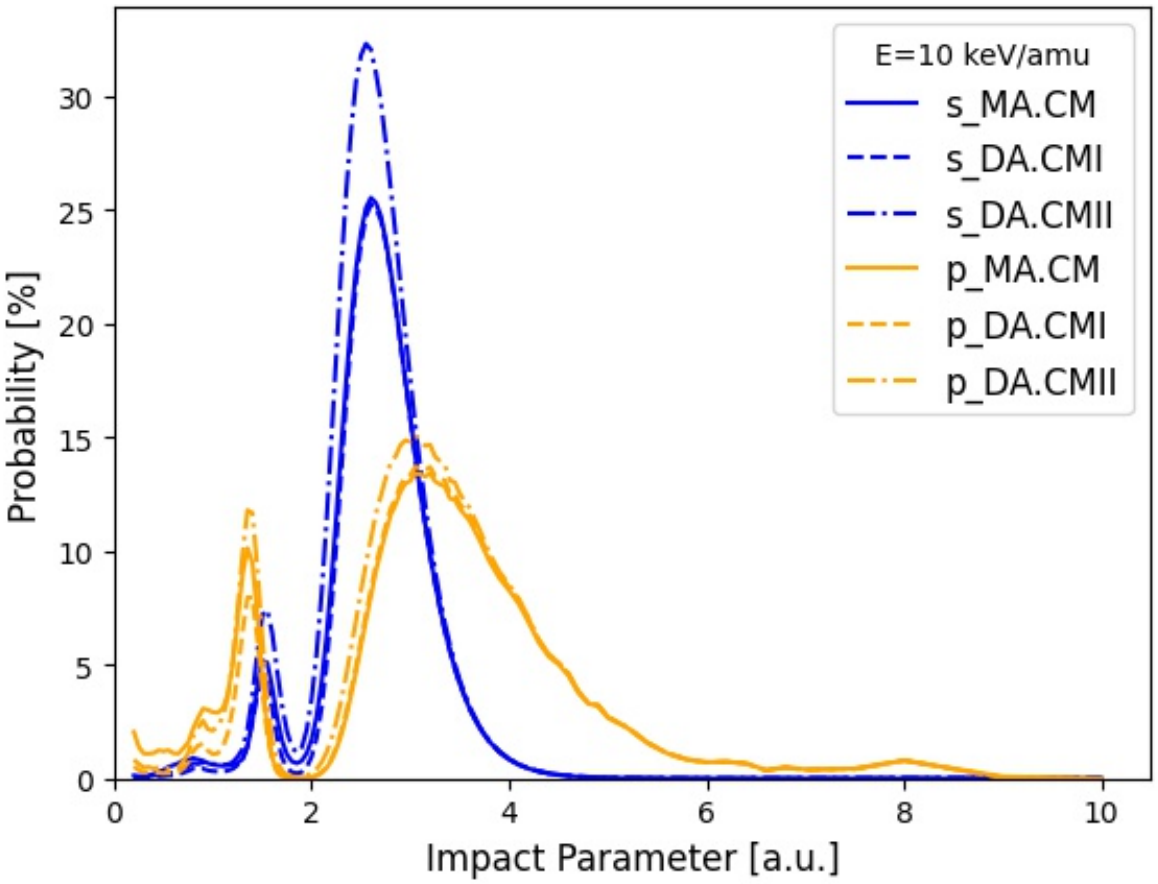


Figure A.37: $He^{2+}$–$Ne_2$ ion–dimer collisions in parallel orientation at 10 keV/amu. Single-electron removal probability comparing MA.CM (solid lines), DA.CMI (dashed lines) and DA.CMII (dashed-dotted lines).

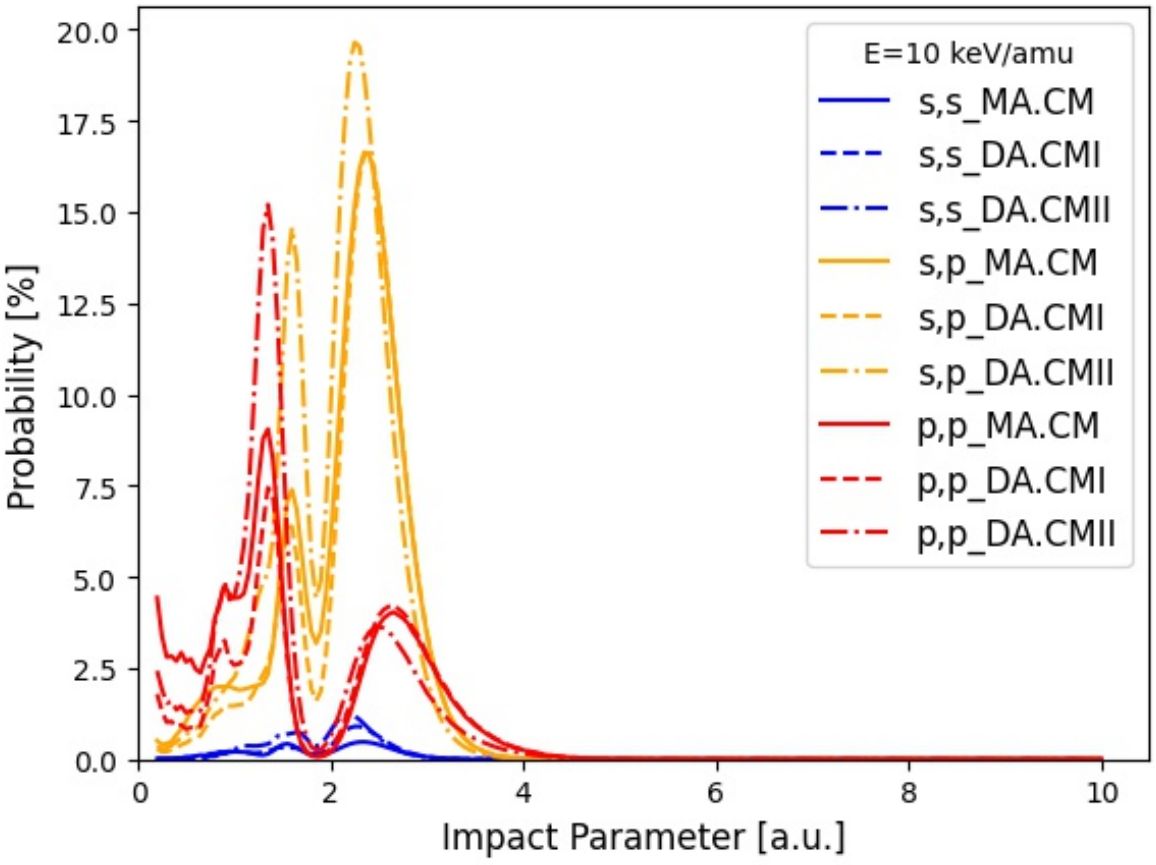


Figure A.38: $He^{2+}$–$Ne_2$ ion–dimer collisions in parallel orientation at 10 keV/amu. Two-site two-electron removal probability comparing MA.CM (solid lines), DA.CMI (dashed lines) and DA.CMII (dashed-dotted lines).

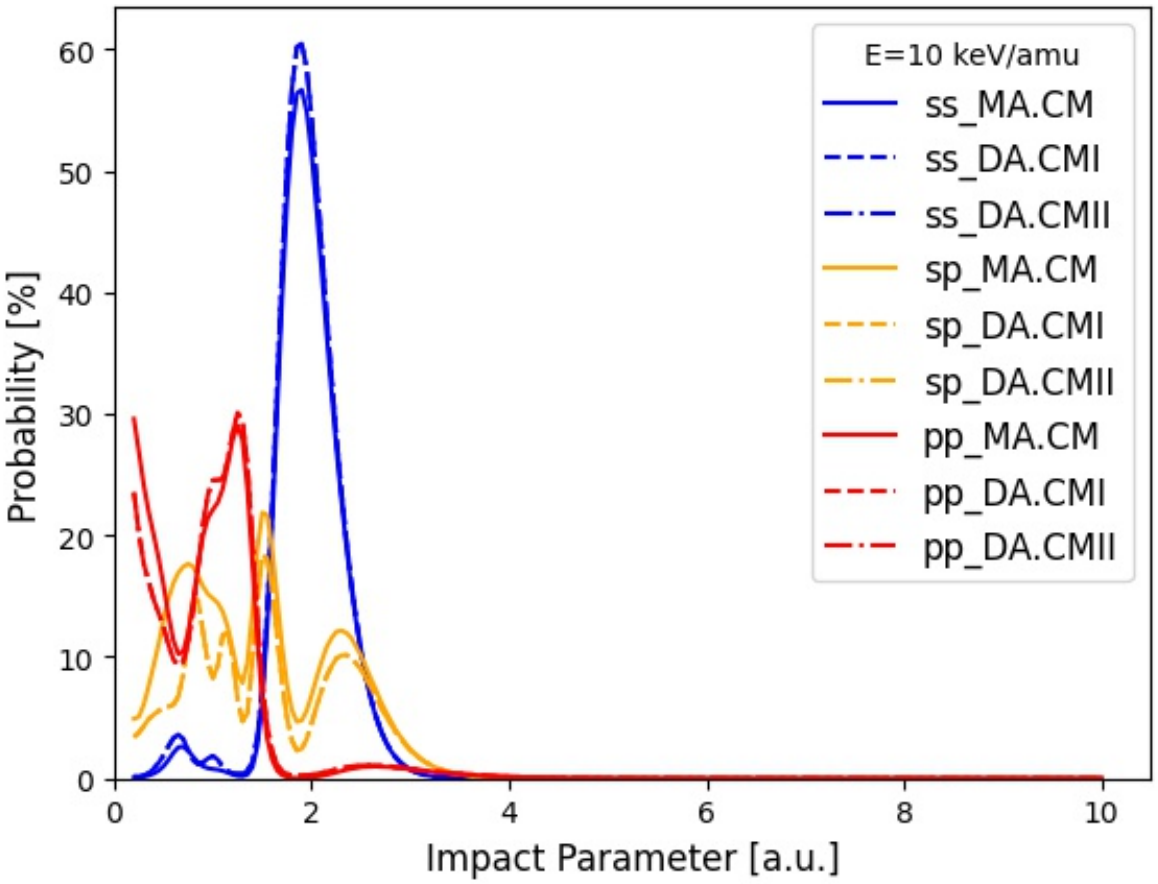


Figure A.39: $He^{2+}$–$Ne_2$ ion–dimer collisions in parallel orientation at 10 keV/amu. One-site two-electron removal probability comparing MA.CM (solid lines), DA.CMI (dashed lines) and DA.CMII (dashed-dotted lines).

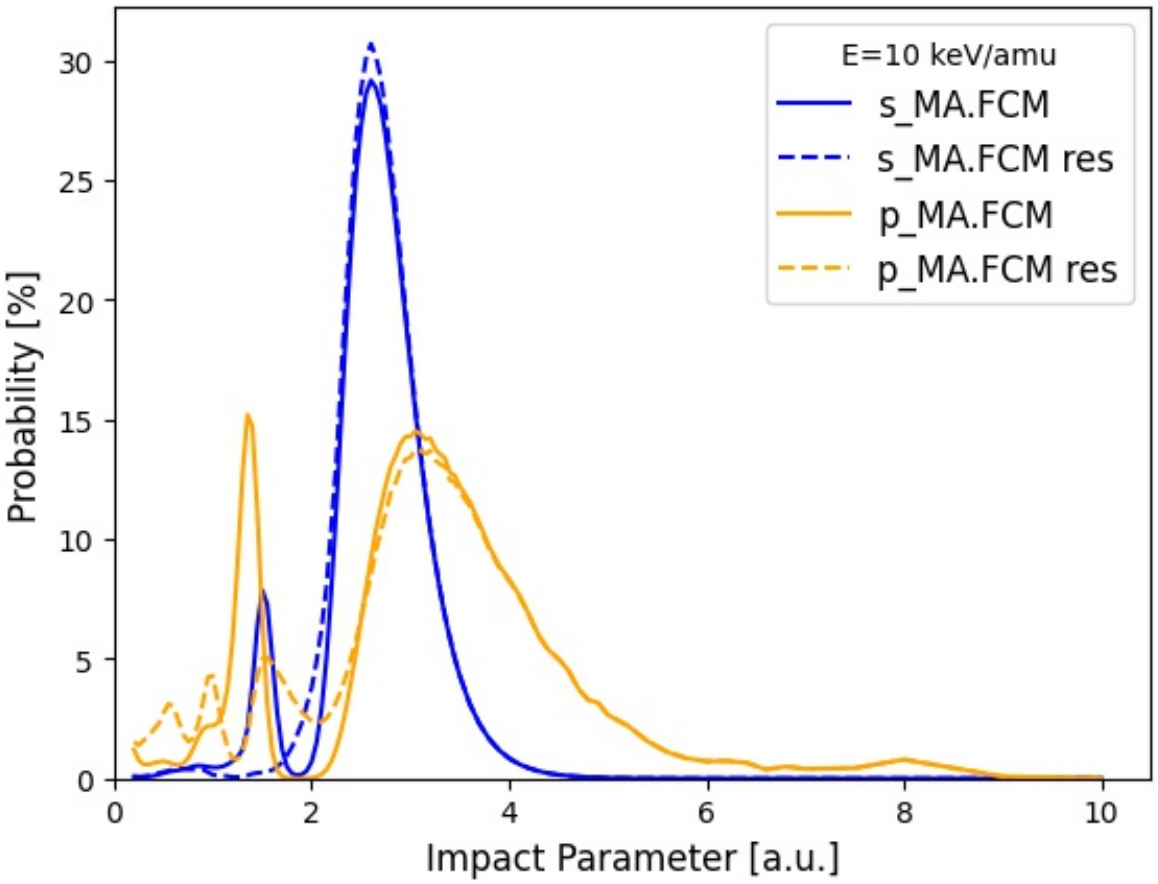


Figure A.40: $He^{2+}$–$Ne_2$ ion–dimer collisions in parallel orientation at 10 keV/amu. Single-electron removal probability comparing MA.FCM without response (solid line) and with response (dashed line).

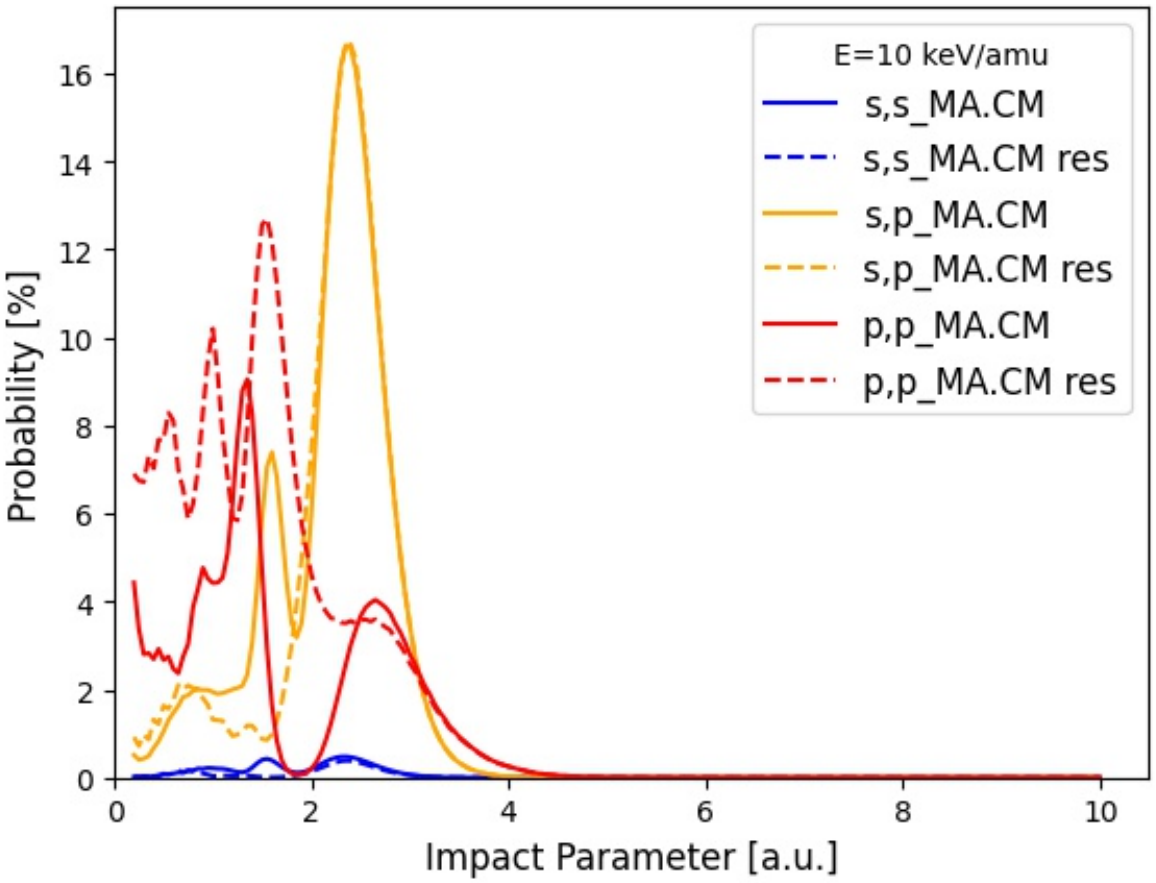


Figure A.41: $He^{2+}$–$Ne_2$ ion–dimer collisions in parallel orientation at 10 keV/amu. Two-site two-electron removal probability comparing MA.CM without response (solid line) and with response (dashed line).

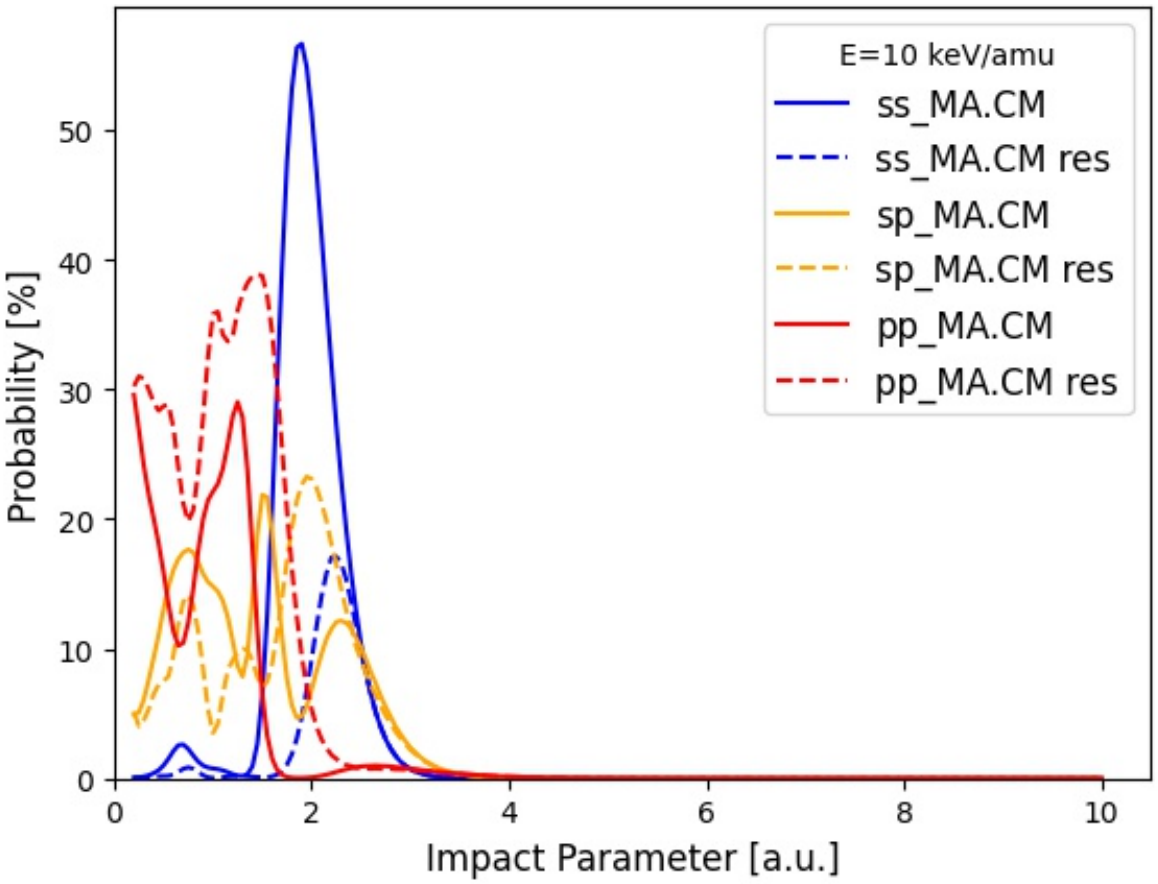


Figure A.42: $He^{2+}$–$Ne_2$ ion–dimer collisions in parallel orientation at 10 keV/amu. One-site two-electron removal probability comparing MA.CM without response (solid line) and with response (dashed line).

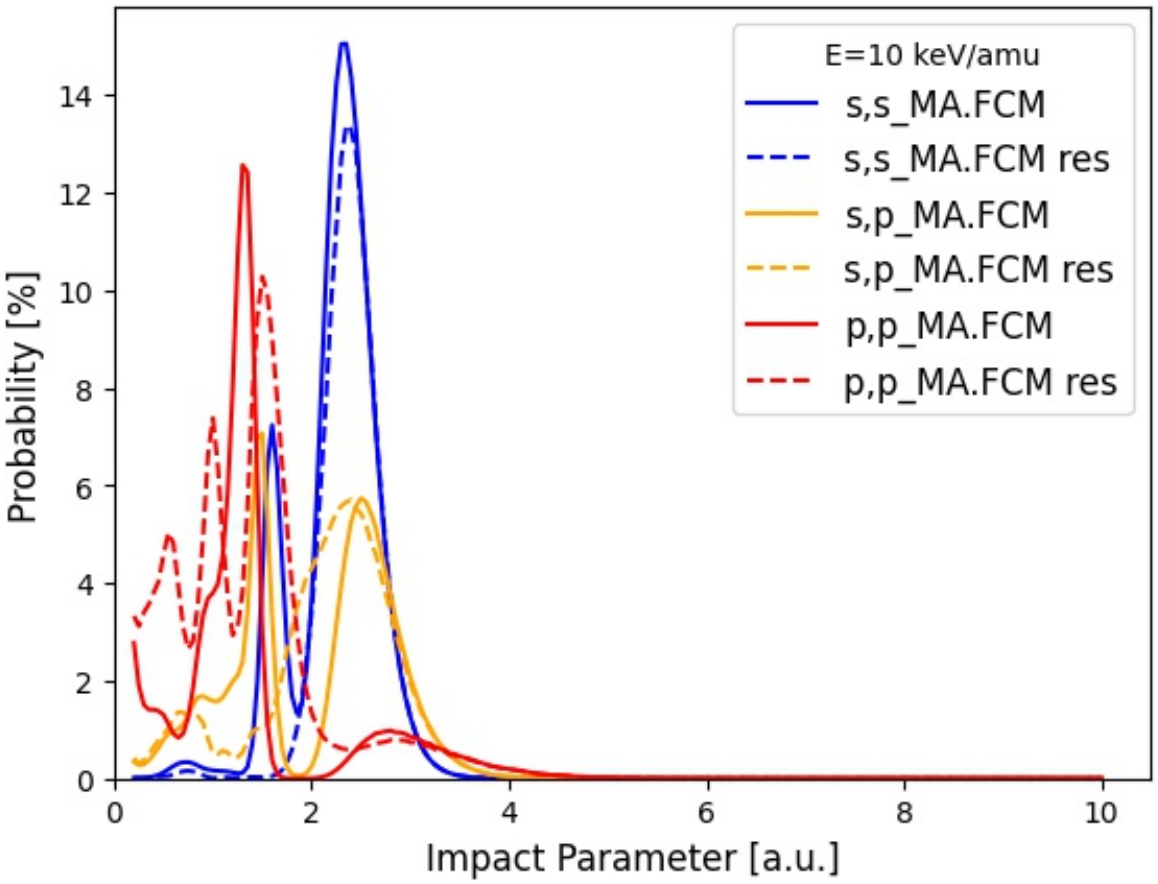


Figure A.43: $He^{2+}$–$Ne_2$ ion–dimer collisions in parallel orientation at 10 keV/amu. Two-site two-electron removal probability comparing MA.FCM without response (solid line) and with response (dashed line).

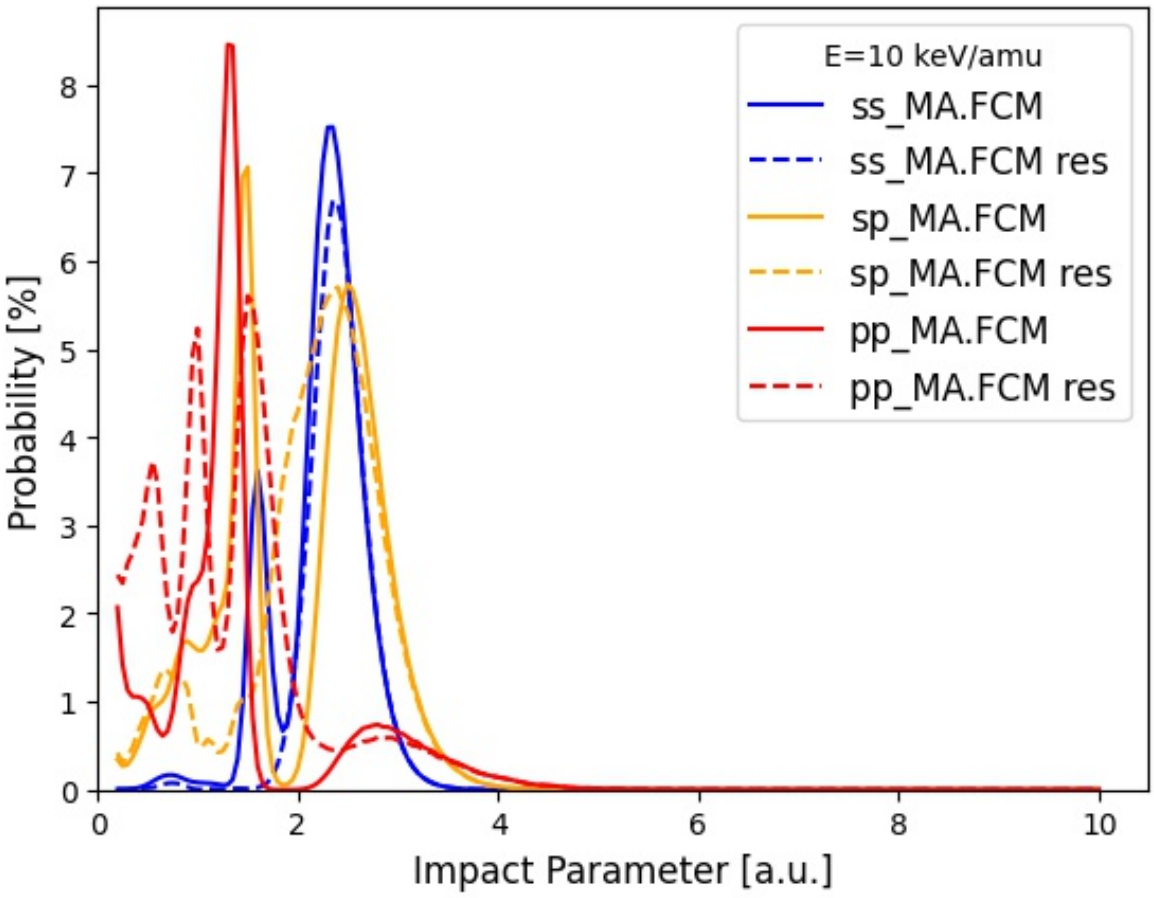


Figure A.44: $He^{2+}$–$Ne_2$ ion–dimer collisions in parallel orientation at 10 keV/amu. One-site two-electron removal probability comparing MA.FCM without response (solid line) and with response (dashed line).

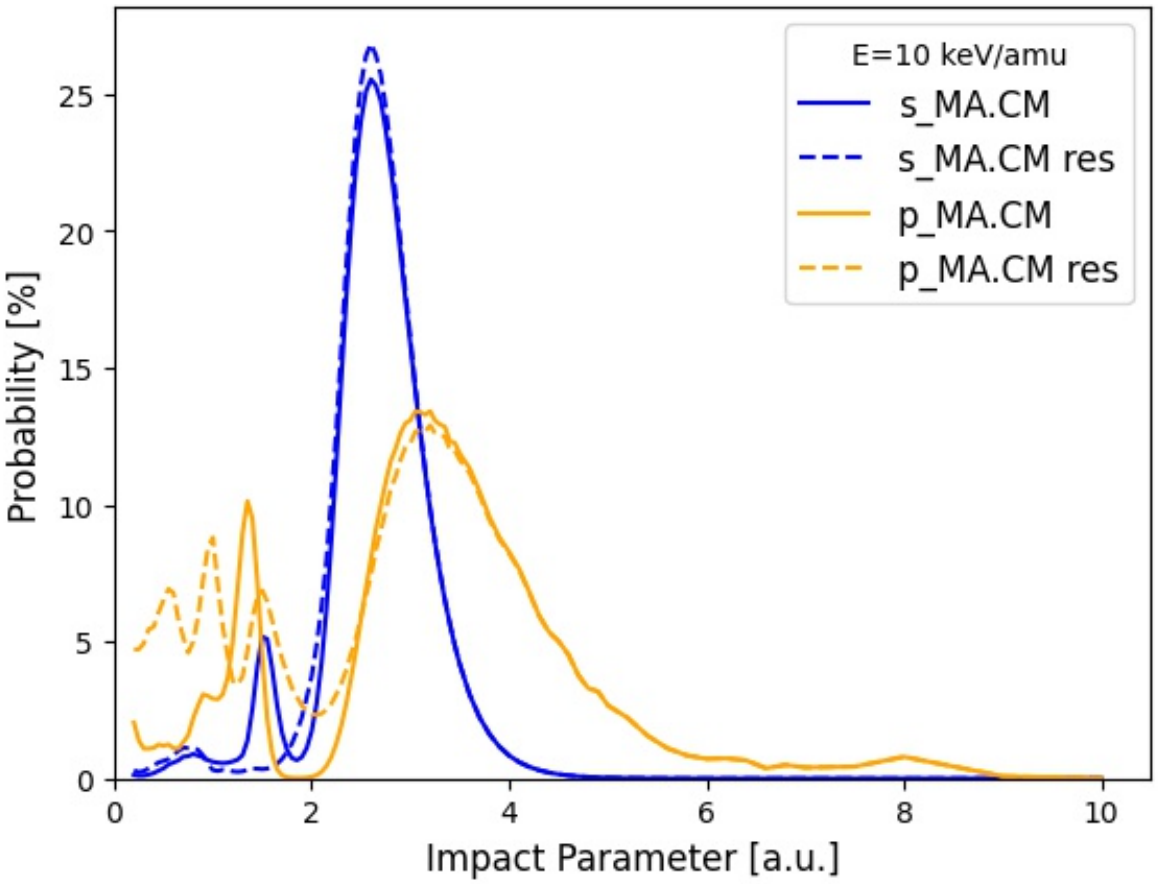


Figure A.45: $He^{2+}$–$Ne_2$ ion–dimer collisions in parallel orientation at 10 keV/amu. Single-electron removal probability comparing MA.CM without response (solid line) and with response (dashed line).

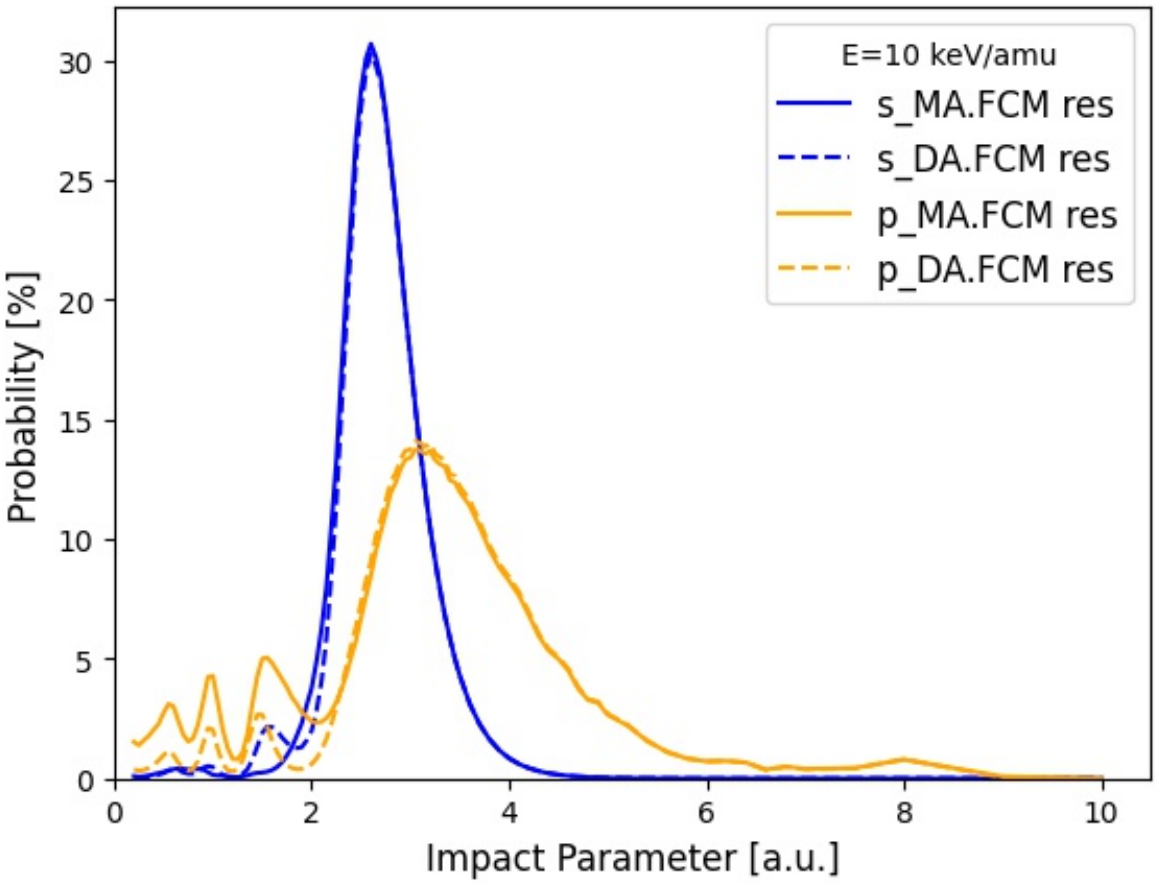


Figure A.46: $He^{2+}$–$Ne_2$ ion–dimer collisions in parallel orientation at 10 keV/amu. One-electron removal probability comparing MA.FCM with response (solid line) and DA.FCM with response (dashed line).

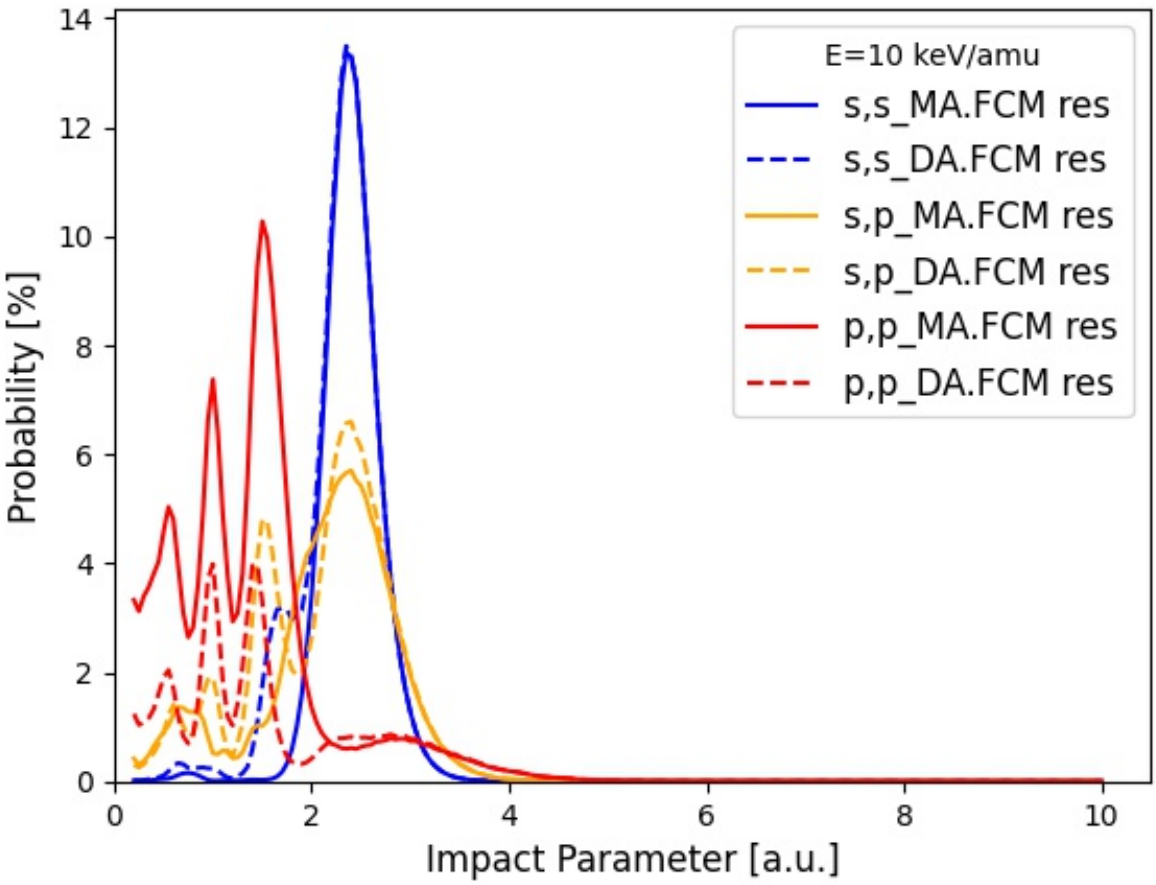


Figure A.47: $He^{2+}$–$Ne_2$ ion–dimer collisions in parallel orientation at 10 keV/amu. Two-site two-electron removal probability comparing MA.FCM with response (solid line) and DA.FCM with response (dashed line).

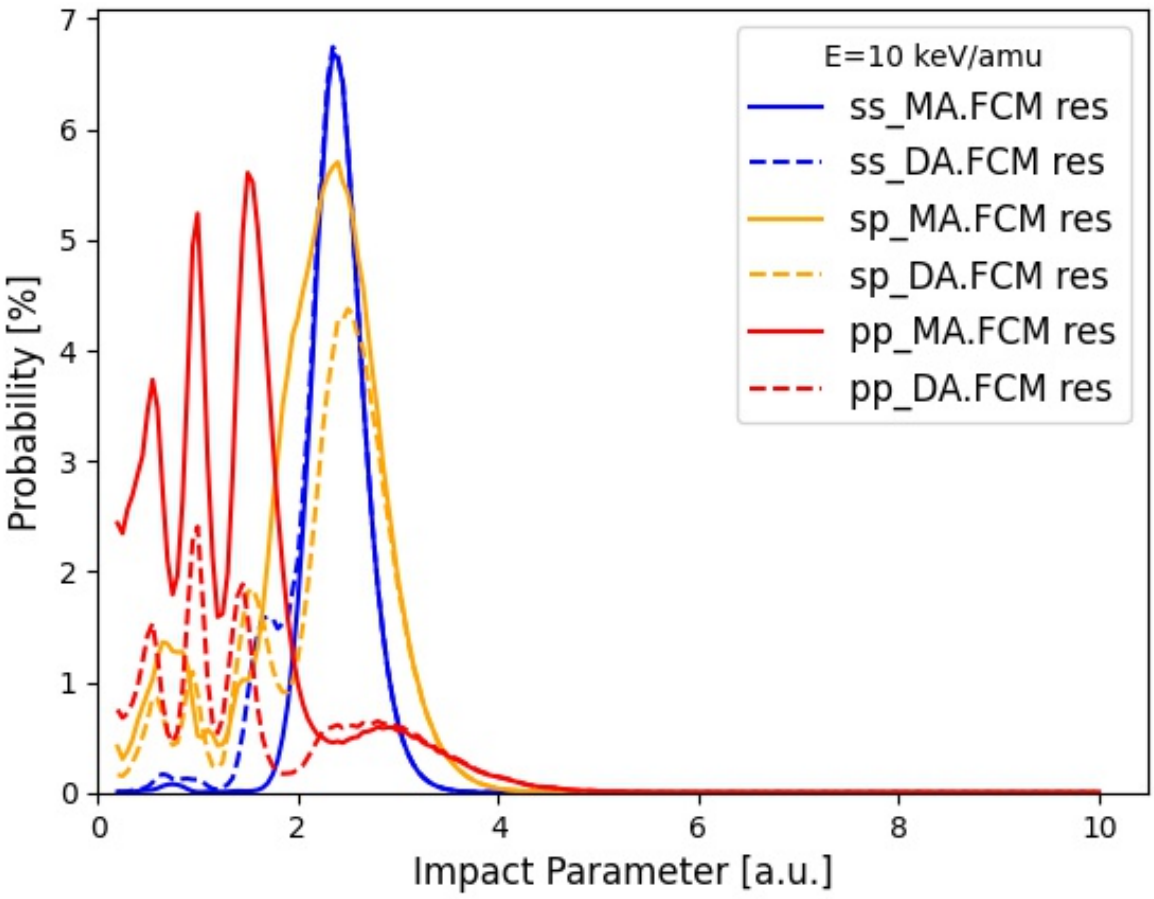


Figure A.48: $He^{2+}$–$Ne_2$ ion–dimer collisions in parallel orientation at 10 keV/amu. One-site two-electron removal probability comparing MA.FCM with response (solid line) and DA.FCM with response (dashed line).

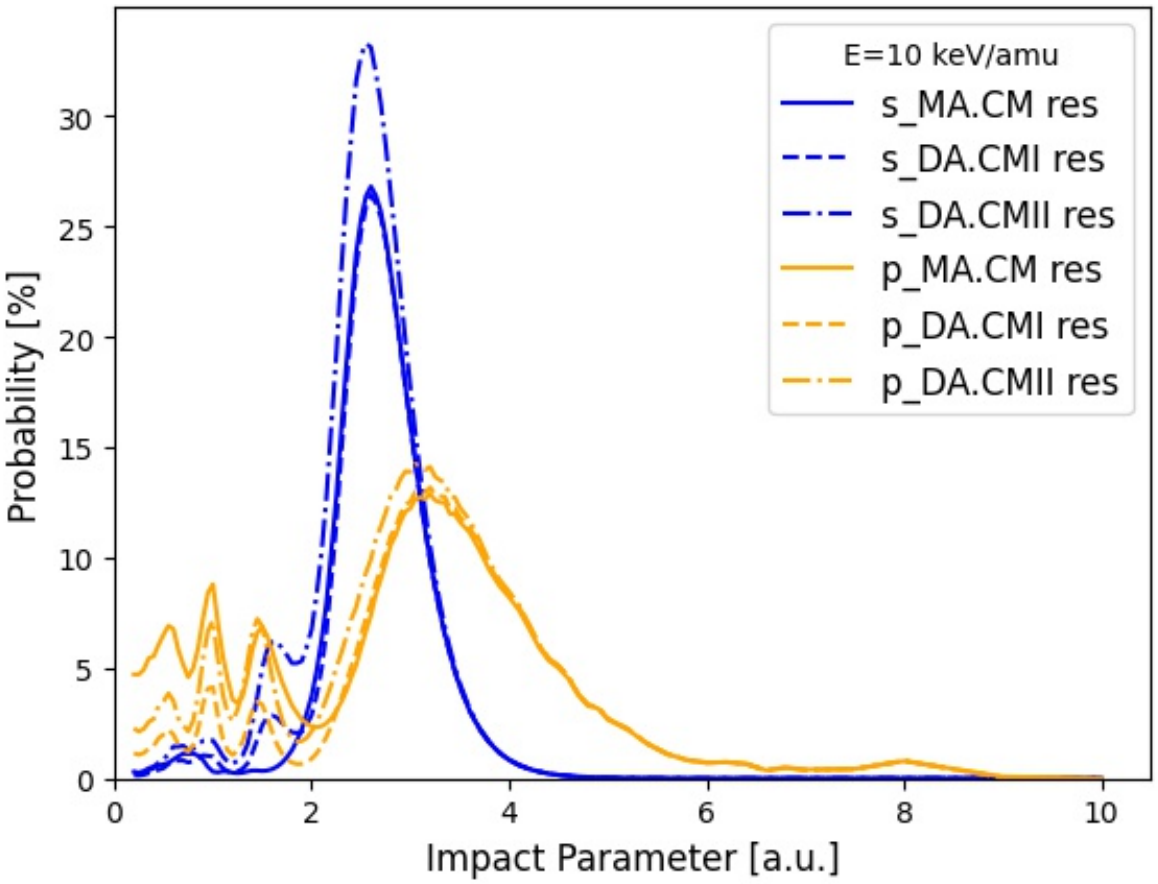


Figure A.49: $He^{2+}$–$Ne_2$ ion–dimer collisions in parallel orientation at 10 keV/amu. One-electron removal probability comparing MA.CM with response (solid line), DA.CMI without response (dashed line) and DA.CMII with response (dashed-dotted line).

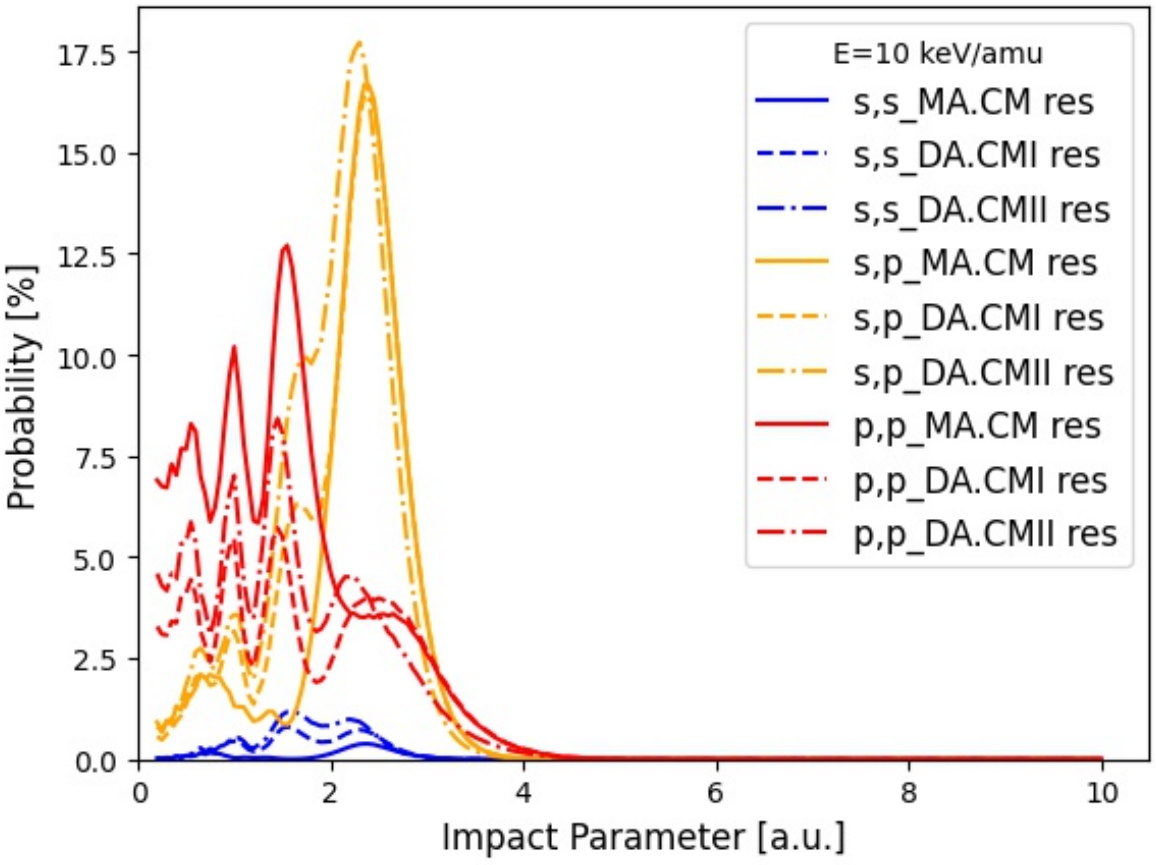


Figure A.50: $He^{2+}$–$Ne_2$ ion–dimer collisions in parallel orientation at 10 keV/amu. Two-site two-electron removal probability comparing MA.CM with response (solid line), DA.CMI without response (dashed line) and DA.CMII with response (dashed-dotted line).

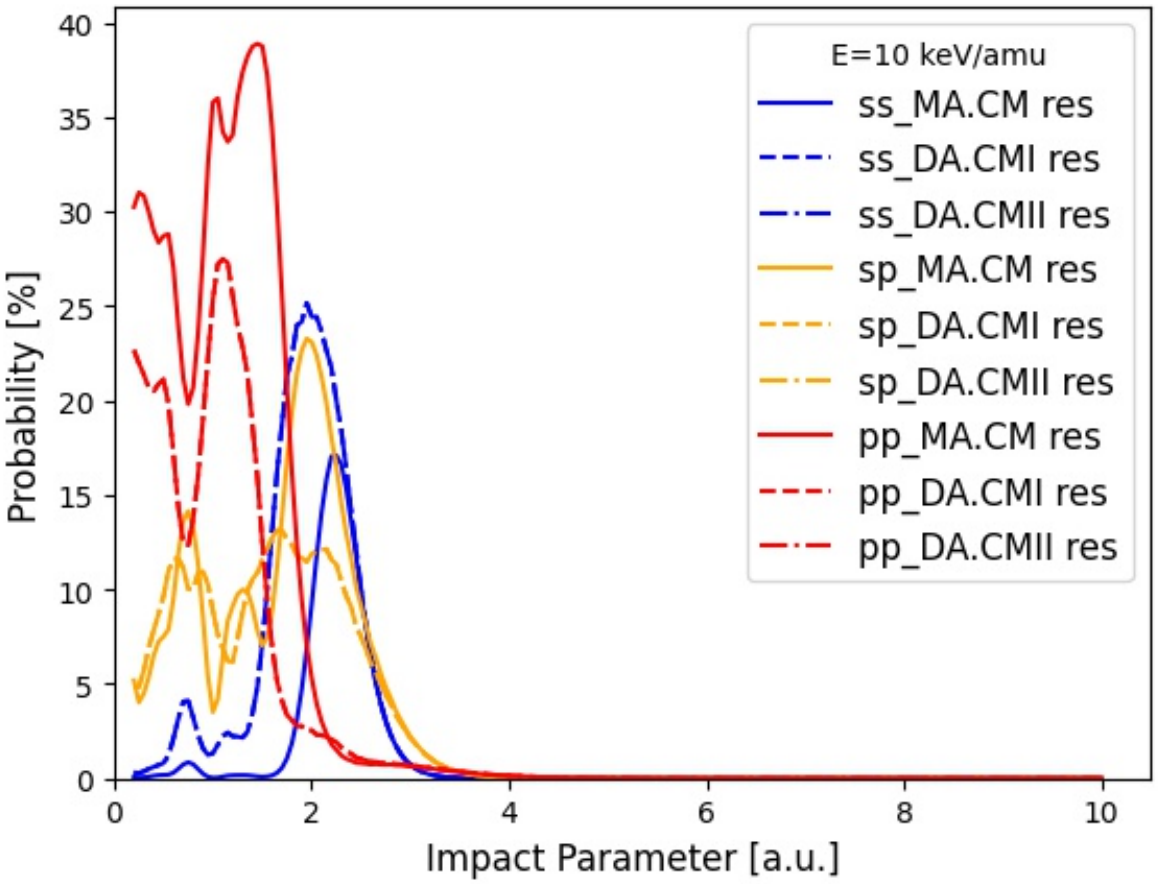


Figure A.51: $He^{2+}$–$Ne_2$ ion–dimer collisions in parallel orientation at 10 keV/amu. One-site two-electron removal probability comparing MA.CM with response (solid line), DA.CMI without response (dashed line) and DA.CMII with response (dashed-dotted line).

### 2. $He^+$ Projectile

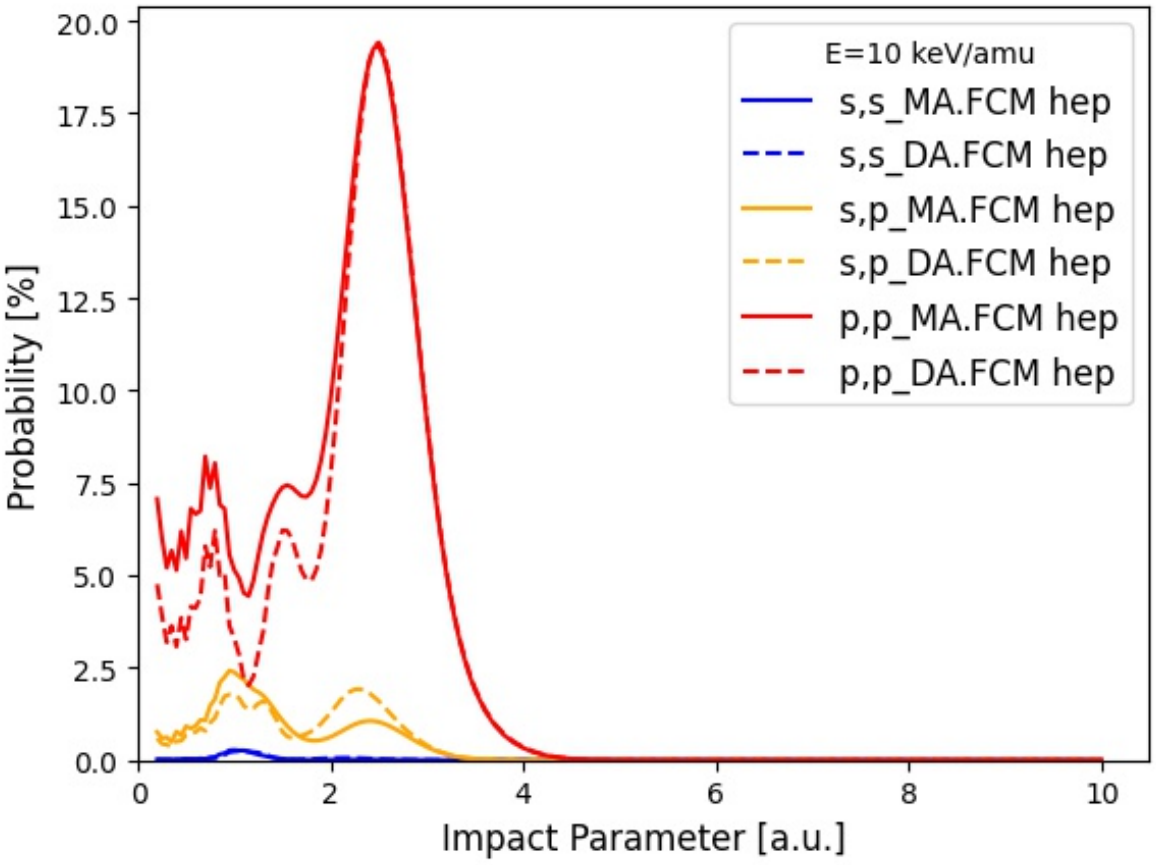


Figure A.52: $He^+$–$Ne_2$ ion–dimer collisions in parallel orientation at 10 keV/amu. Two-site two-electron removal probability comparison for MA.FCM (solid line) and DA.FCM (dashed line).

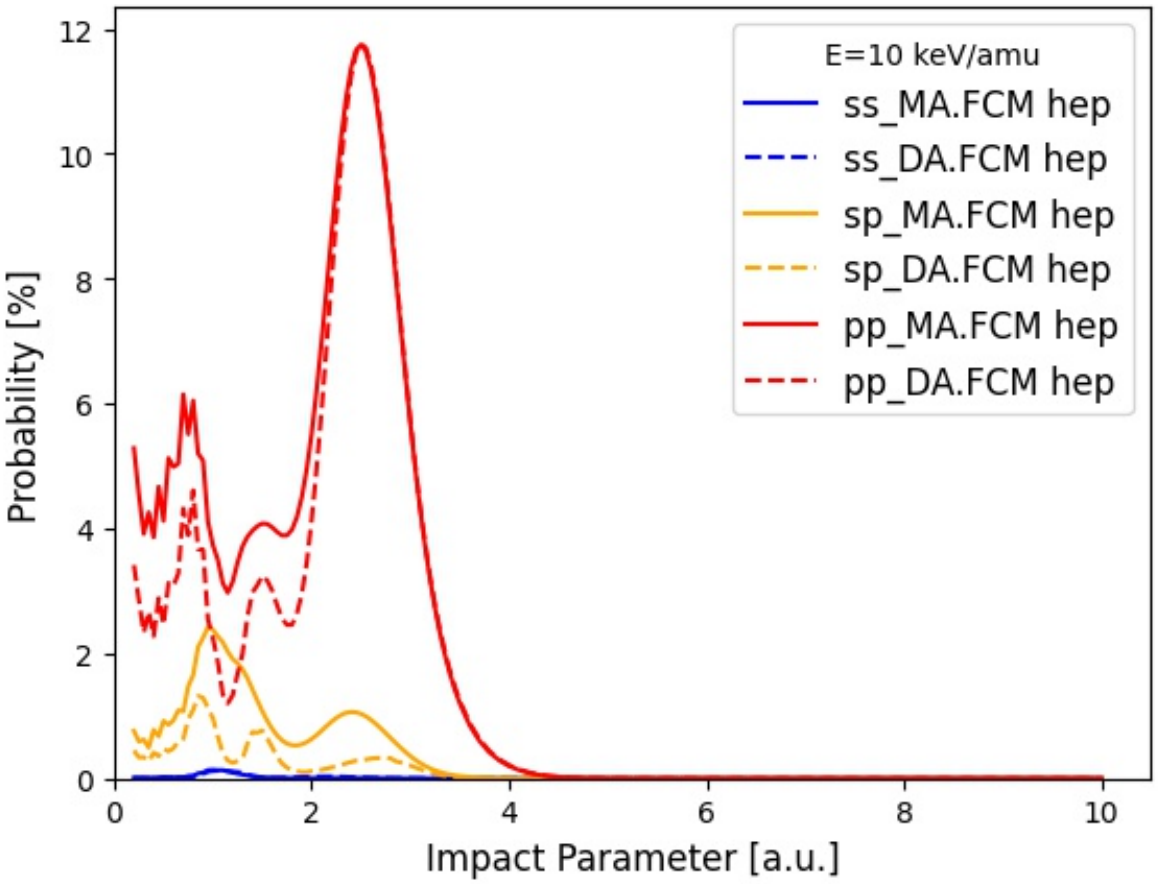


Figure A.53: $He^+$–$Ne_2$ ion–dimer collisions in parallel orientation at 10 keV/amu. One-site two-electron removal probability comparison for MA.FCM (solid line) and DA.FCM (dashed line).

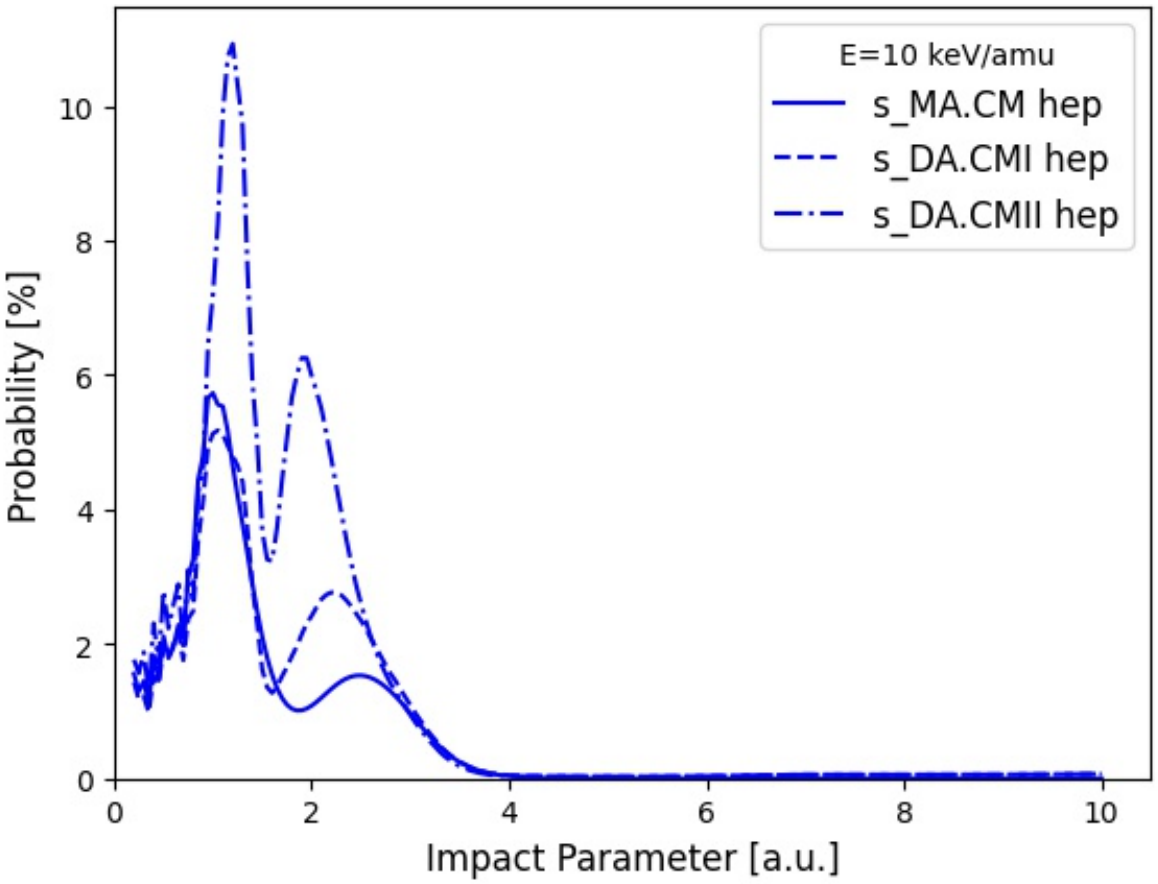


Figure A.54: $He^+$–$Ne_2$ ion–dimer collisions in parallel orientation at 10 keV/amu. Single $2s$ electron removal probability comparison for MA.CM (solid line), DA.CMI (dashed line) and DA.CMII (dashed-dotted line).

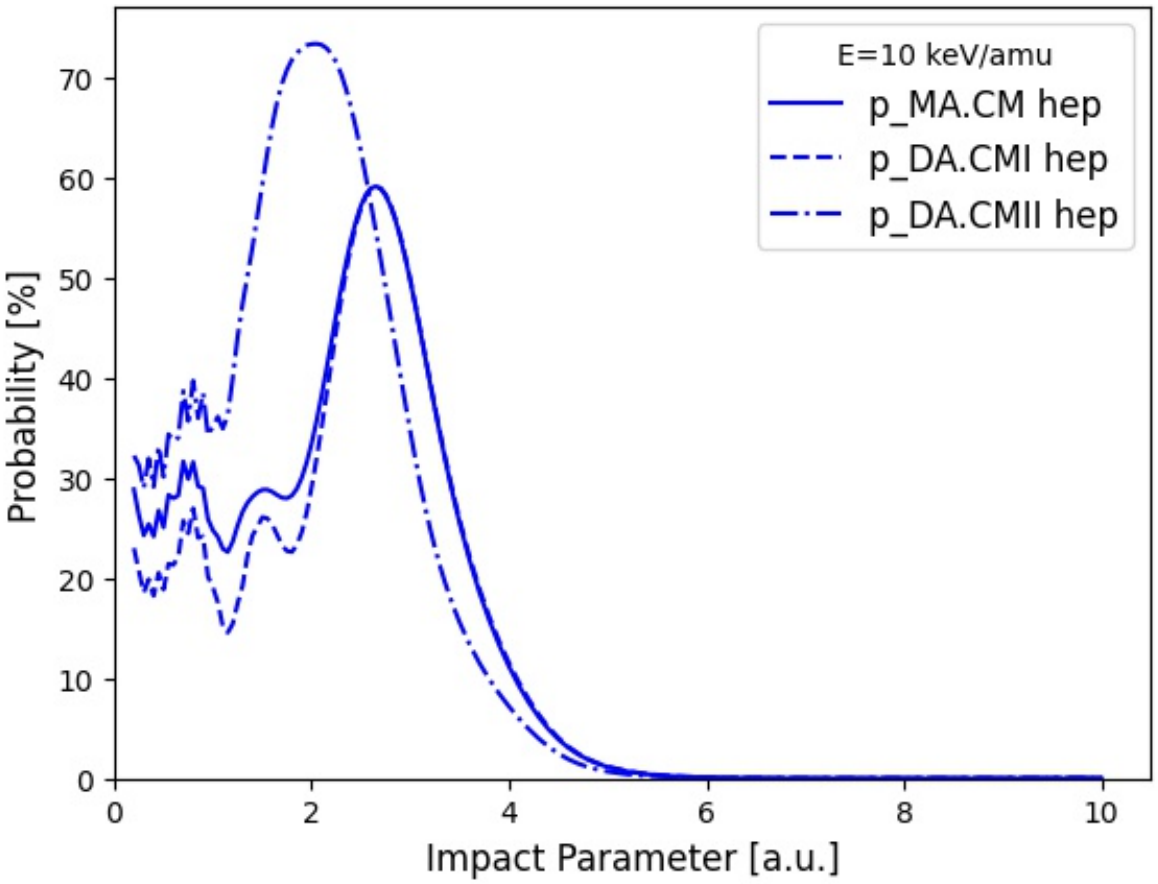


Figure A.55: $He^+$–$Ne_2$ ion–dimer collisions in parallel orientation at 10 keV/amu. Single $2s$ electron removal probability comparison for MA.CM (solid line), DA.CMI (dashed line) and DA.CMII (dashed-dotted line).

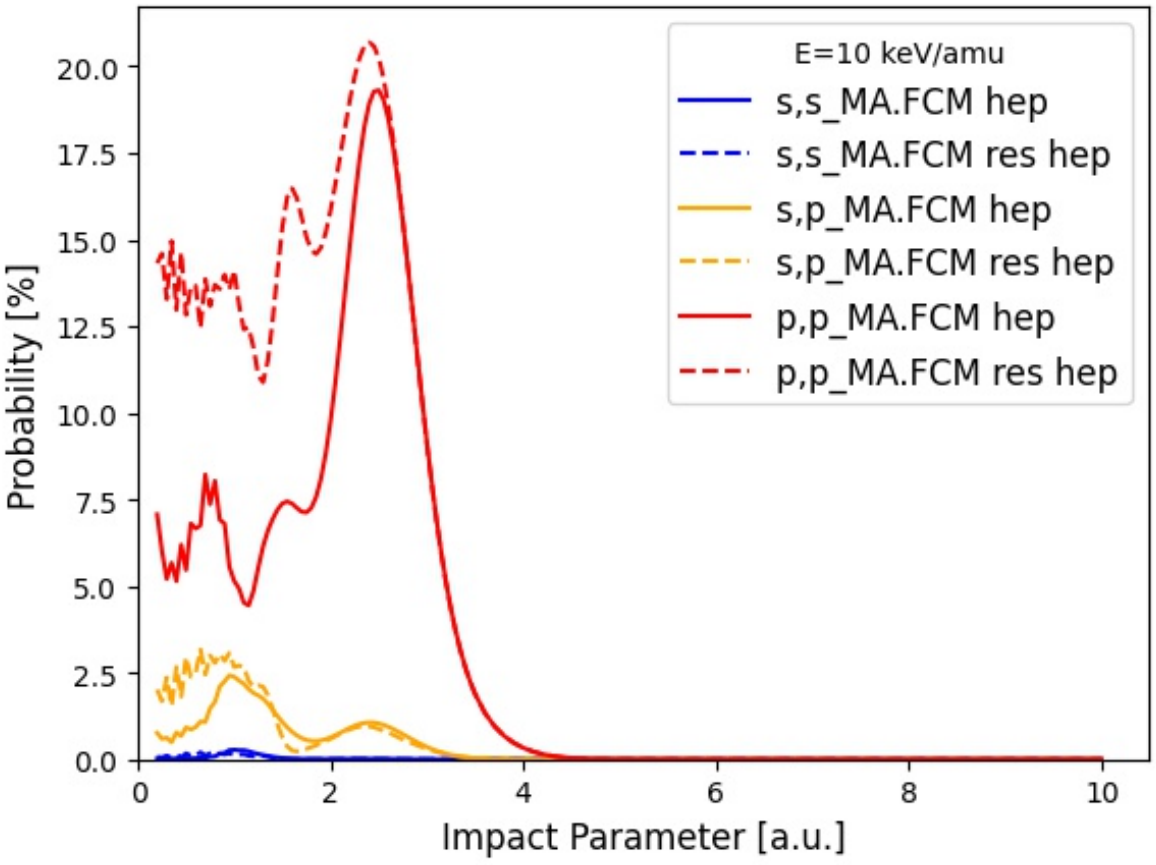


Figure A.56: $He^+$–$Ne_2$ ion–dimer collisions in parallel orientation at 10 keV/amu. Two-site two-electron removal probability comparison for MA.FCM without response (solid line) and with response (dashed line).

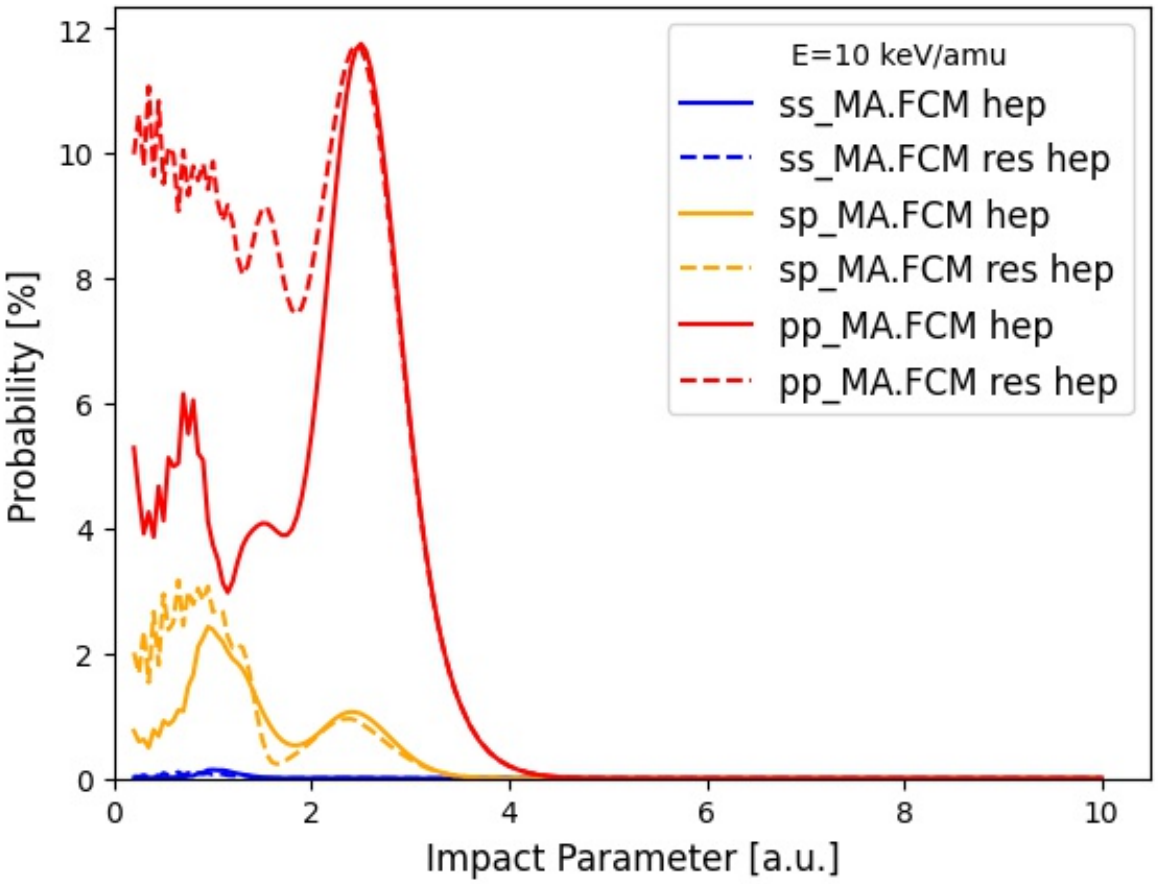


Figure A.57: $He^+$–$Ne_2$ ion–dimer collisions in parallel orientation at 10 keV/amu. One-site two-electron removal probability comparison for MA.FCM without response (solid line) and with response (dashed line).

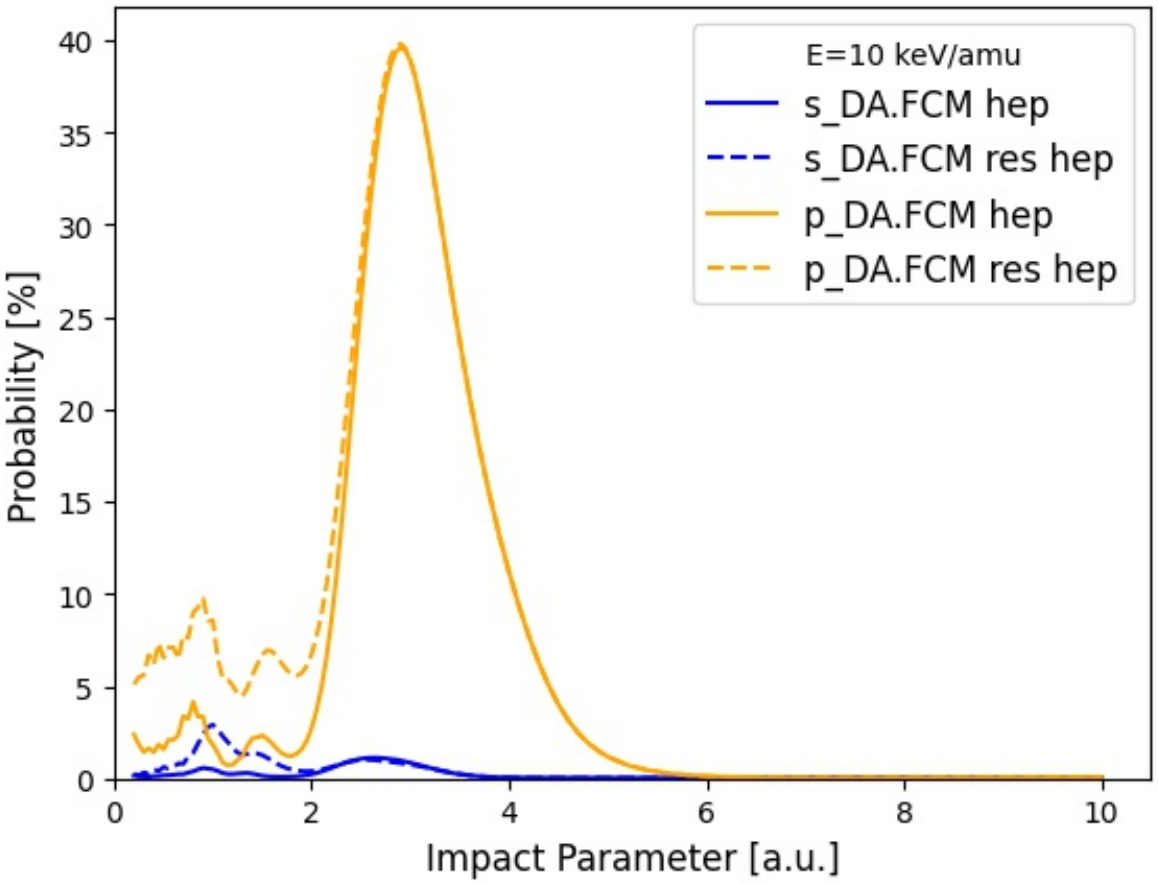


Figure A.58: $He^+$–$Ne_2$ ion–dimer collisions in parallel orientation at 10 keV/amu. Single-electron removal probability comparison for DA.FCM without response (solid line) and with response (dashed line).

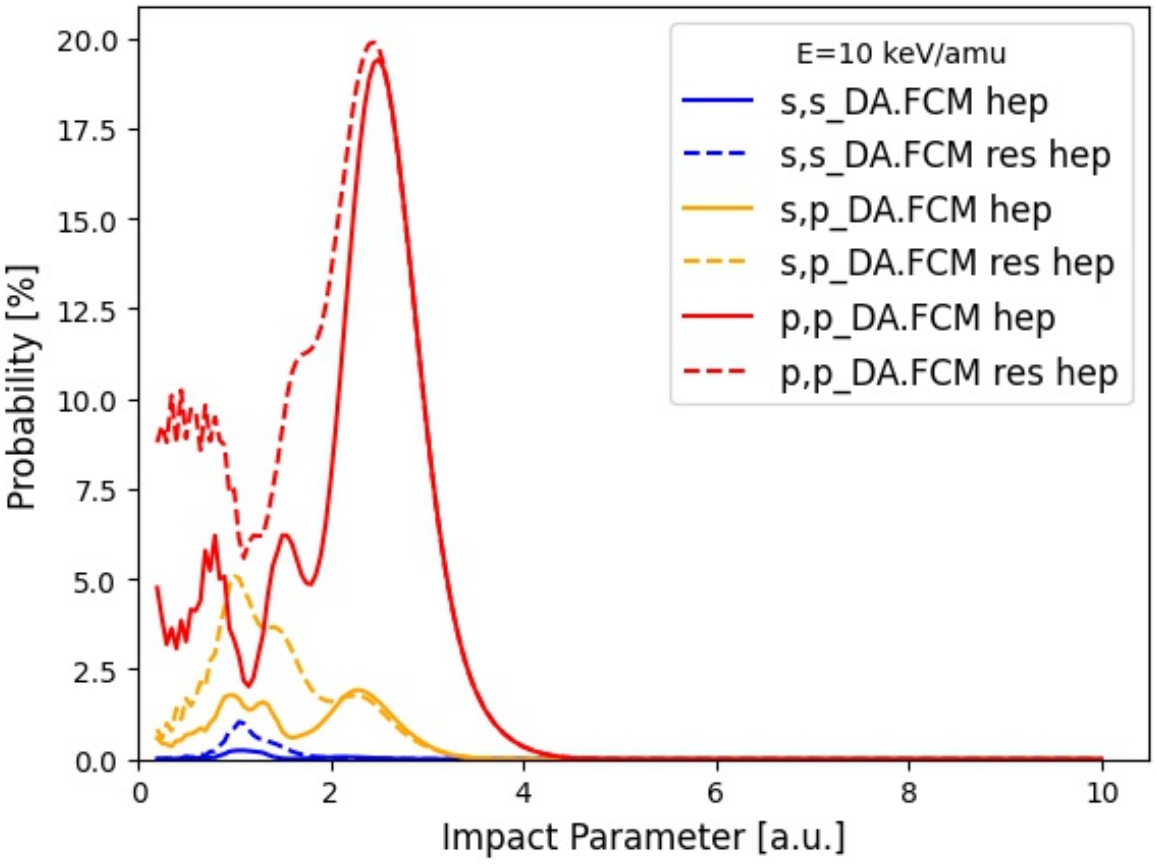


Figure A.59: $He^+$–$Ne_2$ ion–dimer collisions in parallel orientation at 10 keV/amu. Two-site two-electron removal probability comparison for DA.FCM without response (solid line) and with response (dashed line).

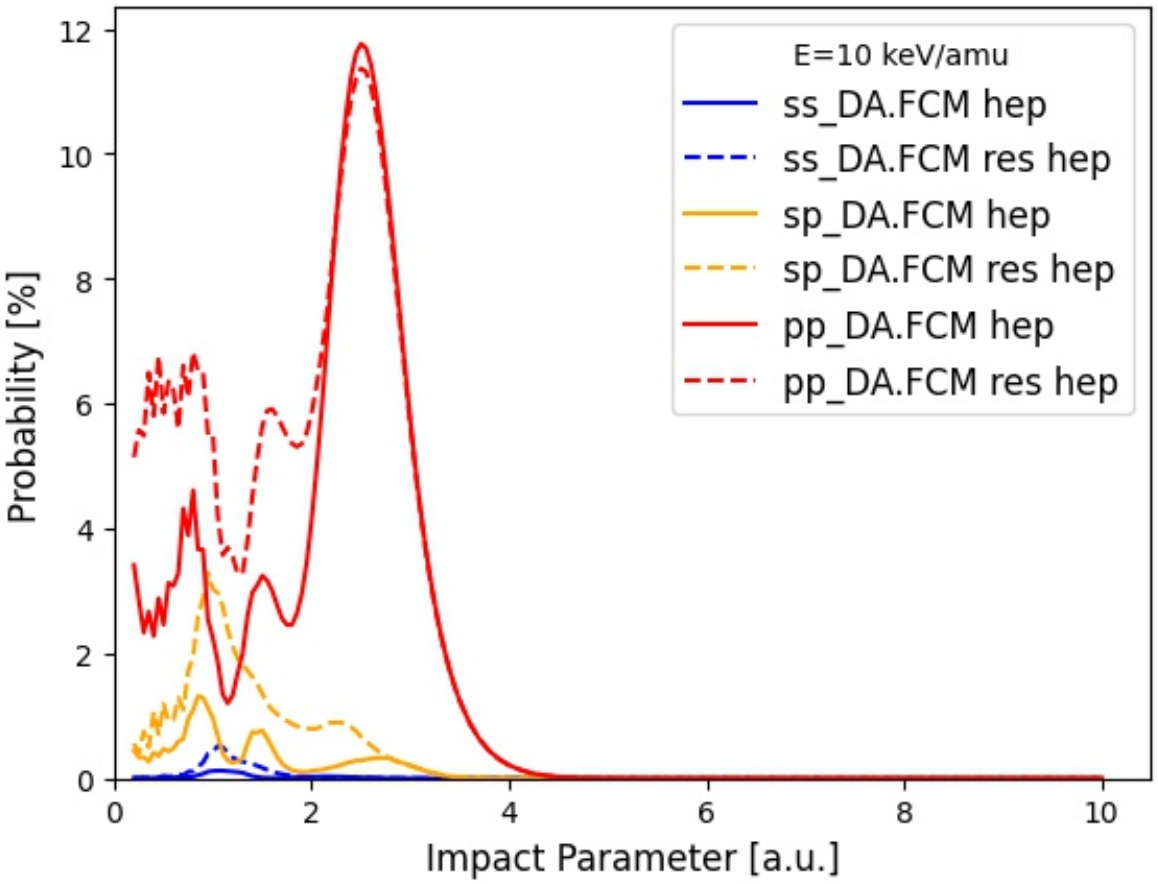


Figure A.60: $He^+$–$Ne_2$ ion–dimer collisions in parallel orientation at 10 keV/amu. One-site two-electron removal probability comparison for DA.FCM without response (solid line) and with response (dashed line).

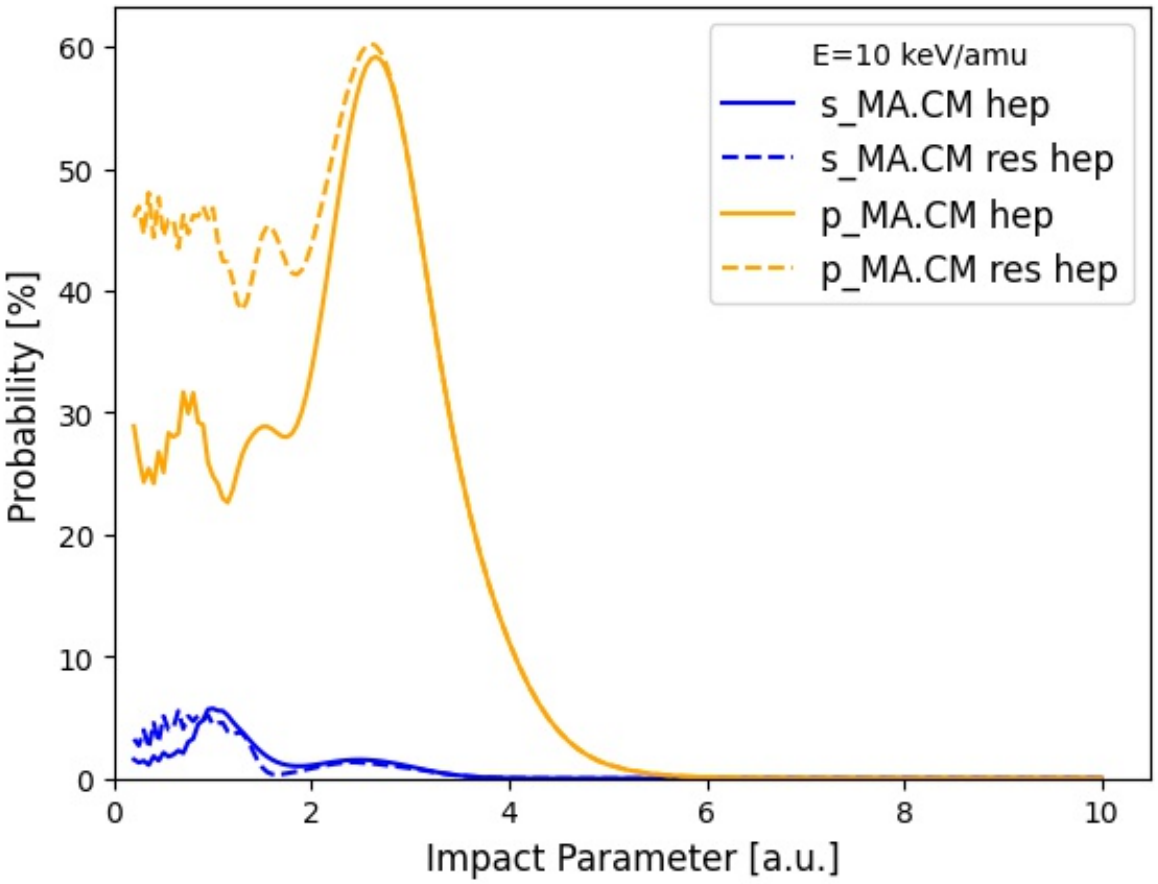


Figure A.61: $He^+$–$Ne_2$ ion–dimer collisions in parallel orientation at 10 keV/amu. Single-electron removal probability comparison for MA.CM without response (solid line) and with response (dashed line).

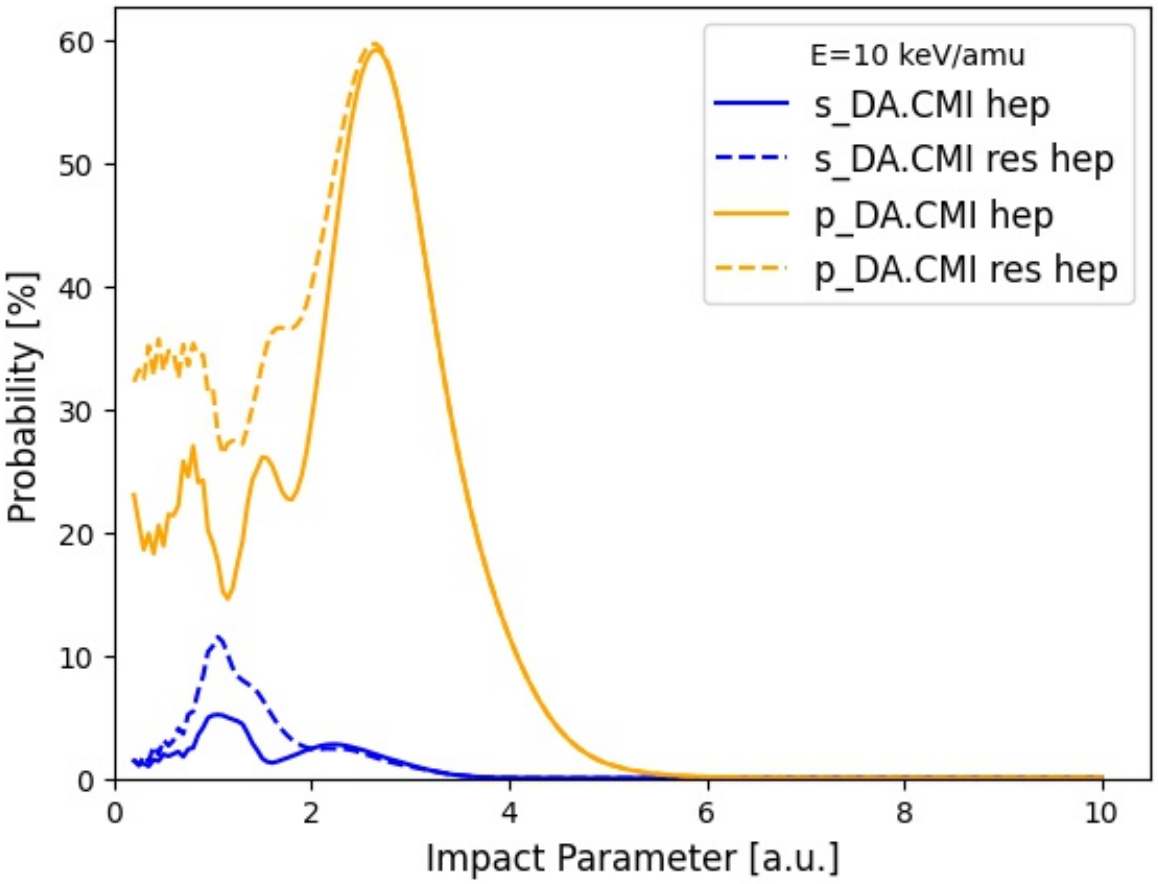


Figure A.62: $He^+$–$Ne_2$ ion–dimer collisions in parallel orientation at 10 keV/amu. Single-electron removal probability comparison for DA.CMI without response (solid line) and with response (dashed line).

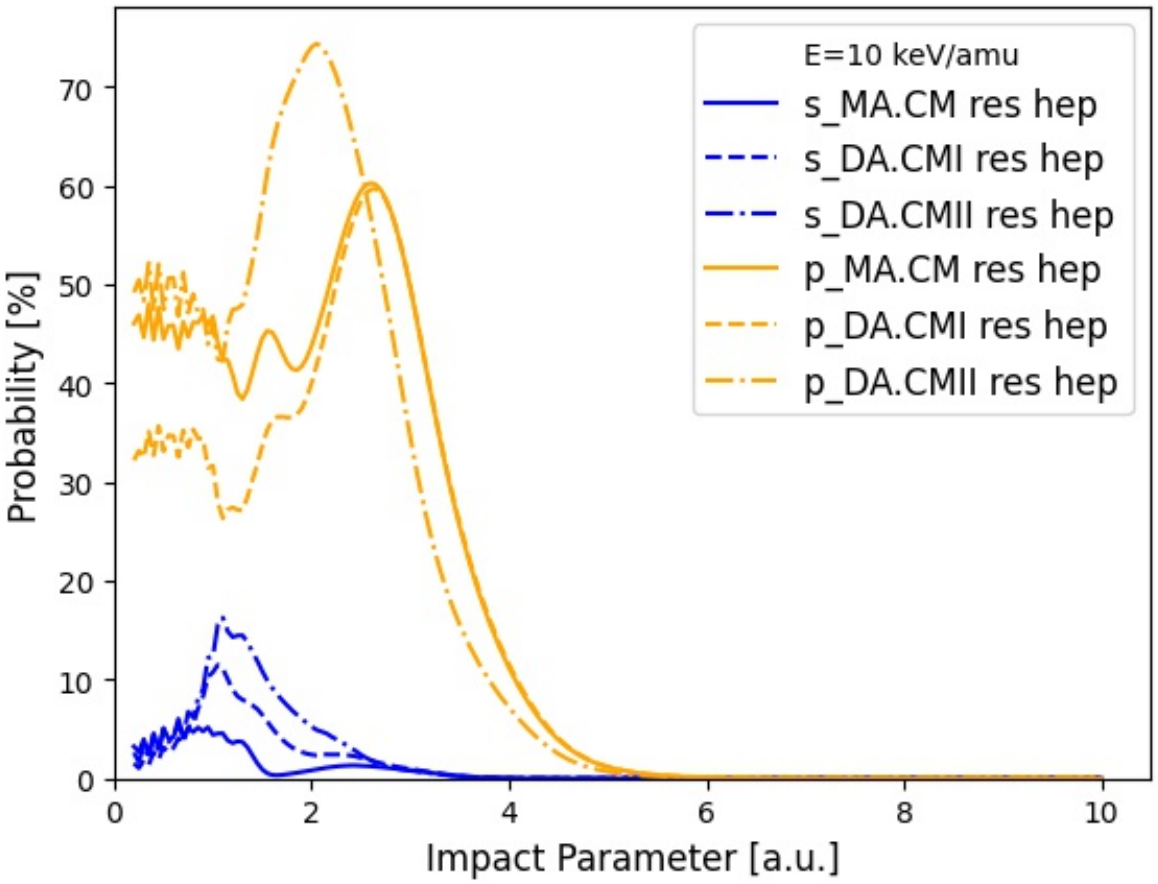


Figure A.63: $He^+$–$Ne_2$ ion–dimer collisions in parallel orientation at 10 keV/amu. Single-electron removal probability comparison for MA.CM with response (solid line), DA.CMI with response (dashed line) and DA.CMII with response (dashed-dotted line).

## Appendix B: Helium Ion - Argon Dimer Target

### 1. $He^{2+}$ Projectile

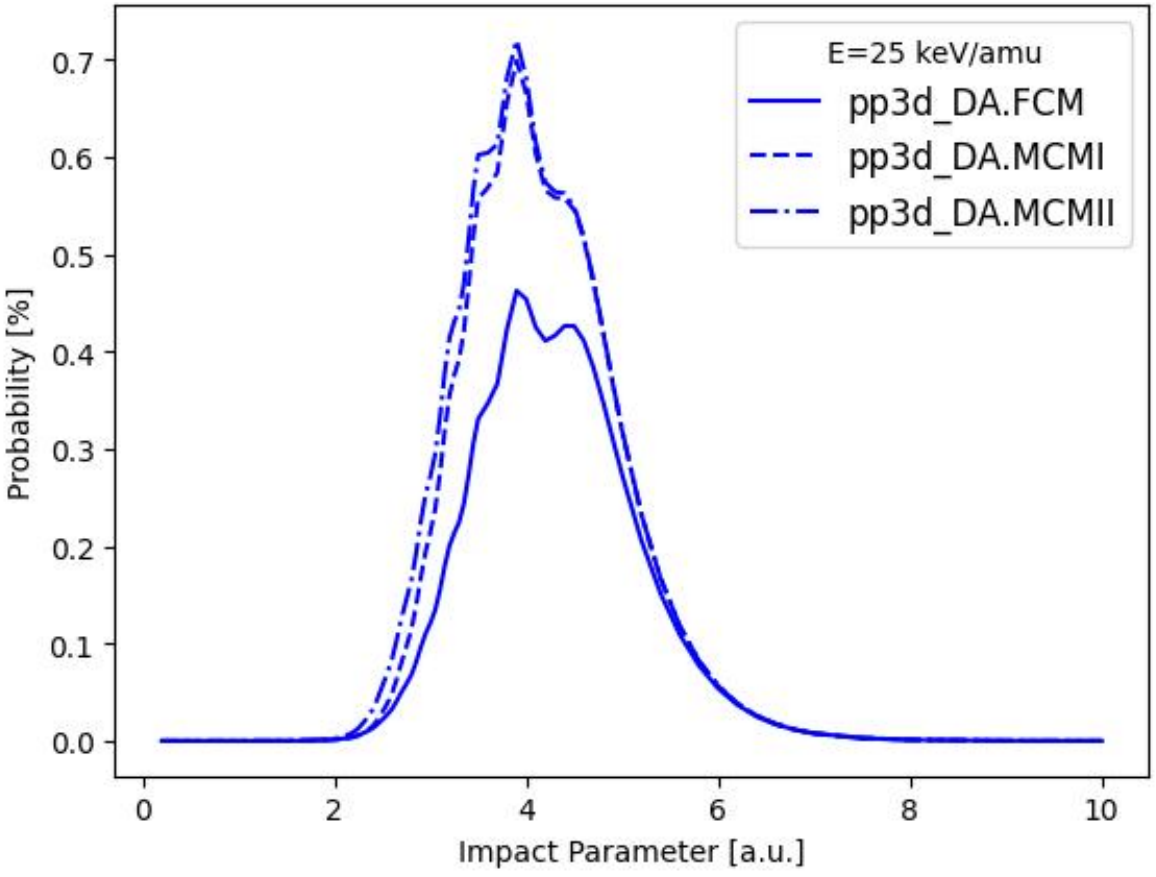


Figure B.64: $He^{2+}$–$Ar_2$ ion–dimer collisions in parallel orientation at 25 keV/amu. Single $3p$ electron removal with simultaneous $3p$ excitation to the $3d$ state probability comparing DA.FCM (solid line) and DA.MCMI (dashed line) and DA.MCMII (dashed-dotted line).

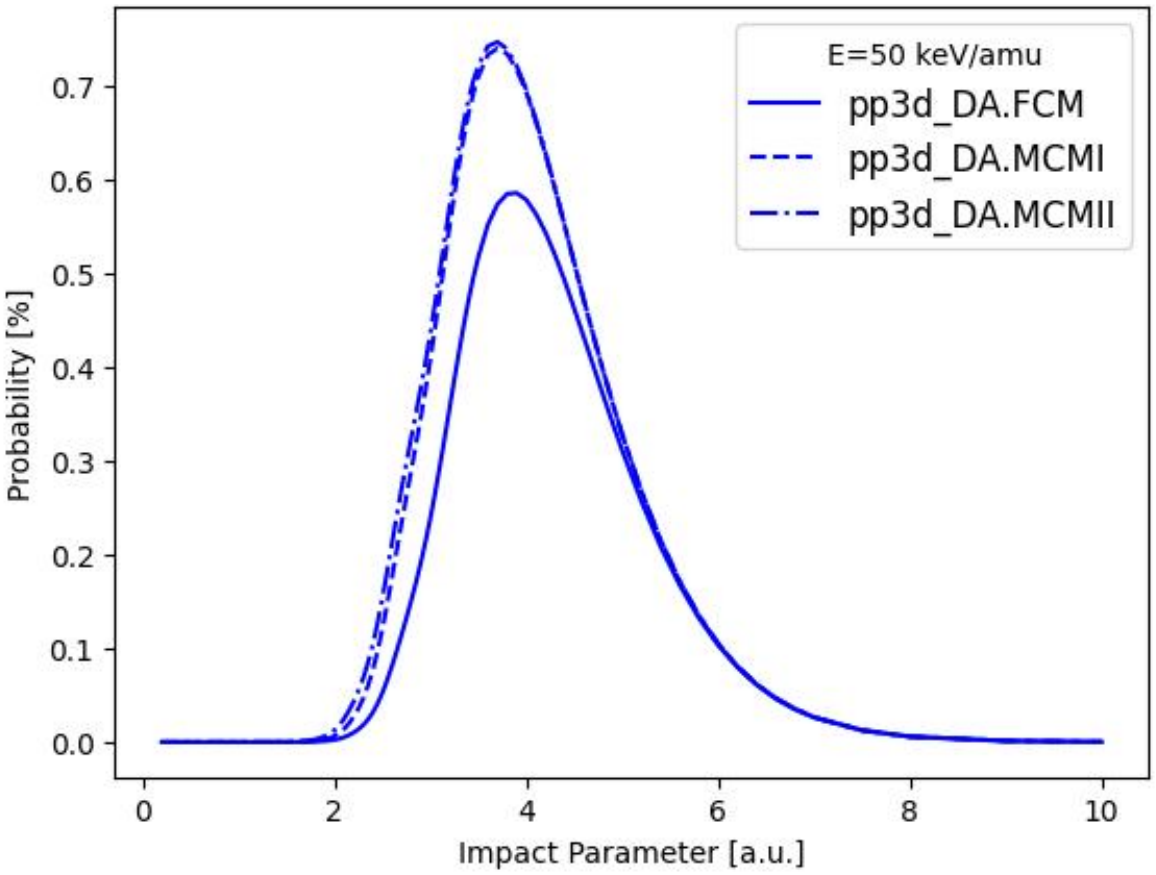


Figure B.65: $He^{2+}$–$Ar_2$ ion–dimer collisions in parallel orientation at 50 keV/amu. Single $3p$ electron removal with simultaneous $3p$ excitation to the $3d$ state probability comparing DA.FCM (solid line) and DA.MCMI (dashed line) and DA.MCMII (dashed-dotted line).

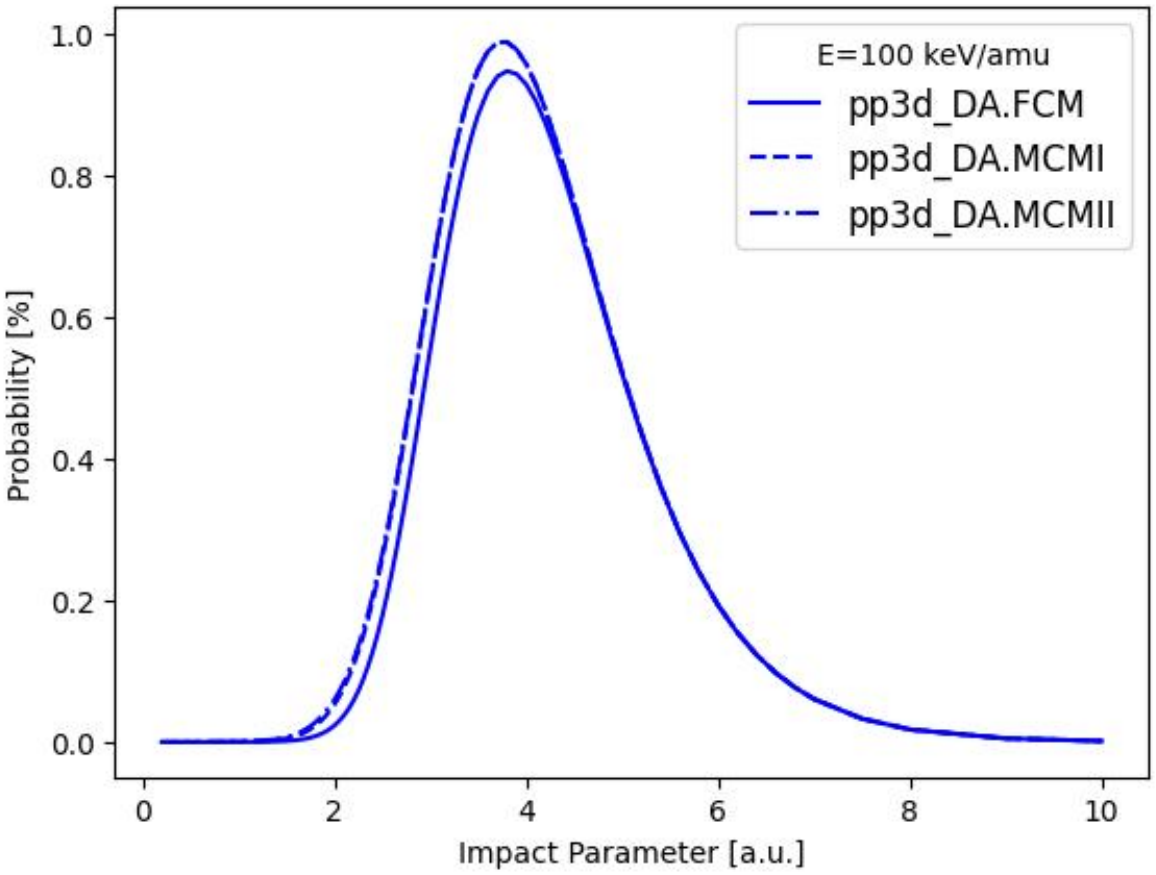


Figure B.66: $He^{2+}$–$Ar_2$ ion–dimer collisions in parallel orientation at 100 keV/amu. Single $3p$ electron removal with simultaneous $3p$ excitation to the $3d$ state probability comparing DA.FCM (solid line) and DA.MCMI (dashed line) and DA.MCMII (dashed-dotted line).

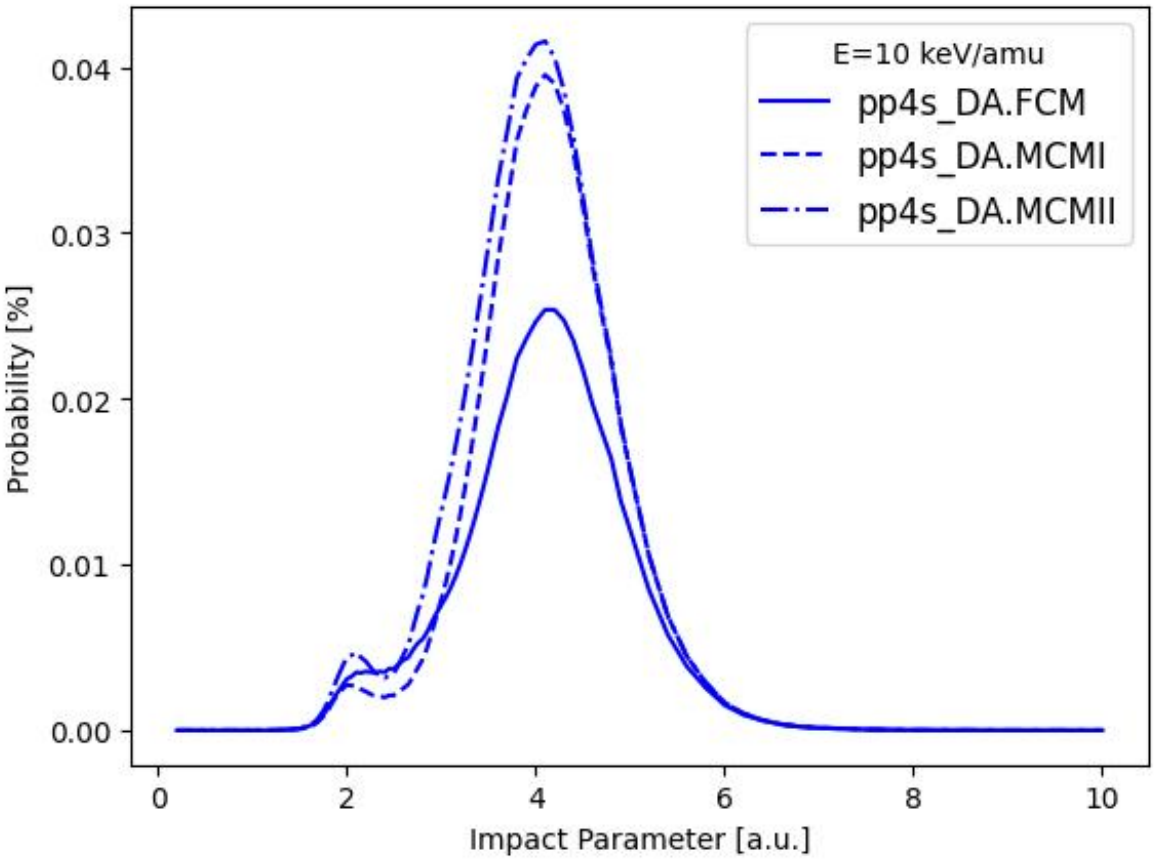


Figure B.67: $He^{2+}$–$Ar_2$ ion–dimer collisions in parallel orientation at 10 keV/amu. Single $3p$ electron removal with simultaneous $3p$ excitation to the $4s$ state probability comparing DA.FCM (solid line) and DA.MCMI (dashed line) and DA.MCMII (dashed-dotted line).

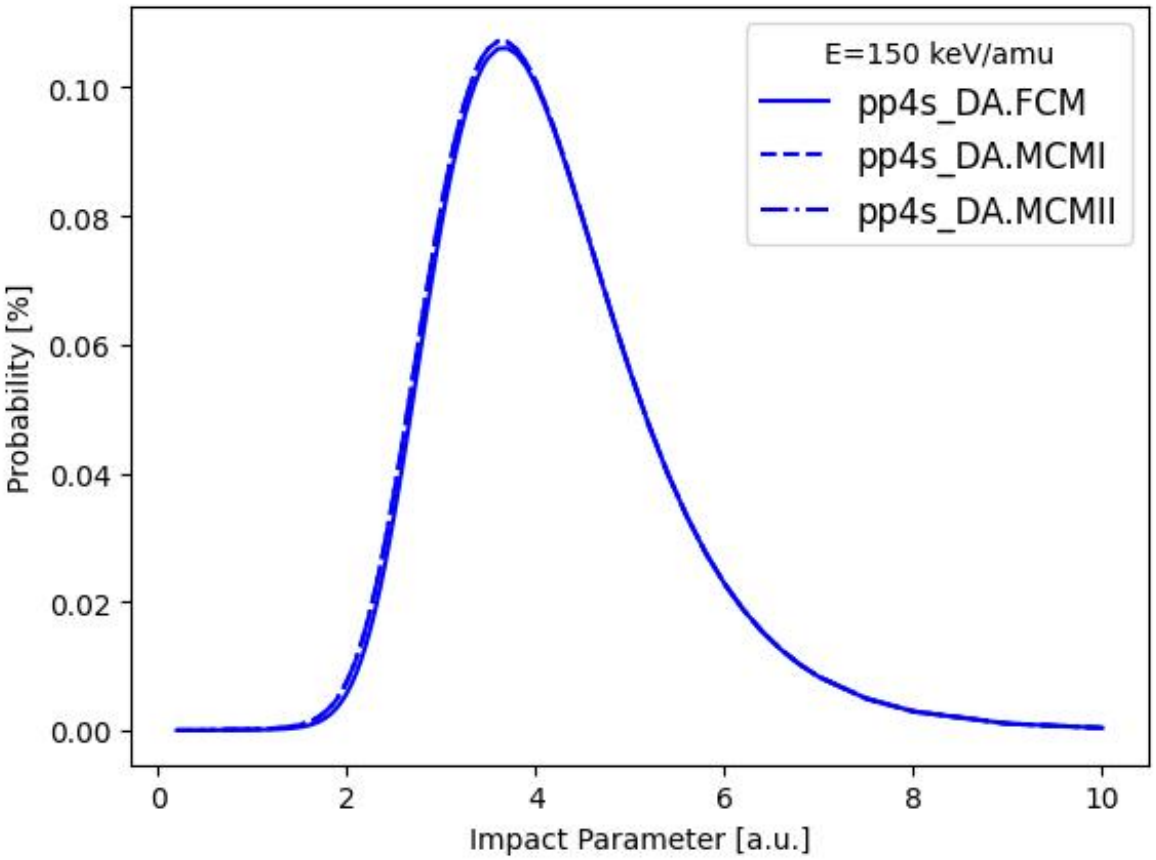


Figure B.68: $He^{2+}$–$Ar_2$ ion–dimer collisions in parallel orientation at 150 keV/amu. Single $3p$ electron removal with simultaneous $3p$ excitation to the $4s$ state probability comparing DA.FCM (solid line) and DA.MCMI (dashed line) and DA.MCMII (dashed-dotted line).

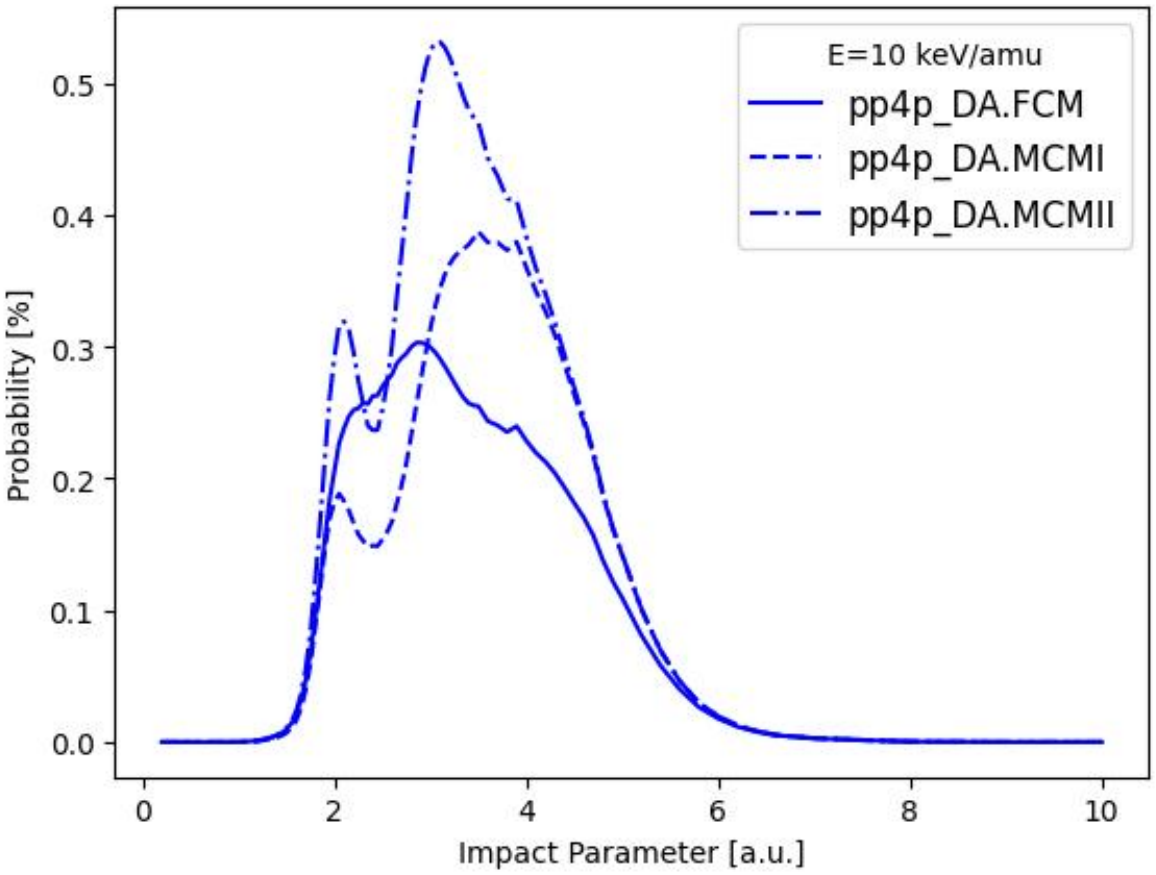


Figure B.69: $He^{2+}$–$Ar_2$ ion–dimer collisions in parallel orientation at 10 keV/amu. Single $3p$ electron removal with simultaneous $3p$ excitation to the $4p$ state probability comparing DA.FCM (solid line) and DA.MCMI (dashed line) and DA.MCMII (dashed-dotted line).

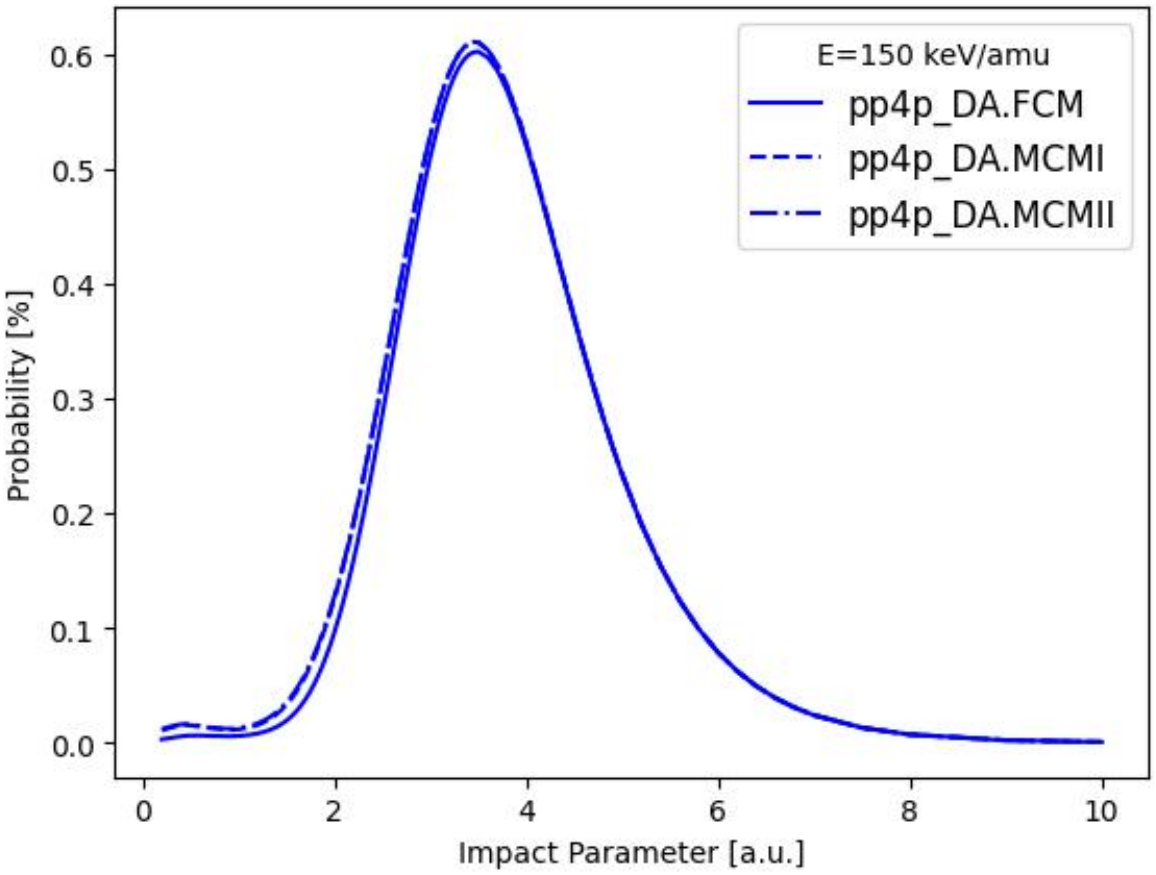


Figure B.70: $He^{2+}$–$Ar_2$ ion–dimer collisions in parallel orientation at 150 keV/amu. Single $3p$ electron removal with simultaneous $3p$ excitation to the $4p$ state probability comparing DA.FCM (solid line) and DA.MCMI (dashed line) and DA.MCMII (dashed-dotted line).

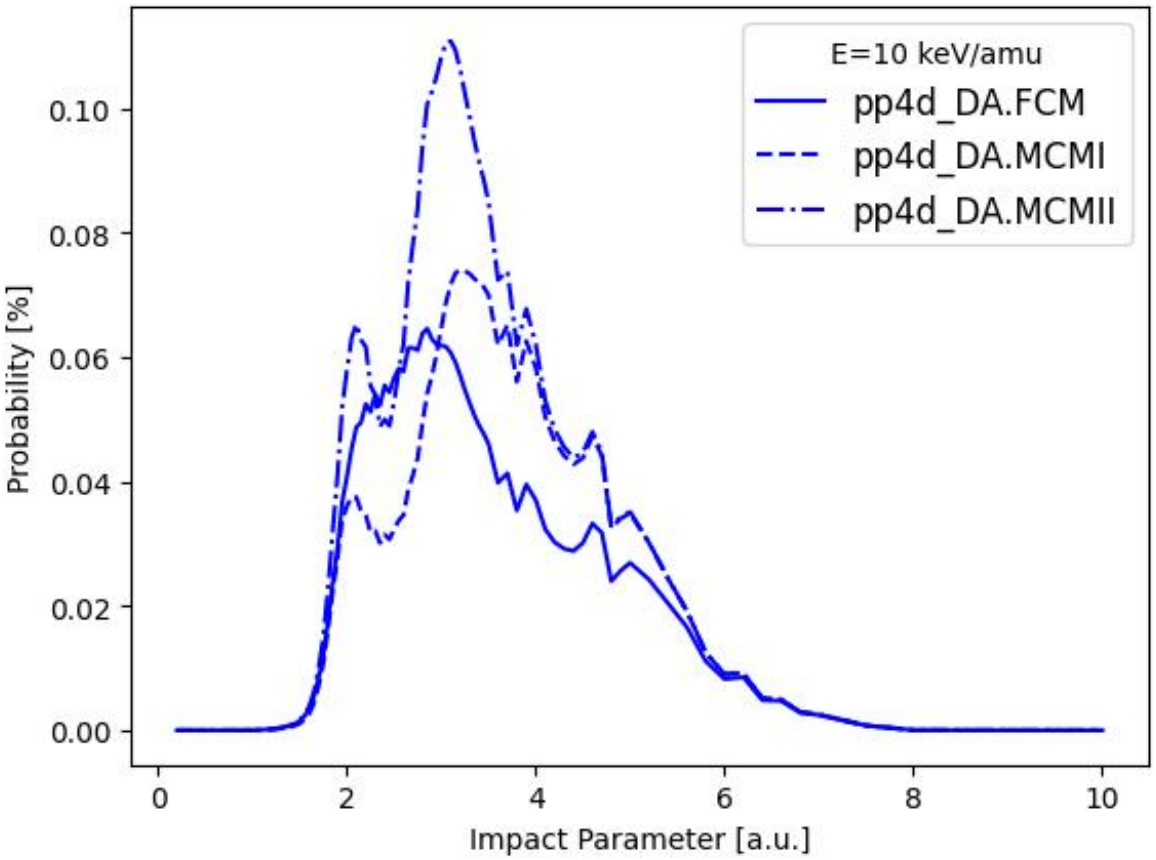


Figure B.71: $He^{2+}$–$Ar_2$ ion–dimer collisions in parallel orientation at 10 keV/amu. Single $3p$ electron removal with simultaneous $3p$ excitation to the $4d$ state probability comparing DA.FCM (solid line) and DA.MCMI (dashed line) and DA.MCMII (dashed-dotted line).

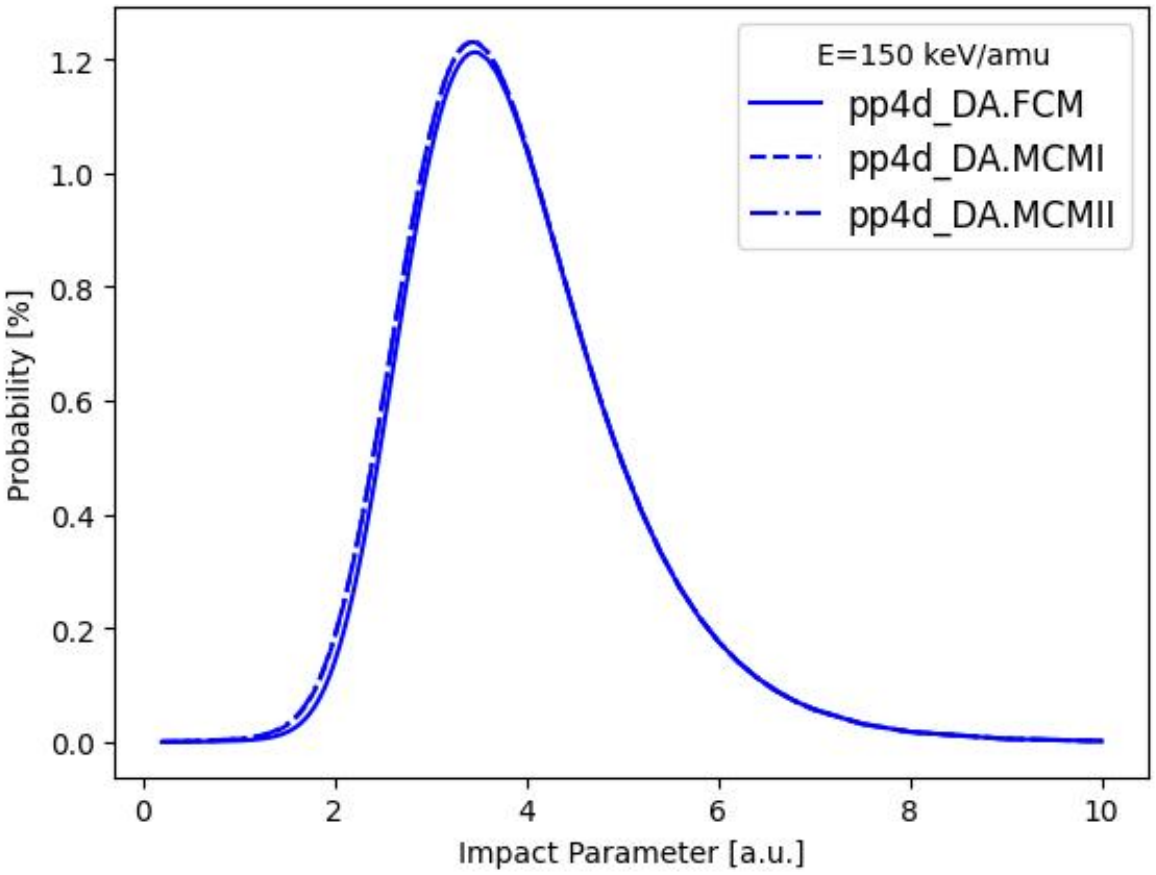


Figure B.72: $He^{2+}$–$Ar_2$ ion–dimer collisions in parallel orientation at 150 keV/amu. Single $3p$ electron removal with simultaneous $3p$ excitation to the $4d$ state probability comparing DA.FCM (solid line) and DA.MCMI (dashed line) and DA.MCMII (dashed-dotted line).

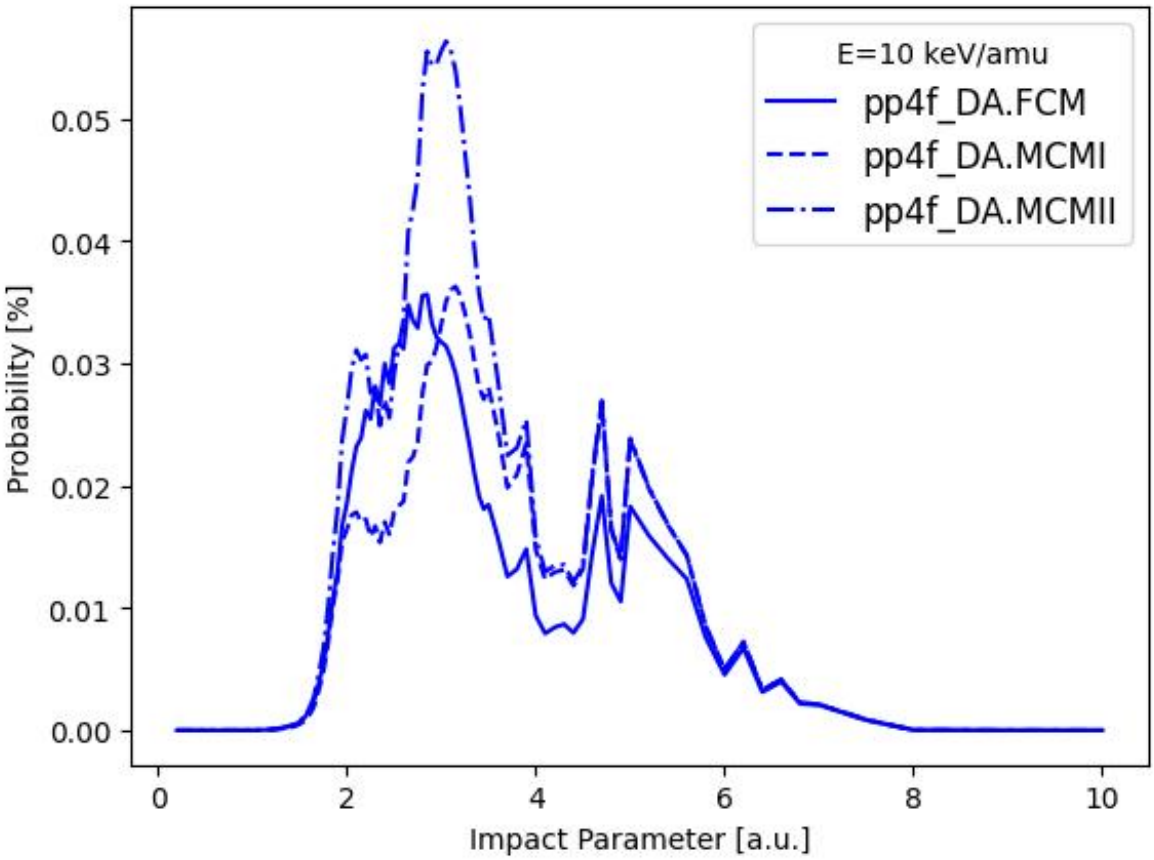


Figure B.73: $He^{2+}$–$Ar_2$ ion–dimer collisions in parallel orientation at 10 keV/amu. Single $3p$ electron removal with simultaneous $3p$ excitation to the $4f$ state probability comparing DA.FCM (solid line) and DA.MCMI (dashed line) and DA.MCMII (dashed-dotted line).

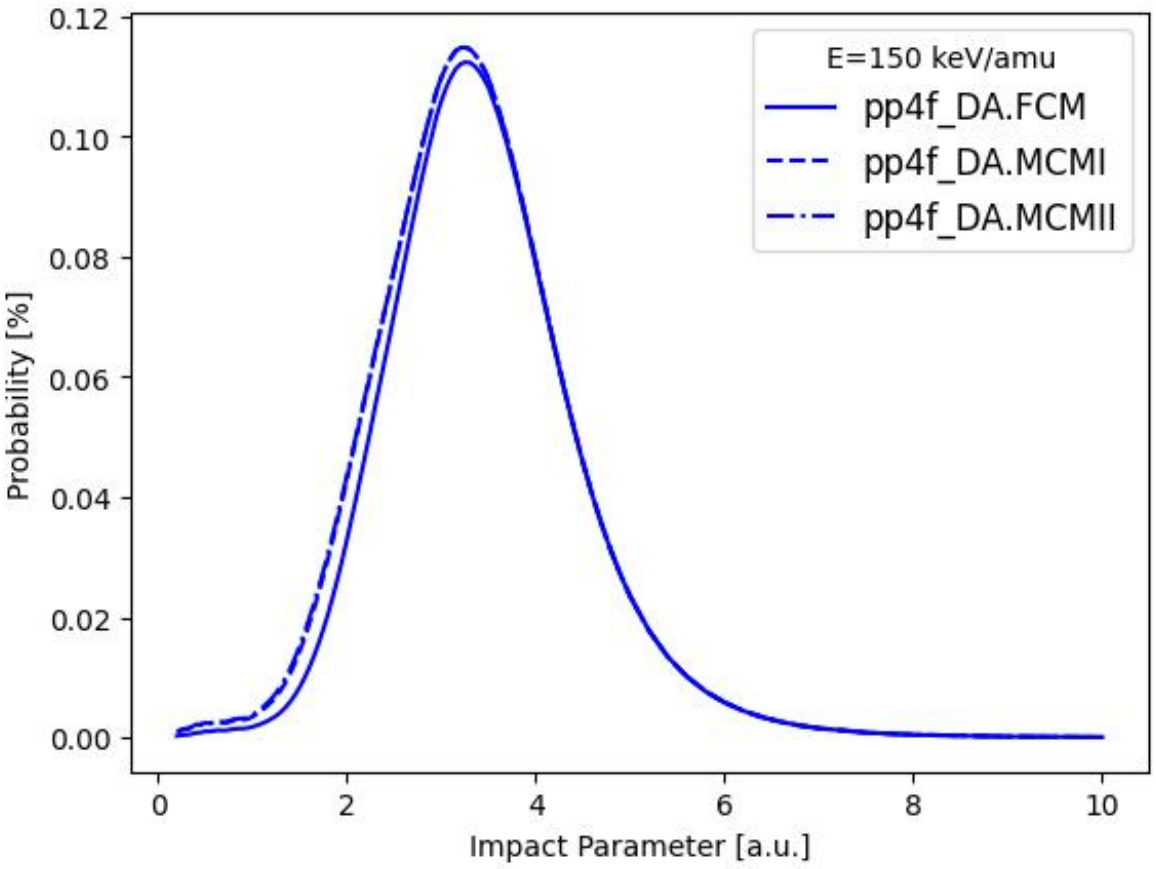


Figure B.74: $He^{2+}$–$Ar_2$ ion–dimer collisions in parallel orientation at 150 keV/amu. Single $3p$ electron removal with simultaneous $3p$ excitation to the $4f$ state probability comparing DA.FCM (solid line) and DA.MCMI (dashed line) and DA.MCMII (dashed-dotted line).

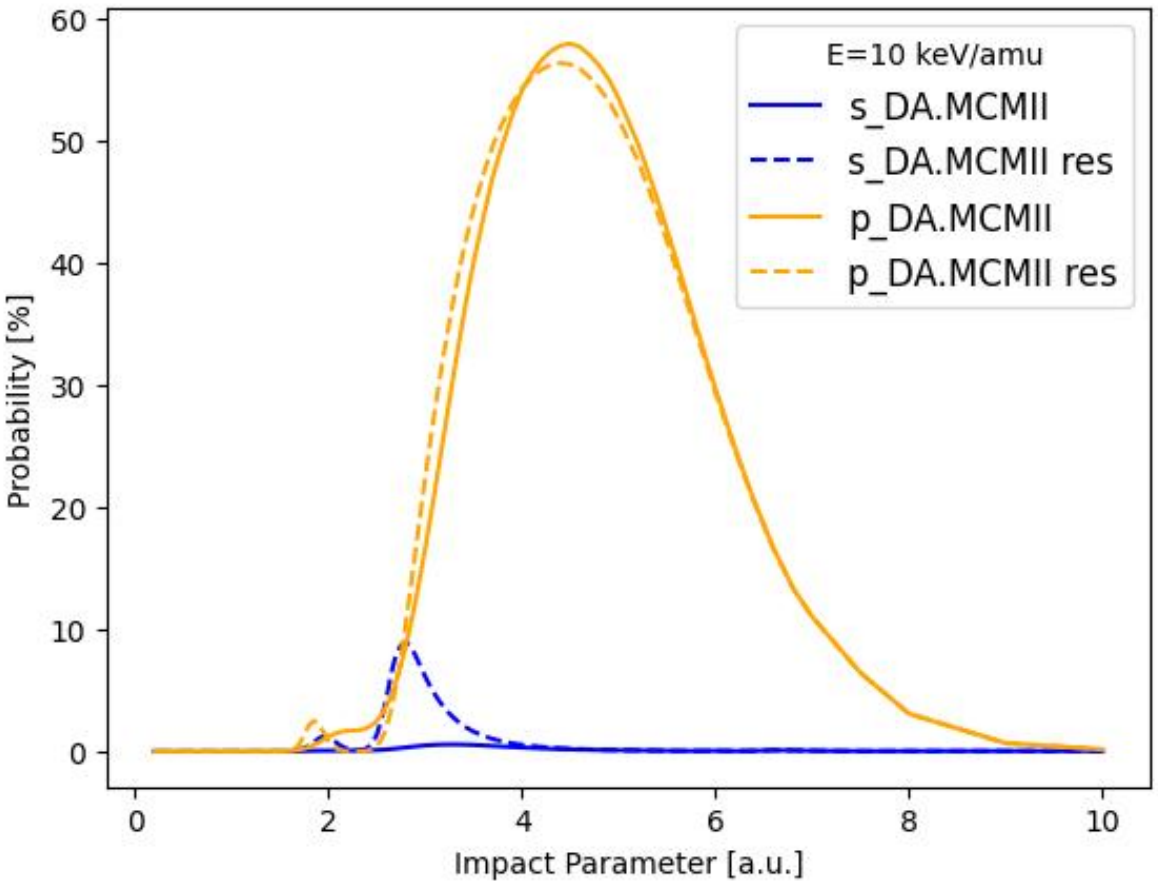


Figure B.75: $He^{2+}$–$Ar_2$ ion–dimer collisions in parallel orientation at 10 keV/amu. Single-electron removal probability comparing DA.MCMII (solid line) and DA.MCMII res (dashed line).

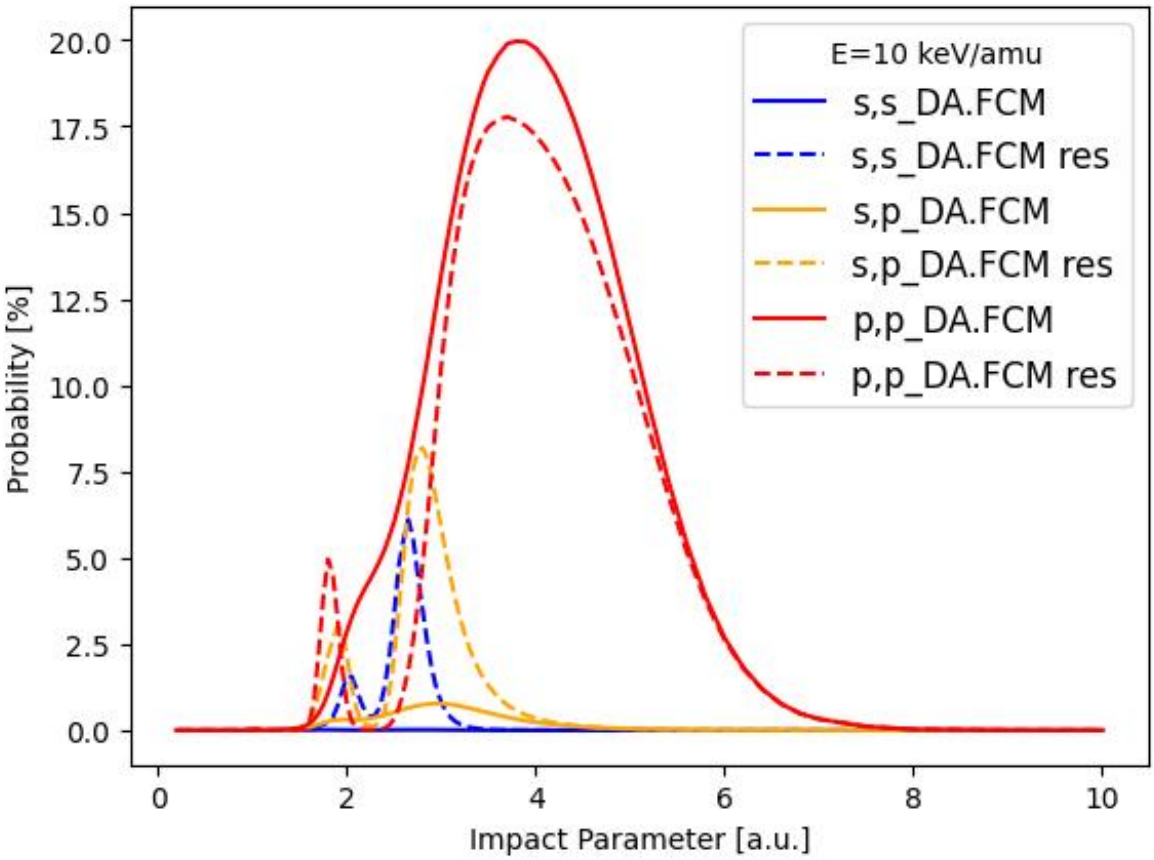


Figure B.76: $He^{2+}$–$Ar_2$ ion–dimer collisions in parallel orientation at 10 keV/amu. Two-site two-electron removal probability comparing DA.FCM (solid lines) and DA.MCMII res (dashed lines).

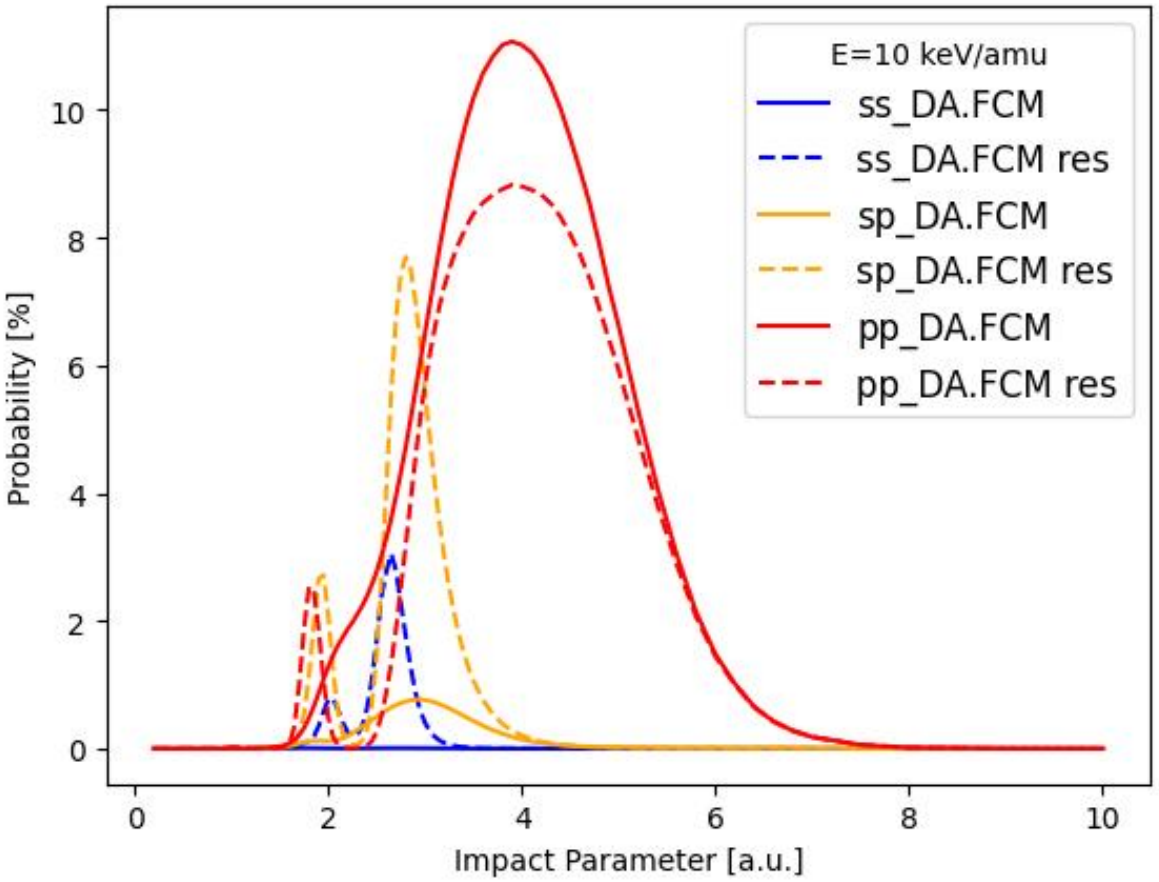


Figure B.77: $He^{2+}$–$Ar_2$ ion–dimer collisions in parallel orientation at 10 keV/amu. One-site two-electron removal probability comparing DA.FCM (solid lines) and DA.MCMII res (dashed lines).

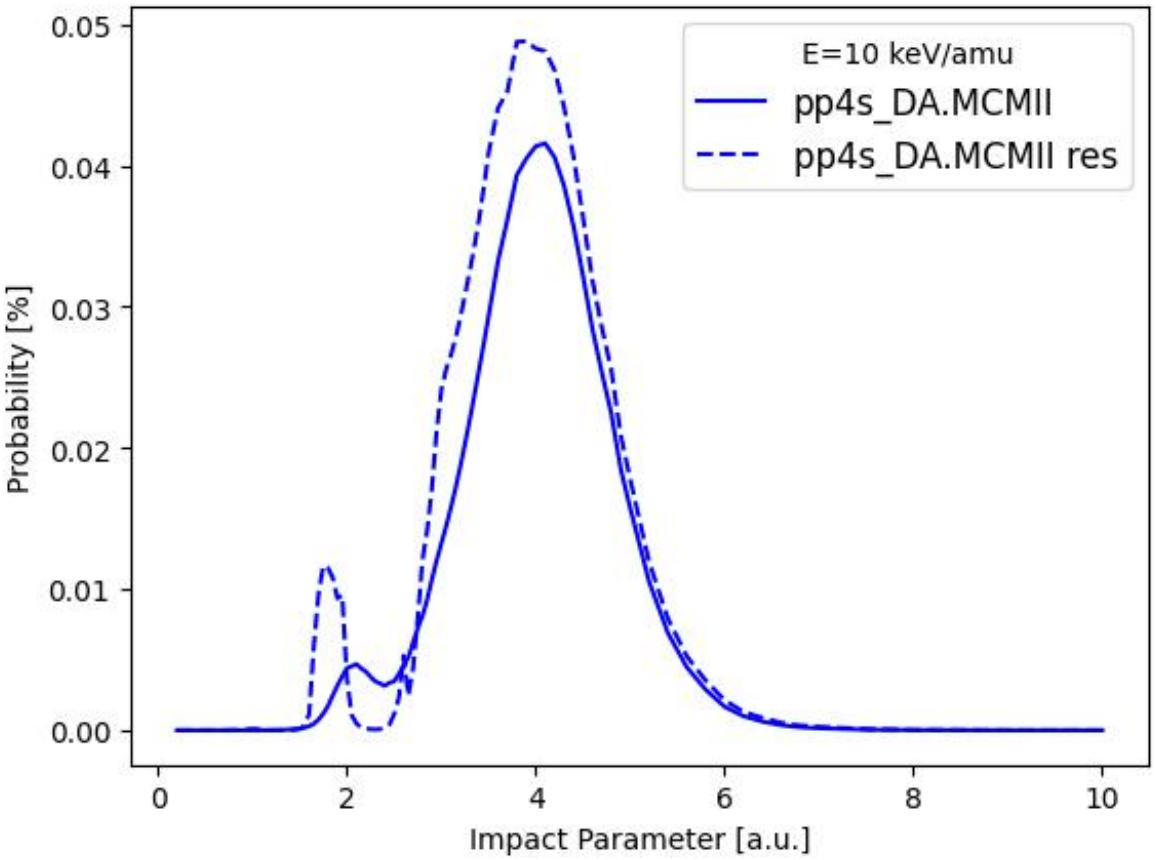


Figure B.78: $He^{2+}$–$Ar_2$ ion–dimer collisions in parallel orientation at 10 keV/amu. Single $3p$ electron removal with simultaneous $3p$ excitation to the $4s$ state probability comparing DA.MCMII (solid line) and DA.MCMII res (dashed line).

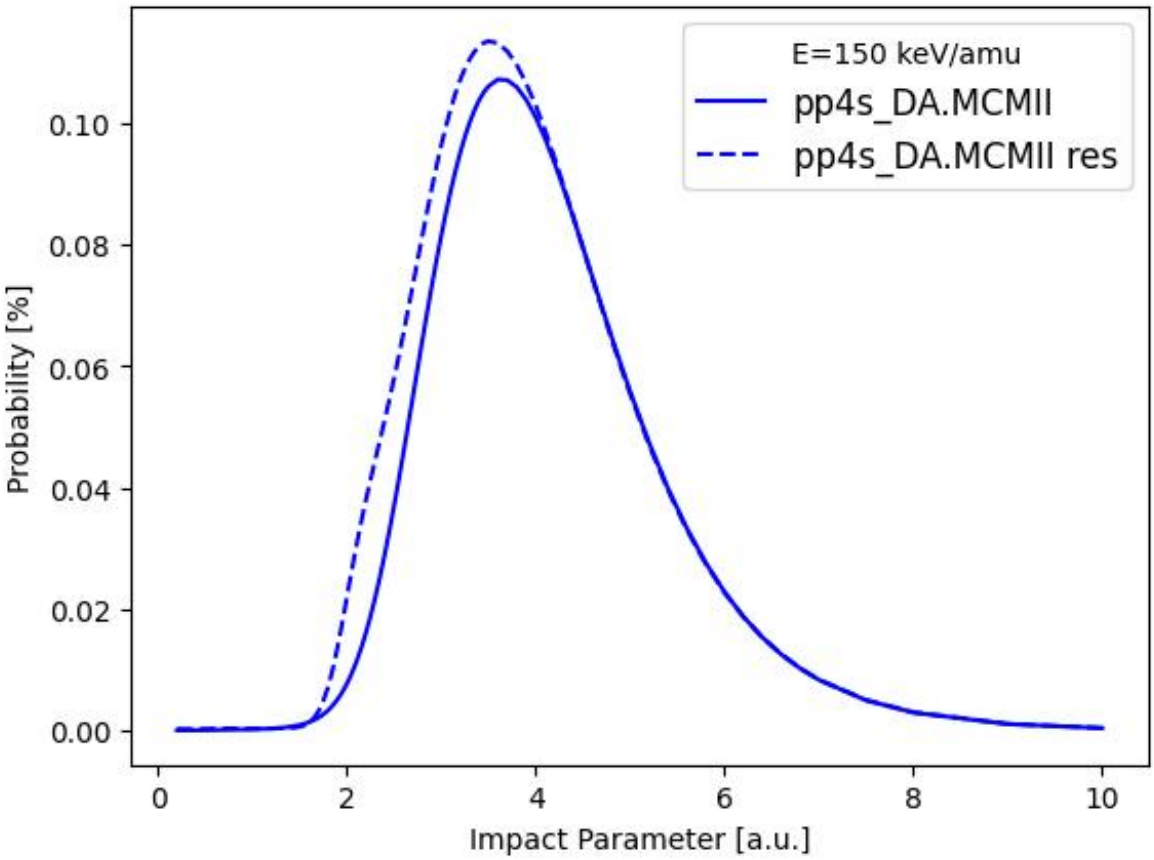


Figure B.79: $He^{2+}$–$Ar_2$ ion–dimer collisions in parallel orientation at 150 keV/amu. Single $3p$ electron removal with simultaneous $3p$ excitation to the $4s$ state probability comparing DA.MCMII (solid line) and DA.MCMII res (dashed line).

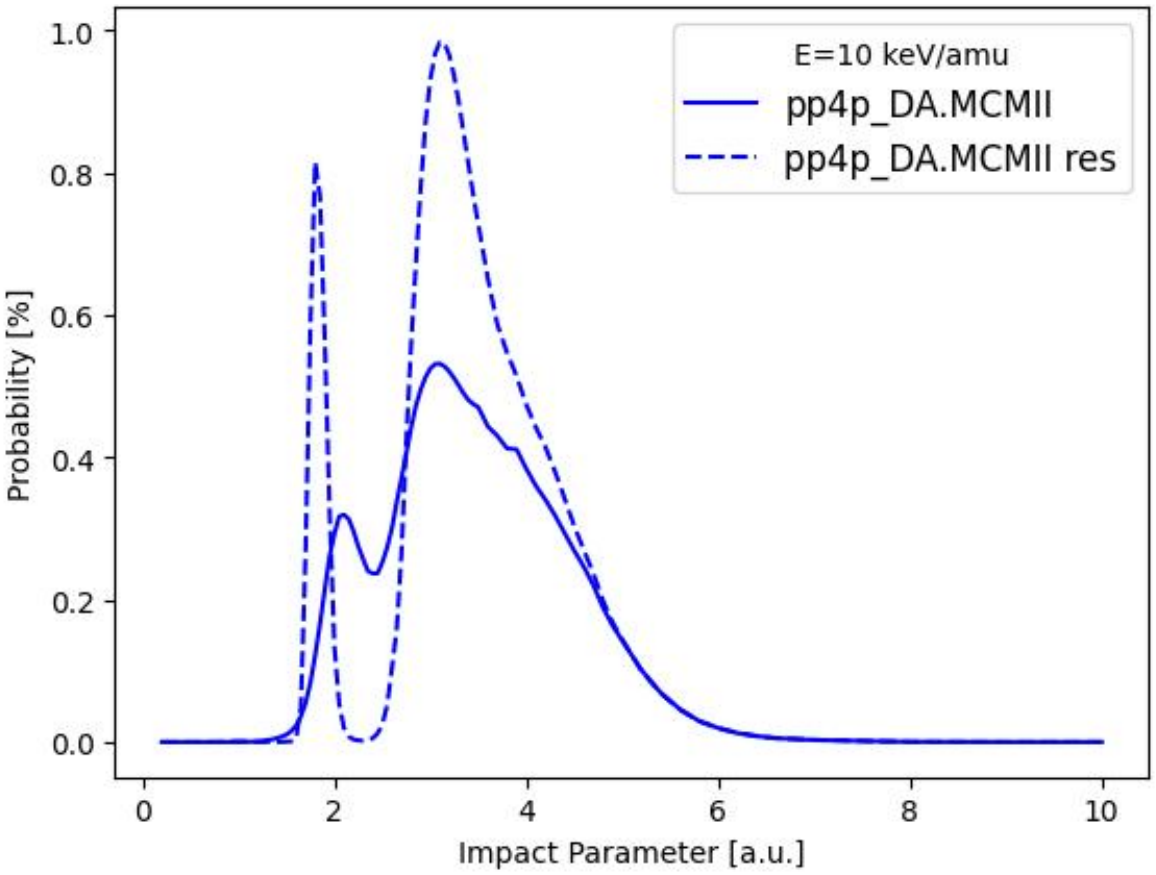


Figure B.80: $He^{2+}$–$Ar_2$ ion–dimer collisions in parallel orientation at 10 keV/amu. Single $3p$ electron removal with simultaneous $3p$ excitation to the $4p$ state probability comparing DA.MCMII (solid line) and DA.MCMII res (dashed line).

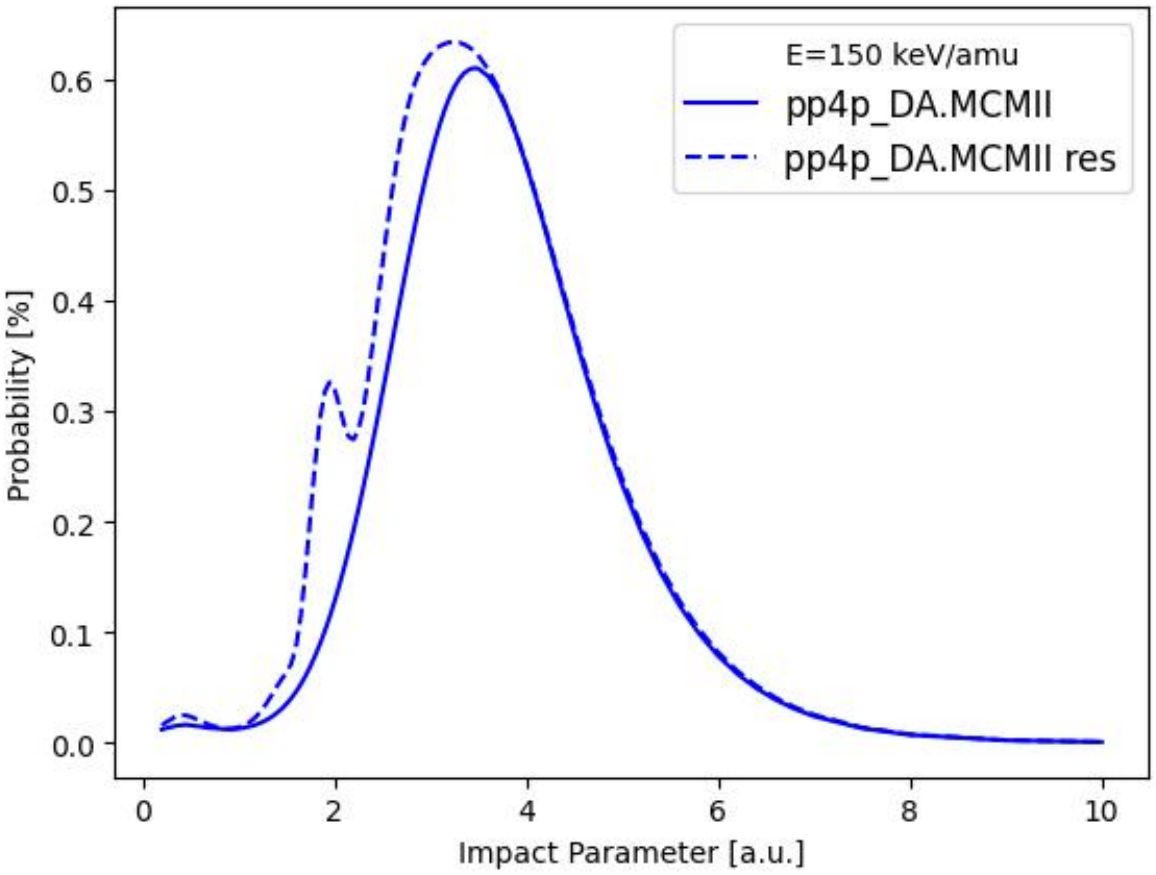


Figure B.81: $He^{2+}$–$Ar_2$ ion–dimer collisions in parallel orientation at 150 keV/amu. Single $3p$ electron removal with simultaneous $3p$ excitation to the $4p$ state probability comparing DA.MCMII (solid line) and DA.MCMII res (dashed line).

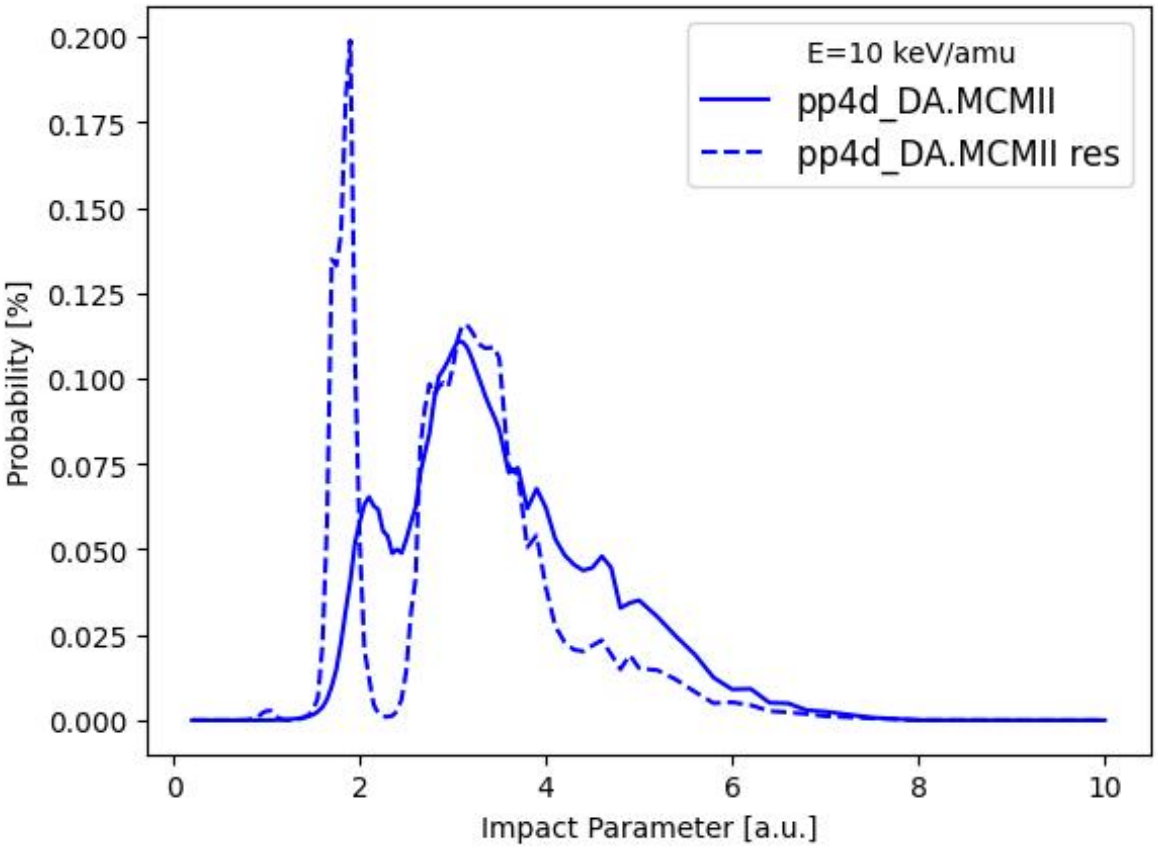


Figure B.82: $He^{2+}$–$Ar_2$ ion–dimer collisions in parallel orientation at 10 keV/amu. Single $3p$ electron removal with simultaneous $3p$ excitation to the $4d$ state probability comparing DA.MCMII (solid line) and DA.MCMII res (dashed line).

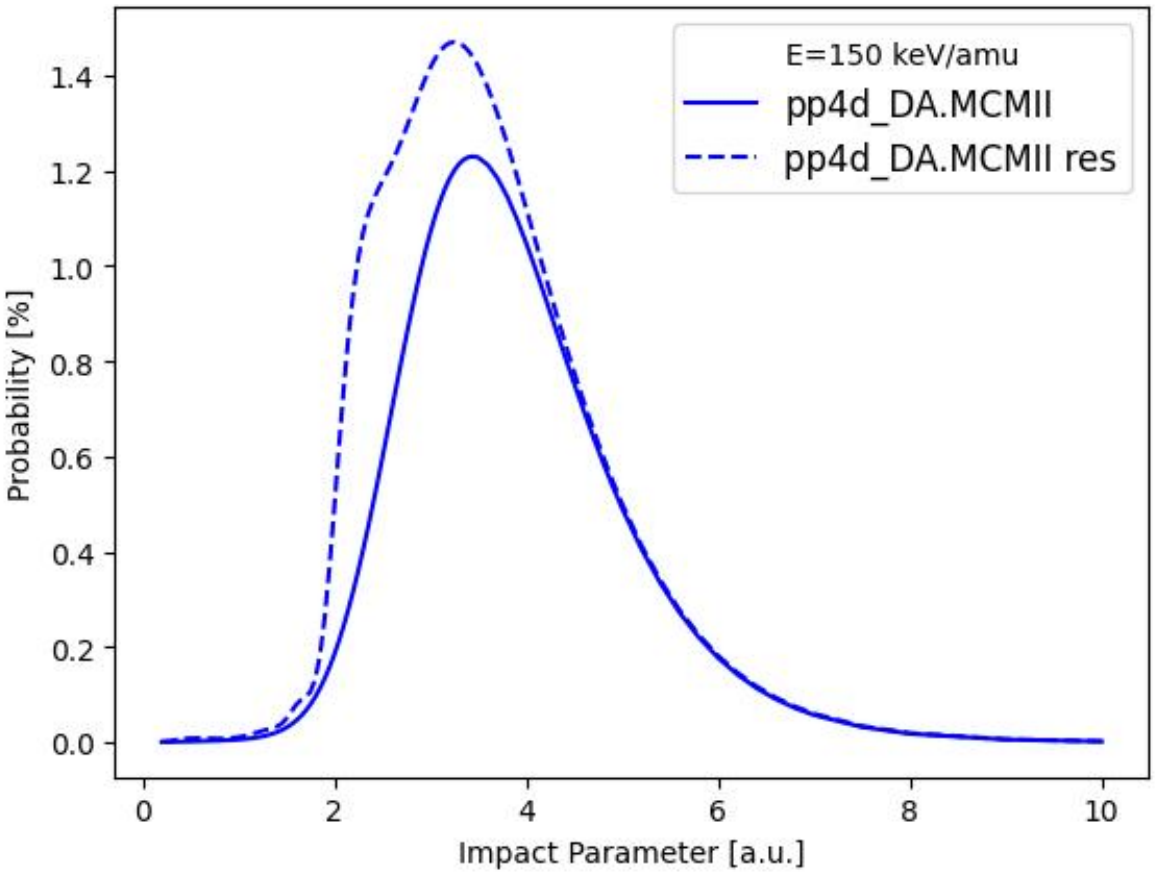


Figure B.83: $He^{2+}$–$Ar_2$ ion–dimer collisions in parallel orientation at 150 keV/amu. Single $3p$ electron removal with simultaneous $3p$ excitation to the $4d$ state probability comparing DA.MCMII (solid line) and DA.MCMII res (dashed line).

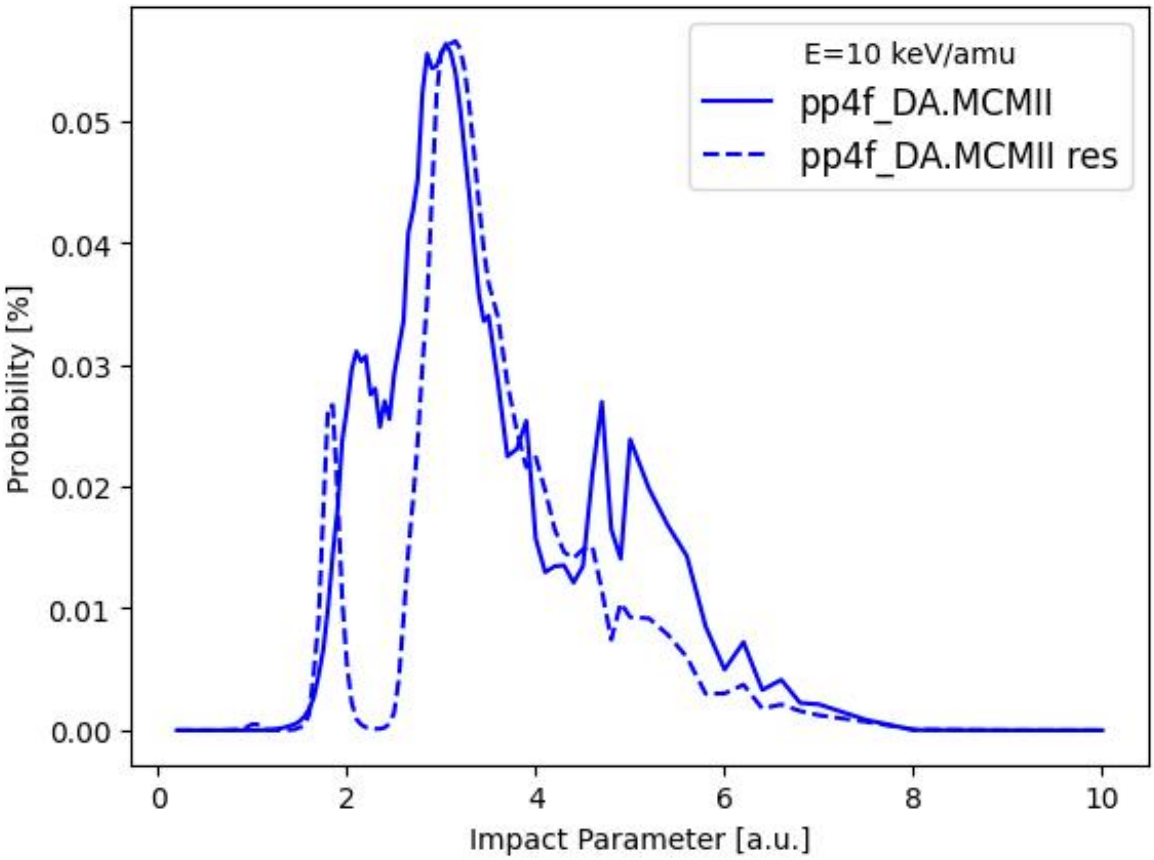


Figure B.84: $He^{2+}$–$Ar_2$ ion–dimer collisions in parallel orientation at 10 keV/amu. Single $3p$ electron removal with simultaneous $3p$ excitation to the $4f$ state probability comparing DA.MCMII (solid line) and DA.MCMII res (dashed line).

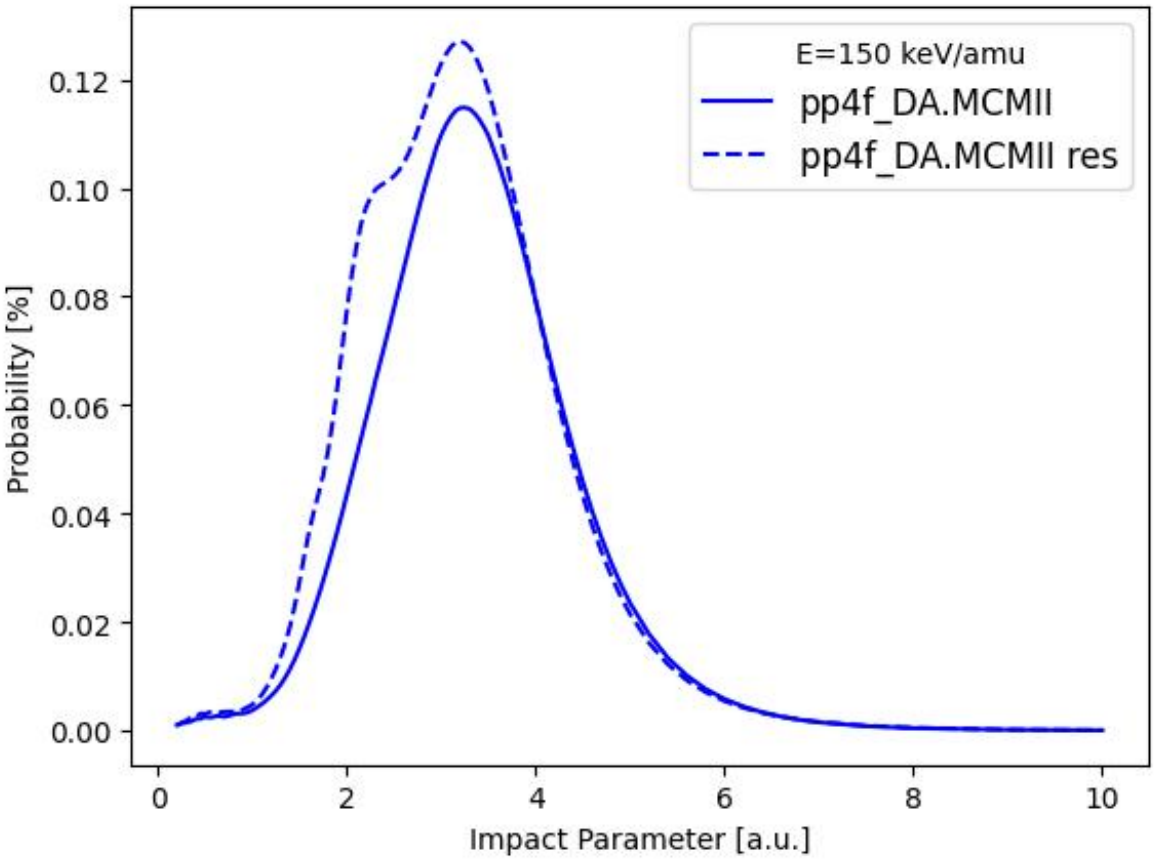


Figure B.85: $He^{2+}$–$Ar_2$ ion–dimer collisions in parallel orientation at 150 keV/amu. Single $3p$ electron removal with simultaneous $3p$ excitation to the $4f$ state probability comparing DA.MCMII (solid line) and DA.MCMII res (dashed line).

### 2. $He^+$ Projectile

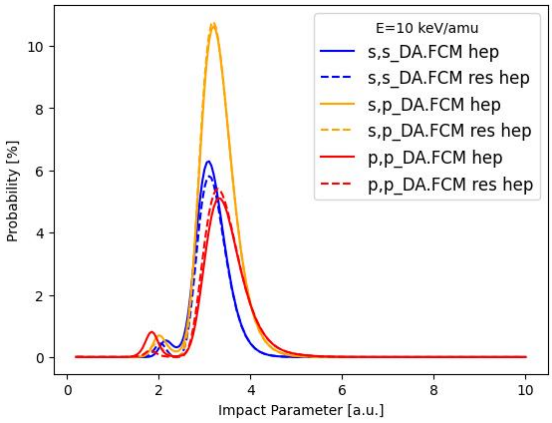


(a) 10 keV/amu

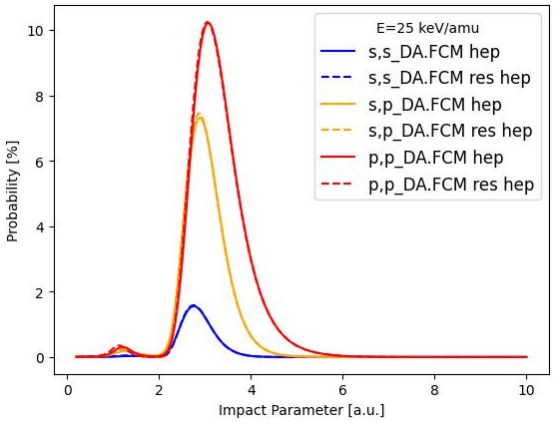


(b) 25 keV/amu

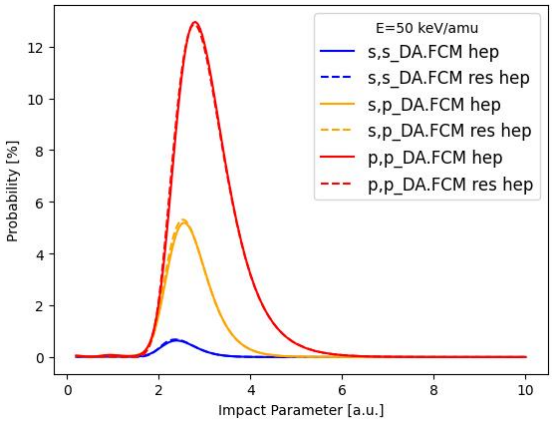


(c) 50 keV/amu

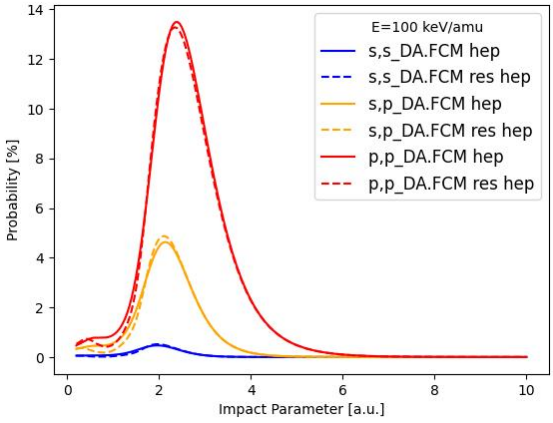


(d) 100 keV/amu

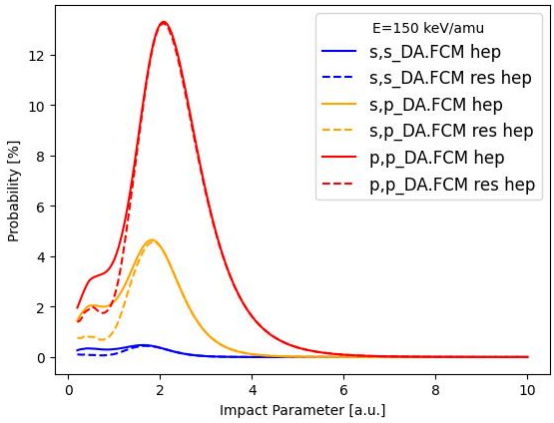


(e) 150 keV/amu

Figure B.86: $He^+$–$Ar_2$ ion–dimer collisions in parallel orientation. Two-site two-electron removal probabilities comparing DA.FCM (solid line) and DA.FCM res (dashed line) across different projectile impact energies.

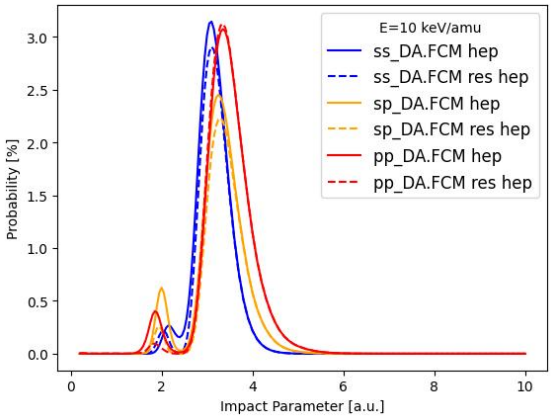


(a) 10 keV/amu

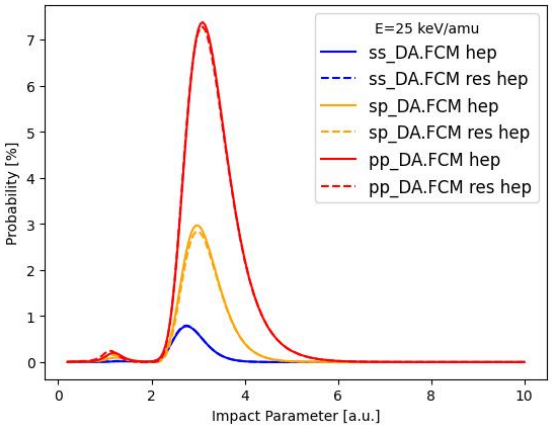


(b) 25 keV/amu

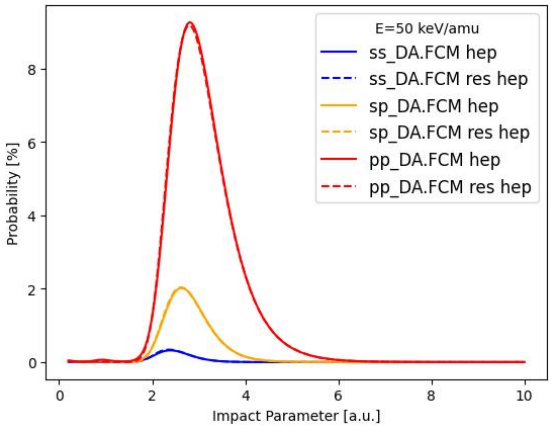


(c) 50 keV/amu

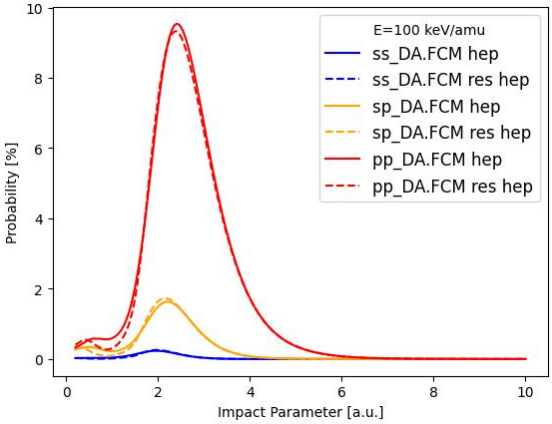


(d) 100 keV/amu

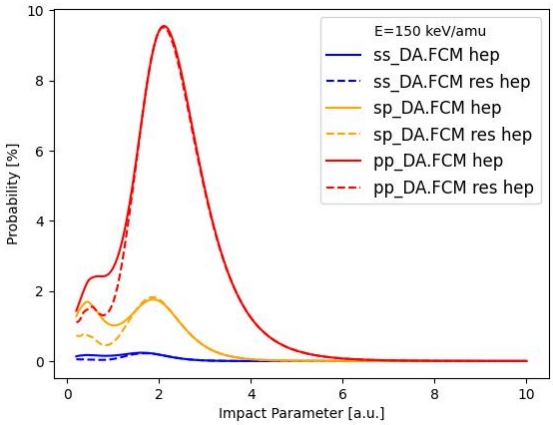


(e) 150 keV/amu

Figure B.87: $He^+$–$Ar_2$ ion–dimer collisions in parallel orientation. One-site two-electron removal probabilities comparing DA.FCM (solid line) and DA.FCM res (dashed line) across different projectile impact energies.

[1] T. Jahnke et al. Interatomic and Intermolecular Coulombic Decay. *Chemical Reviews*, 120(20):11295–11369, 2020.

[2] L. S. Cederbaum, J. Zobeley, and F. Tarantelli. Giant intermolecular decay and fragmentation of clusters. *Phys. Rev. Lett.*, 79:4778–4781, Dec 1997.

[3] S. Marburger, O. Kugeler, U. Hergenhahn, and T. Möller. Experimental Evidence for Interatomic Coulombic Decay in Ne Clusters. *Phys. Rev. Lett.*, 90:203401, May 2003.

[4] T. Jahnke et al. Experimental Observation of Interatomic Coulombic Decay in Neon Dimers. *Phys. Rev. Lett.*, 93:163401, Oct 2004.

[5] B. Najjari, Z. Wang, and A. B. Voitkiv. Probing the helium dimer by relativistic highly charged projectiles. *Phys. Rev. Lett.*, 127:203401, Nov 2021.

[6] G. Öhrwall et al. Femtosecond Interatomic Coulombic Decay in Free Neon Clusters: Large Lifetime Differences between Surface and Bulk. *Phys. Rev. Lett.*, 93:173401, Oct 2004.

[7] J. T. Moseley, R. P. Saxon, B. A. Huber, P. C. Cosby, R. Abouaf, and M. Tadjeddine. Photofragment spectroscopy and potential curves of $Ar_2^+$. *The Journal of Chemical Physics*, 67(4):1659–1668, 08 1977.

[8] T. Jahnke et al. Experimental Separation of Virtual Photon Exchange and Electron Transfer in Interatomic Coulombic Decay of Neon Dimers. *Phys. Rev. Lett.*, 99:153401, Oct 2007.

[9] Y. Morishita et al. Evidence of interatomic Coulombic decay in ArKr after Ar 2p Auger decay. *Journal of Physics B: Atomic, Molecular and Optical Physics*, 41(2):025101, Jan 2008.

[10] K. Sakai et al. Electron-Transfer-Mediated Decay and Interatomic Coulombic Decay from the Triply Ionized States in Argon Dimers. *Phys. Rev. Lett.*, 106:033401, Jan 2011.

[11] H.-K. Kim et al. Ion-impact-induced interatomic Coulombic decay in neon and argon dimers. *Phys. Rev. A*, 88:042707, Oct 2013.

[12] K. Schnorr et al. Time-Resolved Measurement of Interatomic Coulombic Decay in $Ne_2$. *Phys. Rev. Lett.*, 111:093402, Aug 2013.

[13] W. Iskandar et al. Interatomic Coulombic Decay as a New Source of Low Energy Electrons in Slow Ion-Dimer Collisions. *Phys. Rev. Lett.*, 114:033201, Jan 2015.

[14] S. Yan et al. Interatomic relaxation processes induced in neon dimers by electron-impact ionization. *Phys. Rev. A*, 97:010701, Jan 2018.

[15] A. Hans et al. Core-level interatomic Coulombic decay in van der Waals clusters. *Phys. Rev. Res.*, 2:012022, Jan 2020.

[16] R.C. Bilodeau et al. Photo double detachment of $CN^-$: Electronic decay from an inner-valence hole in molecular anions. *Chemical Physics Letters*, 426(4):237–241, 2006.

[17] T. Jahnke et al. Ultrafast energy transfer between water molecules. *Nature Phys*, 6:139–142, 01 2010.

[18] M. Mucke et al. A hitherto unrecognized source of low-energy electrons in water. *Nature Phys*, 6:143–146, 01 2010.

[19] C. Richter et al. Competition between proton transfer and intermolecular Coulombic decay in water. *Nat Commun*, 9(4988), 11 2018.

[20] X. Ren et al. Experimental evidence for ultrafast intermolecular relaxation processes in hydrated biomolecules. *Nature Phys*, 14:1062–1066, 2018.

[21] M. Shcherbinin et al. Interatomic Coulombic decay in helium nanodroplets. *Phys. Rev. A*, 96:013407, Jul 2017.

[22] S. Kazandjian et al. Frustrated Coulomb explosion of small helium clusters. *Phys. Rev. A*, 98:050701, Nov 2018.

[23] F. Stienkemeier et al. Highly efficient double ionization of mixed alkali dimers by intermolecular coulombic decay. *Nat. Phys.*, 15:247–250, 2019.

[24] R. A. Wilhelm et al. Interatomic Coulombic Decay: The Mechanism for Rapid Deexcitation of Hollow Atoms. *Phys. Rev. Lett.*, 119:103401, Sep 2017.

[25] N. Ottosson et al. Cations strongly reduce electron-hopping rates in aqueous solutions. *J. Am. Chem. Soc.*, 133:13489–13495, 2011.

[26] S. Barik et al. Ambient-light-induced intermolecular Coulombic decay in unbound pyridine monomers. *Nat. Chem.*, 14:1098–1102, 2022.

[27] A. Dubrouil et al. Two-photon resonant excitation of interatomic Coulombic decay in neon dimers. *Journal of Physics B: Atomic, Molecular and Optical Physics*, 48(20):204005, Sep 2015.

[28] D. Iablonskyi et al. Slow Interatomic Coulombic Decay of Multiply Excited Neon Clusters. *Phys. Rev. Lett.*, 117:276806, Dec 2016.

[29] A. C. LaForge et al. Ultrafast Resonant Interatomic Coulombic Decay Induced by Quantum Fluid Dynamics. *Phys. Rev. X*, 11:021011, Apr 2021.

[30] G. A. Grieves and T. M. Orlando. Intermolecular Coulomb Decay at Weakly Coupled Heterogeneous Interfaces. *Phys. Rev. Lett.*, 107:016104, Jul 2011.

[31] S. Yan et al. Observation of interatomic Coulombic decay and electron-transfer-mediated decay in high-energy electron-impact ionization of $Ar_2$. *Phys. Rev. A*, 88:042712, Oct 2013.

[32] T. Pflüger, X. Ren, and A. Dorn. Electron-impact-induced dissociation of small argon clusters. *Phys. Rev. A*, 91:052701, May 2015.

[33] X. Ren et al. Direct evidence of two interatomic relaxation mechanisms in argon dimers ionized by electron impact. *Nat Commun*, 7(11093), Mar 2016.

[34] J. Zhou et al. Concerted double hydrogen-bond breaking by intermolecular Coulombic decay in the formic acid dimer. *J. Phys. Chem. Lett.*, 13:4272–4279, 2022.

[35] H.-K. Kim et al. Enhanced production of low energy electrons by alpha particle impact. *Proceedings of the National Academy of Sciences*, 108(29):11821–11824, 2011.

[36] H.-K. Kim et al. Orientation dependence in multiple ionization of $He_2$ and $Ne_2$ induced by fast, highly charged ions: Probing the impact-parameter-dependent ionization probability in 11.37-MeV/u $S^{14+}$ collisions with He and Ne. *Phys. Rev. A*, 89:022704, Feb 2014.

[37] A. Cassimi et al. Why are atomic and molecular dimers so exciting? *Journal of Physics B: Atomic, Molecular and Optical Physics*, 59(4):042001, Feb 2026.

[38] B. Schütte et al. Low-Energy Electron Emission in the Strong-Field Ionization of Rare Gas Clusters. *Phys. Rev. Lett.*, 121:063202, Aug 2018.

[39] J. Schwestka et al. Charge-exchange-driven low-energy electron splash induced by heavy ion impact on condensed matter. *The Journal of Physical Chemistry Letters*, 10(17):4805–4811, 2019.

[40] B. Boudaïffa et al. Resonant Formation of DNA Strand Breaks by Low-Energy (3 to 20 eV) Electrons. *Science*, 287(5458):1658–1660, 2000.

[41] E. Alizadeh, T. Orlando, and L. Sanche. Biomolecular damage induced by ionizing radiation: The direct and indirect effects of low-energy electrons on dna. *Annual Review Physical Chemistry*, 66:379–398, 2015.

[42] O. Vendrell, S. D. Stoychev, and L. S. Cederbaum. Generation of Highly Damaging $H_2O^+$ Radicals by Inner Valence Shell Ionization of Water. *ChemPhysChem*, 11(5):1006–1009, 2010.

[43] L Pettersson. Radical water. *Nature Chem*, 5:553–554, 2013.

[44] J. Titze et al. Ionization Dynamics of Helium Dimers in Fast Collisions with $He^{++}$. *Phys.*

*Rev. Lett.*, 106:033201, Jan 2011.

[45] D. Bhattacharya and T. Kirchner. Strengthening the case for interatomic Coulomb decay as a subdominant reaction channel in slow $O^{3+}-Ne_2$ collisions with independent-atom-model coupled-channel calculations. *Phys. Rev. A*, 102:062816, Dec 2020.

[46] W. Iskandar et al. Coulomb over-the-barrier Monte Carlo simulation to probe ion-dimer collision dynamics. *Phys. Rev. A*, 98:012701, Jul 2018.

[47] T. Kirchner. Indication of strong interatomic Coulombic decay in slow $He^{2+}-Ne_2$ collisions. *Journal of Physics B: Atomic, Molecular and Optical Physics*, 54(20):205201, Oct 2021.

[48] H. J. Lüdde et al. An independent-atom-model description of ion-molecule collisions including geometric screening corrections. *Eur. Phys. J. D*, 70(82), 2016.

[49] S. Paredes, C. Illescas, and L. Méndez. A study of electron production in proton-biomolecule collisions using additivity rules. *Journal of Physics: Conference Series*, 635, 2015.

[50] D. I. Thwaites. Bragg's rule of stopping power additivity: A compilation and summary of results. *Radiation Research*, 95(3):495–518, 1983.

[51] T. Kirchner and M. Horbatsch. Nonperturbative calculation of projectile-electron loss, target ionization, and capture in $He^+$+Ne collisions. *Phys. Rev. A*, 63:062718, May 2001.

[52] P.-O. Löwdin. Quantum Theory of Many-Particle Systems. III. Extension of the Hartree-Fock Scheme to Include Degenerate Systems and Correlation Effects. *Phys. Rev.*, 97:1509–1520, Mar 1955.

[53] H. Nakashima and H. Nakatsuji. Solving the Schrödinger equation for helium atom and its isoelectronic ions with the free iterative complement interaction (ICI) method. *The Journal of Chemical Physics*, 127(22), 12 2007.

[54] K. J. Schaudt, N. H. Kwong, and J. D. Garcia. Fully converged time-dependent Hartree-Fock results for $He^{2+}$-He: Correlation in inclusive charge transfer. *Phys. Rev. A*, 43:2294–2299, Mar 1991.

[55] J. H. McGuire. Correlation in atomic scattering. *Phys. Rev. A*, 36:1114–1123, Aug 1987.

[56] K. Gramlich, N. Grün, and W. Scheid. The time-dependent Hartree-Fock method within a Gauss-lobe basis and application to proton-He collisions. *Journal of Physics B: Atomic and Molecular Physics*, 19(10):1457, May 1986.

[57] D. A. Micha and K. Runge. Time-dependent many-electron approach to slow ion-atom collisions: The coupling of electronic and nuclear motions. *Phys. Rev. A*, 50:322–336, Jul 1994.

[58] E. Engel and S. H. Vosko. Accurate optimized-potential-model solutions for spherical spin-polarized atoms: Evidence for limitations of the exchange-only local spin-density and generalized-gradient approximations. *Phys. Rev. A*, 47:2800–2811, Apr 1993.

[59] J. D. Talman and W. F. Shadwick. Optimized effective atomic central potential. *Phys. Rev. A*, 14:36–40, Jul 1976.

[60] W. Kohn and L. J. Sham. Self-consistent equations including exchange and correlation effects. *Phys. Rev.*, 140:A1133–A1138, Nov 1965.

[61] R. M. Dreizler and E. K. U. Gross. *Density Functional Theory: An Approach to the Quantum-Many Problem*. Springer Berlin, Heidelberg, 1990.

[62] H.J. Lüdde, M. Horbatsch, and T. Kirchner. A screened independent atom model for the description of ion collisions from atomic and molecular clusters. *Eur.Phys.J.B*, 91(99), June 2018.

[63] E. Engel and R. M. Dreizler. *Density Functional Theory: An Advanced Course*, chapter 6, pages 227–306. Springer Berlin, Heidelberg, 1st edition, 2011.

[64] E. Engel, C. Fiolhais, F. Nogueira, and M. A. L. Marques. *A Primer in Density Functional Theory*, chapter Orbital-Dependent Functionals for the Exchange-Correlation Energy: A Third Generation of Density Functionals, pages 56–122. Springer Berlin Heidelberg, 1st edition, 2003.

[65] D. Starko and T. Kirchner. Investigations of electron removal processes in slow $He^{2+}$- and $He^{+}$-$Ne_2$ collisions and of their implications for the subsequent dimer fragmentation through interatomic Coulombic decay. *Journal of Physics B: Atomic, Molecular and Optical Physics*, 58(7):075204, Apr 2025.

[66] T. Kirchner, A. L. Ford, J. F. Reading, and in: G.W.F. Drake. *Springer Handbook of Atomic, Molecular, and Optical Physics*, chapter Ion–Atom and Atom–Atom Collisions, pages 785–794. Springer International Publishing, Cham, 2023.

[67] D. Starko and T. Kirchner. Interatomic Coulombic decay initiated by electron removal and excitation processes in helium ion and argon dimer collisions. *Eur. Phys. J. Spec. Top.*, May 2026.

[68] T. Kirchner, M. Horbatsch, H. J. Lüdde, and R. M. Dreizler. Time-dependent screening effects in ion-atom collisions with many active electrons. *Phys. Rev. A*, 62:042704, Sep 2000.

[69] G. Schenk. *On the Role of Projectile Electrons in an Independent Electron Model Description of Dressed-Ion Impact on Atoms*. PhD thesis, York University, 06 2016.

[70] T. Kirchner, M. Horbatsch, and H. J. Lüdde. Coupled mean-field description of electron removal processes in $He^+$–Ne and $He^+$–Ar collisions. *Journal of Physics B: Atomic, Molecular and Optical Physics*, 37(11):2379, May 2004.

[71] W. Stich, H.J. Lüdde, and R.M. Dreizler. Time-dependent Hartree-Fock description of one and two electron capture in collisions of $(He + He)^{2+}$. *Physics Letters A*, 99(1):41–45, 1983.

[72] G. Schenk and T. Kirchner. Multiple ionization of neon atoms in collisions with bare and dressed ions: A mean-field description considering target response. *Phys. Rev. A*, 91:052712, May 2015.

[73] M. Zapukhlyak et al. Inner- and outer-shell electron dynamics in proton collisions with sodium atoms. *J. Phys. B*, 38(14):2353, 2005.

[74] O. J. Kroneisen, H. J. Lüdde, T. Kirchner, and R. M. Dreizler. The basis generator method: optimized dynamical representation of the solution of time-dependent quantum problems. *Journal of Physics A: Mathematical and General*, 32(11):2141, Mar 1999.

[75] H. J. Lüdde, A. Henne, T. Kirchner, and R. M. Dreizler. Optimized dynamical representation of the solution of time-dependent quantum problems. *Journal of Physics B: Atomic, Molecular and Optical Physics*, 29(19):4423, Oct 1996.

[76] T. Kirchner, M. Horbatsch, H. J. Lüdde, and R. M. Dreizler. Time-dependent screening effects in ion-atom collisions with many active electrons. *Phys. Rev. A*, 62:042704, Sep 2000.

[77] T. Kirchner, M. Horbatsch, and H. J. Lüdde. Time-dependent independent-particle model calculation of multiple capture and ionization processes in $p - \mathrm{Ar}$, $\overline{p} - \mathrm{Ar}$, and $He^{2+} - \mathrm{Ar}$ collisions. *Phys. Rev. A*, 66:052719, Nov 2002.

[78] T. Kirchner, M. Horbatsch, and H. J. Lüdde. Nonperturbative calculation of charge-changing processes in $C^{4+}$ scattering from neon atoms. *Phys. Rev. A*, 64:012711, Jun 2001.

[79] T. Kirchner, H. J. Lüdde, and R. M. Dreizler. Effective single-particle description of single and multiple processes in $p^{\pm} + \mathrm{Ne}$ collisions. *Phys. Rev. A*, 61:012705, Dec 1999.

[80] T. Spranger and T. Kirchner. Auger-like processes in multiple ionization of noble gas atoms by protons. *Journal of Physics B: Atomic, Molecular and Optical Physics*, 37(20):4159, Oct 2004.

[81] T. Kirchner. *Quantentheoretische Beschreibung von Vielelektronenprozessen in Ion-Atom-Stößen*. PhD thesis, Goethe University Frankfurt, 1999.

[82] P. Reinhed et al. Precision Lifetime Measurements of $He^-$ in a Cryogenic Electrostatic Ion-

Beam Trap. *Phys. Rev. Lett.*, 103:213002, Nov 2009.

[83] H. J. Lüdde and R. M. Dreizler. Comment on inclusive cross sections. *Journal of Physics B: Atomic and Molecular Physics*, 18(1):107, Jan 1985.

[84] A. Toepfer, H. J. Lüdde, B. Jacob, and R. M. Dreizler. Many-electron aspects in ion-atom collisions: 2p-2s vacancy transfer in the $Ne^{+}$+Ne system. *Journal of Physics B: Atomic and Molecular Physics*, 18(10):1969, May 1985.

[85] A. Kramida, Yu. Ralchenko, J. Reader, and and NIST ASD Team. NIST Atomic Spectra Database (ver. 5.12), [Online]. Available: `https://physics.nist.gov/asd` [2025, December 4]. National Institute of Standards and Technology, Gaithersburg, MD., 2024.

[86] M. Keim, A. Achenbach, H.J. Lüdde, and T. Kirchner. Time-dependent density functional theory calculations for collisions of bare ions with helium. *Nuclear Instruments and Methods in Physics Research Section B: Beam Interactions with Materials and Atoms*, 233(1):240–243, 2005.